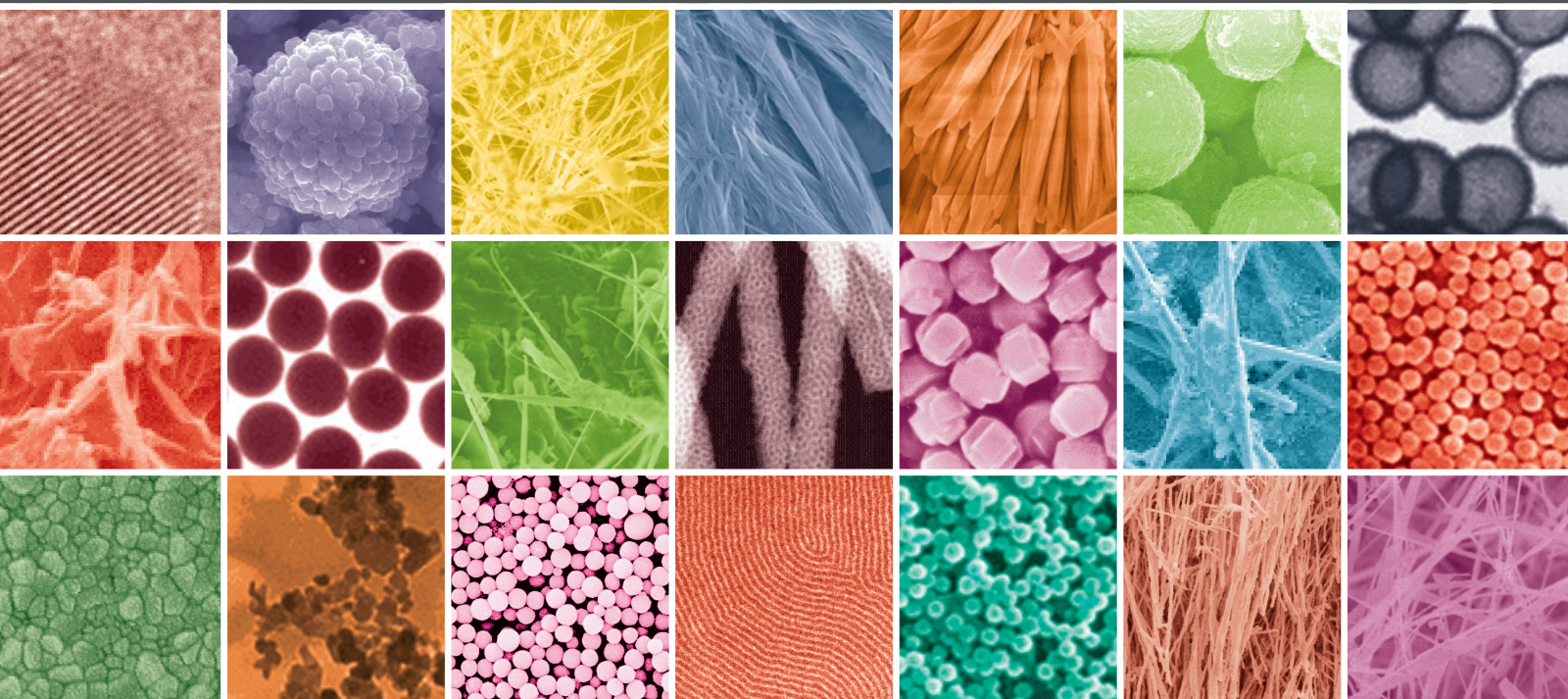


1D Nanomaterials

Guest Editors: Raymond L. D. Whitby, Steve F. A. Acquah,
Renzhi Ma, and Yanqiu Zhu





1D Nanomaterials

Journal of Nanomaterials

1D Nanomaterials

Guest Editors: Raymond L. D. Whitby, Steve F. A. Acquah,
Renzhi Ma, and Yanqiu Zhu



Copyright © 2010 Hindawi Publishing Corporation. All rights reserved.

This is a special issue published in volume 2010 of “Journal of Nanomaterials.” All articles are open access articles distributed under the Creative Commons Attribution License, which permits unrestricted use, distribution, and reproduction in any medium, provided the original work is properly cited.

Editor-in-Chief

Michael Z. Hu, Oak Ridge National Laboratory, USA

Advisory Board

James H. Adair, USA
C. Jeffrey Brinker, USA
T. Hyeon, Republic of Korea
Nathan Lewis, USA

Ed Ma, USA
Alon V McCormick, USA
Gary L. Messing, USA
Zhonglin Wang, USA

Enge Wang, China
Ching Ping Wong, USA
N. Xu, China
Jackie Y. Ying, Singapore

Associate Editors

Xuedong Bai, China
Theodorian Borca-Tasciuc, USA
Christian Brosseau, France
Sang-Hee Cho, Republic of Korea
Cui ChunXiang, China
Ali Eftekhari, USA
Claude Estournes, France
Alan Fuchs, USA
Lian Gao, China
Hongchen Chen Gu, China
Michael Harris, USA
Justin D. Holmes, Ireland
David Hui, USA
Wanqin Jin, China

Rakesh K. Joshi, USA
Do Kyung Kim, Republic of Korea
Kin Tak Lau, Hong Kong
Burtrand Lee, USA
Jun Li, Singapore
Shijun Liao, China
Gong Ru Lin, Taiwan
J. -Y. Liu, USA
Jun Liu, USA
Songwei Lu, USA
Daniel Lu, China
Gaurav Mago, USA
Sanjay R. Mathur, Germany
Nobuhiro Matsushita, Japan

Sherine Obare, USA
P. Panine, France
Edward Andrew Payzant, USA
Donglu Shi, USA
Bohua Sun, South Africa
Maryam Tabrizian, Canada
Theodore Tsotsis, USA
Xiaogong Wang, China
Yong Wang, China
Michael S. Wong, USA
Ping Xiao, UK
Zhi-Li Xiao, USA
Doron Yadlovker, Israel
Kui Yu, Canada

Contents

ID Nanomaterials, Raymond L. D. Whitby, Steve F. A. Acquah, Renzhi Ma, and Yanqiu Zhu
Volume 2010, Article ID 597851, 3 pages

Role of Reaction and Factors of Carbon Nanotubes Growth in Chemical Vapour Decomposition Process Using Methane **A Highlight**, Sivakumar VM, Abdul Rahman Mohamed, Ahmad Zuhairi Abdullah, and Siang-Piao Chai
Volume 2010, Article ID 395191, 11 pages

A Facile and Generic Strategy to Synthesize Large-Scale Carbon Nanotubes, Yong Hu, Ting Mei, Libo Wang, and Haisheng Qian
Volume 2010, Article ID 415940, 5 pages

One-Step Route to Synthesize Multiwalled Carbon Nanotubes Filled with MgO Nanorods, Jing Liu, Chunli Guo, Xiaojian Ma, Changhui Sun, Fengxia Li, and Yitai Qian
Volume 2010, Article ID 671863, 5 pages

Simple Synthesis and Growth Mechanism of Core/Shell CdSe/SiO_x Nanowires, Guozhang Dai, Shengyi Yang, Min Yan, Qiang Wan, Qinglin Zhang, Anlian Pan, and Bingsuo Zou
Volume 2010, Article ID 427689, 6 pages

Fabrication of Mesostructured Silica and Titania Rods on Substrates by Using Polycarbonate Membranes, Norihiro Suzuki and Yusuke Yamauchi
Volume 2010, Article ID 382043, 4 pages

Biomimetic Synthesis of Zinc Oxide 3D Architectures with Gelatin as Matrix, Yong Gan, Fubo Gu, Dongmei Han, Zhihua Wang, and Guangsheng Guo
Volume 2010, Article ID 289173, 7 pages

Preparation of ITO Nanoparticles by Liquid Phase Coprecipitation Method, Zhanlai Ding, Cunran An, Qiang Li, Zhezhe Hou, Jianqiang Wang, Haibo Qi, and Fangjuan Qi
Volume 2010, Article ID 543601, 5 pages

Synthesis and Field Emission Properties of Hierarchical ZnO Nanostructures, Deyan Peng, Yanjun Huang, Ke Yu, Lijun Li, and Ziqiang Zhu
Volume 2010, Article ID 560409, 5 pages

Improved Field Emission Characteristics of Large-Area Films of Molybdenum Trioxide Microbelt, Dongmei Ban, Shaozhi Deng, Ningsheng Xu, Jun Chen, Juncong She, and Fei Liu
Volume 2010, Article ID 136860, 6 pages

Determination of X-Ray Diffraction on the Phase Transformation of Microwave-Assisted Titanate Nanotubes during Thermal Treatment, Hsin-Hung Ou, Ching-Hui Liao, and Shang-Lien Lo
Volume 2010, Article ID 837384, 5 pages

First-Principles Studies on the Structural Transition of ZnO Nanowires at High Pressure, Zhanjun Gao, Yousong Gu, and Yue Zhang
Volume 2010, Article ID 462032, 5 pages

Synthesis of GaN Nanorods by a Solid-State Reaction, Keyan Bao, Liang Shi, Xiaodi Liu,



Changzhong Chen, Wutao Mao, Lingling Zhu, and Jie Cao
Volume 2010, Article ID 271051, 6 pages

Solvothermal Synthesis of $Gd_2O_3 : Eu^{3+}$ Luminescent Nanowires, Guixia Liu, Song Zhang, Xiangting Dong, and Jinxian Wang
Volume 2010, Article ID 365079, 5 pages

Synthesis and Fluorescence Property of Mn-Doped ZnSe Nanowires, Dongmei Han, Chunfeng Song, and Xiaoyu Li
Volume 2010, Article ID 290763, 4 pages

The Progress of Photoluminescent Properties of Rare-Earth-Ions-Doped Phosphate One-Dimensional Nanocrystals, Lixin Yu and Hai Liu
Volume 2010, Article ID 461309, 6 pages

Diameter-Controllable Magnetic Properties of Co Nanowire Arrays by Pulsed Electrodeposition, Youwen Yang, Yanbiao Chen, Yucheng Wu, Xiangying Chen, and Mingguang Kong
Volume 2010, Article ID 793854, 4 pages

Editorial

1D Nanomaterials

Raymond L. D. Whitby,¹ Steve F. A. Acquah,² Renzhi Ma,³ and Yanqiu Zhu⁴

¹*Nanoscience & Nanotechnology Group, School of Pharmacy and Biomolecular Sciences, University of Brighton, Lewes Road, Brighton BN2 4GJ, UK*

²*The Kroto Group, Department of Chemistry & Biochemistry, Florida State University, Tallahassee, FL 32306-4390, USA*

³*Soft Chemistry Group, International Center for Materials Nanoarchitectonics (MANA), National Institute for Materials Science (NIMS), Namiki 1-1, Tsukuba, Ibaraki 305-0044, Japan*

⁴*College of Engineering, Mathematics, and Physical Sciences, University of Exeter, North Park Road, Exeter EX4 4QF, UK*

Correspondence should be addressed to Raymond L. D. Whitby, r.whitby@brighton.ac.uk

Received 18 August 2010; Accepted 18 August 2010

Copyright © 2010 Raymond L. D. Whitby et al. This is an open access article distributed under the Creative Commons Attribution License, which permits unrestricted use, distribution, and reproduction in any medium, provided the original work is properly cited.

The advent of nanoscience and nanotechnology is widely regarded as coming to fruition at the result of two key papers. The first in 1985 reported an intriguing artefact of stabilisation of carbon clusters from high temperature plumes [1], though fullerene molecules have since been discovered created by shockwave in a 1.28 billion-year-old impact site [2]. The second in 1991 reported detailed images of what was later termed carbon nanotubes [3], although a comprehensive search of past papers [4] uncovered reports of carbon nanotubes in 1976 and 1952 [5, 6] and a further discovery that a seventeenth century Damascus steel sword contained carbon nanotubes [7]. Whilst it is important to properly ascertain the history of nanoscience, the papers of Kroto et al. and Iijima are no less deserving of their estimable renown.

It should be without any doubt that nanoscience and nanotechnology has had a significant global impact in redefining existing and developing novel research avenues over the last two decades. Where bottom-up assembly meets conventional top-down refinements, nanomaterials proffer the necessary bridge between atomistic processes and useable macroscale devices. Focus has largely been towards preparative methods with specific interest in controlling the fundamental properties and architecture, where the inextricable link between size & geometry and properties of one-dimensional (1D) nanomaterials, for example, nanotubes, nanowires, nanorods, reveals a wide variety of promising applications. It is hoped this will in turn unlock the potential of such nanomaterials in devices. In this special issue on

1-dimensional nanomaterials, we have invited a number of authors to address such matters and thus provide an up-to-date consideration of the field.

The first paper, by Sivakumar et al. [8], appraises the synthesis of carbon nanotubes via chemical vapour deposition (CVD) techniques. They explore the different types of CVD growth available, the influence of catalytic particles and reaction conditions. The second paper, by Hu et al. [9], report the use of “green” chemistry in the non-toxic and non-hazardous large scale CVD synthesis of carbon nanotubes with uniform diameters. This facile approach should prove useful for industrial scale-up in an increasingly environmentally conscious market. The third paper, by Liu et al. [10], examines carbon nanotube-metal oxides composites, where the formed MgO nanorods are determined to facilitate the growth of the encapsulating carbon nanotube. This is an important avenue of exploration where control over the length, diameter and geometry of carbon nanomaterials is important.

Template growth of nanomaterials has proven a useful methodology for controlling the architecture and in turn the properties of nanomaterials [11]. The fourth paper, by Dai et al. [12], explores such a route in the formation of coaxial CdSe-SiO_x nanocomposites with the potential of controlling the final electronic properties. The fifth paper, by Suzuki et al. [13], presents a removable template growth of silica and titania in a one-pot approach that promises to be useful for the generation of nanosize systems. Temporary

templates have also been demonstrated to prove useful for nucleation of nanomaterials where Gan et al. [14], in the sixth paper, explored the biomimetic assembly of ZnO on top of gelatin, which then spontaneously formed into 3-dimensional nanostructures.

A number of other approaches have been investigated for the formation of inorganic nanostructures [15]. The seventh paper, by Ding et al. [16], investigates the co-precipitation of indium tin oxide nanoparticles. Thermal evaporation heightens the stochastic energetics of chemical fragments, which has the greatest potential of diversifying nanoscale architecture on cooling. The eighth paper, by Peng et al. [17] and ninth paper, by Ban et al. [18], uses thermal evaporation techniques leading to the generation of elegant hierarchical ZnO and MoO₃ nanostructures respectively.

Both high temperature and high pressure treatment on existing nanomaterials can alter their crystal phase, which is potentially useful for a range of purposes from heterogeneous catalysis to piezoelectronics [19]. The tenth paper, by Ou et al. [20], addresses high temperature crystal phase alterations for titanate and its resulting enhancement of its photocatalytic degradation of chlorinated hydrocarbons. The eleventh paper, by Gao et al. [21], looks at the density functional treatment of ZnO nanowires at high pressures, converting from wurtzite to a rocksalt structure. The phase transformation should prove useful in exploring electronic, piezoelectric and photoconducting applications. Bao et al. [22] in the twelfth paper investigate the high temperature chemical transformation of orthorhombic GaOOH nanorods into wurtzite GaN nanorods, a useful compound for optical devices operating at blue and ultraviolet wavelengths and in high-temperature electronic devices.

At the other end of the scale, the development of red-emitting phosphors and field emission display devices shows great promise from the synthesis of Eu-doped Gd₂O₃ nanowires. Liu et al. [23], in the thirteenth paper, explore the use of solvothermal techniques for the formation of these doped nanomaterials, which (along with hydrothermal techniques) represents a facile approach that could be used to synthesize other rare earth oxide materials. This is demonstrated in the fourteenth paper, by Han et al. [24], in the formation of Mn-doped ZnSe nanowires and also by Yu et al. [25], in the fifteenth paper, where a review of phosphate nanowires doped with rare earth elements are considered. These composites exhibit great promise in the development of biological probes, photonic crystals and optical communication devices.

The final paper, by Yang et al. [26], looks at the fundamental correlation of magnetism with the size of Co nanowires, revealing that the magnetic property can be adjusted through changing the diameter of the nanowire. This is an important discovery for the fabrication of high-density magnetic recording devices.

The breadth of advancement of nanomaterials and their incorporation into useable products has been both extensive and intensive since their inception [27]. Whilst this special issue could not cover every aspect, it endeavours to provide exciting insight into a number of key avenues.

Acknowledgments

The editors would like to express their sincere appreciation and thanks to all the authors and coauthors for their scientific contribution to this special issue. They convey their gratitude to all the reviewers for their time and dedication.

Raymond L. D. Whitby
Steve F. A. Acquah
Renzhi Ma
Yanqiu Zhu

References

- [1] H. W. Kroto, J. R. Heath, S. C. O'Brien, R. F. Curl, and R. E. Smalley, "C-60-Buckminsterfullerene," *Nature*, vol. 318, pp. 162–163, 1985.
- [2] L. Becker, J. L. Bada, R. E. Winans, J. E. Hunt, T. E. Bunch, and B. M. French, "Fullerenes in the 1.85-billion-year-old Sudbury impact structure," *Science*, vol. 291, pp. 1530–1533, 2001.
- [3] S. Iijima, "Helical microtubules of graphitic carbon," *Nature*, vol. 354, pp. 56–58, 1991.
- [4] M. Monthieux and V. L. Kuznetsov, "Who should be given the credit for the discovery of carbon nanotubes?" *Carbon*, vol. 44, pp. 1621–1623, 2006.
- [5] A. Oberlin, M. Endo, and T. Koyama, "Filamentous growth of carbon through benzene decomposition," *Journal of Crystal Growth*, vol. 32, pp. 335–349, 1976.
- [6] L. V. Radushkevich and V. M. Lukyanovich, "O strukture ugleroda, obrazujucesja pri termiceskom razlozenii okisi ugleroda na zeleznom kontakte " About the structure of carbon formed by thermal decomposition of carbon monoxide on iron substrate," *Zhurnal Fizicheskoi Khimii*, vol. 26, pp. 88–95, 1952.
- [7] M. Reibold, P. Paufler, A. A. Levin, W. Kochmann, N. Patzke, and D. C. Meyer, "Materials-Carbon nanotubes in an ancient Damascus sabre," *Nature*, vol. 444, pp. 286–286, 2006.
- [8] S. V. Sivakumar, A. R. Mohamed, A. Z. Abdullah, and S.-P. Chai, "Role of reaction and factors of carbon nanotubes growth in chemical vapour decomposition process using Methane—a highlight," *Journal of Nanomaterials*, vol. 2010, Article ID 395191, 11 pages, 2010.
- [9] Y. Hu, T. Mei, L. Wang, and H. Qian, "A facile and generic strategy to synthesize large-scale carbon nanotubes," *Journal of Nanomaterials*, vol. 2010, Article ID 415940, 5 pages, 2010.
- [10] J. Liu, C. Guo, X. Ma, C. Sun, F. Li, and Y. Qian, "One-step route to synthesize multiwalled carbon nanotubes filled with MgO Nanorods," *Journal of Nanomaterials*, vol. 2010, Article ID 671863, 5 pages, 2010.
- [11] R. L. D. Whitby, W. K. Hsu, Y. Q. Zhu, H. W. Kroto, and D. R. M. Walton, "Novel nanoscale architectures: coated nanotubes and other nanowires," *Philosophical Transactions of the Royal Society A: Mathematical, Physical and Engineering Sciences*, vol. 263, pp. 2127–2142, 2004.
- [12] G. Dai, S. Yang, M. Yan et al., "Simple synthesis and growth mechanism of core/shell CdSe/SiO_x nanowires," *Journal of Nanomaterials*, vol. 2010, Article ID 427689, 6 pages, 2010.
- [13] N. Suzuki and Y. Yamauchi, "Fabrication of mesostructured silica and titania rods on substrates by using polycarbonate membranes," *Journal of Nanomaterials*, vol. 2010, Article ID 382043, 4 pages, 2010.

- [14] Y. Gan, F. Gu, D. Han, Z. Wang, and G. Guo, "Biomimetic synthesis of zinc oxide 3D architectures with gelatin as matrix," *Journal of Nanomaterials*, vol. 2010, Article ID 289173, 7 pages, 2010.
- [15] X. G. Hu and S. J. Dong, "Metal nanomaterials and carbon nanotubes - synthesis, functionalization and potential applications towards electrochemistry," *Journal of Materials Chemistry*, vol. 18, pp. 1279–1295, 2008.
- [16] Z. Ding, C. An, Q. Li et al., "Preparation of ITO nanoparticles by liquid phase coprecipitation method," *Journal of Nanomaterials*, vol. 2010, Article ID 543601, 5 pages, 2010.
- [17] D. Peng, Y. Huang, K. Yu, L. Li, and Z. Zhu, "Synthesis and field emission properties of hierarchical ZnO nanostructures," *Journal of Nanomaterials*, vol. 2010, Article ID 560409, 5 pages, 2010.
- [18] D. Ban, S. Deng, N. Xu, J. Chen, J. She, and F. Liu, "Improved field emission characteristics of large-area films of molybdenum trioxide microbelt," *Journal of Nanomaterials*, vol. 2010, Article ID 136860, 6 pages, 2010.
- [19] B. Gilbert, H. Z. Zhang, F. Huang, M. P. Finnegan, G. A. Waychunas, and J. F. Banfield, "Special phase transformation and crystal growth pathways observed in nanoparticles," *Geochemical Transactions*, vol. 4, pp. 20–27, 2003.
- [20] H.-H. Ou, S.-L. Lo, and C.-H. Liao, "Determination of Xray diffraction on the phase transformation of microwaveassisted titanate nanotubes during thermal treatment," *Journal of Nanomaterials*, vol. 2010, Article ID 837384, 5 pages, 2010.
- [21] Z. Gao, Y. Gu, and Y. Zhang, "First-principles studies on the structural transition of ZnO nanowires at high pressure," *Journal of Nanomaterials*, vol. 2010, Article ID 462032, 5 pages, 2010.
- [22] K. Bao, X. Liu, W. Mao et al., "Synthesis of GaN nanorods by a solid-state reaction," *Journal of Nanomaterials*, vol. 2010, Article ID 271051, 6 pages, 2010.
- [23] G. Liu, S. Zhang, X. Dong, and J. Wang, "Solvothermal synthesis of $\text{Gd}_2\text{O}_3:\text{Eu}^{3+}$ luminescent nanowires," *Journal of Nanomaterials*, vol. 2010, Article ID 365079, 5 pages, 2010.
- [24] D. Han, C. Song, and X. Li, "Synthesis and fluorescence property of Mn-doped ZnSe nanowires," *Journal of Nanomaterials*, vol. 2010, Article ID 290763, 4 pages, 2010.
- [25] L. Yu and H. Liu, "The progress of photoluminescent properties of rare-earth-ions-doped phosphate one-dimensional nanocrystals," *Journal of Nanomaterials*, vol. 2010, Article ID 461309, 6 pages, 2010.
- [26] Y. Yang, Y. Chen, Y. Wu, X. Chen, and M. Kong, "Diameter-controllable magnetic properties of Co nanowire arrays by pulsed electrodeposition," *Journal of Nanomaterials*, vol. 2010, Article ID 793854, 4 pages, 2010.
- [27] B. Bhushan, Ed., *Springer handbook of nanotechnology*, Springer, Berlin, 2nd edition, 2007.

Review Article

Role of Reaction and Factors of Carbon Nanotubes Growth in Chemical Vapour Decomposition Process Using Methane—A Highlight

Sivakumar VM,¹ Abdul Rahman Mohamed,¹ Ahmad Zuhairi Abdullah,¹
and Siang-Piao Chai²

¹ School of Chemical Engineering, Engineering Campus, Universiti Sains Malaysia, Seri Ampangan, Nibong Tebal, Pulau Pinang 14300, Malaysia

² School of Engineering, Monash University, Jalan Lagoan Selatan, Bandar Sunway, Selangor 46150, Malaysia

Correspondence should be addressed to Abdul Rahman Mohamed, chrahman@eng.usm.my

Received 5 November 2009; Accepted 13 April 2010

Academic Editor: Steve Acquah

Copyright © 2010 Sivakumar VM et al. This is an open access article distributed under the Creative Commons Attribution License, which permits unrestricted use, distribution, and reproduction in any medium, provided the original work is properly cited.

One of the remarkable achievements in the field of nanotechnology is Carbon Nanotubes (CNT) synthesis. Since their discovery in 1991 by Iijima, CNTs have attracted much attention across the world. The CNTs are broadly classified into single-walled carbon nanotubes (SWNTs) and multiwalled carbon nanotubes (MWNTs). The most distinguished features of SWNTs and MWNTs are their electrical, mechanical, chemical, and electronic properties which in turn find their potential applications in almost all fields of science, engineering, and technology. Based on the previous research studies to till date, chemical vapour deposition (CVD) is considered to be the simplest method with high energy efficiency and precise control of reaction parameters compared to other different methods for synthesizing CNTs. Since production of CNTs is becoming the most important factor in the applications point of view, most industries today are opting for the CVD technique. This paper reviewed the synthesis of CNT by CVD especially focusing on methane CVD. Various parameters influencing the reaction and CNT growth were also discussed. A detailed review was made over the different types of CVD process, influence of metal, supports, metal-support interaction, effect of promoters, and reaction parameters role in CNTs growth.

1. Introduction

Carbon nanotubes (CNTs) are sheets of graphite rolled into tubes and possess excellent properties due to their symmetric structure [1]. They are broadly classified into single-walled carbon nanotubes (SWNTs) and multiwalled carbon nanotubes (MWNTs). Among them SWNTs are the key materials to the emerging field of nanotechnology [2]. CNTs have reached the forefront of many industrial research projects nowadays. Due to their high strength, stiffness, and electrical conductivity [3], CNTs are designated as one of the most attractive materials for reinforcing the material in composites [4, 5] and for nanoelectronics applications. Theoretical and experimental elastic modulus (1TPa) and tensile strength of these materials are in the range of tens of GPa, respectively [6]. In general, CNTs can be produced

by carbon arc discharge method (CA) [7], chemical vapour deposition method (CVD) [8], pulsed laser vaporization technique (PLV) [9], and high-pressure carbon monoxide conversion (HiPco) process [10]. In CA and PLV methods, although high quality materials can be produced, the high temperature employed for evaporating the carbon atoms from solid carbon sources (over 3000 K) make them difficult to scale up the process in a cost-effective way. Hence, chemical vapour decomposition (CVD) has gained importance owing to its easiest and economic way of production in a larger scale [11]. CVD method is believed as the most suitable synthesis method in terms of product quality and quantity [12]. A review by Baddour and Briens, 2005, concluded that catalytic technique such as CVD is simple, inexpensive, energy-efficient and can produce high purity CNTs in high yield (>75%) [13]. As the applications for CNTs range from

nanoelectronics [14, 15], sensors [16, 17], and field emitters [18] to composites [19], reliable growth techniques capable of yielding high-purity material in desirable quantities are critical to realize CNT potential. This need is satisfied by CVD and the CNT growth factors. Since, there is a huge demand for CNTs production and application in the global market, it is necessary to maximize the yield and minimize the production cost. Hence, methane, which is found to be the most cheaply available resource from natural gas with high thermal stability and low Gibbs free energy, is suitable to be used. In addition, the current focus on SWNTs synthesis and its requirement of low carbon content source are fulfilled by methane. These properties and advantages paved way for the recent research on CVD focused towards using methane as hydrocarbon source.

2. Chemical Vapour Deposition

Catalytic chemical vapour decomposition (CCVD) was first introduced by José-Yacamán et al. in 1993 to produce CNTs [20]. A simple representation of the chemical vapour deposition process is shown in Figure 1. CVD synthesis is achieved by putting carbon source in gas phase into a reactor and using an energy source, such as plasma or a resistively heated coil, to decompose the gaseous carbon molecule. In CCVD method, CNTs are produced by decomposition of carbon-containing molecules with the presence of catalytic materials. Commonly used carbon sources include methane, ethylene, hexane, ethanol, naphthalene, anthracene, carbon monoxide, carbon dioxide, acetylene, and benzene. Thermal or electrical energy source is used to crack the molecule into reactive atomic carbon. Then, the carbon diffuses into the supported metal, usually transition metal in Group VIII of the periodic table such as Ni, Fe, or Co. CNTs will be formed if the proper process conditions like reaction temperature, pressure, flow rate and concentration of hydrocarbon source, carrier gas, and so forth, are maintained. The appropriate metal catalyst among the transition group can grow SWNTs, DWNTs (double-walled carbon nanotubes), and MWNTs are shown in Figures 2(a), 2(b), and 2(c), respectively. Excellent alignment, size, diameter, growth rate as well as positional control on nanometer scale for the synthesized CNTs can be achieved by using CVD method.

2.1. Modified CVD Process. Nowadays the CVD process is under research with minor changes in their energy source to initiate the CNT growth. The process had been categorized according to their nature and source of energy (as shown in Figure 3). For examples, microwave [24, 25], inductively coupled plasma CVD [26], low pressure [27], hot filament (HF) [28, 29], alcohol catalytic [30], and so forth were reported.

Varadan and Xie [24], Fidalgo et al. [25] synthesized MWNTs by microwave CVD. The microwave system consists of a microwave magnetron with adjustable power supply ranging from 0 to 3000 W at a frequency of 2.45 GHz. No vacuum was maintained and reaction was operated at 1 atmosphere pressure. Straight and helical CNTs were

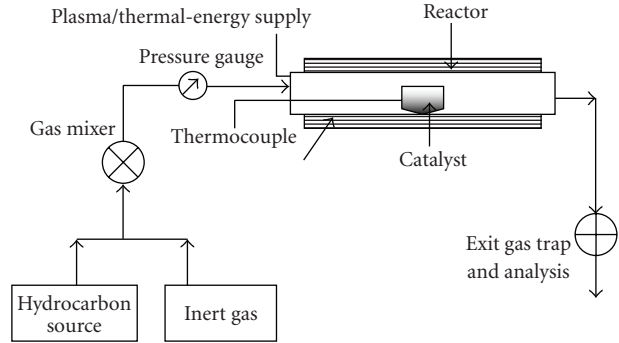


FIGURE 1: Schematic diagram of a CVD process for CNT synthesis.

obtained by decomposing acetylene in microwave energy field over the cobalt catalyst supported on Y-zeolite, alumina, and SiC at 700°C. High resolution transmission electron microscope (HRTEM) analysis results confirmed the presence of MWNTs. It was also reported that CNTs obtained using alumina support was found to have more impurities than zeolite. The main advantage of microwave CVD system is rapid heating and cooling process with a chance to produce helical CNTs with diameter range 80–100 nm.

Ikuno et al. [27] produced CNTs by low-pressure thermal chemical deposition (LPTCD) using pure ethylene. CNT bridges were grown on Ta electrodes at 800°C in vacuum. By nitriding the surface of the Ta electrode/SiO₂/Si substrates, Fe nanoparticles with a moderate size were effectively formed, resulting in bridging CNTs between the electrodes. It was found that under a low pressure of 100 Pa, straight CNTs are preferentially bridged between the Fe nanoparticles.

Yen et al. [26] synthesized well-aligned CNTs using a high inductively coupled plasma chemical vapor deposition (ICP-CVD) system. A gas mixture of CH₄-H₂ was used as the carbon source and Ni as the catalyst for the CNTs growth. The effect of process parameters, such as inductive RF power, DC bias voltage and ratio, on the growth characteristics of CNTs was investigated. It was found that generation and transport of ions to the substrate are the two underlying factors in determining the growth of CNTs.

Kadlečíková et al. [28] studied the effect of electric field upon the aligned growth of CNTs and had successfully produced bundles of CNTs by hot filament CVD method. The author stated that the key role in the formation of CNTs depends on the energy of ion bombardment and plasma discharge applied during the growth of CNTs after temperature and pressure were set in the deposition chamber.

Although various types of plasma enhanced CVD with specialized power supplies such as microwave, hot filament [28], radio-frequency, and direct-current (DC) exist and recognized as the most promising technique in growing CNTs at a relatively low temperature, this technique has a drawback of difficulty in scaling up the plasma technology to grow CNTs on a large scale and high voltages used lead to the sputtering of the electrode, causing both contamination of the plasma and damage to the CNT structure.

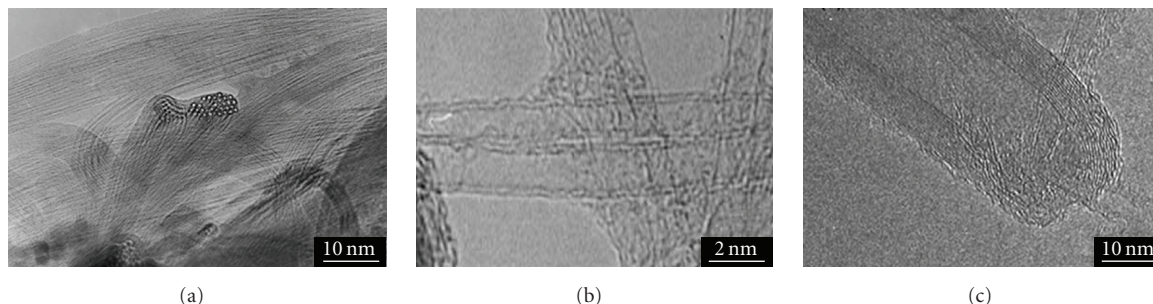


FIGURE 2: Transmission electron microscopy images (a) single-walled carbon nanotubes [21]; (b) double-walled carbon nanotubes [22]; (c) multiwalled carbon nanotubes [23].

Unalan and Chhowalla [30] investigated SWNT growth parameters using alcohol catalytic chemical vapour deposition (ACCVD). Alcohol vapours like ethanol or methanol were used as the carbon sources and a mixture of Fe–Co acetate was used as catalytic material with MgO as its support. Dip-coating method was utilized for loading catalyst particles on the substrate. SWNTs with narrow diameter distribution without the presence of amorphous carbon were obtained at temperatures above 750°C, whereas defective MWNTs were observed at a lower temperature. It was reported that use of methanol as carbon source, with catalyst dissolved in deionised water (DI) rather than alcohol lead to growing more uniform SWNTs on the substrate surface.

In addition, a type of CCVD using fluidized bed reaction was also used for producing CNTs [30, 31]. Though the above techniques were tried with advancement in technologies, it still faces several drawbacks in scaling up the process. Moreover, the CCVD process is still found to be better for commercial synthesis of CNTs in proper controlled conditions [32, 33].

In the last decade, different techniques such as plasma enhanced CVD, thermal CVD, alcohol-catalytic (ACCVD) [34], vapour phase growth, and laser assisted CVD [35, 36] for the CNTs synthesis have been developed. Colomer et al. [37] confirmed that CCVD is easier, cheaper, and an adaptable approach for large-scale production CNTs at low temperature and ambient pressure via decomposing the hydrocarbon gas. Kong et al. [38] has already proved that CVD of methane can be a successful route for the growth of SWNTs.

2.2. Methane CVD. The following review has been made to highlight the current importance towards methane CVD in CNT synthesis using metal supported catalyst. High-temperature decomposition of hydrocarbons leads to the formation of deposited carbon. Morphology of the carbon deposits over the catalyst/support during CVD process was closely related to the thermodynamic properties and nature of the hydrocarbon source. Gaseous hydrocarbons such as acetylene [39–41], methane [42, 43], and ethylene [27] have been widely used for producing CNT deposits. Besides gaseous hydrocarbons, some liquid hydrocarbons such as hexane, benzene [44], toluene [45], xylene [46], and so forth,

have also been effectively used for the growth of SWNTs and MWNTs in floating CVD methods.

Li et al. [47] studied the effect of various hydrocarbons like methane, hexane, cyclohexane, benzene, naphthalene, and anthracene over Fe catalyst impregnated on MgO support. The author reported that there was a strong dependence of nature of hydrocarbon precursors on the formation of different structure of CNTs. It was also reported that methane would be most preferable for the growth of high-purity SWNTs rather than any other gaseous hydrocarbons, as it was comparatively chemically stable at high temperature and has the simplest structure [48]. However, the achievement for the methane CVD growth of SWNTs would largely depend on the features of catalyst as well.

de Almeida et al. [49] studied the methane decomposition using porous-nickel alumina spheres as catalyst. It was observed that during catalytic decomposition reaction, methane is initially adsorbed and decomposed on the metal surface of the catalyst particle, resulting in the formation of chemisorbed carbon species and the release of gaseous hydrogen. The carbon species was found to proceed further to dissolve in and diffuse through the bulk of the metal particle. Some of the aromatic hydrocarbons like benzene could be decomposed at a lower temperature when compared with methane [50]. But it was experimentally proven that benzene decomposition temperature should be kept at 800°C to favor the SWNTs formation, whereas in the case of methane, it could be achieved at a lower temperature of 650°C with lower Gibbs free energy ($\Delta G = -27.2$ KJ) [51]. SWNTs could not be obtained with hexane and cyclohexane though their reaction due to Gibbs free energies are much lower than that of benzene and methane. It was further revealed that the formation and morphology of carbon deposits were not simply determined by the pyrolytic behaviors of hydrocarbons.

Muradov [52] made a significant study of methane decomposition reaction (pressure: atmospheric, temperature: 850°C, methane flow rate: 5.0 ± 0.2 mL/min; sample amount: 0.3 ± 0.001 g) over 30 different samples of elemental carbon, including a variety of activated carbons (ACs), carbon blacks (CBs), nanostructured carbons (including CNTs and fullerenes), graphite, glassy carbon, and synthesized diamond powders. Catalytic activity of these carbons samples in methane decomposition was determined by their

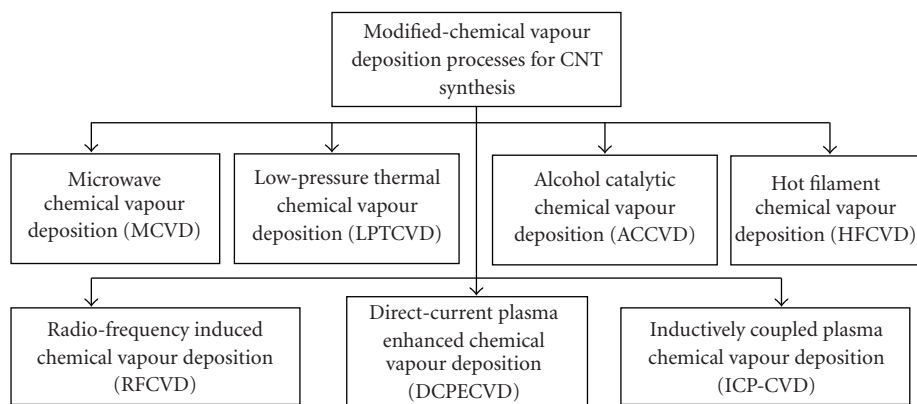


FIGURE 3: Classification of CVD processes according to their energy source.

origin, structure, and surface area. ACs were found to provide the highest initial activity of methane decomposition with 90 vol% of H_2 formed for 10 s residence time with carbon sample bed. On the contrary, this highest methane decomposition rate with CO/CO_2 -free hydrogen in a single step could not be obtained for experiments conducted with silica (surface area: $600 \text{ m}^2/\text{gm}$) and that of Ni- and Fe-based catalysts measured at identical conditions.

In 2007, Chuang et al. [53] developed sea urchin-like CNTs by catalytic decomposition of methane over catalyst-seeded mesoporous carbon and the catalysts were prepared by dip-coating method. The area density of CNTs/carbon nanowires (CNWs) was found to be higher at 900°C than that at 800°C . Most recently, Chuang et al. [53] and Fidalgo et al. [25] investigated the growth of nanofilaments on activated carbon and carbon fibre materials by microwave-assisted methane decomposition and they found that for pure methane flow at 800°C for 130 minutes, only amorphous carbon was formed over the activated carbon and carbon fibres.

It can be concluded that the nature of hydrocarbons plays a crucial role in CVD process for CNT formation, as well in economic aspects. It should be noted that the formation of SWNTs or MWNTs does not merely depend on carbon precursors, but also has strong correlations with other growth conditions. Since methane being a rich source from natural gas, several studies of CCVD using methane as the hydrocarbon source are under progress for investigating the other growth influencing conditions like nature of metal catalysts, support, metal-support interaction, their characteristics, temperature, pressure, gas flow rate, concentration, reaction time, and so forth.

3. CNT Growth Parameters

Li et al. [23] studied that SWNTs or MWNTs formation does not alone depend on the nature of hydrocarbon source. There are also other important parameters playing more crucial role in the growth of different morphology of CNT. Based on distinguished CNT structure and chirality, their properties and end use applications are found to be significant. The main parameters for CNT growth are (i)

properties, composition, and preparation method of metal catalyst, (ii) addition of promoter elements, (iii) metal-support interactions, (iv) reaction conditions like reaction temperature, pressure, inert/methane gas ratio, and gas flow rate.

3.1. Catalyst. Metals used to catalyze CNT formation are most often transition metals, in particular iron (Fe), cobalt (Co), and nickel (Ni), due to the solubility of carbon in these metals is finite [54]. It is noteworthy to find a large number of literatures reporting about CNT growth using different metals and their alloys [55]. The main reason of using transition metals is that they have nonfilled “d” shells and for that reason it is able to interact with hydrocarbons and show catalytic activity. In CVD process, transition metal particles act as a seed of nanotubes so that they strongly influence the structure and quality of the nanotubes. Though the transition metals can decompose hydrocarbons, they need a support for the growth of nanotubes. Materials like silica [56, 57], alumina [58, 59], zeolite [44], and recently MgO [60–62] were used as supports for active metals in developing different forms of carbon nanostructures like SWNT, DWNT, MWNT, and nanofibres. Different catalyst preparation techniques like impregnation [63–69], coprecipitation [70], sol-gel technique [71–73], thin film deposition using electron beam evaporation, and photolithography [74] for patterned catalyst on the support were studied. Among the above mentioned techniques, wet impregnation is the easiest way and mostly adopted by many of the researchers for preparing the catalyst.

Ichi-oka et al. [68] made a comparative study for the amount of carbon deposited via CVD of methane using nine different metals (Fe, Co, Ni, Ru, Rh, Pd, Os, Ir, and Pt) catalyst impregnated over MgO. It was reported that there was an increase in carbon content in the order of transition metal series: first < second < third row transition elements and the index of crystallinity (I_G/I_D) for CNTs in Raman bands decreased in the order: $8 > 9 > 10$ group elements in the periodic table.

Qian et al. [75] reported that higher conversion of methane into good morphology of CNTs was achieved over

Fe and Mo catalyst. It was also reported that the metal particles with relatively small diameter distribution, high activity and thermal stability at high temperatures would meet the requirements of thermodynamics of methane conversion. Combined process of catalyst reduction and hydrocarbon decomposition were found to result with higher yield of CNT. Qian et al. [75] studied Co catalyst impregnated over Al_2O_3 support and reported 3–4 times of higher yield for combined process rather than separated methane decomposition in fluidized bed reactor.

He et al. [76] studied on the morphology of vertically aligned CNTs by using Fe on silicon substrates by CVD process. It was reported that decrease in the thickness of catalyst film reduced the diameter and increased the length of CNTs. He et al. [42] studied methane CVD over Ni/Al composite prepared by homogenous deposition and precipitation. The authors reported that MWNTs of 10–20 nm diameter range were formed from 20% wt Ni catalyst and carbon onions (5 to 50 nm) from 80% wt Ni catalyst. It was further found that the Ni/Al catalyst with 80 wt% Ni is less beneficial for CNT growth due to its increasing particle size which in turn leads to very low carbon solubility and resulted with carbon onions growth.

Zhu et al. [21] found that methane CVD over Co/MgO catalyst with the addition of Mo remarkably increased the yield of SWNTs by 10% at least with suppressed amorphous carbon formation. It was reported that too many metallic Co particles with respect to Mo and support would form aggregated larger particles during preparation resulting with MWNTs.

Proper control of the catalyst particle size and metal concentration is critical for a high production rate of CNT. Yu et al. [77] studied the effect of Fe catalyst on silica particle size by CO disproportionation method and revealed that particle sizes of 13–15 nm are optimum for maximum CNT growth rate. Therefore, small particle sizes do not always lead to a high growth rate. Li et al. [47] studied methane CVD for Co catalyst impregnated over MgO support. Co concentrations of 2.5–5 wt% were found to be efficient for growing DWNTs with diameters of 2–4 nm. It was reported that the growth was significantly influenced by catalyst concentration and type of supports. The important factors for a good catalyst are the control of the loading of the active metal and maintaining a good metal dispersion on the catalyst support [78].

Muradov [52] found that activated carbon (AC) catalyst played a significant role in methane conversion with initial H_2 concentration reaching up to 90 vol%. Also, it was stated that similar methane decomposition could not be achieved with silica gel (surface area: $600\text{ m}^2/\text{gm}$) and that of Ni- & Fe-based catalysts measured at the identical conditions. The mechanism of methane decomposition over different forms of carbon as catalyst and their activity were yet to be explored in CCVD process for CNTs growth.

3.2. Metal-Support Interaction. Catalyst supports are also reported to have great determination on the activity of

a catalyst and the morphology of the produced CNTs. Metal-support interaction (MSI) is a very important factor in nanotube formation which is dependent on the nature of catalyst/support particle size, their surface area and the catalyst pretreatment process like calcination, reduction, and so forth. It has been found that CNT can be formed either with (i) tip-growth or (ii) base-growth model. Strong metal-support interaction of catalyst resulted CNTs to grow followed the base growth model, whereas tip-growth model is applied to CNTs grown by catalyst with weak MSI.

According to Vander Wal et al. [79] the formation of CNT structures is controlled by the effect of MSI. Though different sizes and shapes (helical, coiled, straight, and Y-shaped) of CNTs were produced so far, the growth mechanism of nanotubes is still a vague phenomenon for the researchers.

Several MSI studies for methane CVD have been carried out both in fluidized bed and fixed bed reactor system [80]. Catalytic performance of supported-NiO catalysts over methane decomposition at 550°C and 700°C by Chai et al. [81] shows that there is a decrease in activity of catalyst in the order of $\text{NiO}/\text{SiO}_2 > \text{NiO}/\text{HZSM-5} > \text{NiO}/\text{CeO}_2 > \text{NiO}/\text{Al}_2\text{O}_3$. From their XRD results, the dispersion of NiO particles on Al_2O_3 is found to be better compared to other support types. Also the formation of MWNTs at 550°C and SWNTs at 700°C is an indication of methane decomposition as well as the catalyst deactivation rate with respect to the increase in temperature. Similar studies on silica, zeolite, and alumina-supported Co catalysts for MWNT by acetylene decomposition show that percentage carbon deposition and diameter of CNT formed are based on the type and nature of support material [82]. The size of the pores on porous substrates determines the SWNTs or MWNTs formation. Substrate roughness studies by Ward et al. [11] also emphasize on the future research on substrate-catalyst interaction mechanism towards CNTs growth.

de Almeida et al. [49] quoted that methane decomposition at low temperatures ($400\text{--}500^\circ\text{C}$) can be achieved using binary metal (Fe-M where $M = \text{Pd}, \text{Mo}, \text{or Ni}$) catalysts supported on alumina. Also, Muradov [52] studied methane decomposition over elemental carbon and reported that carbon materials are capable of producing H_2 rich gases at moderate temperatures. The author stated that catalytic activity of carbon was determined by their origin and surface properties. At higher temperature, such as at 830°C , NiAl_2O_4 phase is formed due to the strong metal-support interaction. Methane decomposition conversion values were found to increase with increasing reaction temperature. Hence, it can be concluded that the lower calcination temperature gave the catalyst with weak MSI but increased the methane conversion. In the case of higher calcination temperatures, Ni was incorporated strongly with alumina and thus methane conversion was low.

Ward et al. [11] studied CNT synthesis on various substrates (alumina, silica carbide, silicon, quartz, sapphire, MgO, porous silicon, aerogel, fused silica, etc.) and its effect with Al-Fe-Mo by multilayer thin films deposition (electron beam evaporation). They found that Fe thin films spun on alumina to be the best for growing SWNTs and all other supports would give the formation of MWNTs primarily.

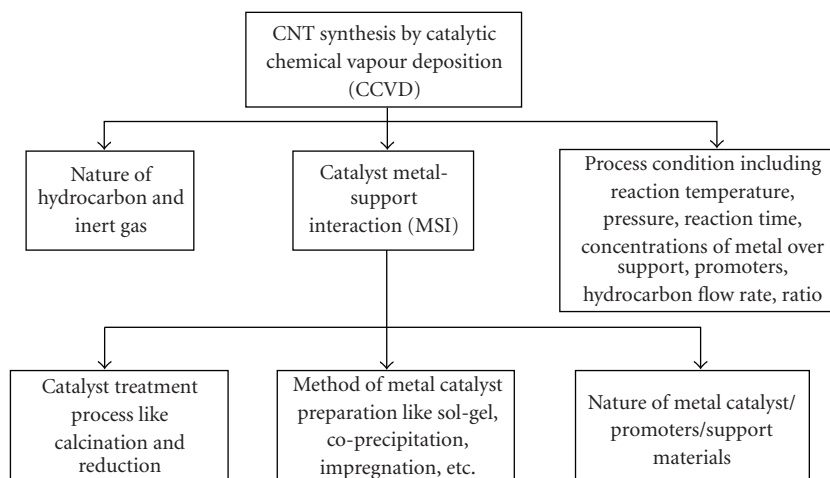


FIGURE 4: The network of the important factors for CNT synthesis.

Authors reported that the property of the substrates/supports like amount of crystallinity, pore size, and surface roughness had a major effect in the growth of either SWNTs or MWNTs

Chai et al. [83] studied the effect of CuO, FeO, and NiO added onto CoO/Al₂O₃ for methane decomposition. It was found that addition of these metal oxides shortened the catalyst lifetime and decreased the methane conversion. Catalyst lifetime and carbon capacity were found to increase with MoO-CoO/Al₂O₃. The carbon capacity over the supported CoO catalyst was found to decrease in the order of silica > zeolite > alumina > ceria > titania > magnesia > calcium oxide and the best catalytic carbon capacity was observed over CoO/SiO₂.

According to various researches, it was found that catalyst with weak MSI is efficient in methane decomposition whereas, for a catalyst with strong MSI, the metal particles are not easily detached from the support. Moreover, strong interaction increased the surface carbon accumulation over catalyst and enhanced the catalyst deactivation in methane decomposition.

3.3. Promoters. Some of the metals like molybdenum, boron [84], and sulphur [85] have been used as promoters for catalyst towards the decomposition of hydrocarbon gas into Y-shaped and helical CNTs. Molybdenum was found to be an effective dispersive agent for the catalyst when it is present at the optimum composition in the catalysts as reported by Yu et al. [62]. Ago et al. [86] found that the catalytic activity increases in the following order Fe-Mo > Fe > Co > Ni. The addition of molybdenum to iron catalyst increases the initial methane conversion and prevents the rapid deactivation of the catalyst.

Li et al. [47] studied the effect of Mo on MgO support. The formation of magnesium molybdate (MgMoO₄) phase was found to play a main role in MWNT synthesis. They suggested that ratio of Mo/Mg should be <1 for the growth of MWNT bundles. It was found that an appropriate amount of water vapour on the catalytic nanotube growth increases the CNT yield by 35%. Zhu et al. [21] showed that addition

of molybdenum (Mo/Co = 1/5) in an optimum level to Co/MgO catalysts (prepared by mechanical mixing and combustion synthesis with citric acid) yielded 10 time's higher generation of SWNTs and less amorphous carbon. Liu et al. [48] studied the CCVD of methane over Fe-Mo/Al₂O₃ catalyst. They reported that the yield of 70% SWNTs and 30% DWNTs are related to the weight of Fe-Mo metal in Fe-Mo/Al₂O₃. Similarly, Kang et al. [87] synthesized SWNTs and DWNTs over Fe-Mo/MgO catalyst and reported that proportion of DWNTs increased with an increase in reaction temperature. Moreover, Mo was known to be a catalytic centre for promoting the aromatization of methane. Zhang et al. [78] synthesized DWNTs by methane CVD on Fe/Al/MgO catalyst. The author found that introduction of Al species into Fe/MgO would reduce the size of MgO crystallites, providing a better dispersion of the metal particles on the support.

Sulfur was introduced as an additive in methane CVD process for the production of CNTs over Co-Mo/MgO catalyst prepared with sol-gel method [85]. It was found that the use of sulfur compounds during the sol-gel catalyst preparation process led to a significant change in the matrix composition and matrix-catalyst interaction. In this case, enhanced growth of Helical (HCNTs) was reported. Similarly, Y-shaped CNTs (YCNTs) growth was favored when sulfur in the form of thiophene vapours was used over the sol-gel prepared Co-Mo/MgO catalyst.

Phosphorous was reported in the literature by Ci et al. [88] for promoting effect in the formation of carbon filaments. Addition of phosphorous from a solution of H₃PO₄ in ethanol to the substrate, and followed by impregnation with Fe₃(CO)₁₂ was found to be effective in promoting the growth of vapour grown carbon fibres (VGCFs) [89]. Also, it was found that an increase in the amount of Phosphorous/Fe ratio >0.25 had an inhibiting effect on the VGCFs. He et al. [59] synthesized binary and triple CNTs over Ni/Cu/Al₂O₃ in the ratio 2 : 1 : 1 (prepared by sol-gel method) using -20 mesh to +40 mesh particles size for methane CVD at 550°C and the findings show that copper element provoked the formation of CNT.

4. Reaction Parameters

The impact of reaction parameters like reaction temperature, reaction time, concentration of H_2 , and flow rate ratio ($CH_4:H_2$) plays a major role in deciding the types of CNTs formation, and its yield. Recently, studies on effect of aforementioned reaction parameters in CNT formation using methane CVD in presence of Ni-Mo/MgO were reported by Zhan et al. [90]. Morphological structure of CNTs was also found to depend much on the reaction temperatures [91], reaction time [92], and CH_4 to H_2 gas ratio [93] in methane CVD.

Yu et al. [62] studied the influence of reaction atmosphere on Fe/MgO and Fe-Mo/MgO catalyst in argon and nitrogen by methane CVD. It was reported that there was an increase in diameter of SWNTs, MWNTs, and CNFs formed as the reaction was enriched in nitrogen atmosphere. On the other hand, pure SWNTs were obtained with Ar atmosphere. Ni et al. [61] studied the kinetics of CNT synthesis by methane CVD over Mo/Co/MgO and Co/MgO catalyst. It was found, the rate of CNT synthesis is proportional to the methane pressure, indicating that the dissociation of methane is the rate-determining step for a catalyst.

Zhao et al. [94, 95] claimed that reaction time would influence the morphology and diameter of CNTs. Carbon onions and two kinds of herringbone CNFs were obtained with 5 wt% Ni coprecipitated aluminium matrix. The catalysts used were calcined at 240°C and 400°C for 2 hours. Decomposition reaction was conducted in horizontal quartz boat at 550°C/600°C for 1 hour and 2 hours by varying the ratio of $CH_4:N_2$ from 1:4 to 1:5.5. The findings confirmed that carrier gas (N_2) plays an important role in CNT synthesis. The authors reported that cone-shaped catalyst was formed at 550°C and cylinder shape catalyst at 600°C. Influence of temperature over the shape and size of the catalyst was reported and thus the morphology of herringbone CNFs. Hence, by extending the growth time from 1 to 2 hours, carbon onions were formed.

Noda et al. [96] quoted various studies on methane decomposition over different catalyst and supports for the formation of SWNTs and MWNTs at different reaction temperatures. Effect of 1% and 5% of Ni loaded on SiO_2 in the temperature range of 625–800°C were studied in a fixed bed quartz tube reactor. Catalyst with 1% Ni favored SWNT formation at all reaction temperatures whereas 5% Ni formed MWNTs at low temperature and SWNT at high temperature. Also, it was found that the amount of CNT decreased at high temperature for both concentrations due to sintering process.

de Almeida et al. [49] studied CH_4 deposition by preheating Ni/ Al_2O_3 samples at 350, 550 and 700°C under air flow for 1 hour and reaction at atmospheric pressure with molar ratio of $N_2:CH_4 = 6:1$ at 600°C, 700°C, and 800°C. He reported that higher calcination temperature lowers the residual amorphous carbon present within the pores of crystalline catalyst sample, resulting in mesopore formation and increasing surface area and pore volume.

Qian et al. [31] investigated the combination of catalyst reduction and methane decomposition over Ni and Co

in fluidized bed reactor. Co/Mo/ Al_2O_3 of ratio 1/4/50 wt ratio and Ni/Cu/ Al_2O_3 of 15/3/2 wt were prepared by coprecipitation and decomposed in the range of 550°C–850°C with methane to argon ratio of 1:1. Higher methane conversion and 3–4 times better yield of CNTs were reported for this combination. He states that when the metal catalysts are reduced, they provide energy for the endothermic methane decomposition and make methane decomposition equilibrium shift to the direction of hydrogen & carbon and CNTs production.

Bustero et al. [97] studied the effect of temperature, mass of catalyst, initial feed gas composition, and reaction time on the yield of CNT. Optimal operating conditions for the synthesis of CNTs by CVD as reported by the authors are the reaction time: 10 min; temperature: 1000°C; catalyst Mass: 0.5 g; ratio of H_2/CH_4 is 1:1. A mathematical expression was established between the processing condition and the yield of carbon deposits. The derived expression also confirms that it is difficult to determine the optimal reaction conditions for the CNT synthesis by CVD.

Ni et al. [61] studied the effect of pressure and temperature on CNT synthesis by methane CVD over Mo/Co/MgO and Co/MgO catalyst. An increase in carbon yield was observed for an increase in methane pressure from 7.5 Torr to 78.0 Torr. Even at high methane pressures, no significant deactivation of the Mo/Co/MgO catalysts was noted. It was found that the rate of methane disassociation was reduced due to the addition of Mo into Co/MgO catalysts.

In 2007, Chuang et al. [53] conducted catalytic methane CVD over metal catalyst supported over mesoporous carbon (prepared by dip-coating method) at different temperatures (800°C and 900°C). It was concluded that at 900°C, CNTs and carbon nanowires (CNWs) could be obtained in high density rather than at 800°C. Recently, Fidalgo et al. [25] studied the influence of different CH_4/N_2 ratio with respect to nanofilaments formation. Methane CVD was conducted over Fe and Ni catalyst impregnated over activated carbon and carbon fibres at 800°C for 130 minutes. The growth of nanofilaments was found to be more abundant using $CH_4:N_2$ ratio of 1:3 rather than 1:1. It is concluded that the presence of N_2 in methane CVD could influence the carbon yield. The factors of CNT growth have been summarized in the Figure 4.

It was found that methane CVD processes had been influenced by the process and CNT growth parameters like methane/carrier gas ratio, reduction atmosphere, methane/inert gas volumetric flow rate, reaction temperature, time of reaction and operating pressure, and so forth. Hence all the above-mentioned parameters would be crucial in deciding the nature, properties, yield, and quality of CNTs.

5. Conclusions

The current focus on the CCVD of methane for CNTs synthesis was reviewed. Methane being a highly available hydrocarbon source with high thermal stability and thermodynamic properties as discussed, still needs to be studied with the other influencing parameters on CNT growth.

The carbon-based supports like AC is found to be a good material in decomposing methane at low temperatures. As mentioned by various researchers, each step starting from the metal catalyst preparation to removal of impurities from the synthesized CNTs would reflect in its product type, quality, yield, and ultimately its market demand for their potential applications. In the economic aspects, the value of CNT material, which at present greater than the value of gold, can be made available in bulk by proper control and optimization of the reaction parameters. Growth mechanism, which is still a vague phenomenon for many researchers, needs further investigations. Method of purification, a deciding factor for the purity of CNTs, needs to be identified to selectively separate the material based on its shape and size. At present, several research studies on CVD reaction using fixed/fluidized bed with horizontal/vertical reactors and CNTs growth parameters are being conducted only in lab scale. Hence, it is of the opinion to further explore the potential of using methane as hydrocarbon source with carbon-based supports for metal catalyst will be an opt route to the bulk and low-cost production of CNTs to meet the future global demand.

Acknowledgments

The authors gratefully acknowledge the financial support provided by the Ministry of Science, Technology and Innovations (MOSTI) under E-Science Fund (Project A/c no: 6013327) and the Universiti Sains Malaysia (USM) for funding this project under the Research University (RU) Grant Scheme (Project A/c No: 814004) and Student Fellowship.

References

- [1] E. B. Barros, A. Jorio, G. G. Samsonidze, et al., "Review on the symmetry-related properties of carbon nanotubes," *Physics Reports*, vol. 431, no. 6, pp. 261–302, 2006.
- [2] S. B. Sinnott and R. Andrews, "Carbon nanotubes: synthesis, properties, and applications," *Critical Reviews in Solid State and Materials Sciences*, vol. 26, no. 3, pp. 145–249, 2001.
- [3] Z. L. Wang, P. Poncharal, and W. A. de Heer, "Measuring physical and mechanical properties of individual carbon nanotubes by in situ TEM," *Journal of Physics and Chemistry of Solids*, vol. 61, no. 7, pp. 1025–1030, 2000.
- [4] P. M. Ajayan, L. S. Schadler, C. Giannaris, and A. Rubio, "Single-walled carbon nanotube-polymer composites: strength and weakness," *Advanced Materials*, vol. 12, no. 10, pp. 750–753, 2000.
- [5] K. T. Lau, M. Lu, and D. Hui, "Coiled carbon nanotubes: synthesis and their potential applications in advanced composite structures," *Composites Part B*, vol. 37, no. 6, pp. 437–448, 2006.
- [6] Z. L. Wang, R. P. Gao, P. Poncharal, W. A. de Heer, Z. R. Dai, and Z. W. Pan, "Mechanical and electrostatic properties of carbon nanotubes and nanowires," *Materials Science and Engineering C*, vol. 16, no. 1-2, pp. 3–10, 2001.
- [7] S. Iijima, "Helical microtubules of graphitic carbon," *Nature*, vol. 354, no. 6348, pp. 56–58, 1991.
- [8] M. Endo, K. Takeuchi, S. Igarashi, K. Kobori, M. Shiraishi, and H. W. Kroto, "The production and structure of pyrolytic carbon nanotubes (PCNTs)," *Journal of Physics and Chemistry of Solids*, vol. 54, no. 12, pp. 1841–1848, 1993.
- [9] T. Guo, P. Nikolaev, A. Thess, D. T. Colbert, and R. E. Smalley, "Catalytic growth of single-walled nanotubes by laser vaporization," *Chemical Physics Letters*, vol. 243, no. 1-2, pp. 49–54, 1995.
- [10] P. Nikolaev, M. J. Bronikowski, R. K. Bradley, et al., "Gas-phase catalytic growth of single-walled carbon nanotubes from carbon monoxide," *Chemical Physics Letters*, vol. 313, no. 1-2, pp. 91–97, 1999.
- [11] J. W. Ward, B. Q. Wei, and P. M. Ajayan, "Substrate effects on the growth of carbon nanotubes by thermal decomposition of methane," *Chemical Physics Letters*, vol. 376, no. 5-6, pp. 717–725, 2003.
- [12] B. Zheng, Y. Li, and J. Liu, "CVD synthesis and purification of single-walled carbon nanotubes on aerogel-supported catalyst," *Applied Physics A*, vol. 74, no. 3, pp. 345–348, 2002.
- [13] C. E. Baddour and C. Briens, "Carbon nanotube synthesis: a review," *International Journal of Chemical Reactor Engineering*, vol. 3, 2005.
- [14] P. Avouris, T. Hertel, R. Martel, T. Schmidt, H. R. Shea, and R. E. Walkup, "Carbon nanotubes: nanomechanics, manipulation, and electronic devices," *Applied Surface Science*, vol. 141, no. 3-4, pp. 201–209, 1999.
- [15] K. Tsukagoshi, N. Yoneya, S. Uryu, et al., "Carbon nanotube devices for nanoelectronics," *Physica B*, vol. 323, no. 1–4, pp. 107–114, 2002.
- [16] G. A. Rivas, M. D. Rubianes, M. C. Rodríguez, et al., "Carbon nanotubes for electrochemical biosensing," *Talanta*, vol. 74, no. 3, pp. 291–307, 2007.
- [17] Y. Yun, Z. Dong, V. Shanov, et al., "Nanotube electrodes and biosensors," *Nano Today*, vol. 2, no. 6, pp. 30–37, 2007.
- [18] R. Martel, T. Schmidt, H. R. Shea, T. Hertel, and P. Avouris, "Single- and multi-wall carbon nanotube field-effect transistors," *Applied Physics Letters*, vol. 73, no. 17, pp. 2447–2449, 1998.
- [19] J. N. Coleman, U. Khan, W. J. Blau, and Y. K. Gun'ko, "Small but strong: a review of the mechanical properties of carbon nanotube-polymer composites," *Carbon*, vol. 44, no. 9, pp. 1624–1652, 2006.
- [20] M. José-Yacamán, M. Miki-Yoshida, L. Rendón, and J. G. Santiesteban, "Catalytic growth of carbon microtubules with fullerene structure," *Applied Physics Letters*, vol. 62, no. 2, pp. 202–204, 1993.
- [21] H. Zhu, X. Li, C. Xu, and D. Wu, "Co-synthesis of single-walled carbon nanotubes and carbon fibers," *Materials Research Bulletin*, vol. 37, no. 1, pp. 177–183, 2002.
- [22] W. Ren, F. Li, J. Chen, S. Bai, and H.-M. Cheng, "Morphology, diameter distribution and Raman scattering measurements of double-walled carbon nanotubes synthesized by catalytic decomposition of methane," *Chemical Physics Letters*, vol. 359, no. 3-4, pp. 196–202, 2002.
- [23] Q. Li, H. Yan, J. Zhang, and Z. Liu, "Effect of hydrocarbons precursors on the formation of carbon nanotubes in chemical vapor deposition," *Carbon*, vol. 42, no. 4, pp. 829–835, 2004.
- [24] V. K. Varadan and J. Xie, "Large-scale synthesis of multi-walled carbon nanotubes by microwave CVD," *Smart Materials and Structures*, vol. 11, no. 4, pp. 610–616, 2002.
- [25] B. Fidalgo, Y. Fernández, L. Zubizarreta, et al., "Growth of nanofilaments on carbon-based materials from microwave-assisted decomposition of CH₄," *Applied Surface Science*, vol. 254, no. 11, pp. 3553–3557, 2008.

- [26] J. H. Yen, I. C. Leu, C. C. Lin, and M. H. Hon, "Synthesis of well-aligned carbon nanotubes by inductively coupled plasma chemical vapor deposition," *Applied Physics A*, vol. 80, no. 2, pp. 415–421, 2005.
- [27] T. Ikuno, M. Katayama, N. Yamauchi, et al., "Selective growth of straight carbon nanotubes by low-pressure thermal chemical vapor deposition," *Japanese Journal of Applied Physics*, vol. 43, no. 2, pp. 860–863, 2004.
- [28] M. Kadlečíková, A. Vojačková, J. Breza, V. Luptáková, M. Michalka, and K. Jesenák, "Bundles of carbon nanotubes grown on sapphire and quartz substrates by catalytic hot filament chemical vapor deposition," *Materials Letters*, vol. 61, no. 23–24, pp. 4549–4552, 2007.
- [29] H. Y. Yap, B. Ramaker, A. V. Sumant, and R. W. Carpick, "Growth of mechanically fixed and isolated vertically aligned carbon nanotubes and nanofibers by DC plasma-enhanced hot filament chemical vapor deposition," *Diamond & Related Materials*, vol. 15, no. 10, pp. 1622–1628, 2006.
- [30] H. E. Unalan and M. Chhowalla, "Investigation of single-walled carbon nanotube growth parameters using alcohol catalytic chemical vapour deposition," *Nanotechnology*, vol. 16, no. 10, pp. 2153–2163, 2005.
- [31] W. Qian, T. Liu, F. Wei, Z. Wang, and Y. Li, "Enhanced production of carbon nanotubes: combination of catalyst reduction and methane decomposition," *Applied Catalysis A*, vol. 258, no. 1, pp. 121–124, 2004.
- [32] T. V. Reshetyenko, L. B. Avdeeva, Z. R. Ismagilov, and A. L. Chuvilin, "Catalytic filamentous carbon as supports for nickel catalysts," *Carbon*, vol. 42, no. 1, pp. 143–148, 2004.
- [33] R. Bonadiman, M. D. Lima, M. J. de Andrade, and C. P. Bergmann, "Production of single and multi-walled carbon nanotubes using natural gas as a precursor compound," *Journal of Materials Science*, vol. 41, no. 22, pp. 7288–7295, 2006.
- [34] K. Y. Tran, B. Heinrichs, J.-F. Colomer, J.-P. Pirard, and S. Lambert, "Carbon nanotubes synthesis by the ethylene chemical catalytic vapour deposition (CCVD) process on Fe, Co, and Fe-Co/Al₂O₃ sol-gel catalysts," *Applied Catalysis A*, vol. 318, pp. 63–69, 2007.
- [35] N. Inami, M. Ambri Mohamed, E. Shikoh, and A. Fujiwara, "Synthesis-condition dependence of carbon nanotube growth by alcohol catalytic chemical vapor deposition method," *Science and Technology of Advanced Materials*, vol. 8, no. 4, pp. 292–295, 2007.
- [36] R. Longtin, C. Fauteux, R. Goduguchinta, and J. Pegna, "Synthesis of carbon nanofiber films and nanofiber composite coatings by laser-assisted catalytic chemical vapor deposition," *Thin Solid Films*, vol. 515, no. 5, pp. 2958–2964, 2007.
- [37] J.-F. Colomer, J.-M. Benoit, C. Stephan, S. Lefrant, G. Van Tendeloo, and J. B. Nagy, "Characterization of single-wall carbon nanotubes produced by CCVD method," *Chemical Physics Letters*, vol. 345, no. 1–2, pp. 11–17, 2001.
- [38] J. Kong, A. M. Cassell, and H. Dai, "Chemical vapor deposition of methane for single-walled carbon nanotubes," *Chemical Physics Letters*, vol. 292, no. 4–6, pp. 567–574, 1998.
- [39] K. Hernadi, Z. Kónya, A. Siska, et al., "The role of zeotype catalyst support in the synthesis of carbon nanotubes by CCVD," *Studies in Surface Science and Catalysis*, vol. 142, pp. 541–548, 2002.
- [40] T. Hiraoka, T. Kawakubo, J. Kimura, et al., "Selective synthesis of double-wall carbon nanotubes by CCVD of acetylene using zeolite supports," *Chemical Physics Letters*, vol. 382, no. 5–6, pp. 679–685, 2003.
- [41] B. C. Liu, S. C. Lyu, S. I. Jung, et al., "Single-walled carbon nanotubes produced by catalytic chemical vapor deposition of acetylene over Fe-Mo/MgO catalyst," *Chemical Physics Letters*, vol. 383, no. 1–2, pp. 104–108, 2004.
- [42] C. He, N. Zhao, C. Shi, X. Du, and J. Li, "Carbon nanotubes and onions from methane decomposition using Ni/Al catalysts," *Materials Chemistry and Physics*, vol. 97, no. 1, pp. 109–115, 2006.
- [43] N. Zhao, Q. Cui, C. He, et al., "Synthesis of carbon nanostructures with different morphologies by CVD of methane," *Materials Science and Engineering A*, vol. 460–461, pp. 255–260, 2007.
- [44] Y. Yang, Z. Hu, Y. N. Lü, and Y. Chen, "Growth of carbon nanotubes with metal-loading mesoporous molecular sieves catalysts," *Materials Chemistry and Physics*, vol. 82, no. 2, pp. 440–443, 2003.
- [45] K. Kidena, Y. Kamiyama, and M. Nomura, "A possibility of the production of carbon nanotubes from heavy hydrocarbons," *Fuel Processing Technology*, vol. 89, no. 4, pp. 449–454, 2008.
- [46] H. Liu, G. Cheng, R. Zheng, Y. Zhao, and C. Liang, "Influence of synthesis process on preparation and properties of Ni/CNT catalyst," *Diamond & Related Materials*, vol. 15, no. 1, pp. 15–21, 2006.
- [47] Y. Li, X. Zhang, X. Tao, et al., "Growth mechanism of multi-walled carbon nanotubes with or without bundles by catalytic deposition of methane on Mo/MgO," *Chemical Physics Letters*, vol. 386, no. 1–3, pp. 105–110, 2004.
- [48] B. C. Liu, S. C. Lyu, T. J. Lee, et al., "Synthesis of single- and double-walled carbon nanotubes by catalytic decomposition of methane," *Chemical Physics Letters*, vol. 373, no. 5–6, pp. 475–479, 2003.
- [49] R. M. de Almeida, H. V. Fajardo, D. Z. Mezalira, et al., "Preparation and evaluation of porous nickel-alumina spheres as catalyst in the production of hydrogen from decomposition of methane," *Journal of Molecular Catalysis A*, vol. 259, no. 1–2, pp. 328–335, 2006.
- [50] R. C. Haddon, J. Sippel, A. G. Rinzler, and F. Papadimitrakopoulos, "Purification and separation of carbon nanotubes," *MRS Bulletin*, vol. 29, no. 4, pp. 252–241, 2004.
- [51] Y. Ando, X. Zhao, T. Sugai, and M. Kumar, "Growing carbon nanotubes," *Materials Today*, vol. 7, no. 9, pp. 22–29, 2004.
- [52] N. Muradov, "Catalysis of methane decomposition over elemental carbon," *Catalysis Communications*, vol. 2, no. 3–4, pp. 89–94, 2001.
- [53] C.-M. Chuang, S. P. Sharma, J.-M. Ting, H.-P. Lin, H. Teng, and C.-W. Huang, "Preparation of sea urchin-like carbons by growing one-dimensional nanocarbon on mesoporous carbons," *Diamond & Related Materials*, vol. 17, no. 4–5, pp. 606–610, 2008.
- [54] A.-C. Dupuis, "The catalyst in the CCVD of carbon nanotubes—a review," *Progress in Materials Science*, vol. 50, no. 8, pp. 929–961, 2005.
- [55] I. Vessélyenyi, K. Niesz, A. Siska, et al., "Production of carbon nanotubes on different metal supported catalysts," *Reaction Kinetics and Catalysis Letters*, vol. 74, no. 2, pp. 329–336, 2001.
- [56] K. Hernadi, A. Fonseca, J. B. Nagy, D. Bernaerts, A. Fudala, and A. A. Lucas, "Catalytic synthesis of carbon nanotubes using zeolite support," *Zeolites*, vol. 17, no. 5–6, pp. 416–423, 1996.
- [57] R. Wang, H. Xu, L. Guo, and J. Liang, "Growth of single-walled carbon nanotubes on porous silicon," *Applied Surface Science*, vol. 252, no. 20, pp. 7347–7351, 2006.
- [58] W. Wongwiriyanpan, M. Katayama, T. Ikuno, et al., "Growth of single-walled carbon nanotubes rooted from Fe/Al

- nanoparticle array," *Japanese Journal of Applied Physics*, vol. 44, no. 1, pp. 457–460, 2005.
- [59] C. He, N. Zhao, C. Shi, X. Du, and J. Li, "Synthesis of binary and triple carbon nanotubes over Ni/Cu/Al₂O₃ catalyst by chemical vapor deposition," *Materials Letters*, vol. 61, no. 27, pp. 4940–4943, 2007.
- [60] W. Z. Li, J. G. Wen, M. Sennett, and Z. F. Ren, "Clean double-walled carbon nanotubes synthesized by CVD," *Chemical Physics Letters*, vol. 368, no. 3-4, pp. 299–306, 2003.
- [61] L. Ni, K. Kuroda, L.-P. Zhou, et al., "Kinetic study of carbon nanotube synthesis over Mo/Co/MgO catalysts," *Carbon*, vol. 44, no. 11, pp. 2265–2272, 2006.
- [62] H. Yu, Q. Zhang, Q. Zhang, et al., "Effect of the reaction atmosphere on the diameter of single-walled carbon nanotubes produced by chemical vapor deposition," *Carbon*, vol. 44, no. 9, pp. 1706–1712, 2006.
- [63] A. Tavasoli, K. Sadagiani, F. Khorashe, A. A. Seifkordi, A. A. Rohani, and A. Nakhaei-pour, "Cobalt supported on carbon nanotubes—a promising novel Fischer-Tropsch synthesis catalyst," *Fuel Processing Technology*, vol. 89, no. 5, pp. 491–498, 2008.
- [64] F. Benissad-Aissani, H. Ait-Amar, M.-C. Schouler, and P. Gadelle, "The role of phosphorus in the growth of vapour-grown carbon fibres obtained by catalytic decomposition of hydrocarbons," *Carbon*, vol. 42, no. 11, pp. 2163–2168, 2004.
- [65] S. H. S. Zein and A. R. Mohamed, "Mn/Ni/TiO₂ catalyst for the production of hydrogen and carbon nanotubes from methane decomposition," *Energy and Fuels*, vol. 18, no. 5, pp. 1336–1345, 2004.
- [66] M. C. Bahome, L. L. Jewell, K. Padayachy, et al., "Fe-Ru small particle bimetallic catalysts supported on carbon nanotubes for use in Fischer-Tröpsch synthesis," *Applied Catalysis A*, vol. 328, no. 2, pp. 243–251, 2007.
- [67] L. Barthe, S. Desportes, M. Hemati, K. Philippot, and B. Chaudret, "Synthesis of supported catalysts by dry impregnation in fluidized bed," *Chemical Engineering Research and Design*, vol. 85, no. 6, pp. 767–777, 2007.
- [68] H.-A. Ichi-oka, N.-O. Higashi, Y. Yamada, T. Miyake, and T. Suzuki, "Carbon nanotube and nanofiber syntheses by the decomposition of methane on group 8-10 metal-loaded MgO catalysts," *Diamond & Related Materials*, vol. 16, no. 4–7, pp. 1121–1125, 2007.
- [69] S. Takenaka, H. Umabayashi, E. Tanabe, H. Matsune, and M. Kishida, "Specific performance of silica-coated Ni catalysts for the partial oxidation of methane to synthesis gas," *Journal of Catalysis*, vol. 245, no. 2, pp. 392–400, 2007.
- [70] M. C. Bahome, L. L. Jewell, D. Hildebrandt, D. Glasser, and N. J. Coville, "Fischer-Tropsch synthesis over iron catalysts supported on carbon nanotubes," *Applied Catalysis A*, vol. 287, no. 1, pp. 60–67, 2005.
- [71] L. Piao, Y. Li, J. Chen, L. Chang, and J. Y. S. Lin, "Methane decomposition to carbon nanotubes and hydrogen on an alumina supported nickel aerogel catalyst," *Catalysis Today*, vol. 74, no. 1-2, pp. 145–155, 2002.
- [72] J. M. Xu, X. B. Zhang, Y. Li, et al., "Preparation of Mg_{1-x}Fe_xMoO₄ catalyst and its application to grow MWNTs with high efficiency," *Diamond & Related Materials*, vol. 13, no. 10, pp. 1807–1811, 2004.
- [73] Y. Chen and Y.-S. Lim, "A comparison of different preparation methods of Fe-Mo-Mg-O catalyst for the large-scale synthesis of carbon nanotubes," *Materials Science Forum*, vol. 510-511, pp. 66–69, 2006.
- [74] S. P. Turano and J. Ready, "Chemical vapor deposition synthesis of self-aligned carbon nanotube arrays," *Journal of Electronic Materials*, vol. 35, no. 2, pp. 192–194, 2006.
- [75] W. Qian, T. Liu, F. Wei, Z. Wang, and H. Yu, "Carbon nanotubes containing iron and molybdenum particles as a catalyst for methane decomposition," *Carbon*, vol. 41, no. 4, pp. 846–848, 2003.
- [76] Q. He, Q. Lin, L.-Z. Yao, W.-L. Cai, and Q. Zhu, "Effect of growth parameters on morphology of vertically aligned carbon nanotubes," *Chinese Journal of Chemical Physics*, vol. 20, no. 2, pp. 207–212, 2007.
- [77] Z. Yu, D. Chen, B. Tøtdal, and A. Holmen, "Effect of catalyst preparation on the carbon nanotube growth rate," *Catalysis Today*, vol. 100, no. 3-4, pp. 261–267, 2005.
- [78] Q. Zhang, W. Qian, Q. Wen, Y. Liu, D. Wang, and F. Wei, "The effect of phase separation in Fe/Mg/Al/O catalysts on the synthesis of DWCNTs from methane," *Carbon*, vol. 45, no. 8, pp. 1645–1650, 2007.
- [79] R. L. Vander Wal, T. M. Ticich, and V. E. Curtis, "Substrate-support interactions in metal-catalyzed carbon nanofiber growth," *Carbon*, vol. 39, no. 15, pp. 2277–2289, 2001.
- [80] J.-F. Colomer, G. Bister, I. Willems, et al., "Synthesis of single-wall carbon nanotubes by catalytic decomposition of hydrocarbons," *Chemical Communications*, no. 14, pp. 1343–1344, 1999.
- [81] S.-P. Chai, S. H. S. Zein, and A. R. Mohamed, "Synthesizing carbon nanotubes and carbon nanofibers over supported-nickel oxide catalysts via catalytic decomposition of methane," *Diamond & Related Materials*, vol. 16, no. 8, pp. 1656–1664, 2007.
- [82] P. Piedigrosso, Z. Konya, J.-F. Colomer, A. Fonseca, G. Van Tendeloo, and J. B. Nagy, "Production of differently shaped multi-wall carbon nanotubes using various cobalt supported catalysts," *Physical Chemistry Chemical Physics*, vol. 2, no. 1, pp. 163–170, 2000.
- [83] S.-P. Chai, S. H. S. Zein, and A. R. Mohamed, "Preparation of carbon nanotubes over cobalt-containing catalysts via catalytic decomposition of methane," *Chemical Physics Letters*, vol. 426, no. 4–6, pp. 345–350, 2006.
- [84] K. C. Mondal, N. J. Coville, M. J. Witcomb, G. Tejral, and J. Havel, "Boron mediated synthesis of multiwalled carbon nanotubes by chemical vapor deposition," *Chemical Physics Letters*, vol. 437, no. 1–3, pp. 87–91, 2007.
- [85] C. Vallés, M. Pérez-Mendoza, P. Castell, M. T. Martínez, W. K. Maser, and A. M. Benito, "Towards helical and Y-shaped carbon nanotubes: the role of sulfur in CVD processes," *Nanotechnology*, vol. 17, no. 17, pp. 4292–4299, 2006.
- [86] H. Ago, N. Uehara, N. Yoshihara, et al., "Gas analysis of the CVD process for high yield growth of carbon nanotubes over metal-supported catalysts," *Carbon*, vol. 44, no. 14, pp. 2912–2918, 2006.
- [87] S.-G. Kang, K.-K. Cho, K.-W. Kim, and G.-B. Cho, "Catalytic growth of single- and double-walled carbon nanotubes from Fe-Mo nanoparticles supported on MgO," *Journal of Alloys and Compounds*, vol. 449, no. 1-2, pp. 269–273, 2008.
- [88] L. Ci, H. Zhu, B. Wei, J. Liang, C. Xu, and D. Wu, "Phosphorus—a new element for promoting growth of carbon filaments by the floating catalyst method," *Carbon*, vol. 37, no. 10, pp. 1652–1654, 1999.
- [89] F. Benissad-Aissani, H. Ait-Amar, M.-C. Schouler, and P. Gadelle, "The role of phosphorus in the growth of vapour-grown carbon fibres obtained by catalytic decomposition of hydrocarbons," *Carbon*, vol. 42, no. 11, pp. 2163–2168, 2004.
- [90] S. Zhan, Y. Tian, Y. Cui, et al., "Effect of process conditions on the synthesis of carbon nanotubes by catalytic decomposition

- of methane,” *China Particuology*, vol. 5, no. 3, pp. 213–219, 2007.
- [91] S. P. Chai, V. M. Sivakumar, S. H. S. Zein, and A. R. Mohamed, “The examination of NiO and CoO_x catalysts supported on Al₂O₃ and SiO₂ for carbon nanotubes production via CCVD of methane,” *Carbon Science & Technology*, vol. 1, pp. 1–3, 2008.
- [92] J.-H. Lin, C.-S. Chen, H.-L. Ma, C.-Y. Hsu, and H.-W. Chen, “Synthesis of MWCNTs on CuSO₄/Al₂O₃ using chemical vapor deposition from methane,” *Carbon*, vol. 45, no. 1, pp. 223–225, 2007.
- [93] F. Ohashi, G. Y. Chen, V. Stolojan, and S. R. P. Silva, “The role of the gas species on the formation of carbon nanotubes during thermal chemical vapour deposition,” *Nanotechnology*, vol. 19, no. 44, 2008.
- [94] N. Q. Zhao, C. N. He, J. Ding, et al., “Bamboo-shaped carbon nanotubes produced by catalytic decomposition of methane over nickel nanoparticles supported on aluminum,” *Journal of Alloys and Compounds*, vol. 428, no. 1-2, pp. 79–83, 2007.
- [95] N. Zhao, C. He, Z. Jiang, J. Li, and Y. Li, “Physical activation and characterization of multi-walled carbon nanotubes catalytically synthesized from methane,” *Materials Letters*, vol. 61, no. 3, pp. 681–685, 2007.
- [96] L. K. Noda, N. S. Gonçalves, A. Valentini, L. F. D. Probst, and R. M. de Almeida, “Effect of Ni loading and reaction temperature on the formation of carbon nanotubes from methane catalytic decomposition over Ni/SiO₂,” *Journal of Materials Science*, vol. 42, no. 3, pp. 914–922, 2007.
- [97] I. Bustero, G. Ainara, O. Isabel, M. Roberto, R. Inés, and A. Amaya, “Control of the properties of carbon nanotubes synthesized by CVD for application in electrochemical biosensors,” *Microchimica Acta*, vol. 152, no. 3-4, pp. 239–247, 2006.

Research Article

A Facile and Generic Strategy to Synthesize Large-Scale Carbon Nanotubes

Yong Hu,^{1,2} Ting Mei,² Libo Wang,² and Haisheng Qian¹

¹Zhejiang Key Laboratory for Reactive Chemistry on Solid Surfaces and Institute of Physical Chemistry, Zhejiang Normal University, Jinhua 321004, China

²School of Electrical and Electronic Engineering, Nanyang Technological University, Singapore 639798

Correspondence should be addressed to Yong Hu, yonghu@zjnu.edu.cn

Received 24 September 2009; Accepted 14 January 2010

Academic Editor: Raymond Whitby

Copyright © 2010 Yong Hu et al. This is an open access article distributed under the Creative Commons Attribution License, which permits unrestricted use, distribution, and reproduction in any medium, provided the original work is properly cited.

An easy method to prepare carbon nanotubes (CNTs) has been demonstrated using a two-step refluxing and calcination process. First, a readily available inorganic salt, $\text{Ni}(\text{NO}_3)_2 \cdot 6\text{H}_2\text{O}$, used as the catalyst precursor was dissolved in the high-boiling-point organic solvents (alcohols or polyhydric alcohol) by refluxing at 190°C for 3 hours. After refluxing, NiO nanoparticles obtained in the solution act as the catalyst, and the organic refluxing solvents are used as the carbon source for the growth of CNTs. Second, CNTs are prepared by calcining the refluxed solution at 800°C in an N_2 atmosphere for 3 hours. Results show that CNT growth possibly originates from carbon rings, with the nanotube walls growing perpendicular to these rings and forming a closed tube at the end.

1. Introduction

Since their emergence, carbon nanotubes (CNTs) [1] have demonstrated their versatility in a variety of applications such as supported catalysts for hydrogenation reactions [2], fuel cells [3], field emission devices [4], and nanoelectronic devices [5], due to their unique mechanical, chemical, and electrochemical properties [6, 7]. Consequently, demand for the consumption of CNT materials is huge, making desirable their fast, efficient, high yield and cost effective fabrication.

Previously, a number of techniques have been developed for fabricating CNTs, including electric arc-discharge [8], laser ablation [9], chemical vapor deposition (CVD) [10, 11], pyrolysis [12], plasma enhanced CVD (PECVD) [13], laser assisted CVD (LACVD) [14], two-stage fluid bed reactor [15], aerosol method [16], solvothermal method [17, 18], and high pressure CO disproportionation process (HiPCO) [19]. Recently, Tang et al. reported a novel catalytic combustion method of synthesizing CNTs in situ in high yield from polypropylene as a carbon source in the presence of organic-modified clay and a supported Ni catalyst [20]. Most of the methods originate from the idea of obtaining adequate active atomic carbon species or clusters from

carbon sources and assembling them into CNTs on catalysts. Although great efforts have been made in the development of synthesis methods, their numerous steps and the adoption of expensive or nonrenewable materials still make the methods complicated. Thus we look for a simple, low-cost, and effective method for the synthesis of CNTs.

Herein, we report a simple and low-cost strategy of CNT synthesis that adopts a refluxing process with readily available inorganic salts $\text{Ni}(\text{NO}_3)_2 \cdot 6\text{H}_2\text{O}$ as the catalyst precursor, and high-boiling-point (BP) di(ethylene glycol) (DEG), glycerol and ethylene glycol (EG), as solvents and carbon source. After refluxing, NiO nanoparticles obtained in the solution act as the catalyst for the growth of CNTs. The final CNT products are successfully prepared by calcining the refluxed solution at 800°C in an N_2 atmosphere for 3 hours. The whole process is kept simple and easy to control because there are not too many parameters required for monitoring.

2. Experimental

2.1. Synthesis of NiO Nanoparticles and CNTs. Chemical reagents purchased from Sigma-Aldrich were used in the experiments with no further purification. For a typical

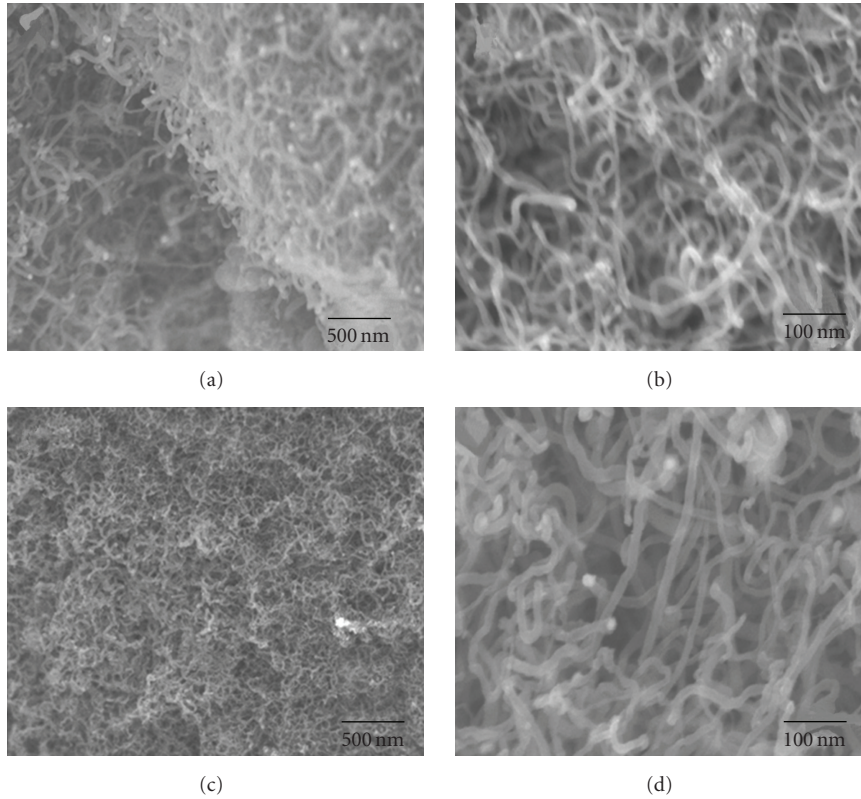


FIGURE 1: FE-SEM images of CNTs prepared by calcining DEG solution: (a) low magnification and (b) high magnification; FE-SEM images of CNTs prepared by calcining (c) glycerol solution and (d) EG solution.

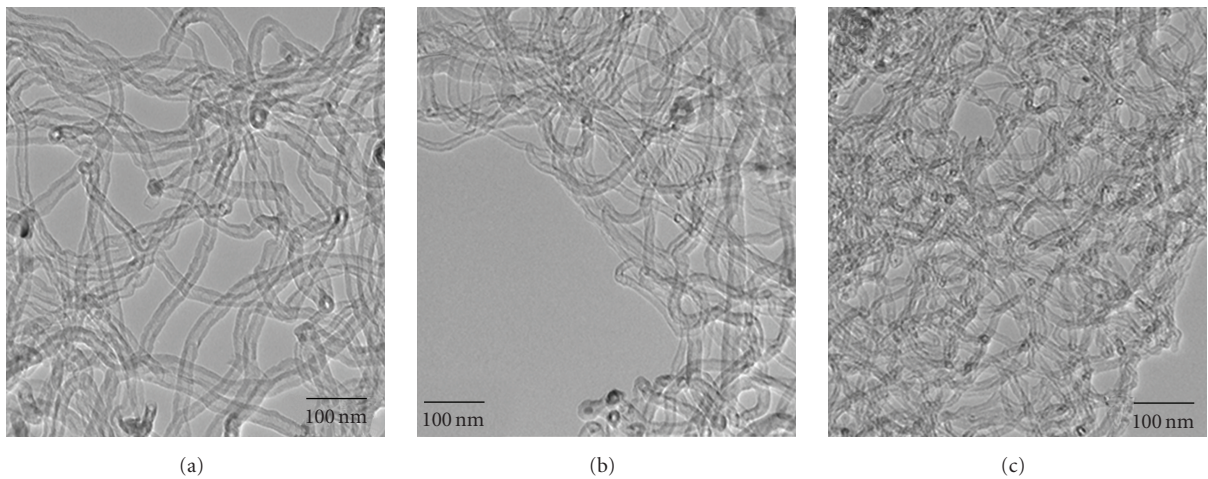


FIGURE 2: TEM images of CNTs prepared by calcining (a) DEG solution; (b) glycerol solution; (c) EG solution.

synthesis procedure, 0.0025 mol (0.73 g) of the metal salt $\text{Ni}(\text{NO}_3)_2 \cdot 6\text{H}_2\text{O}$ was introduced and dissolved in 50 mL of DEG, glycerol, and EG solvent, in three round bottom flasks. The solutions were heated in an oil bath to form a clear solution under reflux with vigorous stirring. When the reflux temperature was increased to 190°C , the clear solution then turned turbid. The reaction was maintained with stirring for aging for at least 3 hours at this fixed temperature.

The flasks were then cooled down to room temperature after the heat source was removed. Subsequently, the three refluxed solutions were injected into quartz crucibles with lid. The final CNT products were obtained by calcination at 800°C in an N_2 atmosphere for 3 hours with a heating rate of 1°C min^{-1} . After calcination, the black precipitates were collected and washed with absolute ethanol, dilute HCl aqueous solution, and deionized water in sequence. Finally,

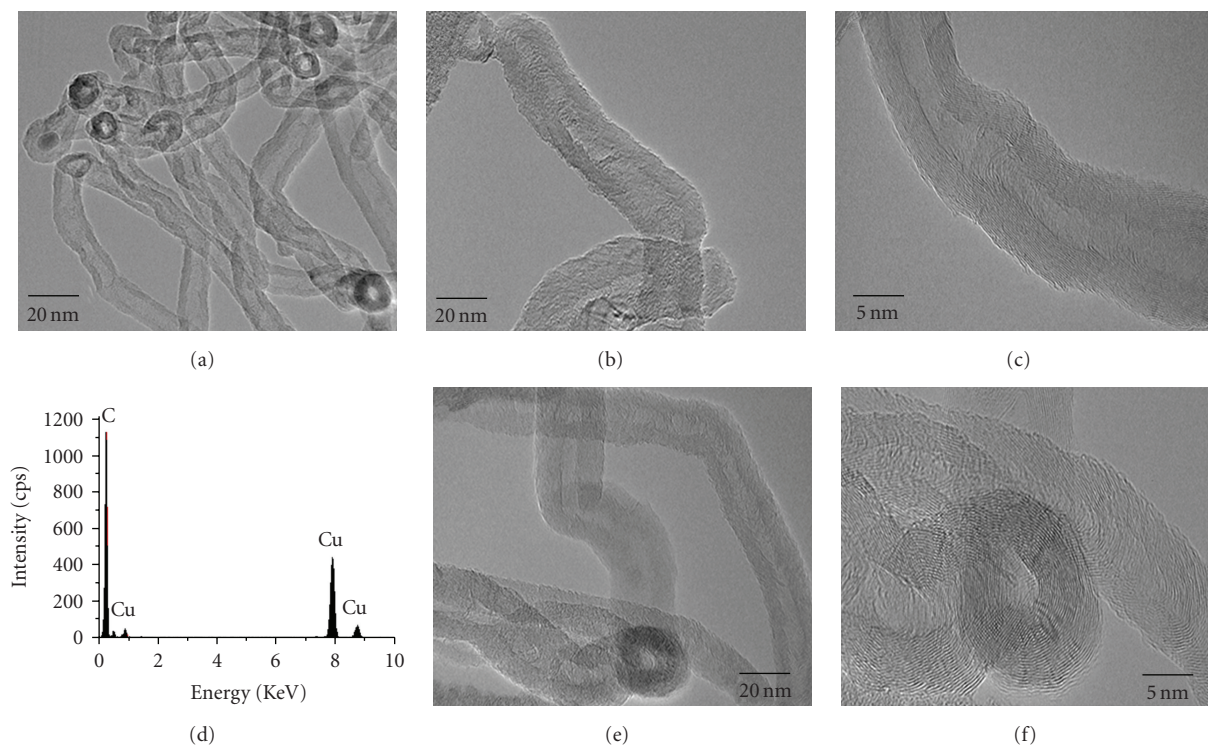


FIGURE 3: HRTEM images of CNTs: (a) nanotubes prepared by calcining DEG solution; (b) the closed bottom of a nanotube; (c) a section of nanotube wall; (d) the EDS pattern of a carbon ring; (e) the open tip of a carbon ring at low magnification and (f) at high magnification.

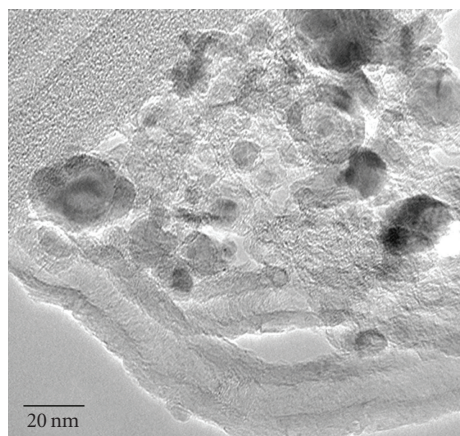


FIGURE 4: TEM image of CNTs prepared by calcination at 700°C.

the obtained samples were dried in vacuum at 60°C for 6 hours.

2.2. Characterization. Morphological and structural examinations of the as-prepared products were performed using field-emission scanning electron microscopy (FE-SEM, JEOL JSM-6340F); transmission electron microscopy (TEM) and high resolution TEM (HRTEM) were conducted at 200 keV with a JEM-2100F field emission machine, after dispersing the sample in ethanol and depositing several drops of the suspension on holey-carbon films supported by copper grids.

Energy-dispersive X-ray spectroscopy (EDS) was performed on a JEM-2100F TEM. The Raman spectrum was recorded at ambient temperature on a Witec Alpha 300 Raman spectrometer with an argon-ion laser at an excitation wavelength of 488 nm.

3. Results and Discussion

The FE-SEM images of CNTs synthesized by calcining DEG solution are shown in Figure 1(a) (lowmagnification) and Figure 1(b) (highmagnification). Figures 1(c) and 1(d) show the images of the products prepared by calcining glycerol and EG solution. These images demonstrate that the approach presented in this paper offers a large-scale production yield for CNTs. These CNT samples present a uniform tube diameter (~15 nm) and a tube length ranging from hundreds of nanometers to several microns.

The TEM images (Figure 2) reveal that the CNTs synthesized by this method are multiwall CNTs (MWCNTs) with strong graphitic structure. Figures 2(a), 2(b), and 2(c) show the characteristics of the MWCNTs with open tips as produced in all solutions. The nanotube sizes observed in these images are in good agreement with those observed using FE-SEM. A further investigation on the tubular structure of the HRTEM image shown in Figure 3(a) clearly reveals an open tip and a closed bottom, which validates that the growth of the nanotubes originated from carbon rings resulting in the formation of closed bottoms. Figures 3(b) and 3(c) show the closed bottom of nanotube and a section of

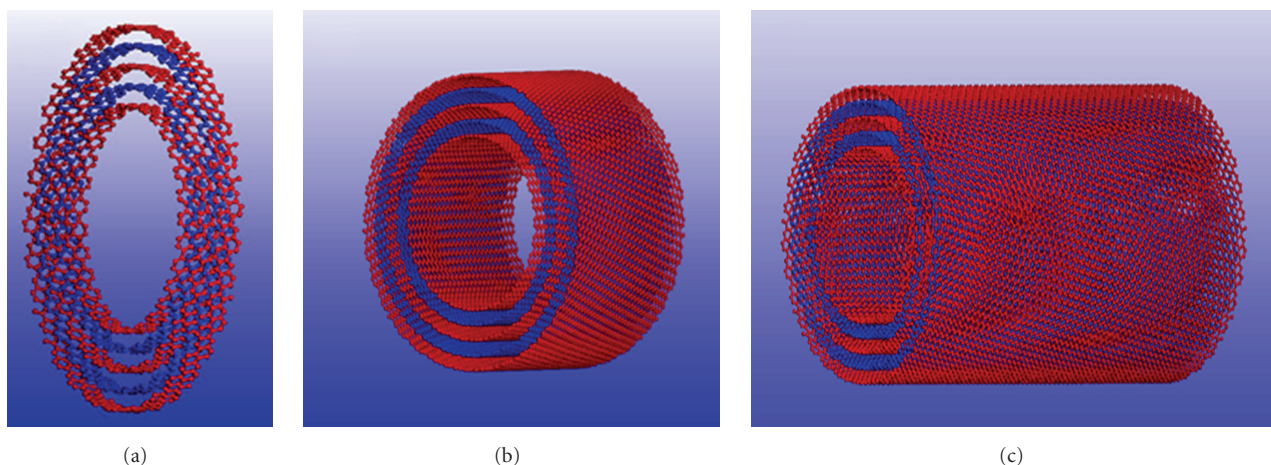


FIGURE 5: Schematic of CNT growth: (a) the formation of the original multi-layer carbon rings; (b) the growth of multi-layer nanotube walls grow perpendicular to the carbon rings; (c) the formed nanotube with an open tip and a closed bottom.

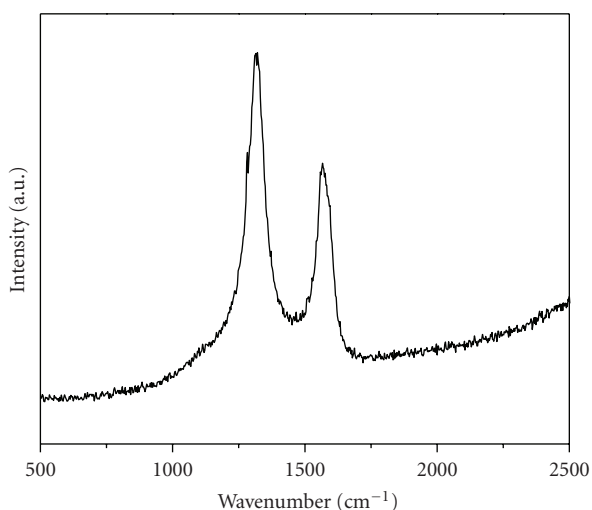


FIGURE 6: Raman spectrum of CNTs.

nanotube wall, which are clearly graphitized. The interlayer spacing in the multiwalls is about 0.34 nm, corresponding to the lattice parameter of graphite carbon in the (002) plane [1]. EDS performed on a ring tip (Figure 3(d)) indicates that the tip only contains carbon; no other element was found. Figures 3(e) and 3(f) show the open tip of a carbon ring at low magnification and at high magnification.

In the refluxing process, NiO nanoparticles used as catalyst could be obtained via the pyrolysis of common metal salts ($\text{Ni}(\text{NO}_3)_2 \cdot 6\text{H}_2\text{O}$) in a high BP organic solvent which acts as a carbon source in the next step. In the calcination process, nucleations of multilayer carbon rings were being formed under the catalyst effect of the NiO nanoparticles, and nanotubes were assembled along the ring axial growth. Meanwhile, because they were observed products at 700°C (Figure 4), we believe that the great amount of ring-like products further favored the growth of nanotubes from the multi-layer carbon rings. In addition, for MWCNTs, it is

quite likely that the presence of the outer wall stabilizes the inner wall, keeping it open for continuous growth [21]. A possible CNT growth mechanism was depicted in detail in Figure 5.

The representative Raman spectrum (Figure 6) of the product calcined in refluxing DEG solution at 800°C shows the typical features of MWCNTs [1]. The spectrum exhibits two peaks at 1318 and 1570 cm^{-1} , indicating the graphite structure of the nanotubes. According to the analysis of Kasuya et al. [22], the complex structure as characterized by the 1540–1600 cm^{-1} region can be understood by zone-folding of the graphite phonon dispersion relation. The IR spectrum demonstrates the peak frequencies of the graphite (G) mode at 1570 cm^{-1} and contains disorder modes at 1318 cm^{-1} (D).

4. Conclusions

We have successfully synthesized CNTs of uniform diameter on a large scale through a novel refluxing and calcination solution process, in which reflux solvents were used as the carbon source and NiO nanoparticles obtained after refluxing were used as the catalyst. The products prepared in this approach were no toxic and corrosive reagents. This approach allows adoption of other metal salts and high BP organic solvents for further exploration. Due to merits such as its simplicity, low cost, high purity, good controllability, and high yield, we believe that this method can be exploited at the scale of industrial production.

Acknowledgments

This material is based on research supported by the Scientific Research Foundation for the Returned Overseas Chinese Scholars, State Education Ministry, and the Singapore National Research Foundation under CRP Award no. NRF-G-CRP 2007-01.

References

- [1] S. Iijima, "Helical microtubules of graphitic carbon," *Nature*, vol. 354, no. 6348, pp. 56–58, 1991.
- [2] C. Pham-Huu, N. Keller, L. J. Charbonniere, R. Ziessel, and M. J. Ledoux, "Carbon nanofiber supported palladium catalyst for liquid-phase reactions. An active and selective catalyst for hydrogenation of C = C bonds," *Chemical Communications*, no. 19, pp. 1871–1872, 2000.
- [3] C. Wang, M. Waje, X. Wang, J. M. Tang, R. C. Haddon, and Y. Yan, "Proton exchange membrane fuel cells with carbon nanotube based electrodes," *Nano Letters*, vol. 4, no. 2, pp. 345–348, 2004.
- [4] S. Fan, M. G. Chapline, N. R. Franklin, T. W. Tomblor, A. M. Cassell, and H. Dai, "Self-oriented regular arrays of carbon nanotubes and their field emission properties," *Science*, vol. 283, no. 5401, pp. 512–514, 1999.
- [5] P. J. de Pablo, E. Graugnard, B. Walsh, R. P. Andres, S. Datta, and R. Reifenberger, "A simple, reliable technique for making electrical contact to multiwalled carbon nanotubes," *Applied Physics Letters*, vol. 74, no. 2, pp. 323–325, 1999.
- [6] R. H. Baughman, A. A. Zakhidov, and W. A. de Heer, "Carbon nanotubes—the route toward applications," *Science*, vol. 297, no. 5582, pp. 787–792, 2002.
- [7] J.-M. Nhut, L. Pesant, J.-P. Tessonier, et al., "Mesoporous carbon nanotubes for use as support in catalysis and as nanosized reactors for one-dimensional inorganic material synthesis," *Applied Catalysis A*, vol. 254, no. 2, pp. 345–363, 2003.
- [8] T. W. Ebbesen and P. M. Ajayan, "Large-scale synthesis of carbon nanotubes," *Nature*, vol. 358, no. 6383, pp. 220–222, 1992.
- [9] A. Thess, R. Lee, P. Nikolaev, et al., "Crystalline ropes of metallic carbon nanotubes," *Science*, vol. 273, no. 5274, pp. 483–487, 1996.
- [10] D. Y. Kim, C.-M. Yang, Y. S. Park, et al., "Characterization of thin multi-walled carbon nanotubes synthesized by catalytic chemical vapor deposition," *Chemical Physics Letters*, vol. 413, no. 1–3, pp. 135–141, 2005.
- [11] G.-Y. Xiong, D. Z. Wang, and Z. F. Ren, "Aligned millimeter-long carbon nanotube arrays grown on single crystal magnesia," *Carbon*, vol. 44, no. 5, pp. 969–973, 2006.
- [12] A. Govindaraj and C. N. R. Rao, "Organometallic precursor route to carbon nanotubes," *Pure and Applied Chemistry*, vol. 74, no. 9, pp. 1571–1580, 2002.
- [13] K. H. Jung, J.-H. Boo, and B. Hong, "Synthesis of carbon nanotubes grown by hot filament plasma-enhanced chemical vapor deposition method," *Diamond and Related Materials*, vol. 13, no. 2, pp. 299–304, 2004.
- [14] S. N. Bondi, W. J. Lackey, R. W. Johnson, X. Wang, and Z. L. Wang, "Laser assisted chemical vapor deposition synthesis of carbon nanotubes and their characterization," *Carbon*, vol. 44, no. 8, pp. 1393–1403, 2006.
- [15] W. Qian, T. Liu, F. Wei, Z. Wang, and Y. Li, "Enhanced production of carbon nanotubes: combination of catalyst reduction and methane decomposition," *Applied Catalysis A*, vol. 258, no. 1, pp. 121–124, 2004.
- [16] A. G. Nasibulin, A. Moisala, H. Jiang, and E. I. Kauppinen, "Carbon nanotube synthesis from alcohols by a novel aerosol method," *Journal of Nanoparticle Research*, vol. 8, no. 3–4, pp. 465–475, 2006.
- [17] L. Jiang and L. Gao, "Carbon nanotubes-magnetite nanocomposites from solvothermal processes: formation, characterization, and enhanced electrical properties," *Chemistry of Materials*, vol. 15, no. 14, pp. 2848–2853, 2003.
- [18] Y. Jiang, Y. Wu, S. Zhang, et al., "A catalytic-assembly solvothermal route to multiwall carbon nanotubes at a moderate temperature," *Journal of the American Chemical Society*, vol. 122, no. 49, pp. 12383–12384, 2000.
- [19] P. Nikolaev, M. J. Bronikowski, R. K. Bradley, et al., "Gas-phase catalytic growth of single-walled carbon nanotubes from carbon monoxide," *Chemical Physics Letters*, vol. 313, no. 1–2, pp. 91–97, 1999.
- [20] T. Tang, X. Chen, X. Meng, H. Chen, and Y. Ding, "Synthesis of multiwalled carbon nanotubes by catalytic combustion of polypropylene," *Angewandte Chemie International Edition*, vol. 44, no. 10, pp. 1517–1520, 2005.
- [21] T. Guo, P. Nikolaev, A. G. Rinzler, D. Tománek, D. T. Colbert, and R. E. Smalley, "Self-assembly of tubular fullerenes," *Journal of Physical Chemistry*, vol. 99, no. 27, pp. 10694–10697, 1995.
- [22] A. Kasuya, Y. Sasaki, Y. Saito, K. Tohji, and Y. Nishina, "Evidence for size-dependent discrete dispersions in single-wall nanotubes," *Physical Review Letters*, vol. 78, no. 23, pp. 4434–4437, 1997.

Research Article

One-Step Route to Synthesize Multiwalled Carbon Nanotubes Filled with MgO Nanorods

Jing Liu,¹ Chunli Guo,² Xiaojian Ma,¹ Changhui Sun,¹ Fengxia Li,¹ and Yitai Qian^{1,3}

¹Key Laboratory of Colloid and Interface Chemistry, Shandong University, Ministry of Education, Jinan 250100, China

²State Key Laboratory of Crystal Materials, Shandong University, Jinan 250100, China

³Hefei National Laboratory for Physical Sciences at Microscale, Department of Chemistry, University of Science and Technology of China, Anhui, Hefei 230026, China

Correspondence should be addressed to Chunli Guo, gcl@sdu.edu.cn and Yitai Qian, ytqian@ustc.edu.cn

Received 2 November 2009; Accepted 19 April 2010

Academic Editor: Yanqiu Zhu

Copyright © 2010 Jing Liu et al. This is an open access article distributed under the Creative Commons Attribution License, which permits unrestricted use, distribution, and reproduction in any medium, provided the original work is properly cited.

Multiwalled carbon nanotubes filled with MgO nanorods were synthesized through the reaction of ethanol and Mg powder in the presence of TiO₂ at 400°C. X-ray powder diffraction indicated that the sample was composed of graphite and cubic MgO. Transmission electron microscopy studies showed that multi-walled CNTs with the outer diameters of 70–130 nm were filled with discontinuous MgO nanorods whose diameter was in the range of 25–40 nm. The ratios of the band intensities ($I_D/I_G = 0.67$) in Raman spectrum implied that carbon nanotubes had good crystallinity. The influence of correlative reaction factors on the morphology of the sample and the possible formation mechanism were discussed.

1. Introduction

Filling foreign materials into the hollow cavities of carbon nanotubes (CNTs) has been of widespread interest due to their special properties [1–3]. And they have broader application compared to pure CNTs or second phases, such as Fe₂O₃-filled CNTs as a negative electrode for an Fe-air battery [4] and spherical Ni(OH)₂/CNTs as the electrode in asymmetric supercapacitor [5]. SnO₂/multi-walled CNT has a high reversible discharge capacity compared to pure nano-SnO₂ [6]. MnO₂/CNT hybrid coaxial nanotubes have also enhanced reversible capacity more than pure MnO₂ nanotubes [7].

MgO has gained extensive application in catalyst [8, 9], refractory materials [10] and optically transparent ceramic windows [11, 12]. Recently the studies indicate that MgO can make ammoniated electrons stable [13] and has weak ferromagnetism [14]. Maybe the MgO/CNTs have potential applications in electrode. And carbon-coated MgO nanoparticles had been prepared by various methods. Motiei et al. [15] had prepared hollow carbon cubes and carbon-coated MgO cubes through the reaction between Mg and Mo(CO)₆ at 900°C. Bedilo et al. [16] had synthesized carbon-coated MgO nanoparticles by the decomposition of dry

magnesium methoxide or resorcinol modified magnesium methoxide. Luo et al. [17] had synthesized MgO/C core-shell nanospheres with the diameters of 300–500 nm at 600°C by reducing ethyl ether with metallic magnesium. Zhou et al. [18] had fabricated carbon-coated MgO by the coprecipitation magnesium nitrate with sucrose. However, there are few reports about the synthesis of CNT-coated MgO nanostructures.

In this study, we report the preparation and characterization of MgO-filled multi-walled CNTs which were obtained by the reaction of ethanol and Mg powder in the presence of TiO₂ at 400°C. Transmission electron microscopy (TEM) showed that multi-walled CNTs filled with discontinuous MgO nanorods are open at the both ends, whose outer diameters were between 70 and 130 nm. A possible mechanism for MgO nanorods encapsulated in multi-walled CNTs is discussed in this study and the research of electrochemical properties of MgO/CNTs is still underway.

2. Experimental Section

All reagents used in this work were analysis-grade reagents from the Shanghai Chemical Factory, China, and were

directly used without further treatment. MgO nanorods encapsulated in multi-walled CNTs were prepared as follows: magnesium powder (1 g), ethanol (10 mL), and TiO₂ (0.5 g) were mixed in a 20 mL stainless autoclave and heated in an electric oven at 400°C for 10 hours, then cooled to room temperature. The wet black powder was collected and washed with dilute hydrochloric and hydrofluoric. The final products were washed with distilled water and absolute ethyl alcohol, and then dried under vacuum at 50°C for 4 hours.

X-ray powder diffraction (XRD) measurements were carried out using a Bruker D8 advanced X-ray diffractometer equipped with graphite-monochromatized Cu K α radiation ($\lambda = 1.5418 \text{ \AA}$). Field-emission scanning electron microscopy (FESEM) images were taken by a JSM-6700F scanning electron microscope. TEM images were obtained by a Hitachi model H-7000 TEM with an accelerating voltage of 100 kV. The high-resolution (HRTEM) images and energy-dispersive X-ray spectroscopy (EDS) were recorded on a JEOL 2100 HRTEM microscope. Raman spectra were obtained using a Horiba Jobin Yvon Raman microscope system. The spectrometer was operated in continuous scanning mode in the range of 500–1700 cm⁻¹ using argon-ion laser of wavelength $\lambda = 514.5 \text{ nm}$.

3. Results and Discussion

Figure 1 shows XRD pattern of the as-prepared products. The diffraction peaks at 43.0 and 62.4° were identified as the (200) and (220) reflections of MgO (JCPDS card no. 65-0476), and those at 26.5 and 44.9° were attributed to the (002) and (101) planes of CNT-related graphite (marked with “c”). There are TiC and a little stable rutile-type titanium dioxide [19] in the XRD pattern.

Figure 2(a) is a SEM image of the samples washed with HCl. A great number of CNTs with outer diameters of 70 ~ 130 nm and lengths of tens of micrometers were observed in Figure 2(a). The top of nanotube displayed in the inset of Figure 2(a) is open, which likes nanocapillary to absorb hydrogen or other gases [20]. Figure 2(b) is a TEM image of the samples. The internal structure of CNTs, inside which discontinuous nanorods were encapsulated with the diameters of 25–40 nm, was observed clearly. The inset in Figure 2(b) is the corresponding EDS of nanorods, suggesting that their chemical compositions were MgO (the Cu peaks are from the copper grid that supports the specimen and C peaks are possibly from the nanotubes). That Ti peak was not observed in EDS indicated that TiC particles were not located inside CNTs. The TEM image of the aggregated particles located outside CNTs was further confirmed (see Figure S1 in supplementary material available online at doi:10.1155/2010/671863 supporting information). A further investigation by HRTEM (Figure 2(c)) reveals that the interlayer separation of 0.34 nm corresponds to the (002) plane of the multi-walled CNTs and the fringe spacing of 0.21 nm matches the (200) reflection of MgO nanorods.

The representative Raman spectrum (Figure 3) of the sample shows the typical features of multi-walled CNTs.

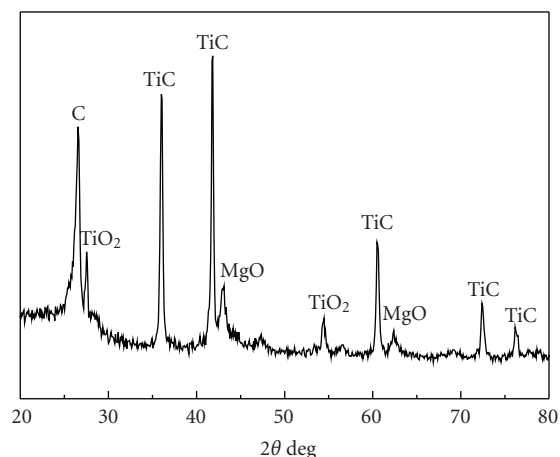
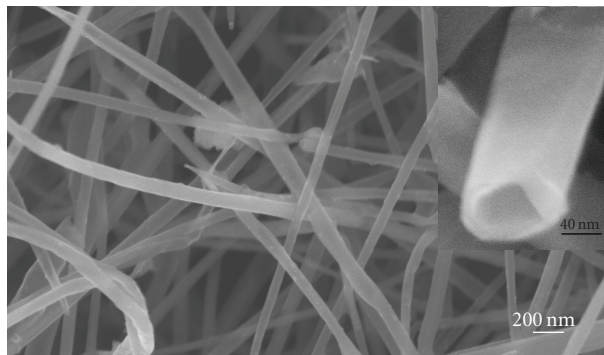


FIGURE 1: The typical XRD patterns of the products washed with dilute acid.

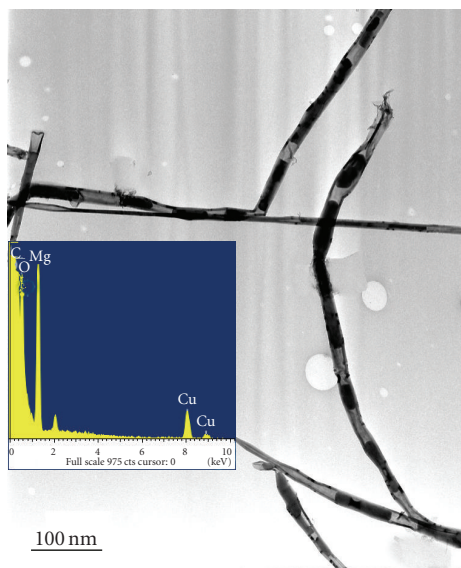
The spectrum demonstrates that the peak frequencies of the graphite (G) mode are at 1575 cm⁻¹ and contains disorder (D) modes that are at 1343 cm⁻¹. An indication of the relative graphitization of the deposited material can be expressed as the ratio of I_D/I_G [21]. The ratios of the band intensities shown in Figure 3 are $I_D/I_G = 0.67$, suggesting a higher degree of graphitization.

Several experimental factors including metal oxides, temperature, and metals were adopted to investigate the possible formation mechanism of the MgO-filled multi-walled CNTs. The introduction of metal oxides played a key role in encapsulating MgO nanorods inside multi-walled CNTs. In the absence of TiO₂, only pure multi-walled CNTs appeared in the products, which agreed with previous results [22]. If the amount of TiO₂ was less than 0.5 g in our experimental route, the encapsulations of MgO inside multi-walled CNTs were difficult to be observed by TEM. As TiO₂ was replaced by other metal oxides such as Fe₂O₃, the main morphology of as-prepared samples was different with that of TiO₂ added in the reaction system. The abovementioned experimental results suggested that the presence of TiO₂ in the reaction system could assist the formation of MgO nanorods encapsulated in multi-walled CNTs. The detail reason for the influence of metal oxides on the products was still under investigation. In addition, the influences of the temperature and metals on the MgO-filled multi-walled CNTs had also been studied. Results showed that the yield of MgO nanorods encapsulated inside multi-walled CNTs was reduced with the reaction temperature decreasing. When the reaction temperature was lower than 200°C, irregular graphite films were the major products. Furthermore, when Mg powder was substituted by Al, Fe, Zn, Co, or Ni, the reaction did not happen. A possible reason is that the activity of Mg powder was higher than that of abovementioned metals.

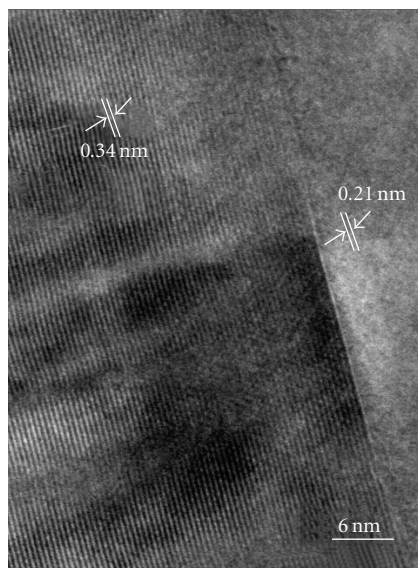
Based on the results of HRTEM and EDS, a possible growth mechanism of multi-walled CNTs filled with MgO nanorods was proposed. It is known that catalyst materials



(a)



(b)



(c)

FIGURE 2: (a) SEM image of CNTs (The inset is a high-resolution image.); (b) TEM image of CNTs filled with MgO nanorods (inset, EDS); (c) HRTEM image of multi-walled CNTs filled with MgO.

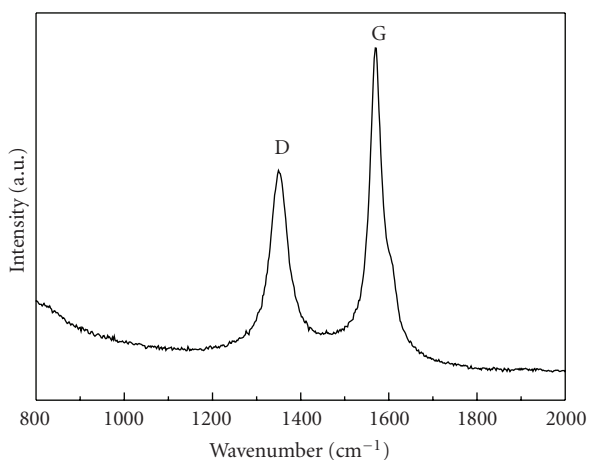
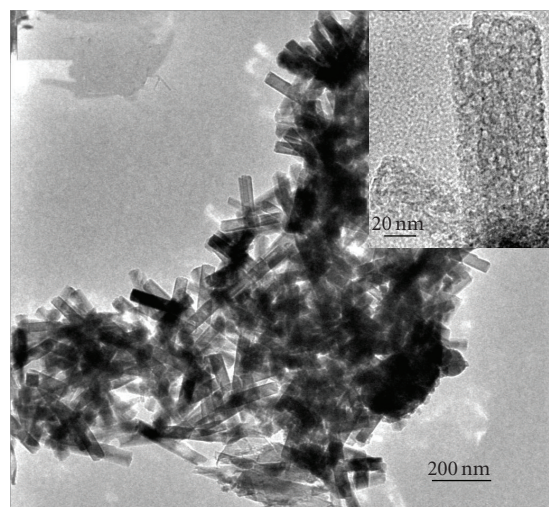


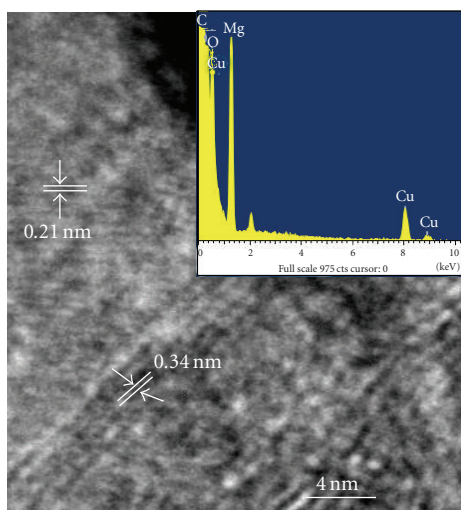
FIGURE 3: Raman spectrum of the as-prepared sample.

at the ends of CNTs were easy to be encapsulated into the CNTs [23–25]. However, in this system, there were no

magnetic catalysts to promote the encapsulation and their growth mechanism cannot be used to explain the growth of the MgO-filled multi-walled CNTs. And there are no other reports on the encapsulation of MgO nanostructures inside multi-walled CNTs. Some porous MgO nanorods with the diameters of 25–40 nm, similar in size to the MgO nanorods encapsulated by multi-walled CNTs, were observed by TEM (Figure 4(a)). The inset in Figure 4(a) is an enlarged individual porous MgO nanorod, which was characterized by HRTEM (Figure 4(b)). The formation of MgO may be ascribed to the reaction of Mg power and TiO_2 . Simultaneously TiC nanoparticles form between Ti coming from TiO_2 and carbon atoms. The inset in Figure 4(b) further proved that the porous nanorods were coated with layers of graphite. Porous structures have high specific surface area and high surface energy [26]. Therefore carbon atoms were easy to deposit on the surface of the MgO nanorods. As the reaction proceeded, the graphite layers turned into highly ordered multi-walled CNTs and finally the MgO-filled CNTs were formed.



(a)



(b)

FIGURE 4: (a) TEM image of the porous products (The inset image shows the enlarged nanorods.); (b) HRTEM analysis of the porous MgO nanorod (The inset image is the EDS spectrum.).

4. Conclusions

MgO nanorods encapsulated in multi-walled CNTs were fabricated by a one-step synthesis in a 20 mL autoclave at 400°C. TEM and HRTEM images show that MgO nanorods with diameters of 25–40 nm were encapsulated inside multi-walled CNTs with outer diameters of 70–130 nm and lengths of tens of micrometers. Raman spectrum suggested that multi-walled CNTs had excellent crystalline. The MgO nanorods are believed to be a template for the multi-walled CNTs growing. The electrochemical properties of MgO/CNTs are being studied.

Acknowledgments

Financial supports from the National Natural Science Foundation of China (no. 20671058), the 973 Projects of China

(no. 2005CB623601), and the Natural Science Foundation of Shandong province (no. 11190004010664) are greatly appreciated. The authors thank Dr. Pamela Holt, Shandong University, for proofreading the manuscript.

References

- [1] P. M. Ajayan and S. Iijima, "Capillarity-induced filling of carbon nanotubes," *Nature*, vol. 361, no. 6410, pp. 333–334, 1993.
- [2] D. Ugarte, A. Châtelain, and W. A. de Heer, "Nanocapillarity and chemistry in carbon nanotubes," *Science*, vol. 274, no. 5294, pp. 1897–1899, 1996.
- [3] J. Sloan, J. Cook, M. L. H. Green, J. L. Hutchison, and R. Tenne, "Crystallisation inside fullerene related structures," *Journal of Materials Chemistry*, vol. 7, no. 7, pp. 1089–1095, 1997.
- [4] B. T. Hang, H. Hayashi, S.-H. Yoon, S. Okada, and J.-I. Yamaki, "Fe₂O₃-filled carbon nanotubes as a negative electrode for an Fe-air battery," *Journal of Power Sources*, vol. 178, no. 1, pp. 393–401, 2008.
- [5] X.-F. Wang, D.-B. Ruan, and Z. You, "Application of spherical Ni(OH)₂/CNTs composite electrode in asymmetric supercapacitor," *Transactions of Nonferrous Metals Society of China*, vol. 16, no. 5, pp. 1129–1134, 2006.
- [6] Y. Fu, R. Ma, Y. Shu, Z. Cao, and X. Ma, "Preparation and characterization of SnO₂/carbon nanotube composite for lithium ion battery applications," *Materials Letters*, vol. 63, no. 22, pp. 1946–1948, 2009.
- [7] A. L. M. Reddy, M. M. Shaijumon, S. R. Gowda, and P. M. Ajayan, "Coaxial MnO₂/carbon nanotube array electrodes for high-performance lithium batteries," *Nano Letters*, vol. 9, no. 3, pp. 1002–1006, 2009.
- [8] D. Gulková, O. Šolcová, and M. Zdražil, "Preparation of MgO catalytic support in shaped mesoporous high surface area form," *Microporous and Mesoporous Materials*, vol. 76, no. 1–3, pp. 137–149, 2004.
- [9] M. J. Climent, A. Corma, S. Iborra, and M. Mifsud, "MgO nanoparticle-based multifunctional catalysts in the cascade reaction allows the green synthesis of anti-inflammatory agents," *Journal of Catalysis*, vol. 247, no. 2, pp. 223–230, 2007.
- [10] M.-A. Faghihi-Sani and A. Yamaguchi, "Oxidation kinetics of MgO-C refractory bricks," *Ceramics International*, vol. 28, no. 8, pp. 835–839, 2002.
- [11] R. Chaim, Z. Shen, and M. Nygren, "Transparent nanocrystalline MgO by rapid and low-temperature spark plasma sintering," *Journal of Materials Research*, vol. 19, no. 9, pp. 2527–2531, 2004.
- [12] D. Chen, E. H. Jordan, and M. Gell, "Pressureless sintering of translucent MgO ceramics," *Scripta Materialia*, vol. 59, no. 7, pp. 757–759, 2008.
- [13] M. Chiesa, E. Giamello, and S. Van Doorslaer, "Ammoniated electrons stabilized at the surface of MgO," *Journal of the American Chemical Society*, vol. 131, no. 35, pp. 12664–12670, 2009.
- [14] J. I. Beltrán, C. Monty, Ll. Balcells, and C. Martínez-Boubeta, "Possible d0 ferromagnetism in MgO," *Solid State Communications*, vol. 149, no. 39–40, pp. 1654–1657, 2009.
- [15] M. Motiei, J. Calderon-Moreno, and A. Gedanken, "The formation of carbon-coated MgO cubes and carbon cubes," *Advanced Materials*, vol. 14, no. 16, pp. 1169–1172, 2002.
- [16] A. F. Bedilo, M. J. Sigel, O. B. Koper, M. S. Melgunov, and K. J. Klabunde, "Synthesis of carbon-coated MgO nanoparticles," *Journal of Materials Chemistry*, vol. 12, no. 12, pp. 3599–3604, 2002.

- [17] T. Luo, X. Yang, J. Liu, W. Yu, and Y. Qian, "A core-shell nanostructure of carbon," *Chemistry Letters*, vol. 34, no. 2, pp. 168–169, 2005.
- [18] Q. Zhou, J.-W. Yang, Y.-Z. Wang, Y.-H. Wu, and D.-Z. Wang, "Preparation of nano-MgO/Carbon composites from sucrose-assisted synthesis for highly efficient dehydrochlorination process," *Materials Letters*, vol. 62, no. 12-13, pp. 1887–1889, 2008.
- [19] M. Kobayashi, V. Petrykin, M. Kakihana, and K. Tomita, "Hydrothermal synthesis and photocatalytic activity of whisker-like rutile-type titanium dioxide," *Journal of the American Ceramic Society*, vol. 92, no. s1, pp. S21–S26, 2009.
- [20] C. Bower, W. Zhu, D. Shalom, D. Lopez, L. H. Chen, P. L. Gammel, and S. Jin, "Large current density from carbon nanotube field emitters," *Applied Physics Letters*, vol. 80, p. 3820, 2002.
- [21] W. Huang, Y. Wang, G. Luo, and F. Wei, "99.9% purity multi-walled carbon nanotubes by vacuum high-temperature annealing," *Carbon*, vol. 41, no. 13, pp. 2585–2590, 2003.
- [22] J. Liu, M. Shao, X. Chen, W. Yu, X. Liu, and Y. Qian, "Large-scale synthesis of carbon nanotubes by an ethanol thermal reduction process," *Journal of the American Chemical Society*, vol. 125, no. 27, pp. 8088–8089, 2003.
- [23] V. Jourdain, H. Kanzow, M. Castignolles, A. Loiseau, and P. Bernier, "Sequential catalytic growth of carbon nanotubes," *Chemical Physics Letters*, vol. 364, no. 1-2, pp. 27–33, 2002.
- [24] C. Ducati, I. Alexandrou, M. Chhowalla, G. A. J. Amaratunga, and J. Robertson, "Temperature selective growth of carbon nanotubes by chemical vapor deposition," *Journal of Applied Physics*, vol. 92, no. 6, pp. 3299–3306, 2002.
- [25] Y. Li, J. Chen, Y. Ma, J. Zhao, Y. Qin, and L. Chang, "Formation of bamboo-like nanocarbon and evidence for the quasi-liquid state of nanosized metal particles at moderate temperatures," *Chemical Communications*, no. 12, pp. 1141–1142, 1999.
- [26] M. H. Lee and D. G. Park, "Preparation of MgO with high surface area, and modification of its pore characteristics," *Bulletin of the Korean Chemical Society*, vol. 24, no. 10, pp. 1437–1443, 2003.

Research Article

Simple Synthesis and Growth Mechanism of Core/Shell CdSe/SiO_x Nanowires

Guozhang Dai,^{1,2} Shengyi Yang,¹ Min Yan,² Qiang Wan,² Qinglin Zhang,²
Anlian Pan,² and Bingsuo Zou^{1,2}

¹Laboratory of Nanophotonics Materials and Technology, School of Material Science and Engineering of Beijing, Institute of Technology, Beijing 100081, China

²Key Lab for Micro-Nano Optoelectronic Devices of Ministry of Education, Hunan University, Changsha 410082, China

Correspondence should be addressed to Bingsuo Zou, bszou@hnu.cn

Received 25 October 2009; Accepted 28 December 2009

Academic Editor: Renzhi Ma

Copyright © 2010 Guozhang Dai et al. This is an open access article distributed under the Creative Commons Attribution License, which permits unrestricted use, distribution, and reproduction in any medium, provided the original work is properly cited.

Core-shell-structured CdSe/SiO_x nanowires were synthesized on an equilateral triangle Si (111) substrate through a simple one-step thermal evaporation process. SEM, TEM, and XRD investigations confirmed the core-shell structure; that is, the core zone is single crystalline CdSe and the shell zone is SiO_x amorphous layer and CdSe core was grown along (001) direction. Two-stage growth process was present to explain the growth mechanism of the core/shell nanowires. The silicon substrate of designed equilateral triangle providing the silicon source is the key factor to form the core-shell nanowires, which is significant for fabrication of nanowire-core sheathed with a silica system. The PL of the product studied at room temperature showed two emission bands around 715 and 560 nm, which originate from the band-band transition of CdSe cores and the amorphous SiO_x shells, respectively.

1. Introduction

In recent years, great efforts have been made to overcome the numerous challenges associated with the design of one-dimensional (1D) nanostructures with well-controlled size, phase purity, crystallinity, and chemical composition, due to their fascinating properties and unique applications [1–3]. With the ongoing development of nanodevices, the preparation of nanocables, such as semiconducting nanowires sheathed with an insulating shell which can passivate existing surface states, enables new interface properties and introduces unique electronic and photonic function that has attracted particular attention [2–7]. Amorphous silicon oxide is optically transparent for the visible absorption/emission of semiconductor nanowires and produces little destruction of their intrinsic optical properties; therefore it is widely used as passivation or insulation layers materials. So far, several kinds of 1D nanocables based on semiconductors sheathed with a silica system have been achieved by employing a thermal evaporation method,

such as CdS/Si coaxial nanowires [8], SiO₂-sheathed ZnO nanowires [9], and ZnS/SiO₂ core-shell nanowires [10, 11]. In this context, the Si source of the passivation layers was provided by coevaporation of Si-based source and the core-semiconducting powder in high temperature (>1000°C) or by the pretreatment of Si wafer in HF solution, in which the high temperature and venenous solution should avoid in the developed growth technologies. Development of simple, low-cost, and environment-friendly growth processes is necessary.

CdSe, with a direct band gap of 1.7 eV at room temperature, is one of the most important materials in making optoelectronic devices [12–14]. As a selenide, unprotect nanostructured CdSe easily suffers surface degradation (such as oxidation) and contamination in atmosphere which severely damage there intrinsic properties. As a heavy metal Cadmium-compound, the decreasing toxicity of the nanostructures is highly desired especial for biorelated applications. Therefore, surface modification on CdSe nanostructures with coating a shell layer is very crucial and urgent

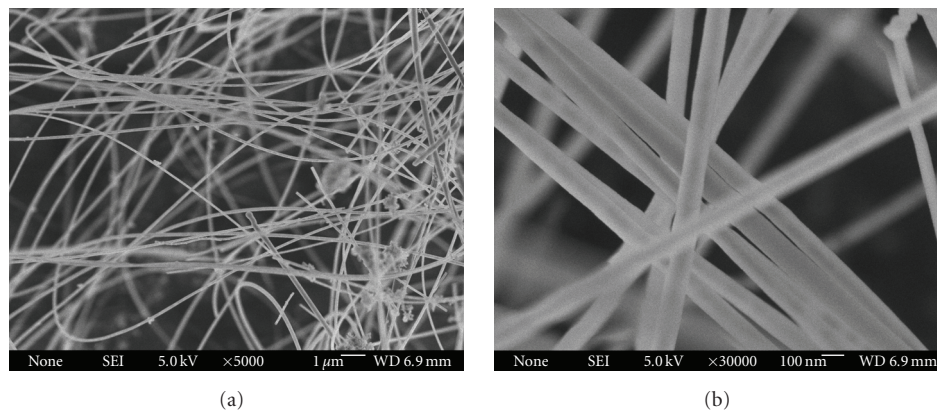


FIGURE 1: Typical scanning electron microscopy (SEM) images of the products: (a) at low magnification; (b) at high magnification.

for their commercial or industrial utilization. In the last few years, the majority of reports on the synthesis of CdSe-core/shell nanostructures were focused on nanoparticles [15, 16], and very few work has been done in the coaxial nanowires except for one paper report on the synthesis of CdSe/SiO₂ nanocables [17], in which the reaction source was added in the Si powder and was sublimated in the temperature above 1200°C. In this article, we report the synthesis of coaxial CdSe/SiO_x nanowires on an equilateral triangle Si substrate through a simple one-step thermal evaporation process at 900°C. The effects of the equilateral triangle Si substrate and local temperatures on the coaxial nanowires growth are significant, which is in contrast to early publications. Photoluminescence properties of these coaxial nanowires were also briefly investigated at room temperature.

2. Experimental

Core-shell nanostructures were synthesized by thermal evaporation. The substrates used for the growth of CdSe nanowires with a coaxial silicon shell were p-type (111) Si wafers. Before used, the Si wafers were cut into an equilateral triangle (the vertex angle is about 60 degrees) and then cleaned ultrasonically for 30 minutes in acetone solution. An Au film about 20 nm in thickness was deposited onto the ultrasonically-cleaned Si wafers by sputtering. About 0.1 g commercial-grade CdSe powder (Strem Chemicals, 99.999+%-Cd purity) was placed in the center of a single zone tube furnace and evacuated for several hours to purge oxygen in the chamber. The treated Si substrates were placed 5 cm away from the CdSe powders and along the downstream side of the flowing Ar (90%) and H₂ (10%). Typically, the CdSe source temperature was controlled at about 900°C at a rate of 100°C/min. During the growth process, the mixture carrier-gas flow was kept at a constant rate of 10~20 sccm. After 60 minutes of typical deposition time the samples were cooled down to room temperature. Dark-brown products appeared on the Si wafers.

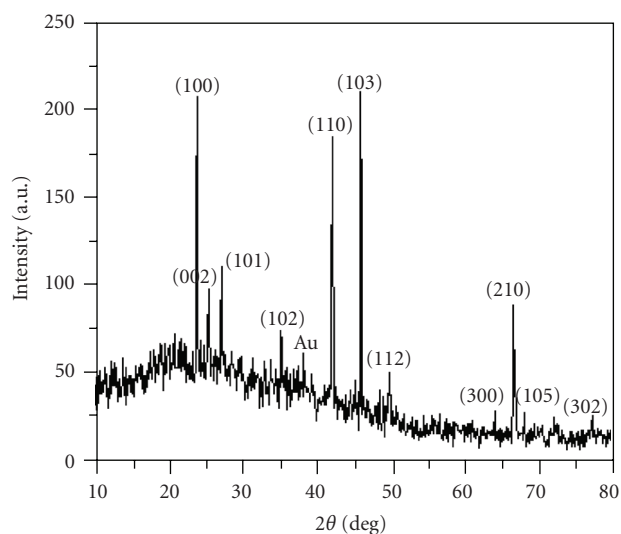


FIGURE 2: The XRD pattern of the products collected from the silicon substrate.

X-ray powder diffraction (XRD) data were obtained on a Siemens D-5000 type diffractometer equipped with graphite-monochromatized CuKα1 radiation ($\lambda = 1.54056 \text{ \AA}$). The morphologies and chemical composition of the products were examined by a field emission scanning electron microscope (FE-SEM, JSM-6700F) and transmission electron microscopy (TEM, JEM-3010) with an energy-dispersive X-ray (EDX) spectroscopy attached to the JEM. Room-temperature photoluminescence (PL) was taken on a Confocal Optical Microscope (Witec) using an Ar-ion laser (488 nm) as an excitation light source.

3. Results and Discussion

The as-deposited products were first examined by SEM observation. Figure 1(a) showed the typical low-SEM images taken from the as-prepared products on Si substrates. The image shows that samples were formed in long and wirelike

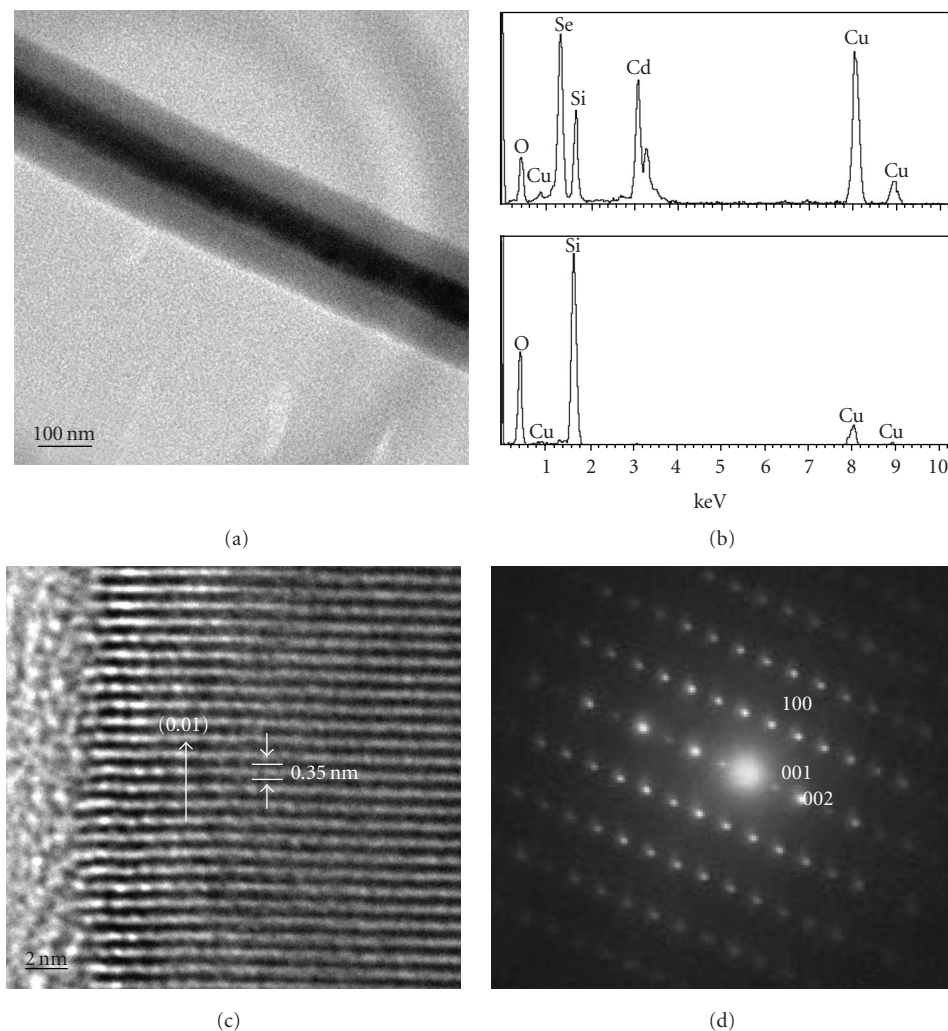


FIGURE 3: (a) Typical TEM images of nanowires, showing a core/shell structure. (b) The EDX patterns on the core and the shell areas of the nanowire signed by white box, respectively. (c) High-resolution TEM image of the interface between the crystalline core and amorphous sheath. (d) The SAED pattern of the core areas indicates a hexagonal wurtzite structure single crystalline layer and an amorphous layer.

nanostructures. The high-magnification SEM image was given in Figure 1(b) which indicated that the diameter of the nanowire is about 100 nm. Furthermore, nanosized particles (marked with an arrow in Figure 1(b)) were found attached to the ends of the nanowires, indicating a likely vapor-liquid-solid (VLS) process for the formation of core nanowires [18]. XRD measurements were made on the nanowires to assess the structure and phase purity. A typical XRD pattern of the nanowires was shown in Figure 2. The main diffraction peaks match well with a wurtzite (hexagonal) structure of bulk CdSe with lattice constants of $a = 4.299 \text{ \AA}$ and $c = 7.010 \text{ \AA}$ (PDF No. 77-2307). A weak Au diffraction peak from catalytic Au nanoparticles was detected. Besides, a broad peak located at ~ 22 degree, which indicates that there are some amorphous materials in the product.

Morphology and microstructural analyses were further performed using TEM. Figure 3(a) shows a typical TEM image of the nanowires. From this image we can identify

clearly that the nanowires have a core-shell nanostructure; that is, a relatively thick sheath with light contrast is formed outside the surface of nanowires with dark contrast. Furthermore, the diameter of the core and the thickness of the shell of individual nanowire are uniform and the typical dimensions are all in the range of 30 to 40 nm. To further investigate the composition of the sample, EDX was taken of the core and shell areas of the nanowire and is presented in Figure 3(b). It can be found that the core of the nanowire is mainly composed of Se and Cd and the shell is mainly made up of Si and O. The extra Cu shown in the EDX spectrum stems from the Cu grid. HRTEM image was taken with the electron beam along a single nanowire, as is shown in Figure 3(c), which reveals the clear crystalline-core/amorphous-shell interface. Moreover, the measured lattice spacing of crystalline core is 0.35 nm, corresponding to the (001) lattice planes of hexagonal wurtzite CdSe. Figure 3(d) shows a selected-area electron diffraction (SAED) pattern taken from the core zone of

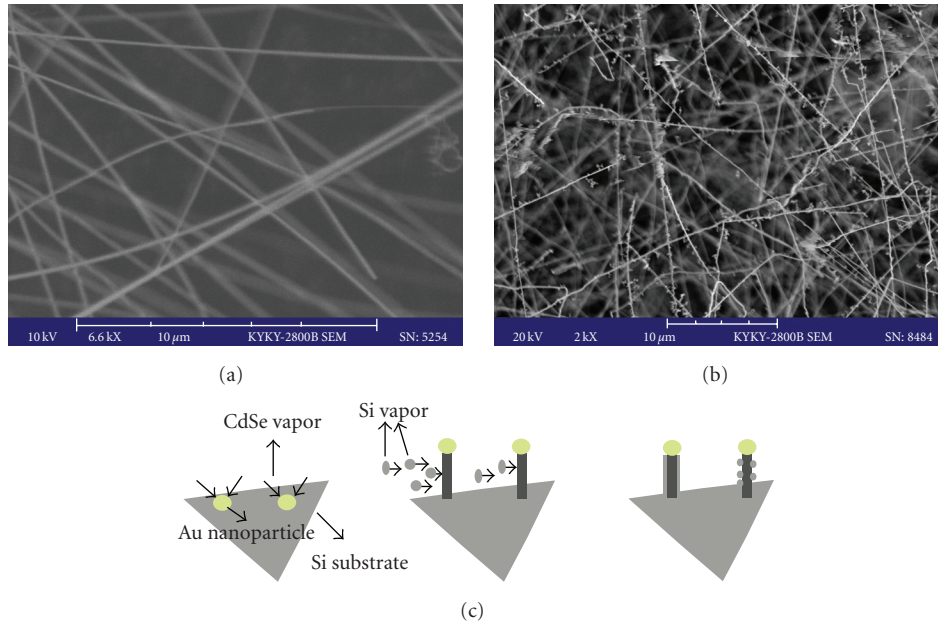


FIGURE 4: SEM image of the sample with different temperature region: (a) 750–800°C; (b) 700–750°C; (c) schematic illustration of the growth process of the core-shell CdSe/SiO_x nanowires.

the nanowire, which could be indexed for the (001) zone axis of single crystalline CdSe. Since only one set of diffraction spots from wurtzite structure of CdSe was found, it can be inferred that the core zone is single crystalline CdSe and the shell zone must be amorphous layer. These results indicate that the nanowire composed of a crystalline CdSe core and an amorphous SiO_x shell.

To investigate the growth mechanism of the core-shell CdSe/SiO_x nanowires, we examined products on the different collection positions, that is, at distinctive deposition temperature. Figures 4(a) and 4(b) show the SEM image of the sample with a distinctive collection temperature region range of 750–800°C and 650–700°C, respectively. It can be seen from Figure 4(a) that the nanowires have the uniform diameter and smooth surface. These suggest that the core/shell nanowires form completely. However, at a comparatively low-temperature region, the nanowires, as given in Figure 4(b), with the coarse sheath would be obtained. Some snowflake-like aerosol adsorbed on the surface of the core wire. We suppose that the growth process of the core/shell nanowires is mainly divided into two stages. The first stage is an ordinary vapor-liquid-solid (VLS) growth process. The conclusion can be supported by nanosized particles marked with an arrow in Figure 1(b). During this process step, the density of CdSe vapor is far denser than the Si vapor which came from the special triangle Si substrate used in this experiment. The main two reasons are as follows. (1) The CdSe source is relatively sufficient in the initial stage and enough CdSe powder can sublime at a suitable temperature zone (~900°C). (2) Addition of H₂ could accelerate the evaporation of CdSe powders as indicated in the following reaction equation: CdSe(s) ↔ CdSe(g) CdSe(s) + H₂(g) ↔ Cd(g) + H₂Se(g).

Thus, we can assume that the first step is a fast growth CdSe as guided by a gold catalyst based on the VLS growth process.

With the reaction continue and the CdSe powders exhausting, the Si vapor density starts to increase and is carried by the mixture carrier gas to a lower temperature zone, where it condenses. In the second stage, the CdSe nanowires serves as the preferable adsorption site for the Si in the vapor phase and eventually works as the template for the one-dimensional growth of Si. Meanwhile, the surface of the silicon was oxidized to form SiO_x (the trace remnant of oxygen that was not eliminated completely by flushing with mixed gas and/or from the leakage of the furnace serves as the oxidant) during heating, resulting in the CdSe-core/SiO_x-sheath nanocable structure. Therefore, this process is mainly grows the SiO_x shell on the CdSe-core nanowires via the vapor-solid (VS) mechanism. The growth of nanostructures always abides to the thermodynamic/kinetic issues [19]. In the high-temperature region, the dynamics effect is remarkable and the Si vapor is sufficient. The CdSe-core/SiO_x-sheath structure of the uniform diameter and smooth surface can be obtained (Figure 4(a)). However, in the comparatively low-temperature position where is far away from the CdSe powder, the situations are different. The intensity of Si steam is comparatively low and Si aerosol adsorbed on CdSe nanowire templated slowly and unorderly, liking semiwraps nanowires. (Figure 4(b)). Then, we can regard it as the intermediate state of the final core/sheath nanowires shown in Figure 4(a). The stage of the growth process can be seen in Figure 4(c).

We need to point out that the silicon source is provided by the silicon substrate. This was in contrast to early publication which added the silicon-based materials in the mixture source powder [17]. The supported experimental

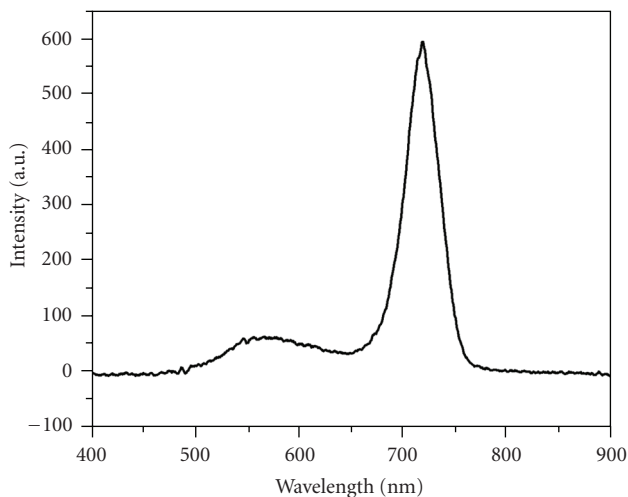


FIGURE 5: Room temperature PL spectrum of the core/shell CdSe/SiO_x nanowire. λ_{exc} was 488 nm.

facts are as follows: (1) no extra silicon source is provided; (2) the core/shell nanostructures are only found on the silicon substrate close to the precursor powder source, indicating that the Si substrate is the Si source. Moreover, the Si wafer used in the experiment was cut into equilateral triangle and has not corroded processing. In the deposition sample, the vertex angle of the Si wafer was facing to the CdSe powder source. We think that the triangle Si substrate is the only substance to produce the Si source, since only the CdSe nanostructures can be found under similar conditions except the shape of the Si substrate changing to the ordinary rectangle. On the one hand, the forefront silicon substrate of the triangle Si wafer reacts more intense at the same temperature when the shape of the Si substrate changes from the broad rectangle to narrow triangle. On the other hand, the substrates used for the growth were p-type (111) Si wafers and the active (111) planes were naked and reacted completely with the source vapor when it was designed in equilateral triangle. Therefore, the triangle Si substrate is easy to sublime and provided the Si source even in the moderate reaction condition. The ways which provide the Si source by changing the shape of Si substrate may be useful for future design of other Si compound nanostructures.

One typical room-temperature photoluminescence (PL) spectrum of the CdSe/SiO_x coaxial nanowires is shown in Figure 5, which reveals an intensive peak centered at 715 nm and a weak peak located at about 560 nm. The longer wavelength peak is explained as the band-to-band emission of CdSe-core nanowires with a bandgap of about 1.74 eV. There is a blue-shift of about 15 nm (0.04 eV) with respect to the emission of bulk CdSe (730 nm; 1.7 eV), which may be related to quantum-confinement effects [20]. The lower PL intensity peak may be attributed to the amorphous SiO_x shell. Literatures [21] have reported the oxidized SiO₂ nanotubes emission peak at about 570 nm. The PL band around 550 nm also was indexed to the SiO_x shell of Si/SiO_x nanowires [22]. Here, we think that the visible emission at

560 nm also come from the amorphous silica shell, in which the dissimilar peak position may be linked to the different density of oxygen vacancies.

4. Conclusion

In summary, we synthesized coaxial CdSe/SiO_x nanowires through simple one-step thermal evaporation process on an equilateral triangle Si substrate. The structures and growth mechanism have been presented. We found that the temperature and the Si substrates of designed equilateral triangle have the critical effect on the formation core/shell nanowires. The PL studies present two emission bands about 560 nm and 715 nm, which originate from the intrinsic transition of CdSe cores and the amorphous SiO_x shells, respectively. We believe that this simple preparation technique can be useful for synthesis of other core-semiconductor/shell-Si nanostructures.

Acknowledgments

The authors thank the financial supports of NSFC of China (no. 90606001, 90923014, and 20903038), Program for New Century Excellent Talents in University (NCET-06-0077), and Beijing NOVA program (2006B20) for financial support.

References

- [1] C. M. Lieber and Z. L. Wang, "Functional nanowires," *MRS Bulletin*, vol. 32, pp. 99–104, 2007.
- [2] X. Fang, Y. Bando, U. K. Gautam, C. Ye, and D. Golberg, "Inorganic semiconductor nanostructures and their field-emission applications," *Journal of Materials Chemistry*, vol. 18, no. 5, pp. 509–522, 2008.
- [3] R. Yan, D. Gargas, and P. Yang, "Nanowire photonics," *Nature Photonics*, vol. 3, no. 10, pp. 569–576, 2009.
- [4] L. J. Lauhon, M. S. Gudiksen, D. Wang, and C. M. Lieber, "Epitaxial core-shell and core-multishell nanowire heterostructures," *Nature*, vol. 420, no. 6911, pp. 57–61, 2002.
- [5] G. Shen, D. Chen, and C. J. Lee, "Fabrication of coaxial Zn/ZnS core/shell fibers on a large scale," *Journal of Physical Chemistry C*, vol. 111, no. 15, pp. 5673–5676, 2007.
- [6] X. Jiang, Q. Xiong, S. Nam, F. Qian, Y. Li, and C. M. Lieber, "InAs/InP radial nanowire heterostructures as high electron mobility devices," *Nano Letters*, vol. 7, no. 10, pp. 3214–3218, 2007.
- [7] J. A. Czaban, D. A. Thompson, and R. R. LaPierre, "GaAs core-shell nanowires for photovoltaic applications," *Nano Letters*, vol. 9, no. 1, pp. 148–154, 2009.
- [8] X. L. Fu, L. H. Li, and W. H. Tang, "Preparation and characterization of CdS/Si coaxial nanowires," *Solid State Communications*, vol. 138, no. 3, pp. 139–142, 2006.
- [9] J. He, Y. Huang, Y. Zhang, Y. Gu, Z. Ji, and C. Zhou, "Large-scale synthesis, microstructure and growth mechanism of self-assembled core-shell ZnO/SiO_x nanowires," *Materials Letters*, vol. 60, no. 2, pp. 150–153, 2006.
- [10] D. Moore, J. R. Morber, R. L. Snyder, and Z. L. Wang, "Growth of ultralong ZnS/SiO₂ core-shell nanowires by volume and surface diffusion VLS process," *Journal of Physical Chemistry C*, vol. 112, no. 8, pp. 2895–2903, 2008.

- [11] Y. Li, C. Ye, X. Fang, L. Yang, Y. Xiao, and L. Zhang, "Fabrication and photoluminescence of SiO₂-sheathed semiconducting nanowires: the case of ZnS/SiO₂," *Nanotechnology*, vol. 16, no. 4, pp. 501–505, 2005.
- [12] S. Coe, W.-K. Woo, M. Bawendi, and V. Bulovic, "Electroluminescence from single monolayers of nanocrystals in molecular organic devices," *Nature*, vol. 420, no. 6917, pp. 800–803, 2002.
- [13] V. L. Colvin, M. C. Schlamp, and A. P. Alivisatos, "Light-emitting diodes made from cadmium selenide nanocrystals and a semiconducting polymer," *Nature*, vol. 370, no. 6488, pp. 354–357, 1994.
- [14] C. Fuentes-Hernandez, D. J. Suh, B. Kippelen, and S. R. Marder, "High-performance photorefractive polymers sensitized by cadmium selenide nanoparticles," *Applied Physics Letters*, vol. 85, no. 4, pp. 534–536, 2004.
- [15] K. Palaniappan, C. Xue, G. Arumugam, S. A. Hackney, and J. Liu, "Water-soluble, cyclodextrin-modified CdSe-CdS core-shell structured quantum dots," *Chemistry of Materials*, vol. 18, no. 5, pp. 1275–1280, 2006.
- [16] X.-S. Wang, T. E. Dykstra, M. R. Salvador, I. Manners, G. D. Scholes, and M. A. Winnik, "Surface passivation of luminescent colloidal quantum dots with poly(dimethylaminoethyl methacrylate) through a ligand exchange process," *Journal of the American Chemical Society*, vol. 126, no. 25, pp. 7784–7785, 2004.
- [17] Z. Wang, Q. Lu, M. Kong, and L. Zhang, "Manipulation of the morphology of semiconductor-based nanostructures from core-shell nanoparticles to nanocables: the case of CdSe/SiO₂," *Chemistry*, vol. 13, no. 5, pp. 1463–1470, 2007.
- [18] R. S. Wagner, W. C. Ellis, K. A. Jackson, and S. M. Arnold, "Study of the filamentary growth of silicon crystals from the vapor," *Journal of Applied Physics*, vol. 35, no. 10, pp. 2993–3000, 1964.
- [19] J. Q. Hu, Q. Li, N. B. Wong, C. S. Lee, and S. T. Lee, "Synthesis of uniform hexagonal prismatic ZnO whiskers," *Chemistry of Materials*, vol. 14, no. 3, pp. 1216–1219, 2002.
- [20] Z. Wang, Q. Lu, X. Fang, X. Tian, and L. Zhang, "Manipulation of the morphology of CdSe nanostructures: the effect of Si," *Advanced Functional Materials*, vol. 16, no. 5, pp. 661–666, 2006.
- [21] Y. B. Li, Y. Bando, D. Golberg, and Y. Uemura, "SiO₂-sheathed InS nanowires and SiO₂ nanotubes," *Applied Physics Letters*, vol. 83, no. 19, pp. 3999–4001, 2003.
- [22] C. Wu, W. Qin, G. Qin, et al., "Spontaneous growth and luminescence of Si/SiO_x core-shell nanowires," *Chemical Physics Letters*, vol. 378, no. 3–4, pp. 368–373, 2003.

Research Article

Fabrication of Mesostructured Silica and Titania Rods on Substrates by Using Polycarbonate Membranes

Norihiro Suzuki¹ and Yusuke Yamauchi^{1,2}

¹World Premier International (WPI) Research Center for Materials Nanoarchitectonics (MANA), National Institute for Materials Science (NIMS), Tsukuba, Ibaraki 305-0044, Japan

²PRESTO, Japan Science and Technology Agency (JST), Kawaguchi, Saitama 332-0012, Japan

Correspondence should be addressed to Yusuke Yamauchi, yamauchi.yusuke@nims.go.jp

Received 30 November 2009; Accepted 11 March 2010

Academic Editor: Yanqiu Zhu

Copyright © 2010 N. Suzuki and Y. Yamauchi. This is an open access article distributed under the Creative Commons Attribution License, which permits unrestricted use, distribution, and reproduction in any medium, provided the original work is properly cited.

By using the polycarbonate membrane a template, mesoporous silica rods are fabricated on a silicon substrate in one pot. From scanning electron microscope (SEM) images, the creation of fibrous morphology is confirmed over the entire area. The diameter of the obtained rods is consistent with that of the template. Transmission electron microscope (TEM) images revealed that the tubular mesochannels are uniaxially oriented parallel to the longitudinal axis of the silica rods. The mesoporous titania rods with anatase crystalline frameworks are also fabricated.

1. Introduction

Mesoporous/mesostructured one-dimensional (1D) materials (such as rods and tubes) are attractive, because they can be utilized as noble optical, electric and magnetic devices. One of the fabrication methods for the 1D material is the template-directed synthesis. In this process, the precursor solution is introduced into the pores of the template. By adding the surfactant into the precursor solution, the self-organization of surfactant micelles occurs, which derives the ordered mesostructures within the template. After removing the template and surfactants, the mesoporous 1D materials can be obtained.

The fabrication of the mesoporous 1D materials on a substrate is important for practical application. Recently, Zhu et al. reported the synthesis of mesostructured silica tubes on a silicon substrate using the porous anodic alumina (PAA) template [1]. In this study, though the fabricated tubes were oriented perpendicularly to the substrate, a strong vacuum condition was required to enter the surfactant/silica source into the pores of the PAA template. Furthermore, because the PAA template was removed by the use of phosphoric acid, this fabrication method is not applicable to compositions with low tolerance for acid.

To overcome it, we focus on the polycarbonate (PC) membrane. The PC membrane has several advantages compared to the PAA [2–4]. Firstly, since the PC is stable under acidic condition, the side reactions are prevented. In addition, the PC membrane and the surfactants can be removed simultaneously by calcination. In this paper, we demonstrate the one-pot fabrication of mesoporous silica rods on a silicon substrate using the PC template. Without using the strong vacuum condition, the silica rods were successfully fabricated on the substrate. Our facial fabrication procedure was also applied for the fabrication of mesoporous titania rods.

2. Experimental

2.1. Materials. Tetraethyl orthosilicate (TEOS, extra pure reagent) as a silica source was purchased from Nacalai Tesque, Inc. Titanium tetraisopropoxide (as titania source) was obtained from Wako Pure Chemical Industries, Ltd. Ethanol, dilute hydrochloric acid (pH = 2), and concentrated hydrochloric acid (35.5 w%) were obtained from Nacalai Tesque, Inc. A triblock copolymer P123 was obtained from Sigma-Aldrich, Inc. Polycarbonate membrane filters with 200 nm diameter pores were purchased from Advantec Co., Ltd.

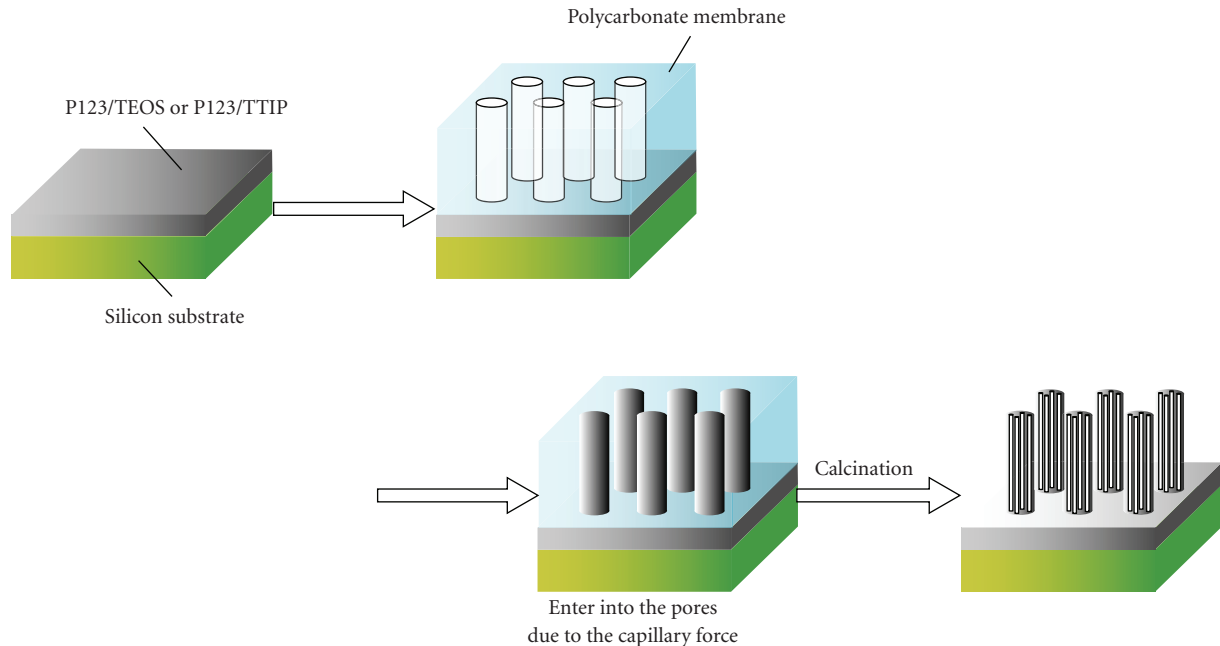


FIGURE 1: Schematic presentation of the fabrication of mesoporous silica and titania rods using the polycarbonate (PC) membrane as the template on a silicon substrate.

2.2. Preparation of Precursor Solutions. The mixture of tetraethyl orthosilicate (TEOS, 5.2 g), ethanol (6 g), and dilute aqueous HCl (pH = 2, 2.7 g) was stirred for 20 minutes. Then triblock copolymer P123 (1.38 g) and ethanol (4 g) were added and the mixture was stirred for 3 hours [5]. In the preparation of the titania precursor solution, we followed the paper by Wu et al. [6]. Concentrated HCl (35.5 w%, 0.74 g) was added into titanium tetraisopropoxide (TTIP, 1.05 g) and stirred vigorously for 10 minutes. This solution was added drop by drop into an ethanol solution (3 g) of P123 (0.2 g), then stirred for 15 minutes.

2.3. Preparation of Mesoporous Silica and Titania Rods. The fabrication procedure of mesoporous rods is shown schematically in Figure 1. The thin film was prepared by spin-coating at 8000 rpm (Silica) and 4000 rpm (Titania) on a silicon wafer cleaned with ethanol. After the spin-coating, a polycarbonate membrane filter was placed on the film. Because the surface of the spin-coated film was not dried out completely, P123/TEOS and P123/TTIP sources can penetrate into the pores of the PC membrane due to the capillary force. The silica film with the PC membrane was dried in air for 1 day and the titania film was aged at -20°C for 1 day. These as-synthesized films were calcined at 500°C for 8 hours (Silica) or 400°C for 4 hours (Titania) to remove the PC membrane and surfactants simultaneously.

2.4. Characterization. SEM images were recorded with a Hitachi S-4800 field emission scanning electron microscope. Before the observation, SEM samples were coated with Pt. TEM images were obtained using a JEOL JEM-2010. During the measurement, the accelerating voltage of the electron beam was set to be 200 kV.

3. Results and Discussion

The SEM image of the silica rods is shown in Figure 2(a). A large number of rods were successfully fabricated over the entire area of the substrate. The estimated diameter of the obtained fiber was about 200 nm, which consisted with the pore size of the PC membranes. These facts indicate that the size of rods can be controlled by changing the pore sizes of the PC membranes. The length of the fabricated fibers ranged between $1\ \mu\text{m}$ to $2\ \mu\text{m}$, which was much shorter than the PC membrane thickness (about $10\ \mu\text{m}$). The main reason is that the spin-coated film was so thin that the precursor source cannot fulfill the entire pore space of the PC template. Titania rods were also fabricated as shown in Figure 2(b), revealing that our procedure is applicable beyond silica. The densities of the rods were lower rather than that of the silica tubes/rods prepared by PAA membranes [2, 7–10], because the number of the pores in the PC membranes is relatively lower (Figure 3). Also, the fabricated rods were randomly placed and inclined to the substrate (Figure 2), because the pores in the PC membranes are randomly dispersed and the pores are not oriented completely perpendicular, but are tilted to the substrate (Figure 3).

Almost the P123/TEOS and P123/TTIP sources could penetrate into the pores of the PC membrane due to the capillary force, because the continuous films regions on the Si substrate were not observed clearly from the cross-sectional SEM images (Figures 2(c) and 2(d)). But, it was revealed that, from a highly magnified SEM image (Figure 4), very thin films (less than 30 nm) with uniform mesopores covered the area of the substrate.

Furthermore, the mesostructures inside the silica rods were investigated directly by taking the TEM images perpendicular to the long axis of the fibers (Figure 5). Tubular

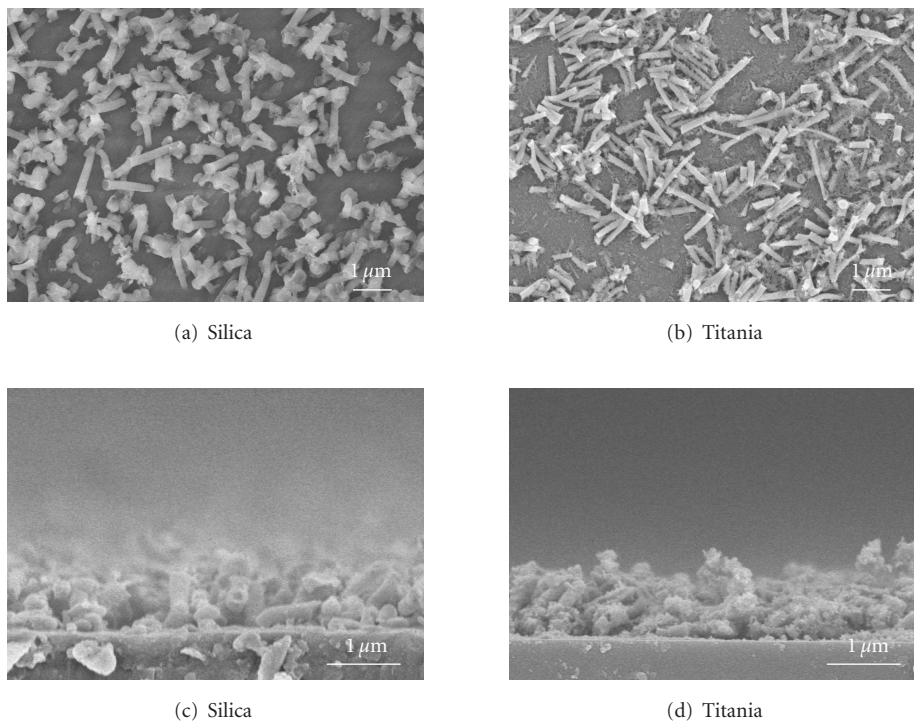


FIGURE 2: SEM images of mesoporous silica (a) and (c) and titania (b) and (d) rods on the silicon substrate: Figures (a) and (b) are top-surface images, while Figures (c) and (d) are cross-sectional images.

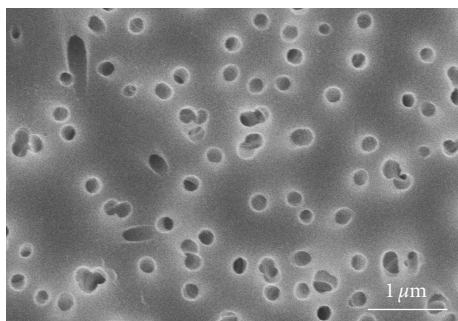


FIGURE 3: SEM image of top-surface of the used PC membranes. Although the pore size is uniform (around 200 nm), the pores are randomly distributed on the surface.

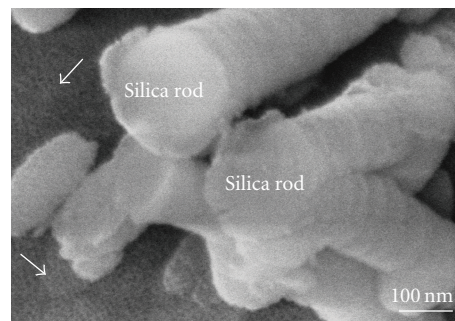


FIGURE 4: High-magnified SEM image. The mesoporous silica rods are deposited on the substrate. The arrows indicate the formation of uniform mesopores on the substrate surface.

mesopores were observed in the rod and these mesochannels were uniaxially oriented parallel to the longitudinal axis of the rod. The pore diameter of mesopores was estimated to be 6.2 nm, which coincided well with the result of N_2 gas adsorption-desorption (6.0 nm) [4]. In the SAXS profiles of silica rods, peaks assignable to (10), (11), and (20) peaks of 2D hexagonal symmetries ($p6m$) were observed (not shown), confirming the mesostructural ordering.

The appearance of the mesopore channels parallel to the longitudinal axis is noteworthy. It has been well known that there are two types of orientations of the mesochannels in a cylindrical confined space. One is “columnar orientation” in which the tubular mesochannels are aligned along the long

axis of the cylinders. The other one is “circular orientation” in which the mesochannels are circularly formed inside the cylinders (i.e., stacked-donuts structures) [7]. In the use of porous anodic alumina (PAA) membranes with P123 surfactants, the “circular orientation” is mainly formed inside the cylindrical channels, even though the mesochannels orientation with respect to the long axis of the cylinders can be tuned according to the silica-to-P123 ratio and the salt content in the precursor solution and the relative humidity during the solvent evaporation [7–9]. On the other hand, in the use of PC membranes with P123 surfactants, the interaction of silica-P123 species with the PC surfaces is weaker than that with the PAA surfaces, and any preferred

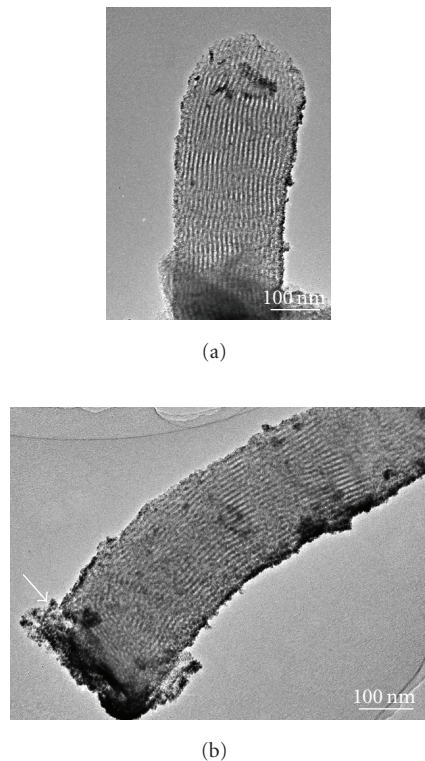


FIGURE 5: TEM images of the mesoporous silica rod after the calcination. The arrow in Figure (b) indicates the interface between the silica rod and the Si substrate (i.e., the edge of the mesoporous silica rod).

orientations were not confirmed. In this case, both the “columnar orientation” and the “circular orientation” were observed [4]. In the present system, however, only “columnar orientation” was observed in the rods. When the P123/TEOS source penetrates into the pores of the membrane due to the capillary force (Figure 1), the motion of silica-P123 species in a uniaxial direction to the long axis of the PC channels occurs. At this stage, the tubular mesochannels can be anisotropically arranged along the flow direction (i.e., along the cylinders of the PC membranes), because an interaction between the P123/TEOS sources and the PC surface is weak. At the interface between the silica rod and the Si substrate, it was proved that the mesochannels were oriented parallel to the Si substrate, due to the strong interaction between the silica-P123 species and the Si substrate surface. This phenomenon has been normally observed previously [5].

In the case of the mesoporous titania rods, it is expected that crystallization as well as template removal will occur during the calcination procedure [6]. Disordered mesostructures are observed inside the rods (not shown). In the XRD pattern of titania samples, several diffraction peaks were detected (not shown). These peaks were well matched with the diffraction pattern of anatase titania, revealing that fabricated titania rods have anatase crystalline frameworks. The crystal size of anatase titania was estimated using the Scherrer equation: by using (101) reflection peak, the crystal size was roughly estimated to be around 4.8 nm. Fabrication

of mesoporous rods with such crystallized frameworks will be important for a practical application such as catalyst.

4. Conclusion

Mesostructured silica and titania rods on a silicon substrate were successfully produced by using the polycarbonate membranes as templates. Because the polycarbonate template and surfactants were burned out simultaneously, the mesoporous rods were fabricated in one pot, which facilitates the production of the arrays in comparison with the previous work using PAA membranes [1]. In the case of mesoporous titania rods, the crystallization also occurred during calcination procedure. This facial synthesis method can be utilized to fabricate various types of metal oxide rods on a substrate.

References

- [1] W. Zhu, Y. Han, and L. An, “Synthesis of ordered mesostructured silica nanotubular arrays,” *Microporous and Mesoporous Materials*, vol. 84, no. 1–3, pp. 69–74, 2005.
- [2] Z. Liang and A. S. Susha, “Mesostructured silica tubes and rods by templating porous membranes,” *Chemistry—A European Journal*, vol. 10, no. 19, pp. 4910–4914, 2004.
- [3] P. Lai, M. Z. Hu, D. Shi, and D. Blom, “STEM characterization on silica nanowires with new mesopore structures by space-confined self-assembly within nano-scale channels,” *Chemical Communications*, no. 11, pp. 1338–1340, 2008.
- [4] Y. Yamauchi, N. Suzuki, and T. Kimura, “Formation of mesoporous oxide fibers in polycarbonate confined spaces,” *Chemical Communications*, no. 38, pp. 5689–5691, 2009.
- [5] Y. Yamauchi, M. Sawada, M. Komatsu, et al., “Magnetically induced orientation of mesochannels in mesoporous silica films at 30 Tesla,” *Chemistry—An Asian Journal*, vol. 2, no. 12, pp. 1505–1512, 2007.
- [6] C.-W. Wu, T. Ohsuna, M. Kuwabara, and K. Kuroda, “Formation of highly ordered mesoporous titania films consisting of crystalline nanopillars with inverse mesospace by structural transformation,” *Journal of the American Chemical Society*, vol. 128, no. 14, pp. 4544–4545, 2006.
- [7] Y. Wu, G. Cheng, K. Katsov, et al., “Composite mesostructures by nano-confinement,” *Nature Materials*, vol. 3, no. 11, pp. 816–822, 2004.
- [8] D. Wang, R. Kou, Z. Yang, J. He, Z. Yang, and Y. Lu, “Hierarchical mesoporous silica wires by confined assembly,” *Chemical Communications*, no. 2, pp. 166–167, 2005.
- [9] B. Platschek, N. Petkov, and T. Bein, “Tuning the structure and orientation of hexagonally ordered mesoporous channels in anodic alumina membrane hosts: a 2D small-angle X-ray scattering study,” *Angewandte Chemie—International Edition*, vol. 45, no. 7, pp. 1134–1138, 2006.
- [10] Y. Yamauchi, A. Sugiyama, M. Sawada, et al., “Magnetically induced orientation of mesochannels inside porous anodic alumina membranes under ultra high magnetic field of 30 T: confirmation by TEM,” *Journal of the Ceramic Society of Japan*, vol. 116, no. 1359, pp. 1244–1248, 2008.

Research Article

Biomimetic Synthesis of Zinc Oxide 3D Architectures with Gelatin as Matrix

Yong Gan, Fubo Gu, Dongmei Han, Zhihua Wang, and Guangsheng Guo

State Key Laboratory of Chemical Resource Engineering, Beijing University of Chemical Technology, Beijing 100029, China

Correspondence should be addressed to Guangsheng Guo, guogs@mail.buct.edu.cn

Received 27 November 2009; Accepted 31 March 2010

Academic Editor: Steve Acquah

Copyright © 2010 Yong Gan et al. This is an open access article distributed under the Creative Commons Attribution License, which permits unrestricted use, distribution, and reproduction in any medium, provided the original work is properly cited.

Peanut-like and flower-like zinc oxide 3D architectures were synthesized via a facile biomimetic process using gelatin as matrix. Techniques of XRD, SEM, HRTEM, FT-IR, and UV-vis absorption spectra were used to characterize the structure and property of the zinc oxide architectures. The experimental results show that the peanut-like ZnO and flower-like ZnO architectures can be obtained through changing the Zn^{2+} concentration or the aging time. FT-IR spectra indicate that the Zn^{2+} is coupled with the C=O bond of the gelatin molecules through the electrostatic interaction. Based on the experimental process, the possible growth mechanism of the ZnO 3D architectures is proposed. UV-vis absorption spectrum of the peanut-like ZnO has a broad absorption band in the UV region, and the blue-shifting of the band is observed.

1. Introduction

Nanomaterials have attracted much attention because they have special characteristics in optical, photovoltaic, and catalytic applications that differ from those of bulk materials [1]. Zinc oxide has a wide band gap (3.37 eV) and a large exciton binding energy (60 meV) at room temperature and has been extensively investigated for applications in luminescence, photocatalysts, surface acoustic wave filters, piezoelectric transducers and actuators, gas sensors, solar cells and so on [2–8]. Recently, many synthesis methods have been employed for the growth of ZnO nanomaterials such as the hydrothermal process [9–11], the conventional sputter deposition technique [12], the chemical vapor deposition (CVD) [13–15] and the thermal evaporation [4]. Moreover, many graceful nano-architectures have been prepared by different techniques, such as nanowires, nanobridges, nanonails, nanobundles and nanocombs [10, 15, 16]. However, the methods used to prepare these types of ZnO usually require relatively high temperature and sometimes complicated process. Comparatively, the wet chemical method, for it employs a low growth temperature ($<100^{\circ}C$) process and has good potential for scale-up, becomes one of the successful techniques for preparing nanosized ZnO [17–22].

Biominerals are usually formed on the surface of organic templates (or matrixes). Recently, inorganic materials with higher performance and more exquisite morphologies have been obtained by biomimetic synthesis. Simulating the biomineralization process of the nucleation and growth of inorganic materials mediated by organic matrixes has become the focus of material science [23, 24]. Gelatin is the denaturation product of collagen which is the major structural protein in the connective tissue of animal skin and bones. Gelatin has been investigated by *in vitro* biomineralization [25–31]. Heterogeneous nucleation of ZnO using gelatin as the organic matrix has been studied [20]. However, the reported synthetic methods are limited to the growth of 1D or 2D ZnO (thin films) and only few on 3D ordered architectures [6]. In the present work, a simple and biomimetic process was employed to synthesize 3D zinc oxide architectures at room temperature. The biomimetic growth and self-assembly of zinc oxide 3D architectures in the gelatin solution were investigated, and the formation mechanism of the 3D ZnO architectures was also discussed.

2. Experimental Section

2.1. Materials. Gelatin was obtained from Beijing Aoboxing Universeen Bio-Tech Co. Ltd (Beijing, China).

$\text{Zn}(\text{NO}_3)_2 \cdot 6\text{H}_2\text{O}$, absolute ethyl alcohol and ammonia were purchased from Beijing Chemical Reagent Co. Ltd (Beijing, China) and all of reagents were of analytical grade. De-ionized water was used in each synthesis and washing step.

2.2. Synthesis of Zinc Oxide 3D Architectures. In this experiment, a simple biomineralized method to obtain zinc oxide crystals was adopted. In brief, the aqueous solution of gelatin as mineralized solution was prepared using 3 g gelatin dissolved in 100 ml de-ionized water. The concentration of the gelatin was 3%(wt). 1.84 g $\text{Zn}(\text{NO}_3)_2 \cdot 6\text{H}_2\text{O}$ was added in 100 ml as-prepared gelatin solution and dissolved. The mixed solution was stirred continuously and titrated with ammonia (6 mol/L) at room temperature, and then the pH value of the mixed solution was adjusted to 8.0. After being stirred for 30 minutes, the suspension was kept at 30°C for 24 hours. The precipitate was obtained by centrifugation at a speed of 4500 rpm and then washed thoroughly with de-ionized water to remove the diffluent salts. Three cycles of washing and centrifuging were required. Afterwards, the precipitate was washed twice with absolute ethyl alcohol. Finally, the sample was harvested by centrifugation and oven-dried at 60°C for 12 hours. According to the same process, 2.97 g $\text{Zn}(\text{NO}_3)_2 \cdot 6\text{H}_2\text{O}$ was added in gelatin solution and the other sample was obtained.

2.3. Characterization. The crystallization and purity of the samples were characterized by X-ray diffraction (XRD) analysis with a D/max 2500VB2+/PC X-ray diffractometer using graphite monochromatized $\text{Cu K}\alpha$ radiation ($\lambda = 0.15406 \text{ nm}$) at a scanning speed of $10^\circ/\text{min}^{-1}$. Field emission scanning electron microscopy (FESEM, Hitachi S-4700) was employed to characterize the morphological features of the samples that were sputter-coated with gold prior to examination. The detailed morphology and structural characterization were investigated through high-resolution transmission electron microscope (HRTEM, JEM3010). For infrared adsorption analysis, 1 mg of the samples was carefully mixed with 200 mg of KBr (infrared grade) and pelletized (diameter of the disk shaped pellet = 7 mm) under the pressure of 4 tons for 1 minute. The pellets were analyzed by using a Nicolet Avatar 370 MCT Fourier-transform infrared (FT-IR) spectrometer in the range of $4000\text{--}400 \text{ cm}^{-1}$. The optical property of the samples was measured by UV-Vis spectrophotometer (Hitachi Model U-3010).

3. Results and Discussions

3.1. The Structural Characterization of ZnO Nanoarchitectures. Figure 1 shows the XRD patterns of the products. Product A and Product B were obtained when the concentrations of Zn^{2+} were 0.06 mol/L and 0.1 mol/L, respectively. The diffraction peaks were indexed as the (100), (002), (101), (102), (110), (103), (200), (112), (201), (004), (202), (104), and (203) reflections of wurtzite (hexagonal) structured ZnO (JCPDS card No. 65-3411, lattice parameters of $a = b =$

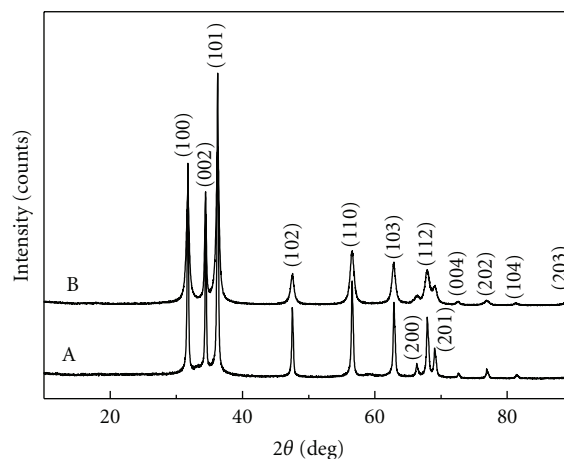


FIGURE 1: XRD patterns of zinc oxide synthesized at the different Zn^{2+} concentration in 3%(wt) gelatin solution: A, 0.06 mol/L $\text{Zn}(\text{NO}_3)_2 \cdot 6\text{H}_2\text{O}$; B, 0.1 mol/L $\text{Zn}(\text{NO}_3)_2 \cdot 6\text{H}_2\text{O}$.

3.25 \AA , $c = 5.207 \text{ \AA}$). The products are well crystallized and the crystallization degree of Product A is better than that of Product B according to the intensity of the XRD pattern. No peaks associated with other crystalline forms are detected, which indicates that ZnO crystals were successfully synthesized through the simple biomimetic process.

3.2. The Morphology of the 3D ZnO Architectures. Figure 2 presents the FESEM images of the 3D ZnO architectures. It can be seen that the as-prepared products are mainly composed of two types of architectures: peanut-like (Figure 2(a)) and flower-like (Figure 2(b)) structures. The peanut-like products are obtained when the concentration of Zn^{2+} is 0.06 mol/L, and the morphologies of the 3D peanut-like ZnO architectures are with length ranging from 500 nm to $1 \mu\text{m}$ and width varying from 200 nm to 300 nm. However, as the concentration of Zn^{2+} ions increases to 0.1 mol/L, flower-like ZnO structures produce, consisting of nano-rods with 80 nm in length and 20 nm in diameter. These experimental results reveal that the development of ZnO architectures in gelatin solution is greatly influenced by the concentration ratio of Zn^{2+} to gelatin.

High-Resolution Transmission electron microscopy (HRTEM) studies were carried out to examine the crystallography and structure of the peanut-like ZnO architectures. Figure 3 shows the HRTEM images of the peanut-like ZnO sample. Figure 3(a) is the low-magnification TEM image of the peanut-like ZnO after sonication treatment in ethanol for 30 minutes. The dimensions of the peanut-like ZnO are about 500–800 nm in length and about 200 nm in width, which are consistent in the FESEM observations. The HRTEM images in Figure 3(b) show that the peanut-like ZnO architectures are organized with nanorods, and have a clean and perfect lattice structure without dislocation and stacking faults. The lattice space of adjacent planes is about 0.25 nm, corresponding to the (101) fringe perpendicular to the growth direction, which is consistent with that of the bulk wurtzite ZnO crystal.

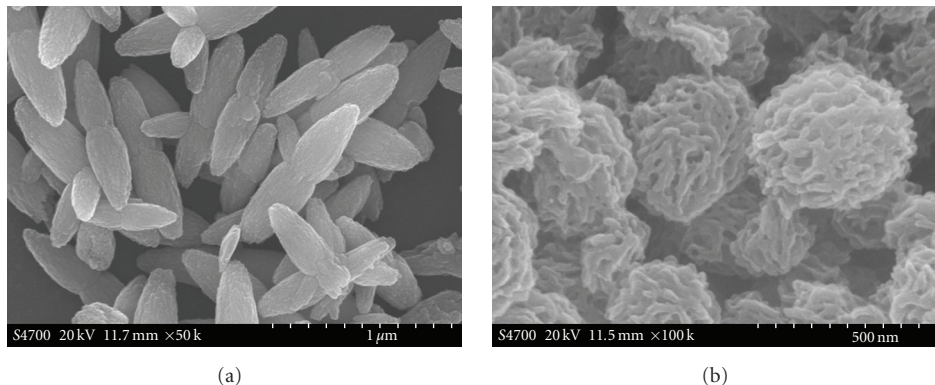


FIGURE 2: FESEM images of the zinc oxide synthesized at the different Zn^{2+} concentration in 3%(wt) gelatin solution: (a), 0.06 mol/L; (b), 0.1 mol/L.

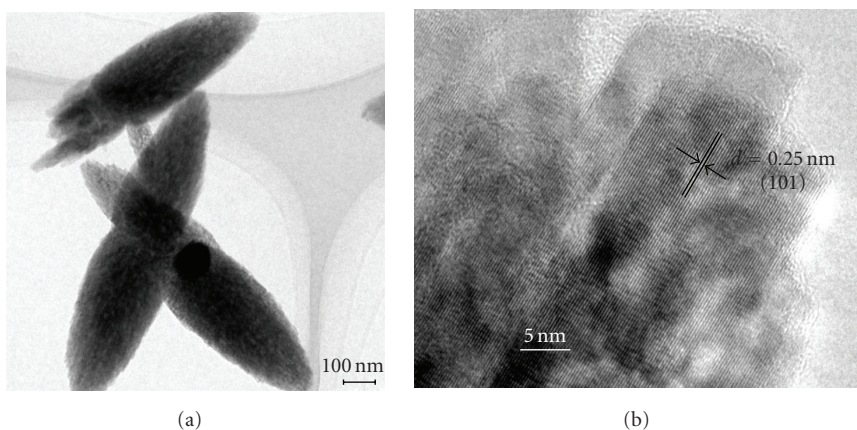


FIGURE 3: HRTEM images of the peanut-like ZnO: (a), low-magnification; (b), high-magnification.

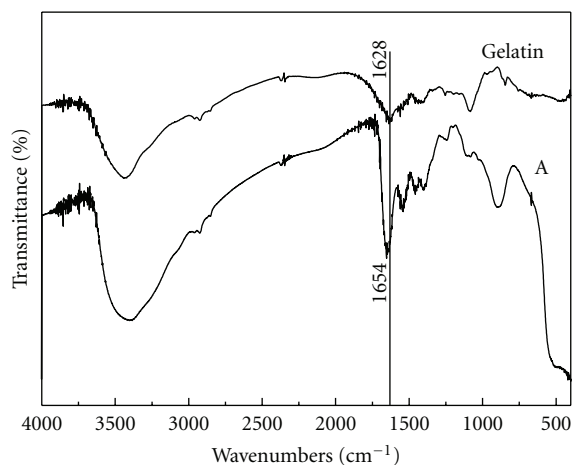


FIGURE 4: FT-IR spectra of the peanut-like ZnO and the gelatin.

3.3. FTIR Measurement. Figure 4 is the FT-IR spectra of the gelatin and the peanut-like ZnO. It shows that the characteristic absorption bands at 1260, 1416 and 1628 cm^{-1} are assigned to the amide I, II, III of gelatin [27]. The 1342 cm^{-1} band in gelatin represents the carboxyl group, which is

attributed to the so-called wagging vibration of praline side chains. These absorption bands indicate that a small amount of gelatin exists in the ZnO architectures. Compared with the spectra, the reflectance strong C=O peak at 1628 cm^{-1} in gelatin shifts to higher wavenumber at 1654 cm^{-1} in the ZnO sample due to the Zn^{2+} ions coupled with the C=O through electrostatic interaction. This result suggests that the nucleation and self-organization of ZnO nanocrystals can be controlled by the gelatin macromolecules, and the carbonyl groups on the surface of gelatin molecules can be the nucleation sites of ZnO. Then, the ZnO nanocrystals precipitate on the surface of the gelatin macromolecules and are spontaneously formed into 3D ZnO architectures.

3.4. The Proposed Growth Model and Mechanism. To further investigate the growth process of the peanut-like ZnO architectures, FESEM studies were carried out for the products obtained at different reaction times. Figure 5 shows the FESEM images of the product obtained at the aging time of 10 minutes, 30 minutes, 1 hour, 2 hours, 6 hours, 12 hours, 18 hours and 24 hours. It can be found that the morphology of as-synthesized samples vary from nanoparticle and flower-like structure to peanut-like structure. When the aging time is less than 2 hours, the particle structures produce, as

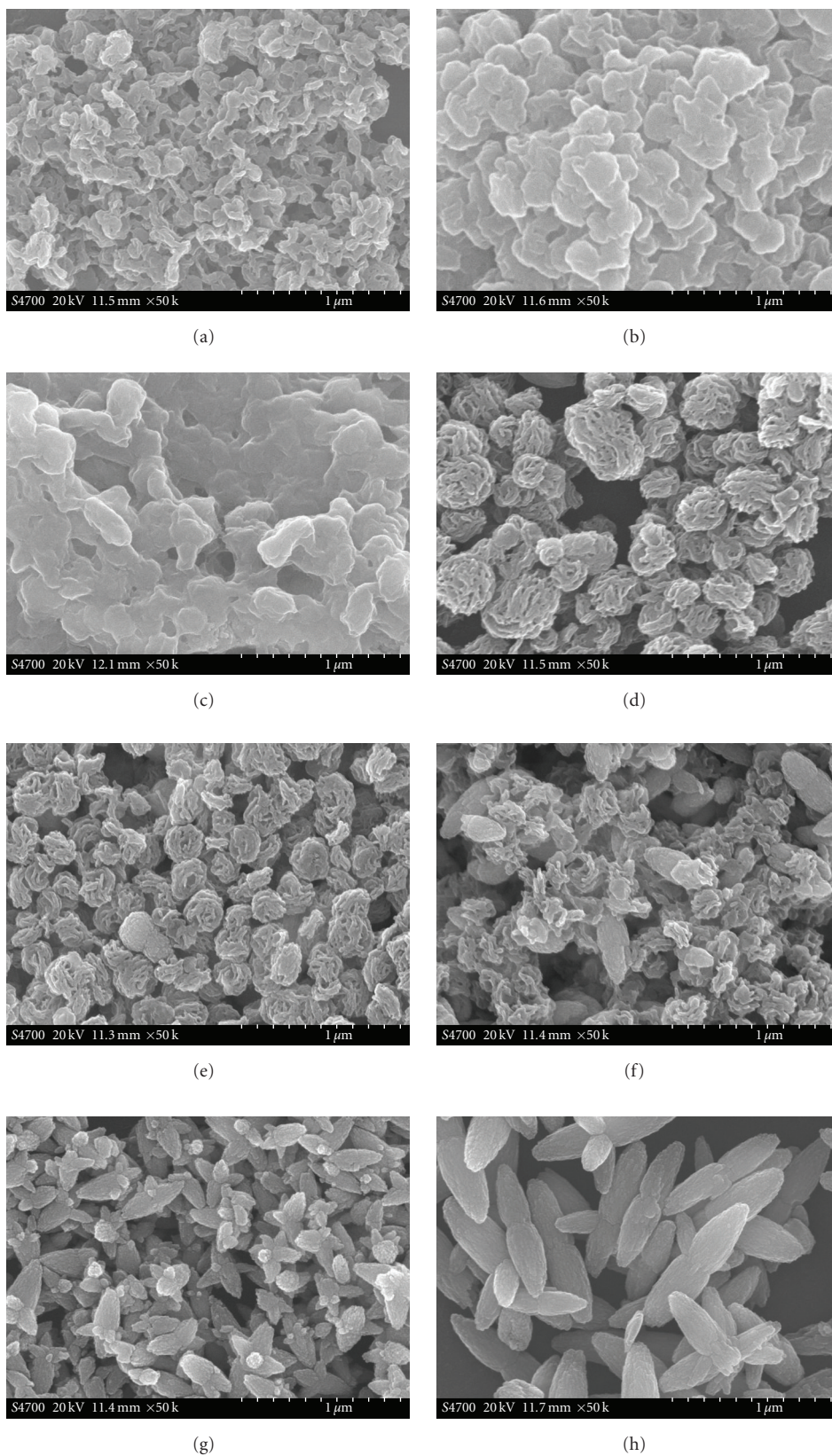
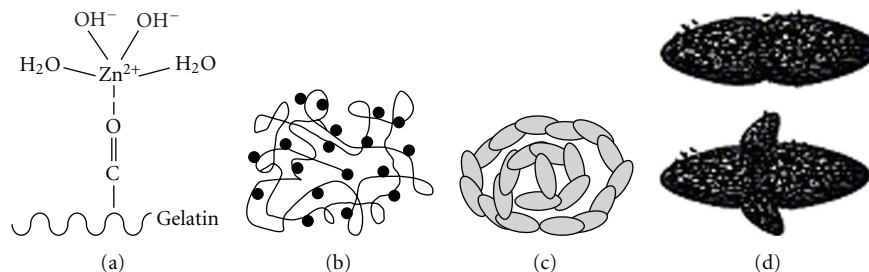


FIGURE 5: FESEM images of the samples synthesized at different reaction times: (a) 10 minutes; (b) 30 minutes; (c) 1 hour; (d) 2 hours; (e) 6 hours; (f) 12 hours; (g) 18 hours; (h) 24 hours.



SCHEME 1: Illustration of growth process of 3D ZnO architectures: (a) nucleation; (b) growth; (c) flower-like structure; (d) peanut-like structure.

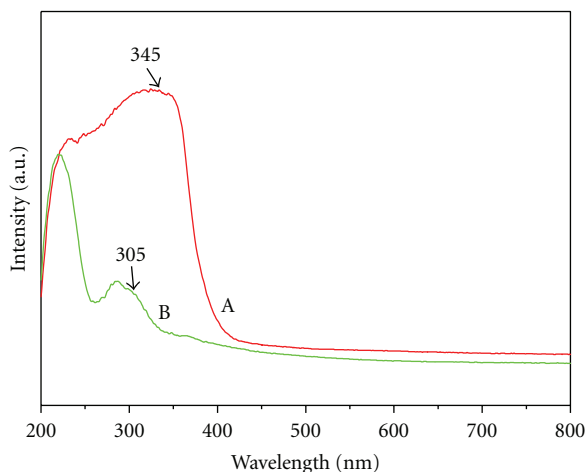


FIGURE 6: UV-vis spectra of the ZnO samples: Curve A is the peanut-like ZnO; Curve B is the flower-like ZnO.

shown in Figures 5(a)–5(c). In comparison, as the aging time reaches 2 hours and 6 hours, the flower-like structures form (Figures 5(d)–5(f)). The peanut-like structures are shown in Figure 5(e) and the quantity of the flower-like structures decreases when the aging time is more than 12 hours. As the time comes up to 18 hours and 24 hours, lots of peanut-like architectures produce (Figure 5(g)). In the growth process, the gelatin molecules can induce the nanoparticles to become flower-like and peanut-like 3D architectures. The formation of 3D ZnO architectures could be a self-assembly process. Individual ZnO nanoparticles self-assemble to hierarchical nanostructures as the primary unit, and then hierarchical nanostructures interact via Van der Waals forces and electrostatic forces, which results in their spontaneous self-organization and the formation of the higher-order structures [12].

Schematic representation of nucleation, growth and self-assembled aggregation of the 3D ZnO architectures are displayed in Scheme 1 based on the process of growth at different aging times. The nucleation begins with the electrostatic attraction between the positive charges of metallic ions and the negative charges of carboxylic groups of the gelatin molecule (Scheme 1(a)) [20]. The gelatin mainly disperses as random coils (Scheme 1(b)) and these random coils behave as organic matrixes holding Zn^{2+} cations on the negative

charge of gelatin molecules, and the nucleation can be initiated from these active sites as a heterogeneous reaction. After nucleation, ZnO growth takes place in the free space among gelatin macromolecule chains with obvious consequences on the morphology of the inorganic deposits. Owing to the effect of the Van der Waals forces, electrostatic forces and hydrogen bonds among the gelatin macromolecules chains, the ZnO nanocrystals as primary units self-organize to the flower-like 3D structures (Scheme 1(c)). According to the XRD results, the crystallization degree of the flower-like ZnO is weaker. As the mineralization is in progress, the ZnO crystals would recrystallize further and the single flower-like 3D architecture can be transformed and organized to the peanut-like 3D architectures as a sub-unit structure of self-assembly process (Scheme 1(d)). The HRTEM results show that the peanut-like architectures, which are composed of rod-like ZnO, are better crystallization and stabler morphology to wurtzite ZnO [30]. Therefore, when the reaction time is more than 18 hours, the final particle structures incline to turn into 3D peanut-like ZnO architectures.

3.5. UV-Vis Characterization. Figure 6 presents the UV-Vis absorption spectra of the ZnO samples. Curve A is the sample of peanut-like ZnO and Curve B is the sample of flower-like ZnO. It can be seen from Curve A in Figure 6 that there is intensive absorption in the ultraviolet band of about 200–400 nm. With respect to the bulk absorption edge appearing at 373 nm at room temperature, a stronger excitonic absorption feature at about 345 nm is blue shifted about 30 nm [1, 32]. The fact that the excitonic peak shifts to blue results from their decreasing crystal size due to the pronounced quantum confinement effect in the ZnO nanocrystallites [32]. As to Curve B, on the other hand, the absorption peak is located at 305 nm and shows a poor UV absorption because of weaker crystallization.

4. Conclusions

In summary, zinc oxide 3D architectures were synthesized by the biomimetic process in the gelatin solution at the room temperature. XRD, FESEM, HRTEM, FT-IR and UV-Vis absorption spectra had been used to characterize the as-obtained ZnO samples. The XRD patterns prove that as-prepared products indexed to the wurtzite (hexagonal) structure of ZnO are well crystallized and have no obvious

impurity phase. By changing concentrations of Zn^{2+} ions or the reaction time, peanut-like 3D ZnO architectures and flower-like 3D ZnO architectures can be successfully synthesized. FT-IR spectra show that the Zn^{2+} ions are coupled with the C=O bond through electrostatic interaction, which suggests that the amide groups and carboxyl groups on the surface of gelatin molecules are the nucleation sites of ZnO. The ZnO nanocrystals then precipitate on the surface of the gelatin and spontaneously self-organize to 3D ZnO architectures. The UV-Vis absorption spectra of the peanut-like ZnO nanocrystals reveal a stronger excitonic absorption feature at about 345 nm. It is expected that this study can offer a convenient and efficient route for the preparation of ZnO architectures.

Acknowledgments

This work was supported by the China National Natural Science Fund (No. 20875007) and Beijing Municipal Science and Technology Development project (No. Z080003032208012).

References

- [1] C. He, T. Sasaki, Y. Shimizu, and N. Koshizaki, "Synthesis of ZnO nanoparticles using nanosecond pulsed laser ablation in aqueous media and their self-assembly towards spindle-like ZnO aggregates," *Applied Surface Science*, vol. 254, no. 7, pp. 2196–2202, 2008.
- [2] K. M. Sulieman, X. Huang, J. Liu, and M. Tang, "Formation of ZnO three-side teathed nanostructures," *Materials Letters*, vol. 61, no. 8-9, pp. 1756–1759, 2007.
- [3] X. An, C. Cao, and H. Zhu, "Bio-inspired fabrication of ZnO nanorod arrays and their optical and photoresponse properties," *Journal of Crystal Growth*, vol. 308, no. 2, pp. 340–347, 2007.
- [4] C. Li, G. Fang, N. Liu, Y. Ren, H. Huang, and X. Zhao, "Snowflake-like ZnO structures: self-assembled growth and characterization," *Materials Letters*, vol. 62, no. 12-13, pp. 1761–1764, 2008.
- [5] L. Wu, Y. Wu, and Y. Lü, "Self-assembly of small ZnO nanoparticles toward flake-like single crystals," *Materials Research Bulletin*, vol. 41, no. 1, pp. 128–133, 2006.
- [6] J. Liu, X. Huang, Y. Li, J. Duan, and H. Ai, "Large-scale synthesis of flower-like ZnO structures by a surfactant-free and low-temperature process," *Materials Chemistry and Physics*, vol. 98, no. 2-3, pp. 523–527, 2006.
- [7] X. Cao, X. Lan, C. Zhao, W. Shen, and D. Yao, "Porous ZnS/ZnO microspheres prepared through the spontaneous organization of nanoparticles and their application as supports of holding CdTe quantum dots," *Materials Research Bulletin*, vol. 43, no. 5, pp. 1135–1144, 2008.
- [8] Z. Jia, L. Yue, Y. Zheng, and Z. Xu, "Rod-like zinc oxide constructed by nanoparticles: synthesis, characterization and optical properties," *Materials Chemistry and Physics*, vol. 107, no. 1, pp. 137–141, 2008.
- [9] Y. Ni, G. Wu, X. Zhang, et al., "Hydrothermal preparation, characterization and property research of flowerlike ZnO nanocrystals built up by nanoflakes," *Materials Research Bulletin*, vol. 43, no. 11, pp. 2919–2928, 2008.
- [10] Z. Fang, K. Tang, G. Shen, D. Chen, R. Kong, and S. Lei, "Self-assembled ZnO 3D flowerlike nanostructures," *Materials Letters*, vol. 60, no. 20, pp. 2530–2533, 2006.
- [11] T. Ghoshal, S. Kar, J. Ghatak, and S. Chaudhuri, "ZnO nanocones: solvothermal synthesis and photoluminescence properties," *Materials Research Bulletin*, vol. 43, no. 8-9, pp. 2228–2238, 2008.
- [12] S. C. Lyu, Y. Zhang, H. Ruh, et al., "Low temperature growth and photoluminescence of well-aligned zinc oxide nanowires," *Chemical Physics Letters*, vol. 363, no. 1-2, pp. 134–138, 2002.
- [13] J.-J. Wu and S.-C. Liu, "Catalyst-free growth and characterization of ZnO nanorods," *Journal of Physical Chemistry B*, vol. 106, no. 37, pp. 9546–9551, 2002.
- [14] M. C. Newton and P. A. Warburton, "ZnO tetrapod nanocrystals," *Materials Today*, vol. 10, no. 5, pp. 50–54, 2007.
- [15] M. Muruganandham and J. J. Wu, "Synthesis, characterization and catalytic activity of easily recyclable zinc oxide nanobundles," *Applied Catalysis B*, vol. 80, no. 1-2, pp. 32–41, 2008.
- [16] H. Yan, R. He, J. Johnson, M. Law, R. J. Saykally, and P. Yang, "Dendritic nanowire ultraviolet laser array," *Journal of the American Chemical Society*, vol. 125, no. 16, pp. 4728–4729, 2003.
- [17] Y. Y. Tay, S. Li, F. Boey, Y. H. Cheng, and M. H. Liang, "Growth mechanism of spherical ZnO nanostructures synthesized via colloid chemistry," *Physica B*, vol. 394, no. 2, pp. 372–376, 2007.
- [18] Z. R. Tian, J. A. Voigt, J. Liu, B. McKenzie, and M. J. Mcdermott, "Biomimetic arrays of oriented helical ZnO nanorods and columns," *Journal of the American Chemical Society*, vol. 124, no. 44, pp. 12954–12955, 2002.
- [19] S. A. Morin, F. F. Amos, and S. Jin, "Biomimetic assembly of zinc oxide nanorods onto flexible polymers," *Journal of the American Chemical Society*, vol. 129, no. 45, pp. 13776–13777, 2007.
- [20] L. P. Bauermann, A. D. Campo, J. Bill, and F. Aldinger, "Heterogeneous nucleation of ZnO using gelatin as the organic matrix," *Chemistry of Materials*, vol. 18, no. 8, pp. 2016–2020, 2006.
- [21] Q. Dong, H. Su, J. Xu, D. Zhang, and R. Wang, "Synthesis of biomorphic ZnO interwoven microfibers using eggshell membrane as the biotemplate," *Materials Letters*, vol. 61, no. 13, pp. 2714–2717, 2007.
- [22] S. Kaluza, M. K. Schröter, R. N. D'Alnoncourt, T. Reinecke, and M. Muhler, "High surface area ZnO nanoparticles via a novel continuous precipitation route," *Advanced Functional Materials*, vol. 18, no. 22, pp. 3670–3677, 2008.
- [23] S. Busch, H. Dolhaine, A. DuChesne, et al., "Biomimetic morphogenesis of fluorapatite-gelatin composites: fractal growth, the question of intrinsic electric fields, core/shell assemblies, hollow spheres and reorganization of denatured collagen," *European Journal of Inorganic Chemistry*, vol. 10, pp. 1643–1653, 1999.
- [24] A. Bigi, E. Boanini, S. Panzavolta, and N. Roveri, "Biomimetic growth of hydroxyapatite on gelatin films doped with sodium polyacrylate," *Biomacromolecules*, vol. 1, no. 4, pp. 752–756, 2000.
- [25] M. A. Martins, C. Santos, M. M. Almeida, and M. E. V. Costa, "Hydroxyapatite micro- and nanoparticles: nucleation and growth mechanisms in the presence of citrate species," *Journal of Colloid and Interface Science*, vol. 318, no. 2, pp. 210–216, 2008.

- [26] H. Cölfen and M. Antonietti, "Mesocrystals: inorganic superstructures made by highly parallel crystallization and controlled alignment," *Angewandte Chemie International Edition*, vol. 44, no. 35, pp. 5576–5591, 2005.
- [27] S. Teng, J. Shi, and L. Chen, "Formation of calcium phosphates in gelatin with a novel diffusion system," *Colloids and Surfaces B*, vol. 49, no. 1, pp. 87–92, 2006.
- [28] J. Li, Y. Chen, Y. Yin, F. Yao, and K. Yao, "Modulation of nano-hydroxyapatite size via formation on chitosan-gelatin network film in situ," *Biomaterials*, vol. 28, no. 5, pp. 781–790, 2007.
- [29] Y. Zhai, F. Z. Cui, and Y. Wang, "Formation of nano-hydroxyapatite on recombinant human-like collagen fibrils," *Current Applied Physics*, vol. 5, no. 5, pp. 429–432, 2005.
- [30] Y. Q. Chen, J. Jiang, Z. Y. He, Y. Su, D. Cai, and L. Chen, "Growth mechanism and characterization of ZnO microbelts and self-assembled microcombs," *Materials Letters*, vol. 59, no. 26, pp. 3280–3283, 2005.
- [31] D. W. James and L. Rintoul, "Protein-water Interactions in solution: the water-gelatin-electrolyte system," *Australian Journal of Chemistry*, vol. 35, pp. 1157–1163, 1982.
- [32] Y. C. Zhang, X. Wu, X. Y. Hu, and R. Guo, "Low-temperature synthesis of nanocrystalline ZnO by thermal decomposition of a "green" single-source inorganic precursor in air," *Journal of Crystal Growth*, vol. 280, no. 1-2, pp. 250–254, 2005.

Research Article

Preparation of ITO Nanoparticles by Liquid Phase Coprecipitation Method

Zhanlai Ding,¹ Cunran An,² Qiang Li,¹ Zhezhe Hou,¹ Jianqiang Wang,¹ Haibo Qi,¹ and Fangjuan Qi¹

¹ School of Material Science and Engineering, Shijiazhuang Railway Institute, Shijiazhuang 050043, China

² College of Science, Hebei University of Science and Technology, Shijiazhuang 050054, China

Correspondence should be addressed to Zhanlai Ding, ding5199@yahoo.com.cn

Received 16 November 2009; Revised 24 January 2010; Accepted 26 January 2010

Academic Editor: Yanqiu Zhu

Copyright © 2010 Zhanlai Ding et al. This is an open access article distributed under the Creative Commons Attribution License, which permits unrestricted use, distribution, and reproduction in any medium, provided the original work is properly cited.

The nanoscale indium tin oxide (ITO) particles are synthesized by liquid phase coprecipitation method under given conditions with solution of indium chloride, tin chloride, and ammonia. The absolute ethyl alcohol or deionized water was used as solvent and the dodecylamine or hexadecylamine surfactant was used as a dispersant in the reaction system. The sample powder was characterized by X-ray diffraction (XRD), transmission electron microscopy (TEM), and high-resolution electron microscopy (HRTEM). Based on the transmission electron micrograph, the influences of the two different solvents and the two different dispersants on the nanoparticle size and dispersion were studied, respectively. The results showed that the ITO particles are finely crystallized body-centered cubic structure. The particle size has distributed in 30 nm to 90 nm.

1. Introduction

Tin-doped indium oxide (Indium tin oxide, ITO), a kind of n-type semiconductor material, has a wide forbidden band (3.3 eV to 4.3 eV). Indium tin oxide thin film has high transparency in the visible light region and lower electric resistivity [1, 2]. It has been used as electrodes in manufacturing of solar cells, flat panel displays, and gas sensors. The tradition deposition techniques of ITO film are DC sputtering, RF sputtering, or electron beam evaporation. It is the first step to fabricate indium and tin alloy target or ITO ceramic target. Afterwards the target is sputtered to glass substrate by the controlled electron beam. These techniques need costly equipments, and the utilization rate of the target materials is as low as 20% [3]. Because indium is a rare metal, it is necessary to explore a new route to deposit ITO thin film with high-Indium utilization rate. The synthesis nanoparticles of metal oxide from aqueous solutions and deposition thin films at low temperatures is an important way for preparation of transparent conductive film [4]. Dip-coating or spray deposition of light transparent, good conductive, and low-membrane resistant ITO film has been studied by the researchers [5–7]. The fabrication

of ITO nanoparticle is important in emulsion (so-called “ink”) preparation for spray deposition or dip-coating ITO film. The ITO thin film’s quality is related to the size and morphology of the nanoparticles. With the development of nanometer material research, several kinds of preparation methods for nanosized ITO emerged. The current methods for nanometer indium tin oxide preparation mainly include solid-phase method, liquid-phase method, and gas-phase method [8–10].

The liquid-phase method, with the advantages of simple operation and controllable granularity, can realize the atomic scale level of mixing. The doping of components achieves easily, and the nanoscale powder material has high-surface activity. The liquid-phase methods include liquid phase precipitation, hydrothermal (high temperature hydrolysis), Sol-gel (colloidal chemistry), radiation chemical synthesis, and so forth [11, 12]. In this research, the ITO nanoparticles, which will be used in spray coating of ITO thin film, are prepared by liquid-phase coprecipitation with indium chloride and tin chloride as main raw material. The ITO nanoparticles were characterized by means of transmission electron microscopy (TEM), and X-ray diffraction (XRD).

2. Experiment Method

2.1. Experiment Process. The synthesis process of ITO nanoparticle by liquid phase co-precipitation is as follows. A certain quality of indium chloride ($\text{InCl}_3 \cdot 4\text{H}_2\text{O}$ 99%, Aldrich) and tin chloride ($\text{SnCl}_4 \cdot 5\text{H}_2\text{O}$ 99%, Aldrich) was dissolved in pure deionized water or ethanol, keeping the ratio of $\text{In}_2\text{O}_3 : \text{SnO}_2 = 9 : 1$. The concentrations of InCl_3 in solution are 0.1, 0.2, and 0.3 mol/L, respectively. Certain concentrations (1.25%, 2.50%, and 5.00%, resp.) of ammonia solutions were made by mixing certain amount of ammonia ($\text{NH}_3 \cdot \text{H}_2\text{O}$, 25%) with pure water. The prepared InCl_3 solution was transferred into fixed three-neck flask, keeping in 303 K to 363 K temperature under electromagnetic agitation. The ammonia solution was added to the flask, controlling the stirring speed and testing the pH value till the required pH value. And a certain amount of dodecylamine or hexadecylamine (DDA or HDA, Fluka) was added as dispersant. The precipitate precursor of ITO was aged a certain time and washed with deionized water and absolute alcohol for three times, respectively. After washing, the precipitates were dried for one hour at 353 K. The dried samples were calcinated for 1, 1.5, and 2 hours at 773 K, 873 K, and 973 K, respectively to get the indium tin oxide nanopowder by thermal decomposing.

2.2. Characterizing Methods. The morphology and structure of the prepared nanoparticles were characterized by means of a transmission electron microscopy (TEM) and X-ray diffraction (XRD). The microstructure of the ITO samples were analysed on a Tecnai G2 20 S-TWIN model TEM with 200 kV acceleration voltage. For TEM analysis, the sample was dispersed in a few milliliters of tetrahydrofuran in an ultrasonic bath, and a drop of this dispersion was placed on a copper grid coated with a carbon film. The XRD measurements of nanopowder were performed on a D8 ADVANCE diffractometer with $\text{Cu K}\alpha$ radiation ($\lambda = 1.5418 \text{ \AA}$).

3. Results and Discussion

3.1. X-Ray Diffraction of the Nanoparticles. The precursor precipitate and the calcinated samples were examined by an X-ray diffractometer (D8 ADVANCE type), respectively to analyze phase and structure. The XRD patterns are shown in Figure 1. The XRD pattern of precursor precipitate prepared in ethyl alcohol solvent is shown in Figure 1(a). A strong and sharp peak can be seen in Figure 1(a), while the other diffraction peaks are more weaker. According to JCPDS calibration (PDF#76-1463), the precursor precipitate is $\text{In}(\text{OH})_3$ with body-centred cubic crystalline structure. The diffraction peaks are more complicated than the PDF76-1463 standard. The reason is that maybe there is a certain amount of $\text{Sn}(\text{OH})_4$ in the precursor. The XRD pattern in Figure 1(b) is the result of calcinating (973 K for 1 h) sample, which its precursor precipitate was prepared in pure water solvent. The XRD patterns of samples at different calcinating temperature (773 K, 873 K, and 973 K) are shown

in Figure 1(c), which their precursors were precipitated in ethyl alcohol solvent. According to the JCPDS (PDF#06-0416), the samples in Figures 1(b) and 1(c) are In_2O_3 powder with body-centred cubic crystalline structure. Kim, and so forth, synthesized ITO particle that had hexagonal structure and cubic structure. As the pH value of coprecipitated solution was increased, the amount of hexagonal crystal was decreased. ITO particle with mostly cubic structure was produced at higher than pH 10 [12]. The ITO particles that we prepared by co-precipitate method only have cubic structure. After 793 K, calcinating the diffraction peaks of the samples are more stronger and sharper, indicating that the In_2O_3 crystalline structure is more perfect. The crystallized characteristic is gradually becoming obvious with the calcinating temperature increasing from 773 K to 973 K by Figure 1(c). By comparison, it can be seen that the calcinating temperature plays a more important role than the calcinating time in improving crystal structure. As long as there is enough calcinating temperature, the perfect In_2O_3 nanocrystal structure can be obtained in a relatively short period of time. There are no peaks that represent the tin oxide, and the In_2O_3 lattice parameter does not change obviously, indicating that the tin atoms arrange into the In_2O_3 crystal lattice.

3.2. The TEM Analysis of ITO Nanoparticles. The particle size and morphology of the ITO samples were analyzed by a transmission electron microscopy (TEM, model Tecnai G² 20 S-TWIN). The TEM photographs of the samples are illustrated in Figure 2. The TEM photographs of the samples prepared in ethanol solvent and calcinated at 773 K and 973 K, respectively are shown in Figures 2(a) and 2(b). The TEM photograph morphology in Figure 2(c) stands for the sample precipitated in deionized water solvent and calcinated at 873 K. Comparing Figure 2(a) with Figure 2(b), it can be seen that at lower calcinating temperature (773 K), the particles of samples are finer, but they are more seriously agglomerated. When the thermal decomposition temperature is higher (973 K), the crystal size increases obviously and the agglomeration degree is reduced. The particles appear hexagon or short rod shapes.

The particle size of indium oxide samples after 773 K°C calcination is 30 to 50 nm, and the average particle size is 36.2 nm, basing on the statistics from a group of images. It is 50 to 90 nm after 973 K calcinations, and the average particle size is 78.3 nm. Comparing Figure 2(b) with Figure 2(c), it can be seen that although its thermo-decomposing temperature in Figure 2(b) is higher than Figure 2(c), its particle size has not grown up significantly, and that the nanoparticles dispersion has no obvious difference. Preparing in ethanol solvent does not improve the In_2O_3 nanoparticle dispersion degree. The high resolution electron microscopy (HRTEM) image of sample (b) is presented in Figure 2(d). The selected area electron diffraction (SAED) pattern is also in the same figure. The ITO nanoparticle is body-center-cubic structure and it crystallized well.

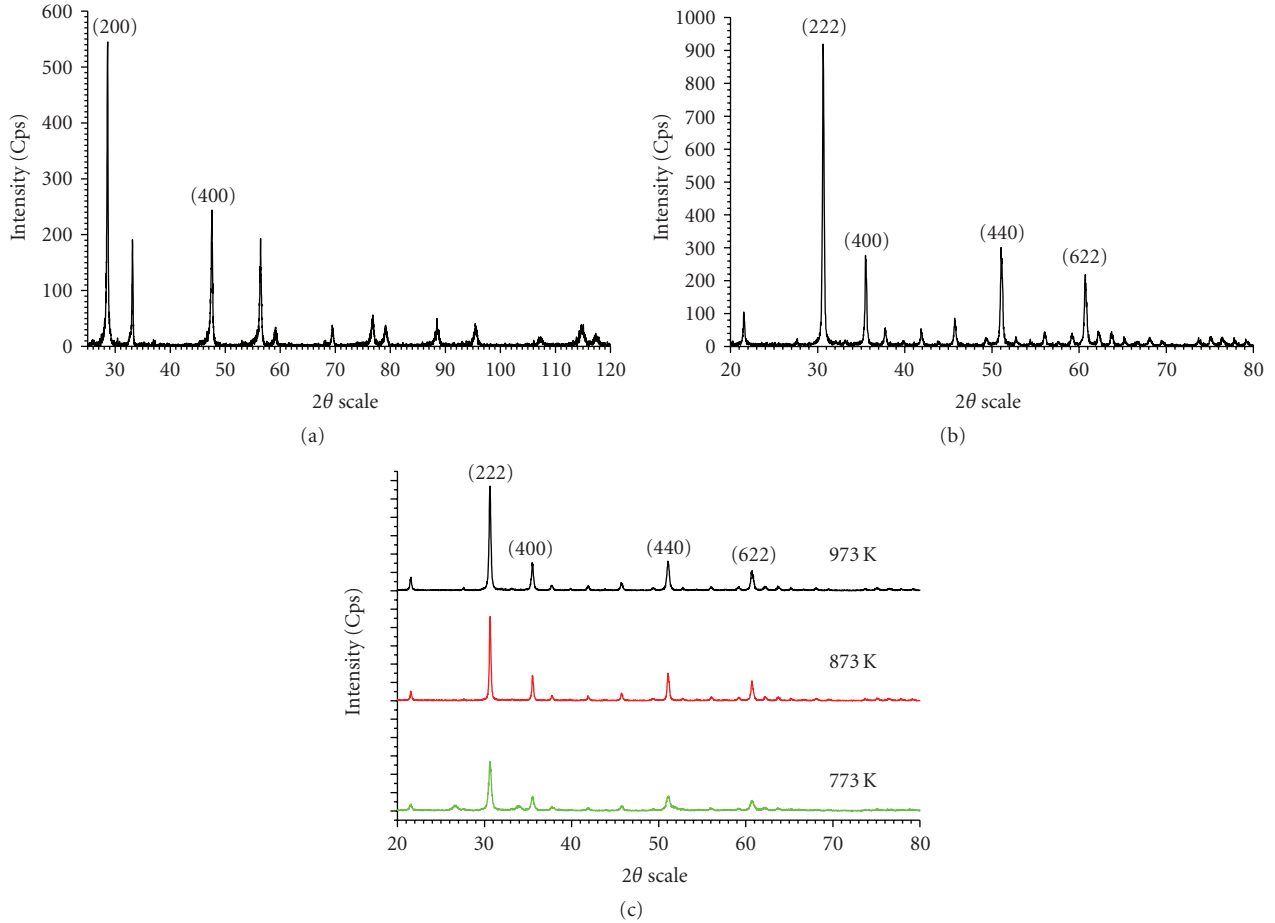


FIGURE 1: The X-ray diffraction patterns of samples. (a) The precursor precipitate, (b) the ITO nanoparticles prepared in deionized water solvent, (c) the ITO nanoparticles prepared in ethyl alcohol solvent and then decomposed at different temperatures.

3.3. *The Particle Size Calculated by Scherrer Equation.* The prepared ITO particles can be calculated by Scherrer equation, based on the XRD pattern. The Scherrer equation is as follow:

$$D_{hkl} = \frac{K\lambda}{\beta_{hkl} \cos \theta_{hkl}}, \quad (1)$$

where D_{hkl} represents particle size (unit nm) being perpendicular to (hkl) crystal plane. β_{hkl} is broadening (unit Rad) of the diffract peak by the grain refinement. θ_{hkl} is diffraction angle of (hkl) crystal plane. λ is the wave length of the X-ray, where it is 1.5406 Å. K is a constant; its numerical value is related to defines of the β_{hkl} . K equals to 0.89 when β_{hkl} takes the half of the broadening of the diffract peak.

The particle size was calculated corresponding to the (222), (440), and (400) diffract peaks for every diffract pattern of calcinating samples. The average value of each sample is listed in Table 1.

Based on the calculated results, the particle size grows up gradually with the increase of the calcination temperature. The average particle size becomes 63 nm of 973 K calcinating from 22 nm of the 773 K calcinating. The calculated results are compared with the statistics of transmission electron

TABLE 1: The calculated results of ITO particle size by Scherrer equation.

Samples at different calcinating temperature (k)	773	873	973
Average particle size value (nm)	22	44	63

microscope. The particle size of indium tin oxide had been statistically analyzed by TEM images as in Figures 2(a) and 2(b), which the calcinating temperatures were 773 K and 973 K, respectively. The particle size of indium oxide samples after 773 K calcination is 30 to 50 nm, and the average particle size is 36.2 nm. It is 50 to 100 nm after 973 K calcinations, and the average particle size is 78.3 nm. The particle size from the TEM photograph results is larger than the calculated results by the Scherrer equation. This is mainly due to the various factors influence on the accuracy of particle size D_{hkl} computed by Scherrer formula, making the calculated value is less than the TEM measurements. First of all, if there is lattice imperfection in the crystal, the broadening of diffraction peak is caused not only by the grain size refinement but also by the lattice imperfection. Second, the X-ray diffraction peak is sharp. It is difficult to

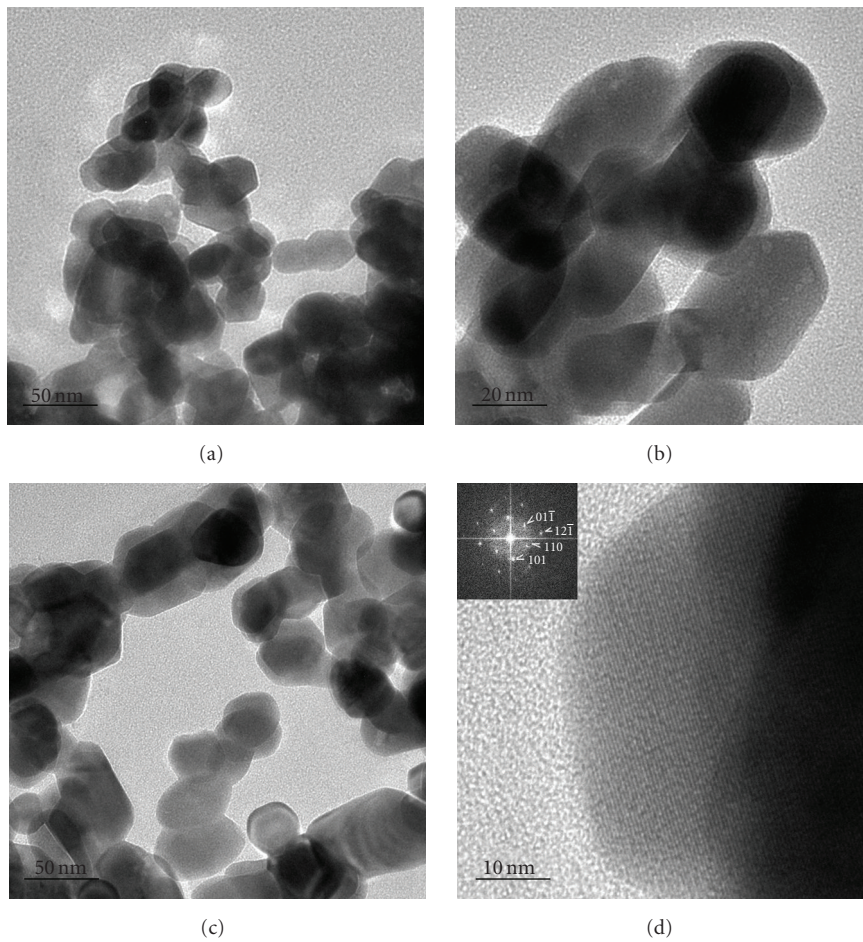


FIGURE 2: The TEM and HRTEM images of ITO nanoparticles synthesized in different solvents. (a) The absolute ethyl alcohol used as solvent and the precipitate decomposed at 737 K, (b) the absolute ethyl alcohol used as solvent and the precipitate decomposed at 937 K, (c) the deionized water used as solvent and the precipitate decomposed at 837 K, (d) the HRTEM photograph and the selective electron diffraction pattern of sample (b).

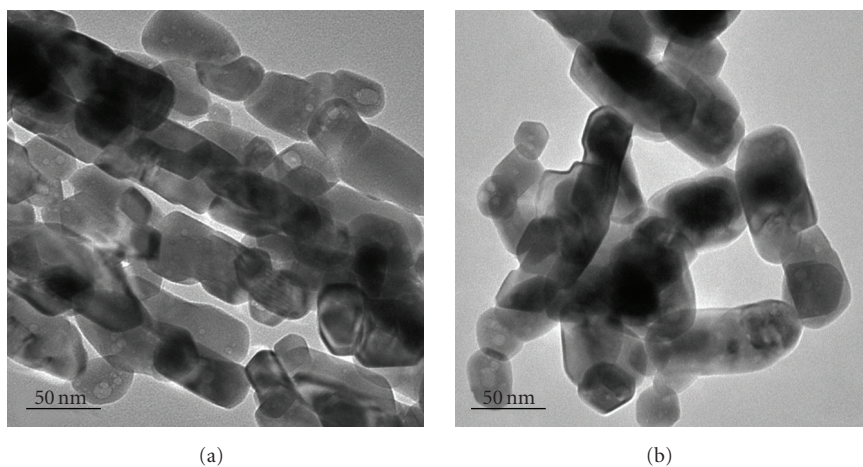


FIGURE 3: The TEM images of ITO nanoparticles with different dispersants. (a) The dodecylamine surfactant as dispersant, (b) the hexadecylamine surfactant as dispersant.

measure the width value accurately, enlarging the calculation deviation.

3.4. Dispersant Effect on the Morphology and Dispersion of the ITO Nanoparticles. Two dispersants were used in the experiments, namely, dodecylamine and hexadecylamine. The dispersion performance of ITO nanoparticle was compared through the contrast experiment. The ITO nanoparticle TEM images, which prepared under the same conditions except using two kinds of dispersant, respectively, are shown in Figure 3. The ITO nanoparticle TEM photo with dodecylamine surfactant as dispersant is in Figure 3(a). While the ITO nanoparticle TEM photo with hexadecylamine surfactant as dispersant is in Figure 3(b). It can be observed from Figure 3 that ITO nanoparticles synthesized with dodecylamine are not dispersed well, and some particles are arranged into the long axis orderly. At the same time, the ITO nanoparticles synthesized with hexadecylamine are dispersed better than with dodecylamine. The morphology of ITO nanoparticles either with dodecylamine or with hexadecylamine as dispersant appears irregular shape. Some of the particles appear hexagon or short rod shapes.

4. Conclusion

The nanoscale indium tin oxide (ITO) particles are successfully synthesized by liquid phase co-precipitation method under given conditions with reactants of indium chloride, tin chloride, and ammonia. The absolute ethyl alcohol or deionized water was used as solvent, and the dodecylamine or hexadecylamine surfactant was used as a dispersant in the reaction system. The ITO particles are finely crystallized body centered cubic structure. The particle size has preferably dispersivity and distributes in 30 nm to 90 nm.

The dispersivity of ITO nanoparticle does not have significant difference prepared in absolute ethyl alcohol or deionized water solvent with hexadecylamine surfactant as dispersant in the reaction system. At certain conditions, the dodecylamine surfactant can organise the indium oxide nanoparticles in lines, but that self-assembly phenomena needs further study.

Acknowledgments

The author is thankful for the financial support of Natural Science Foundation of Hebei Province (no: E2008000429). The author also thanks Dr. Zhang of Nano-science Research Center for the TEM analysis and the discussions on the results.

References

- [1] G. Cheng, E. Stern, S. Guthrie, et al., "Indium oxide nanostructures," *Applied Physics A*, vol. 85, no. 3, pp. 233–240, 2006.
- [2] F. O. Adurodija, L. Semple, and R. Brüning, "Crystallization process and electro-optical properties of In_2O_3 and ITO thin films," *Journal of Materials Science*, vol. 41, no. 21, pp. 7096–7102, 2006.
- [3] S. L. Wang and D. L. Xia, "Fabrication techniques and development of ITO film," *GLASS & ENAMEL*, vol. 32, no. 5, pp. 51–54, 2004.
- [4] T. P. Niesen and M. R. De Guire, "Review: deposition of ceramic thin films at low temperatures from aqueous solutions," *Journal of Electroceramics*, vol. 6, no. 3, pp. 169–207, 2001.
- [5] U. Betz, M. Kharrazi Olsson, J. Marthy, M. F. Escolá, and F. Atamny, "Thin films engineering of indium tin oxide: large area flat panel displays application," *Surface and Coatings Technology*, vol. 200, no. 20–21, pp. 5751–5759, 2006.
- [6] T. Ogi, F. Iskandar, Y. Itoh, and K. Okuyama, "Characterization of dip-coated ITO films derived from nanoparticles synthesized by low-pressure spray pyrolysis," *Journal of Nanoparticle Research*, vol. 8, no. 3–4, pp. 343–350, 2006.
- [7] W. Chang, S. Lee, C. Yang, and T. Lin, "Opto-electronic properties of chromium doped indium-tin-oxide films deposited at room temperature," *Materials Science and Engineering B*, vol. 153, no. 1–3, pp. 57–61, 2008.
- [8] Y. Zhang, H. Ago, J. Liu, et al., "The synthesis of In, In_2O_3 nanowires and In_2O_3 nanoparticles with shape-controlled," *Journal of Crystal Growth*, vol. 264, no. 1–3, pp. 363–368, 2004.
- [9] K. Soulantica, L. Erades, M. Sauvan, F. Senocq, A. Maisonnat, and B. Chaudret, "Synthesis of indium and indium oxide nanoparticles from indium cyclopentadienyl precursor and their application for gas sensing," *Advanced Functional Materials*, vol. 13, no. 7, pp. 553–557, 2003.
- [10] H. S. Kim, P. D. Byrne, A. Facchetti, and T. J. Marks, "High performance solution-processed indium oxide thin-film transistors," *Journal of the American Chemical Society*, vol. 130, no. 38, pp. 12580–12581, 2008.
- [11] S. Deki, S. Iizuka, M. Mizuhata, and A. Kajinami, "Fabrication of nano-structured materials from aqueous solution by liquid phase deposition," *Journal of Electroanalytical Chemistry*, vol. 584, no. 1, pp. 38–43, 2005.
- [12] A. Nakata, M. Mizuhata, and S. Deki, "Novel fabrication of highly crystallized nanoparticles in the confined system by the liquid phase deposition (LPD) method," *Electrochimica Acta*, vol. 53, no. 1, pp. 179–185, 2007.

Research Article

Synthesis and Field Emission Properties of Hierarchical ZnO Nanostructures

Deyan Peng, Yanjun Huang, Ke Yu, Lijun Li, and Ziqiang Zhu

Key Laboratory of Polar Materials and Devices, Department of Electronic Engineering, East China Normal University, Ministry of Education of China, Shanghai 200241, China

Correspondence should be addressed to Ke Yu, yk5188@263.net

Received 30 November 2009; Accepted 21 April 2010

Academic Editor: Steve Acquah

Copyright © 2010 Deyan Peng et al. This is an open access article distributed under the Creative Commons Attribution License, which permits unrestricted use, distribution, and reproduction in any medium, provided the original work is properly cited.

Three novel kinds of hierarchical ZnO nanostructures: nanocombs nanoscrewdrivers and nanonails, have been synthesized in large quantities via a simple thermal evaporation process in the same run of growth in different regions of the quartz tube. The morphologies could be well controlled by adjusting the distances between the source materials and the substrates. These ZnO products were investigated by scanning electron microscopy, X-ray diffraction and Raman spectroscopy. The field emission properties of the ZnO nanostructures were investigated. These hierarchical ZnO nanostructures may be attractive building blocks for field emission microelectronic devices and other devices.

1. Introduction

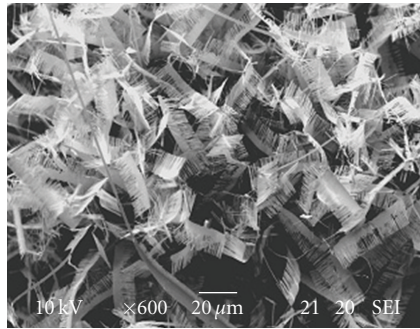
Nanoscale one-dimensional semiconducting materials have attracted much attention due to their importance in understanding the fundamental properties at low dimensionality, as well as for their applications in nanodevices. As an important II-VI semiconductor, zinc oxide (ZnO) is of considerable interest due to its distinguished performance in electronics, optics, and mechanics. ZnO with a band gap of 3.37 eV and large exciton binding energy of 60 meV at room temperature is a key technological material [1, 2]. In particular, it is expected that they possess a good electron field emission (FE) property due to their high aspect ratio and small tip radius of curvature. Intensive investigation has been carried out over the last several decades on field emission due to numerous applications such as flat-panel displays, microwave amplifiers, and vacuum microelectronic devices. Today, field-emission characteristics of carbon nanotubes (CNTs) have been extensively investigated, and there have been a large number of laboratory work reported [3–5]. However, thermal stability and ambient insensitivity are as important as the geometric factors to the operation of field emitters [4]. ZnO exhibits a high melting point, excellent chemical stability, and negative electron affinity. Therefore, a ZnO-based 1D structure could be an appropriate alternative

to CNTs for field emission displays. The field-emission properties for ZnO nanowire arrays [5], tetrapod-like ZnO nanostructures [6], ZnO nanoneedles [7, 8], and cuboid zinc oxide nanorods [9] have been attempted recently. In this paper, the field-emission properties for three kinds of novel ZnO nanostructures: nanocombs, nanoscrewdrivers, and nanonails were reported. It must be noted that the structure determines the properties of a given nanomaterial with respect to its specific application, so the study on field-emission behaviors of them is of great interest both from scientific and technological perspectives.

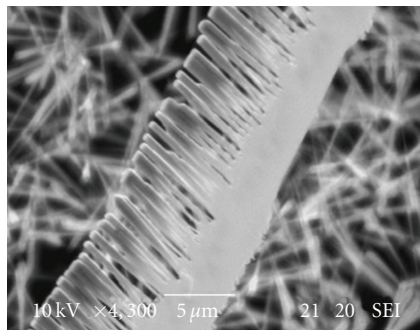
In this paper, using a simple physical evaporation method, we synthesized some ZnO nanostructures: ZnO nanocombs, nanoscrewdrivers, and ZnO nanonails highly aligned as flowers with single-crystal peculiar hexagon nanonails. The morphologies could be well controlled by adjusting the deposition position.

2. Experimental Section

The hierarchical ZnO nanostructures were grown at the atmospheric pressure by thermal evaporation of the mixture of ZnO powders and graphite powder (both 99.9%) in a two-heating-zone furnace system. The distance between the two-heating-zone was about 50 cm. three n-type (111) Si wafers

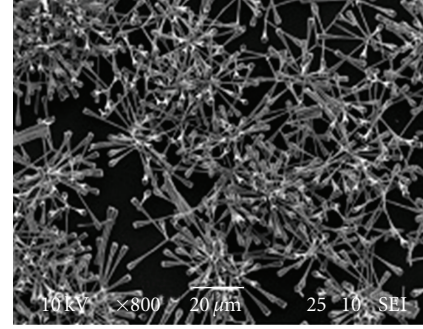


(a)

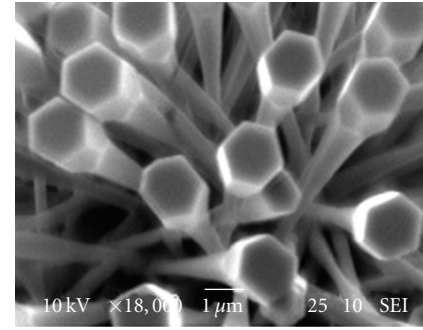


(b)

FIGURE 1: (a) SEM images of ZnO nanocombs grown on silicon substrate 1, (b) A high-magnified SEM image of ZnO nanocombs.

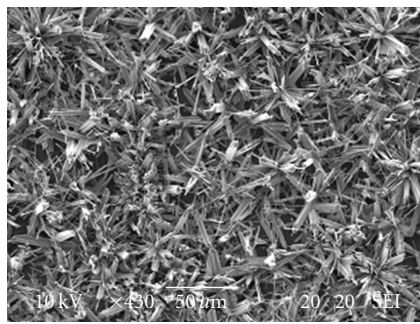


(a)

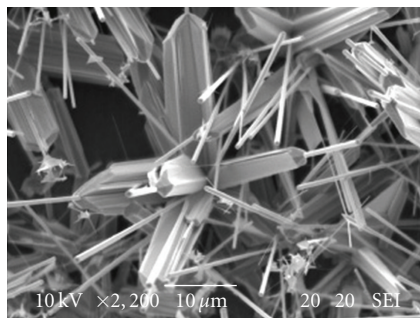


(b)

FIGURE 3: (a) SEM images of ZnO nanonails grown on silicon substrate 3, (b) high-magnified SEM image of ZnO nanonails.



(a)



(b)

FIGURE 2: (a) SEM images of ZnO nanoscrewdrivers grown on silicon substrate 2, (b) A high-magnified SEM image of ZnO nanoscrewdrivers.

were used as the substrates for deposition. The furnace was set to the desired temperature (750°C–1100°C) and a closed-end small quartz tube (60 cm in length, 2 cm in diameter), containing the source material (graphite and ZnO powders with Moore ratio 1:1) and Si substrates, were inserted. The source materials were placed in the high temperature heating zone (upstream), and the n-type (111) Si wafers were placed ordinal in the second heating zone (downstream) to collect the products. After the system was purged with N₂ for 10 min, the system was heated to the desired temperature at a rate of 10°C/min and kept at that temperature with the carrier gas of nitrogen flow rate of 3 L/min. When the substrates were taken out from the quartz tube after an hour, we could see gray-white wool-like products on substrates. The resulting samples were collected for characterization and measurements.

The morphologies were analyzed using scanning electron microscopy (SEM), which looks like nanocombs, nanoscrewdrivers, and nanonails, respectively. Their crystal structure features were characterized using X-ray diffraction (XRD). Furthermore, Raman spectra and field emission properties of them were investigated. Field emission measurements were performed with diode structure in a vacuum chamber under a pressure of 5×10^{-5} Pa. The synthesized nanocombs nanoscrewdrivers and nanonails (as a cathode) were separated from a phosphor/ITO/glass anode by two Teflon spacers, respectively. Through a window of the vacuum chamber, the distribution of the field emission sites on fluorescent anode was recorded with a camera. Meanwhile, the emission

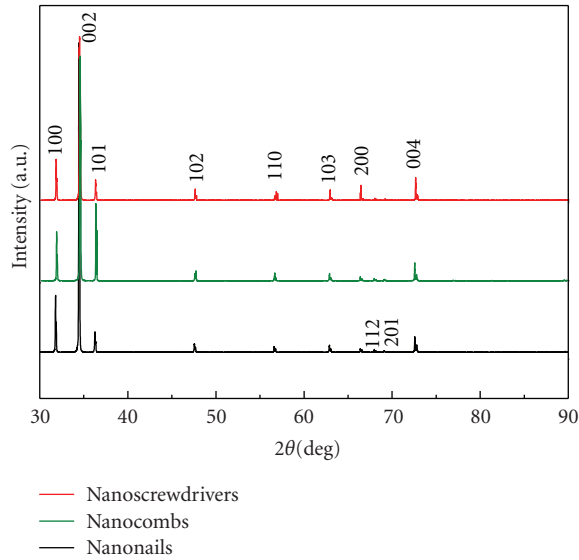


FIGURE 4: XRD patterns of the three kinds of hierarchical ZnO nanostructures: nanoscrewdrivers, nanocombs, and nanonails (from up to down).

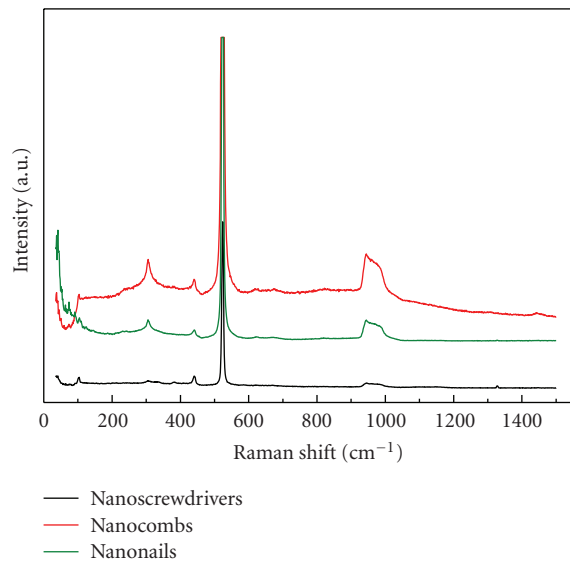


FIGURE 5: Raman spectrum properties of the three kinds of hierarchical ZnO nanostructures: nanoscrewdrivers, nanocombs, and nanonails (from up to down).

current versus voltage curve was measured with standard electronic instruments after the bias voltage sweeps were conducted several times for the emitter to reach a stable emission for each given applied field.

3. Results and Discussion

After thermal evaporation, several self-organized structures were obtained. Figures show typical SEM images with different magnifications of the ZnO products obtained at different regions of the quartz tube.

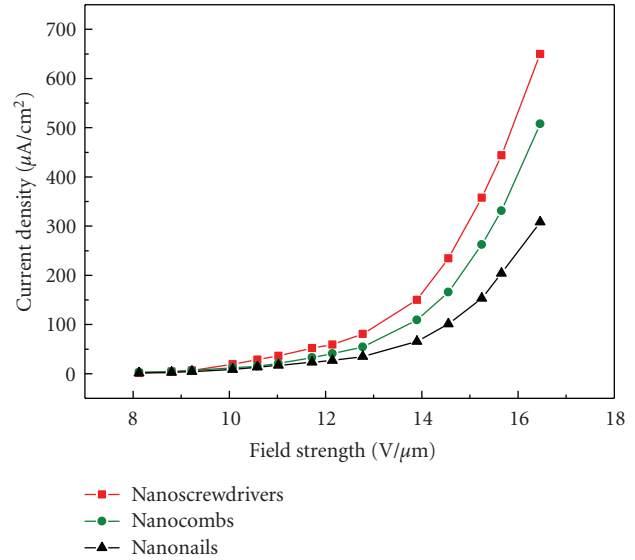


FIGURE 6: FE current density versus electric field ($J-E$) for the three kinds of hierarchical ZnO nanostructures: nanoscrewdrivers, nanocombs, and nanonails (from up to down).

3.1. Nanocombs of ZnO. Figure 1(a) shows the SEM images of the ribbon/comb structures deposited on Si substrates 1. For each comb, the nanorod branches resembling comb teeth are distributed on one side of the belt-like stem. The diameters of the comb teeth range from 80 nm to 200 nm and their lengths are evenly 10 μm . Some of the neighboring teeth have been merged into larger ones, as shown in high magnified Figure 1(b). Noneven teeth are observed in the premature combs, which are possibly due to differences in growth temperature. Comb-like structure is believed to be the result of rapid crystallization at large super saturation, analogous to the appearance of dendrites crystal in bulk crystal growth [10]. The formation of our single-sided ZnO nanocombs may be reasonably explained by the surface polarity-induced asymmetric growth proposed by Wang et al. [11].

3.2. Nanoscrewdrivers of ZnO. SEM image in Figure 2(a) on substrate 2 is an interesting configuration, in which the hexagonal coaxial rods with two segments of different diameters stacking each other. The bigger rods look like screwdrivers with the diameter about 2 μm and the diameter of the smaller rod is about 200 nm. The length of each pod is about 20 μm . From the hexagonal symmetry of the coaxial rod, its growth direction is [0001]. A high-magnified SEM image is shown in Figure 2(b).

3.3. Nanonails of ZnO. In our experiments, it was found that the substrate 3 is covered with a large number of nanonails. These hierarchical structures have been found as shown in Figure 3(a), which look like flowers in which each coaxial rod radically grows from one center. The nanonails are well-distributed as shown in Figure 3(a). The high-magnified SEM images are shown in Figure 3(b) corresponding. And

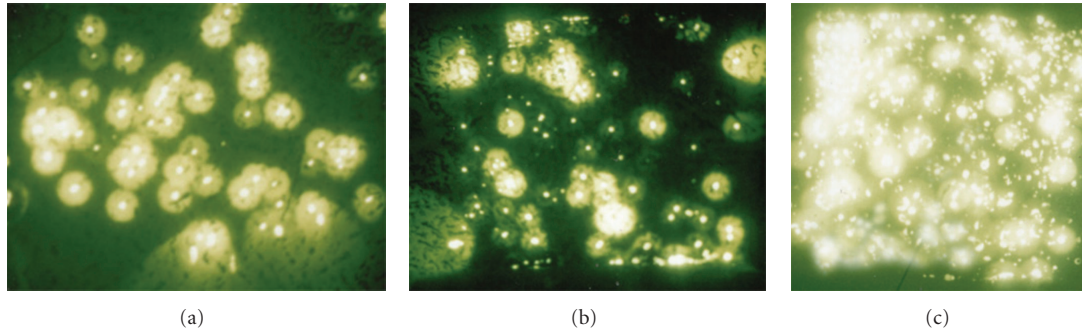


FIGURE 7: Fluorescence screen images of the field emission of the hierarchical ZnO Nanostructures. (a) is for ZnO nanonails; (b) is for ZnO nanocombs; (c) is for ZnO nanoscrewdrivers.

Figure 3(b) shows the high-magnification SEM images like nail morphologies, which indicates clear that the nanostructures are composed of perfect hexagonal prism caps and prism shafts connected with smaller diameter bottom. From the hexagonal symmetry of the nanonail, its growth direction is [0001]. Each nanonail structure is several tens of nanometers in tail diameter with a perfect hexagonal-shaped cap about $0.5\text{--}1\ \mu\text{m}$ in diameter and $10\text{--}20\ \mu\text{m}$ in length. Further studies are necessary to understand the morphologies.

These nanostructures of ZnO have similar XRD pattern as shown in Figure 4. All of the diffraction peaks can be indexed to the Wurtzite-structured (hexagonal) ZnO (JCPDS no. 80-0075). No diffraction peaks from other impurities have been detected. The strong (002) peak of ZnO wurtzite structure and much weaker (100) and (101) peaks are due to the imperfect vertical growth of the nanostructures. The exact growth mechanism undoubtedly needs further studies.

The Raman spectra of the three different ZnO nanostructures are shown in Figure 5. Raman properties of ZnO crystals measurements were carried out at room temperature in a backscattering geometry. In results, the three spectra have similar shapes drawn in Figure 5. The peaks of ZnO at ~ 331 , ~ 440 , and $\sim 1000\ \text{cm}^{-1}$ were clearly observed in Figure 5, with the A1 (TO), E2 (high), and E1 (2LO) vibration modes of ZnO, respectively [12, 13]. The formation of hierarchical ZnO nanostructures indicates that complicated reactions and self-assembled mechanism occurred in the present experiments. Though it is still not completely clear what exactly happened during the growth, undoubtedly deposition temperature plays an important role for these complicated structures as in the above results.

In our experiments, field emission properties of these products were investigated. The turn-on and threshold field, defined as the electric field required to produce a current density of $1\ \mu\text{A}/\text{cm}^2$ and $0.1\ \text{mA}/\text{cm}^2$, respectively. Current density versus electric field ($J\text{--}E$) for them are shown in Figure 6 with the same turn-on field of $8\ \text{V}/\mu\text{m}$, but the screwdriver-like hexagonal coaxial rods with more keen-edged nanotips have the lowest threshold field of $12.6\ \text{V}/\mu\text{m}$, which is attributed to high aspect ratio of the tip of

the screwdriver-like ZnO. Other experimental factors being equal, the nanostructures with sharper tips are easier to emit electrons.

Fluorescence screen images of the field emission of the hierarchical ZnO nanostructures were shown Figure 7. Figure 7(a) is for ZnO nanonails, Figure 7(b) is for ZnO nanocombs, and Figure 7(c) is for ZnO nanoscrewdrivers. The homogeneous emission and high electron emission spot number per unit area of the nanoscrewdrivers may be attributed to a large number of emitters on the surface of the nanoscrewdrivers contributing to emission.

4. Conclusion

In summary, we fabricated ZnO nanocombs, nanoscrewdrivers, and ZnO nanonails structures by a simple method of carbon reduction of ZnO in a tube furnace at atmospheric pressure. Their morphologies are affected by the position of substrate, but these ZnO nanostructures have similar XRD pattern and Raman spectra properties.

Acknowledgments

The authors acknowledge the financial support from the Chinese National Key Basic Research Special Found (Grant no. 2006CB921704), the NSF of China (Grant no. 60976014 and 60976004), the Key Basic Research Project of Scientific and Technology Committee of Shanghai (Grant no. 09DJ1400202), and the Specialized Research Fund for the Doctoral Program of Higher Education (Grant no. 20070269016).

References

- [1] M. H. Huang, S. Mao, H. Feick et al., "Room-temperature ultraviolet nanowire nanolasers," *Science*, vol. 292, no. 5523, pp. 1897–1899, 2001.
- [2] Q. X. Zhao, M. Willander, R. E. Morjan, Q.-H. Hu, and E. E. B. Campbell, "Optical recombination of ZnO nanowires grown on sapphire and Si substrates," *Applied Physics Letters*, vol. 83, no. 1, pp. 165–167, 2003.
- [3] S. Fan, M. G. Chapline, N. R. Franklin, T. W. Tomblor, A. M. Cassell, and H. Dai, "Self-oriented regular arrays of carbon

- nanotubes and their field emission properties,” *Science*, vol. 283, no. 5401, pp. 512–514, 1999.
- [4] D. Kim, H. Yang, H. Kang, and H. Lee, “Novel emission degradation behavior of patterned carbon nanotubes by field emission,” *Chemical Physics Letters*, vol. 368, pp. 439–444, 2003.
- [5] C. J. Lee, T. J. Lee, S. C. Lyu, Y. Zhang, H. Ruh, and H. J. Lee, “Field emission from well-aligned zinc oxide nanowires grown at low temperature,” *Applied Physics Letters*, vol. 81, no. 19, pp. 3648–3650, 2002.
- [6] Q. Wan, K. Yu, T. H. Wang, and C. L. Lin, “Low-field electron emission from tetrapod-like ZnO nanostructures synthesized by rapid evaporation,” *Applied Physics Letters*, vol. 83, no. 11, pp. 2253–2255, 2003.
- [7] Y. W. Zhu, H. Z. Zhang, X. C. Sun et al., “Efficient field emission from ZnO nanoneedle arrays,” *Applied Physics Letters*, vol. 83, no. 1, pp. 144–146, 2003.
- [8] C. X. Xu and X. W. Sun, “Field emission from zinc oxide nanopins,” *Applied Physics Letters*, vol. 83, no. 18, pp. 3806–3808, 2003.
- [9] K. Yu, Y. Zhang, R. Xu et al., “Field emission behavior of cuboid zinc oxide nanorods on zinc-filled porous silicon,” *Solid State Communications*, vol. 133, no. 1, pp. 43–47, 2005.
- [10] H. Yan, R. He, J. Johnson, M. Law, R. J. Saykally, and P. Yang, “Dendritic nanowire ultraviolet laser array,” *Journal of the American Chemical Society*, vol. 125, no. 16, pp. 4728–4729, 2003.
- [11] Z. L. Wang, X. Y. Kong, and J. M. Zuo, “Induced growth of asymmetric nanocantilever arrays on polar surfaces,” *Physical Review Letters*, vol. 91, no. 18, Article ID 185502, 2003.
- [12] T. C. Damen, S. P. S. Porto, and B. Tell, “Raman effect in zinc oxide,” *Physical Review*, vol. 142, no. 2, pp. 570–574, 1966.
- [13] Y. J. Xing, Z. H. Xi, Z. Q. Xue et al., “Optical properties of the ZnO nanotubes synthesized via vapor phase growth,” *Applied Physics Letters*, vol. 83, no. 9, pp. 1689–1691, 2003.

Research Article

Improved Field Emission Characteristics of Large-Area Films of Molybdenum Trioxide Microbelt

Dongmei Ban, Shaozhi Deng, Ningsheng Xu, Jun Chen, Juncong She, and Fei Liu

State Key Lab of Optoelectronic Materials and Technologies, Guangdong Province Key Lab of Display Material and Technology, School of Physics and Engineering, Sun Yat-sen University, Guangdong 510275, China

Correspondence should be addressed to Shaozhi Deng, stsdz@mail.sysu.edu.cn

Received 15 September 2009; Revised 11 November 2009; Accepted 27 November 2009

Academic Editor: Yanqiu Zhu

Copyright © 2010 Dongmei Ban et al. This is an open access article distributed under the Creative Commons Attribution License, which permits unrestricted use, distribution, and reproduction in any medium, provided the original work is properly cited.

We study the field emission characteristics of large-area films of crystalline MoO₃ microbelt grown on silicon substrate by thermal evaporation in air using a commercial infrared sintering furnace. It is found that their turn-on field, threshold field, resistance to microdischarge and field emission current stability are better than MoO₃ nanowires, MoO₃ nanobelts and MoO₃ nanoflower. In addition, good uniform distribution of field emission sites can be observed. The physical reasons are explained responsible for such improvements on field emission characteristics of MoO₃ material. These results indicate that large-area MoO₃ microbelts may be suitable for cold-cathode electron source application.

1. Introduction

Molybdenum trioxide, a wide-bandgap n-type semiconductor, has been studied as an interesting photochromic and electrochromic material with potential application in information display, sensor device, optoelectronic storage device, and smart window [1–12]. Recently, various forms of molybdenum trioxide nanostructure have been reported to exhibit attractive field characteristics, indicating their potential application as cold cathode electron emission material [13–16]. Molybdenum trioxide nanostructures can be produced under some conditions including solution method [17], hydrothermal method [13], and thermal evaporation [14–16]. The synthesis and the growth mechanism of MoO₃ nanostructures have been investigated [13–21]. Recently, we developed an approach to prepare a large-area film of MoO₃ nano/microstructures. With some degree of control, we were able to prepare large-area films of MoO₃ microbelts in air and on ITO glasses or silicon substrates at low temperature without catalyst. In particular, the MoO₃ microbelt films have been found to exhibit improved field emission characteristics as compared to those reported for various MoO₃ nanostructures [13–16]. Here we report these findings and the possible physical reasons.

2. Experimental

Our sample preparation procedure is as below. ITO glasses or silicon substrates were washed with acetone and then with alcohol in an ultrasonic cleaner. The whole growth process was carried out in a commercial infrared sintering furnace, which comprises 6 temperature zones and their temperatures can be set to have a value in a range from room temperature to 1000°C. In the present study, the temperature in different zones was set at 200°C, 200°C, 350°C, 700°C, 700°C, and 100°C, respectively. When the temperatures reached the set values, the substrates (size: 0.45 cm × 0.5 cm) and the quartz boat containing Mo powders were carried to the set zones by the transmission belt. With reference to Figure 1, the evaporation source was placed at the right-hand side of the 700°C zone and the three substrates were located at the positions with the separations between substrate and source of 27 cm, 32 cm, and 37 cm, respectively. In this arrangement, Sample 1 with separation 27 cm was in the 350°C zone, Sample 2 with separation of 32 cm in right hand side of the 350°C zone, and Sample 3 with separation of 37 cm in the 200°C zone. Thus, with reference to Figure 1, Samples 2 and 3 were in the regions where temperatures were below 350°C. The growth time was 60 minutes. Finally, all

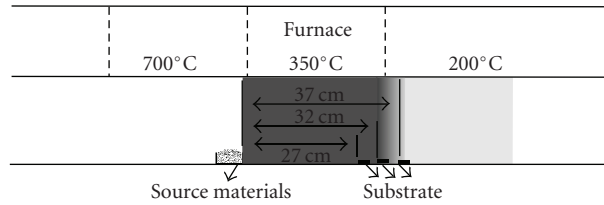
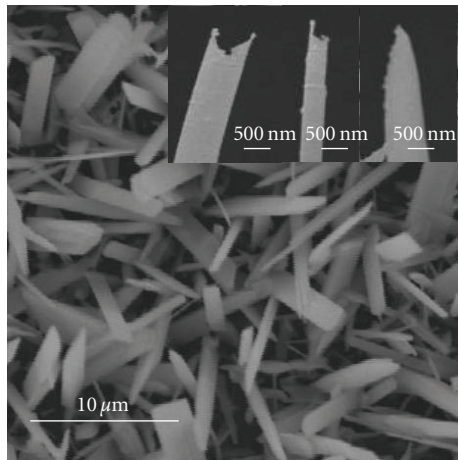
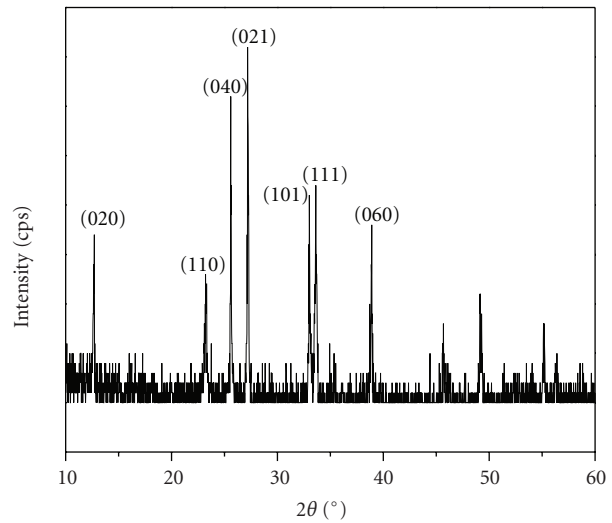


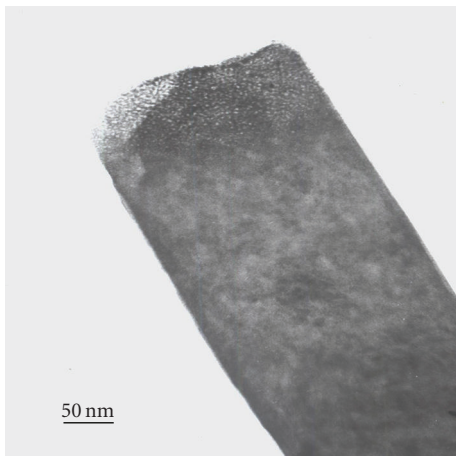
FIGURE 1: Schematic diagram showing how substrate and evaporation source are arranged inside the furnace.



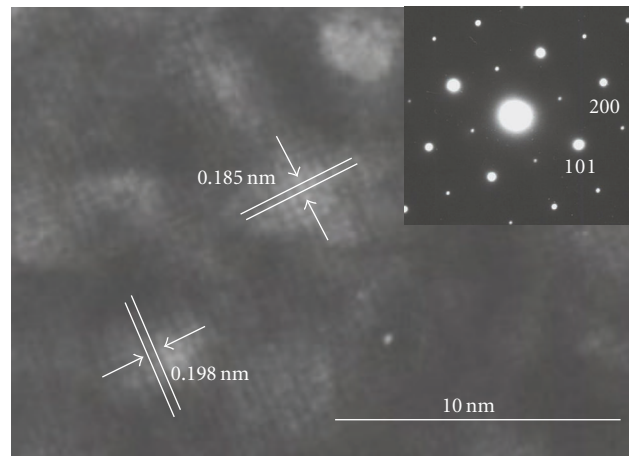
(a)



(b)



(c)



(d)

FIGURE 2: (a) The typical SEM image of the MoO_3 microbelts, the insets showing high resolution SEM images. (b) XRD spectra of the MoO_3 microbelts. (c) TEM image and (d) HRTEM image of a MoO_3 microbelt, the inset showing the corresponding SAED pattern.

the temperature zones were allowed to decrease gradually to room temperature. The substrates appeared white after deposition. The combination of the large area of each temperature zone ($35 \text{ cm} \times 30 \text{ cm}$) and uniformity in the temperature inside the zone may be very important to the development of a large-area film for device application.

3. Results and Discussion

The MoO_3 microbelts were characterized by using X-ray diffraction spectroscopy (D/max 2200 vpc apparatus with $\text{Cu K}\alpha$ radiation), scanning electron microscopy (SEM: Quanta 400 F), and high-resolution transmission

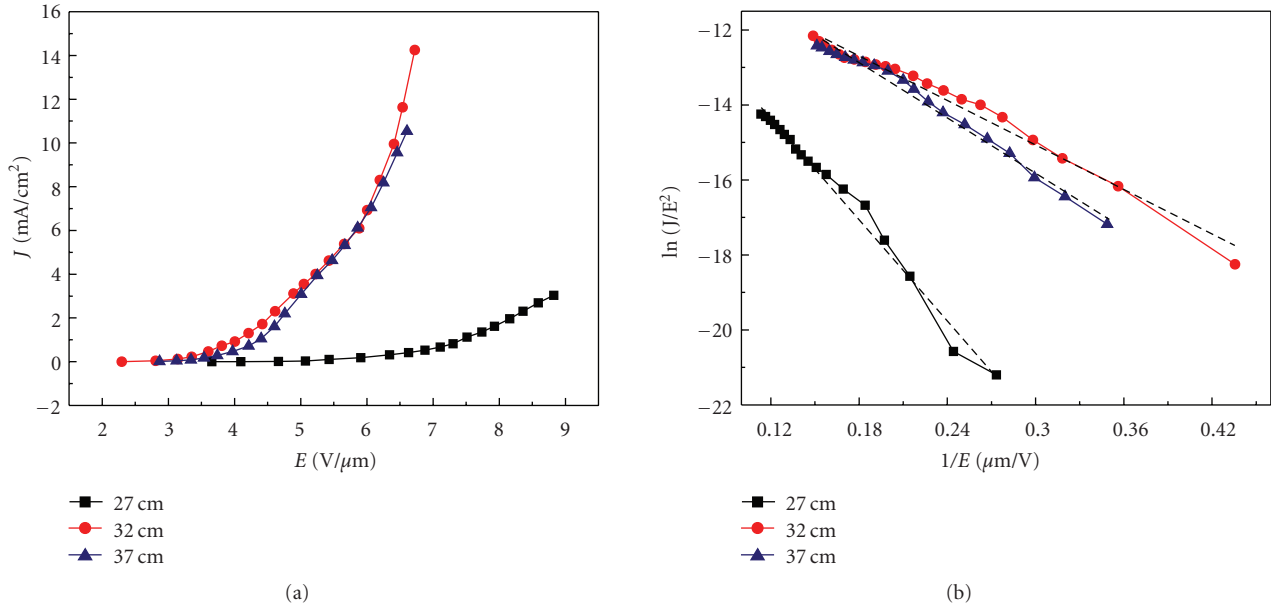


FIGURE 3: (a) The J - E plots of the MoO₃ microbelt films grown with different separations of substrate and evaporation source, (b) their corresponding F-N plots.

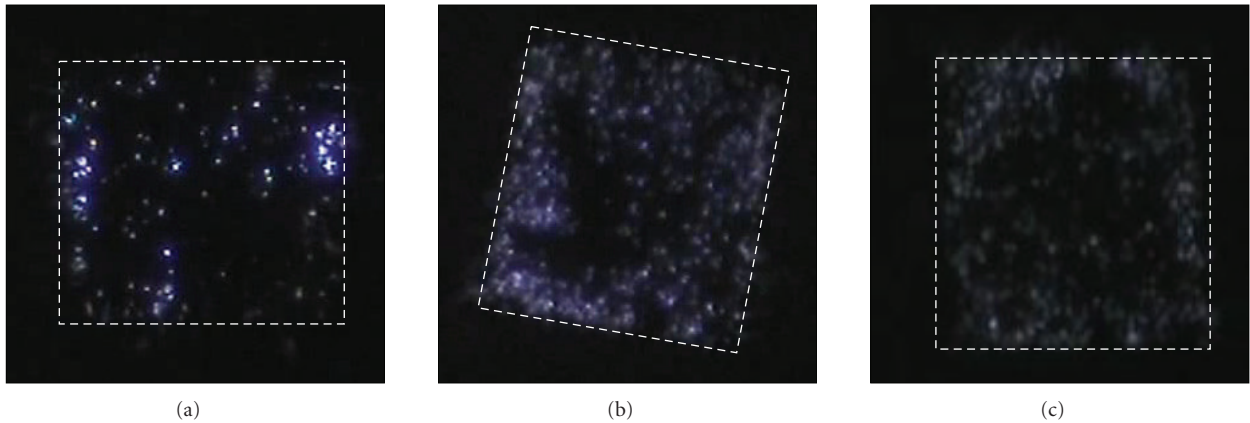


FIGURE 4: Optical images of the site distribution of the MoO₃ microbelt films grown with different separation of substrate and evaporation source: (a) 27 cm, (b) 32 cm, and (c) 37 cm under similar gap fields: (a) $E = 5.43$ V/ μ m, (b) $E = 5.43$ V/ μ m, (c) $E = 5.47$ V/ μ m, the corresponding substrate areas are 0.45 cm \times 0.5 cm, and 0.45 cm \times 0.5 cm and 0.45 cm \times 0.5 cm, respectively. (The sample area is indicated by the dashed line.)

electron microscopy (HRTEM: JEM-2010HR). The SEM image (Figure 2(a)) shows that the average width of MoO₃ microbelts is ~ 1 μ m and their length is up to 10 μ m. The microbelts are straight and their upper ends may be in the rectangular flat shape or have irregular one with sharp corners and nanotips as shown in the high resolution SEM images (insets of Figure 2(a)). The typical XRD pattern (Figure 2(b)) shows the diffraction peaks can be indexed to the orthorhombic structure MoO₃ with the lattice constants $a = 0.396$ nm, $b = 1.386$ nm, $c = 0.37$ nm (JCPDS: 5-0508). Figure 2(c) is the low-magnification TEM image of the MoO₃ microbelts. The high resolution TEM (HRTEM) image (Figure 2(d)) shows the two sets of parallel fringes with a spacing of 0.396 nm and 0.37 nm corresponding to

the (100) and (001) planes, respectively. The SAED patterns (inset of Figure 2(d)) shows that the entire microbelt is single crystalline with a growth direction of [001].

The field emission measurements of microbelts were carried out in a vacuum chamber of $\sim 5.0 \times 10^{-7}$ torr at room temperature. The substrate with microbelts was first adhered to the surface of an oxygen-free, high-conductivity copper disc. A transparent anode, consisting of a quartz plate 4 cm in diameter and coated with conducting indium doped tin oxide film, was placed in front of, and parallel to, the surface of the sample cathode. First, we investigated how the field emission characteristics of the MoO₃ microbelt film may be affected by the arrangement of substrate and evaporation source. Figure 3 shows J - E characteristics and

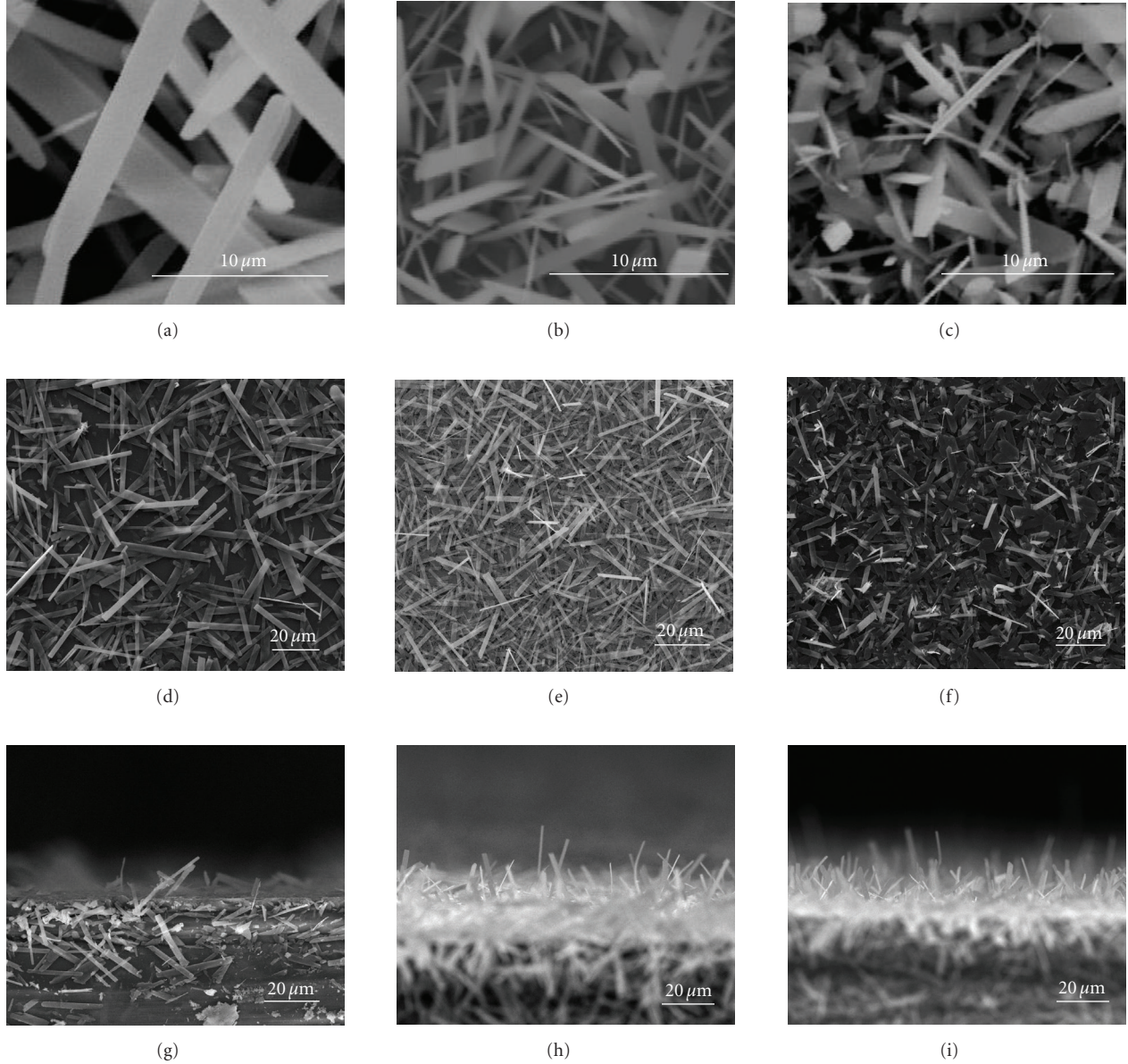


FIGURE 5: The typical SEM images (top view) of the MoO_3 microbelts with different separations between substrate and evaporation: (a), (d) 27 cm, (b) (e) 32 cm, (c), (f) 37 cm, the corresponding cross-section SEM images are in (g), (h) and (i), respectively.

the corresponding F-N plots of the three samples. Sample 1 has poor emission performance and Samples 2 and 3 show attractive characteristics. The turn-on fields (required to obtain field emission current of $10 \mu\text{A}/\text{cm}^2$) of Sample 1, 2, and 3 are 4.6, 2.6, and $3.0 \text{ V}/\mu\text{m}$, respectively, and the threshold fields (required to obtain field emission current of $10 \text{ mA}/\text{cm}^2$) of Samples 2 and 3 are 6.4 and $6.5 \text{ V}/\mu\text{m}$, respectively. Compared to the reports earlier, the best turn-on field of the film of MoO_3 microbelts ($2.6 \text{ V}/\mu\text{m}$) is lower than that of the MoO_3 nanowires ($3.5 \text{ V}/\mu\text{m}$) [14, 15], nanobelt ($8.7 \text{ V}/\mu\text{m}$) [16], and nanoflower ($4.3 \text{ V}/\mu\text{m}$) [13]. This result indicates that the MoO_3 microbelt is a good candidate as cold-cathode material. The good field emission properties of the samples may be attributed to a number of factors, and the first may be the field enhancement effect. The

values of field enhancement factor β of the microbelt samples were calculated by using the F-N formulation [22]

$$S_{\text{FN}} = \frac{d(\ln(J/E^2))}{d(1/E)} = -\frac{6.53 \times 10^9 \phi^{3/2}}{\beta}, \quad (1)$$

where ϕ is the work function of the molybdenum trioxide, S_{FN} is the slope of the F-N plot. The value of the β factor may be derived by using the above expression provided that ϕ is constant. In the calculation, the work function of MoO_3 , $\phi = 5.4 \text{ eV}$ [23], is used. From the F-N plots, we obtain that the values of field enhancement factor β for Samples 1, 2, and 3 are 1822, 4165 and 3861, respectively. The β -value of Sample 1 is much smaller than that of the other two samples. Figure 4 shows the optical images of emission

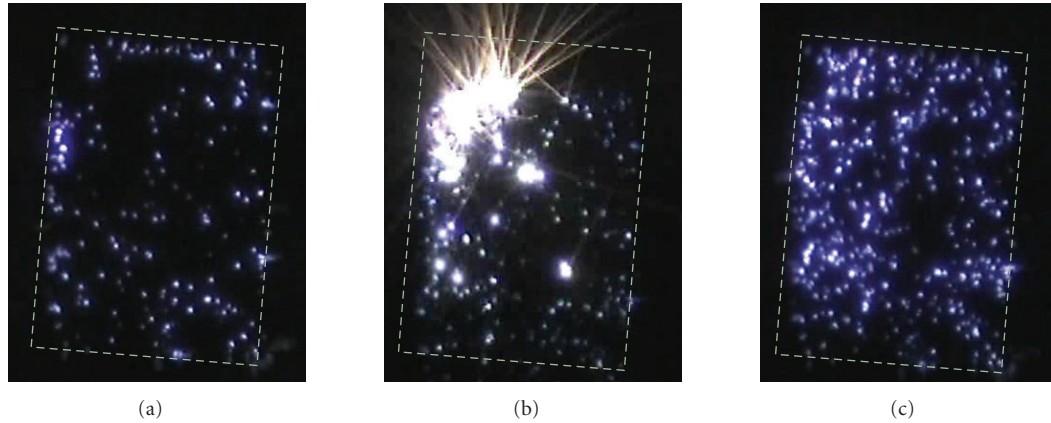


FIGURE 6: The optical images of the site distribution of the MoO_3 microbelts film ($0.5 \text{ cm} \times 0.7 \text{ cm}$) taken under different gap fields: (a) $E = 5.38 \text{ V}/\mu\text{m}$, (b) $E = 5.55 \text{ V}/\mu\text{m}$, (c) $E = 5.82 \text{ V}/\mu\text{m}$. (The sample area is indicated by the dashed line.)

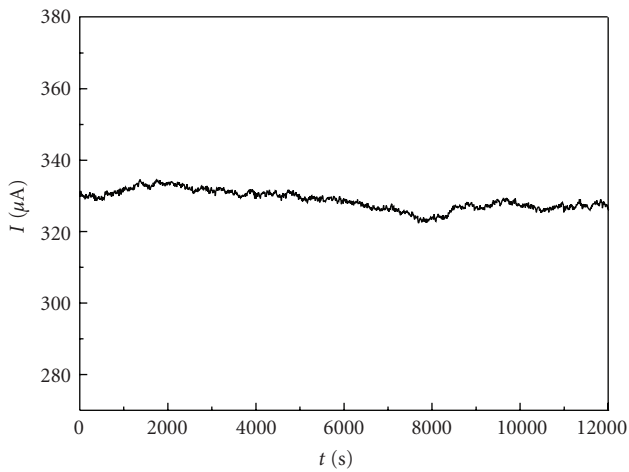


FIGURE 7: The curve of field emission current versus time, showing good stability of field emission of the MoO_3 microbelt film.

site distribution recorded using transparent anode, and it is found that the emission sites of Samples 2 and 3 are distributed over the entire sample surface, while for Sample 1 the number of emission sites and their intensity are relatively low. These differences and similarity may be explained by the observed morphology features of the samples as seen under scanning electron microscope. The top-down SEM images (Figures 5(a) to 5(f)) show that the averaged length of the MoO_3 microbelts of Sample 1 (Figures 5(a) and 5(d)) is longest compared to that of the other two samples (Figures 5(b), 5(c), 5(e) and 5(f)), but the corresponding cross-section image (Figure 5(g)) shows that it grows leaning to the substrate, which is not useful to the field enhancement. On contrary, the orientation of the MoO_3 microbelts of Samples 2 and 3 (Figures 5(h) and 5(i)) is almost vertical to the substrate surface; this can enhance the field at the top ends of these vertically aligned microbelts, and thus strong emission from the apexes of these microbelts may be expected. Thus, these two samples have large β -values. This observation is in consistency with earlier findings that have revealed

that vertically aligned nanowires have better field emission properties because of higher field enhancement at the end of each nanowire [14, 24].

As to the difference between the orientations of the microbelts of Sample 1 and Samples 2 and 3, a brief explanation is given below. Because of thermal radiation, the closer the substrate to the evaporation source is, the higher temperature the substrate is. When the temperature of the substrate is higher, the nucleation for microbelt growth is more difficult in comparison with a lower temperature one. Thus, the density of microbelts is lower for high temperature substrate, and when is too low, microbelts cannot support each other, so they cannot grow vertically to the substrate surface. This can explain why microbelts of Sample 1 grew leaning to the substrate, which was placed at the position less than 27 cm to the source, and was much closer to the source compared to Samples 2 and 3.

Additionally, we should like to explain why the calculated β -values are so large. We believe that this is not all contributed by the geometrical field enhancement. Other factors may be responsible to this, such as reduction in surface potential barrier for field emission or hot electron emission [22]. These are highly possible for field emission from semiconductors such as MoO_3 . If these are the cases, we may have to replace the value of ϕ with a more realistic value that reflects the lowering of the surface potential barrier in the calculation using the F-N formulation. This reduction in the value of ϕ can significantly decrease the β -value. But all these have to be confirmed by further experiments.

Second, using samples grown under the similar conditions described above with separation 32 cm, we found that the films of MoO_3 microbelts are resistant to the effects of local microdischarge event. Figure 6 shows three optical images of emission site distributions of one sample taken under three gap field conditions. One may see that after the local microdischarge events (Figure 6(b)), the emission sites distribution was not obviously changed, by comparing Figures 6(a) and 6(c).

Finally, we observed stable emission of the films over 3 hours time duration. The typical field emission I - t curve is

shown in Figure 7. No significant decrease of current was observed and the fluctuation is about 2% at a constant electric field of $4.47\text{ V}/\mu\text{m}$ for an average emission current of $330\ \mu\text{A}$.

4. Conclusion

In summary, we have demonstrated that large-area films of crystalline MoO_3 microbelts may be grown on ITO glasses or silicon substrates by thermal evaporation in air using a commercial infrared sintering furnace. Their typical turn-on field as low as $2.6\text{ V}/\mu\text{m}$ and threshold field of $6.4\text{ V}/\mu\text{m}$ are superior to the values reported for MoO_3 nanostructures. Their field emission performance may be affected by the orientation of the MoO_3 microbelts; the microbelts vertical to the substrate have a better field emission property. In addition, the good uniform distribution of emission sites on large-area samples is also observed. Finally, the MoO_3 microbelts show good field emission current stability over time.

Acknowledgment

The authors gratefully acknowledge the financial support of the project from the National Natural Science Foundation of China (Grant nos. U0634002, 50725206, 60571035, and 50672135), Science and Technology Ministry of China (National Basic Research Program of China: Grant nos. 2003CB314701, 2007CB935501 and 2008AA03A314), the Science and Technology Department of Guangdong Province, the Department of Information Industry of Guangdong Province, and the Science and Technology Department of Guangzhou City.

References

- [1] E. Comini, L. Yubao, Y. Brando, and G. Sberveglieri, "Gas sensing properties of MoO_3 nanorods to CO and CH_3OH ," *Chemical Physics Letters*, vol. 407, no. 4-6, pp. 368-371, 2005.
- [2] A. M. Taurino, A. Forleo, L. Francioso, P. Siciliano, M. Stalder, and R. Nesper, "Synthesis, electrical characterization, and gas sensing properties of molybdenum oxide nanorods," *Applied Physics Letters*, vol. 88, no. 15, Article ID 152111, 3 pages, 2006.
- [3] Z. Hussain, "Optical and electrochromic properties of heated and annealed MoO_3 thin films," *Journal of Materials Research*, vol. 16, no. 9, pp. 2695-2708, 2001.
- [4] H. C. Zeng, "Chemical etching of molybdenum trioxide: a new tailor-made synthesis of MoO_3 catalysts," *Inorganic Chemistry*, vol. 37, no. 8, pp. 1967-1973, 1998.
- [5] J. N. Yao, K. Hashimoto, and A. Fujishima, "Photochromism induced in an electrolytically pretreated MoO_3 thin film by visible light," *Nature*, vol. 355, no. 6361, pp. 624-626, 1992.
- [6] J. N. Yao, Y. A. Yang, and B. H. Loo, "Enhancement of photochromism and electrochromism in MoO_3/Au and MoO_3/Pt thin films," *Journal of Physical Chemistry B*, vol. 102, no. 11, pp. 1856-1860, 1998.
- [7] Y. A. Yang, Y. W. Cao, B. H. Loo, and J. N. Yao, "Microstructures of electrochromic MoO_3 thin films colored by injection of different cations," *Journal of Physical Chemistry B*, vol. 102, no. 47, pp. 9392-9396, 1998.
- [8] K. Shao, Y. Ma, Y. A. Cao, Z. H. Chen, X. H. Ji, and J. N. Yao, "Inclusion of poly(tetramethyl-*p*-phenyl-enediamine dihydrochloride) into MoO_3 : a cooperative formation route to construct a polymer/ MoO_3 layered structure," *Chemistry of Materials*, vol. 13, no. 2, pp. 250-252, 2001.
- [9] P. Pichat, M. N. Mozzanega, and C. Hoang-Van, "Room temperature photoassisted formation of hydrogen-molybdenum bronzes with an alcohol as a hydrogen source," *Journal of Physical Chemistry*, vol. 92, no. 2, pp. 467-470, 1988.
- [10] C. Bechinger, S. Ferrere, A. Zaban, J. Sprague, and B. A. Gregg, "Photoelectrochromic windows and displays," *Nature*, vol. 383, no. 6601, pp. 608-610, 1996.
- [11] G. Laperrière, M. A. Lavoie, and D. Bélanger, "Electrochromic behavior of molybdenum trioxide thin films, prepared by thermal oxidation of electrodeposited molybdenum trisulfide, in mixtures of nonaqueous and aqueous electrolytes," *Journal of the Electrochemical Society*, vol. 143, no. 10, pp. 3109-3117, 1996.
- [12] T. Maruyama and T. Kanagawa, "Electrochromic properties of molybdenum trioxide thin films prepared by chemical vapor deposition," *Journal of the Electrochemical Society*, vol. 142, no. 5, pp. 1644-1647, 1995.
- [13] G. Wei, W. Qin, D. Zhang, et al., "Synthesis and field emission of MoO_3 nanoflowers by a microwave hydrothermal route," *Journal of Alloys and Compounds*, vol. 481, no. 1-2, pp. 417-421, 2009.
- [14] J. Zhou, S. Z. Deng, N. S. Xu, J. Chen, and J. C. She, "Synthesis and field-emission properties of aligned MoO_3 nanowires," *Applied Physics Letters*, vol. 83, no. 13, pp. 2653-2655, 2003.
- [15] J. Zhou, N. S. Xu, S. Z. Deng, J. Chen, J. C. She, and Z. L. Wang, "Large-area nanowire arrays of molybdenum and molybdenum oxides: synthesis and field emission properties," *Advanced Materials*, vol. 15, no. 21, pp. 1835-1840, 2003.
- [16] Y. B. Li, Y. Bando, D. Golberg, and K. Kurashima, "Field emission from MoO_3 nanobelts," *Applied Physics Letters*, vol. 81, no. 26, pp. 5048-5050, 2002.
- [17] X. L. Li, J. F. Liu, and Y. D. Li, "Low-temperature synthesis of large-scale single-crystal molybdenum trioxide (MoO_3) nanobelts," *Applied Physics Letters*, vol. 81, no. 25, pp. 4832-4834, 2002.
- [18] L. Jiao, H. Yuan, Y. Si, Y. Wang, M. Zhao, and Y. Wang, "A novel method for synthesis of microstructure MoO_3 ," *Materials Letters*, vol. 59, no. 24-25, pp. 3112-3114, 2005.
- [19] G. Li, L. Jiang, S. Pang, H. Peng, and Z. Zhang, "Molybdenum trioxide nanostructures: the evolution from helical nanosheets to crosslike nanoflowers to nanobelts," *Journal of Physical Chemistry B*, vol. 110, no. 48, pp. 24472-24475, 2006.
- [20] G. Wang, Y. Ji, L. Zhang, Y. Zhu, P. I. Gouma, and M. Dudley, "Synthesis of molybdenum oxide nanoplatelets during crystallization of the precursor gel from its hybrid nanocomposites," *Chemistry of Materials*, vol. 19, no. 5, pp. 979-981, 2007.
- [21] I. Navas, R. Vinodkumar, K. J. Lethy, et al., "Growth and characterization of molybdenum oxide nanorods by RF magnetron sputtering and subsequent annealing," *Journal of Physics D*, vol. 42, no. 17, Article ID 175305, 8 pages, 2009.
- [22] N. S. Xu, *High Voltage Vacuum Insulator: Basic Concepts and Technological Practice*, edited by R. V. Latham, chapter 4, Academic, London, UK, 1995.
- [23] J. Cao, X. Jiang, and Z. Zhang, " MoO_x modified Ag anode for top-emitting organic light-emitting devices," *Applied Physics Letters*, vol. 89, no. 25, Article ID 252108, 3 pages, 2006.
- [24] Q. B. Wu, S. Ren, S. Z. Deng, J. Chen, and N. S. Xu, "Growth of aligned Cu_2S nanowire arrays with AAO template and their field-emission properties," *Journal of Vacuum Science and Technology B*, vol. 22, no. 3, pp. 1282-1285, 2004.

Research Article

Determination of X-Ray Diffraction on the Phase Transformation of Microwave-Assisted Titanate Nanotubes during Thermal Treatment

Hsin-Hung Ou, Ching-Hui Liao, and Shang-Lien Lo

Research Center for Environmental Pollution Prevention and Control Technology, Graduate Institute of Environmental Engineering, National Taiwan University, 71 Chou-Shan Rd., Taipei 106, Taiwan

Correspondence should be addressed to Shang-Lien Lo, sllo@ntu.edu.tw

Received 26 November 2009; Revised 20 April 2010; Accepted 21 April 2010

Academic Editor: Renzhi Ma

Copyright © 2010 Hsin-Hung Ou et al. This is an open access article distributed under the Creative Commons Attribution License, which permits unrestricted use, distribution, and reproduction in any medium, provided the original work is properly cited.

Based on the determination of X-ray powder diffraction, this study aims to investigate the thermal effect on the phase transformation of microwave-assisted titanate nanotubes (MTNTs). The phase transformation is highly dependent on the intercalating amount of Na(I) within MTNTs and on the heating atmosphere. In other words, the presence of Na(I) favors the transformation of TNTs phase into $\text{Na}_2\text{Ti}_6\text{O}_{13}$ whereas anatase phase selectively formed in the case of MTNTs with less Na(I) amount. Furthermore, H_2 versus O_2 is able to form anatase phase and establish a newly transformation pathway. The photocatalytic ability of the calcined MTNTs was also evaluated based on the observed rate constant of trichloroethylene degradation. In addition to anatase phase, the newly phase including $\text{Na}_2\text{Ti}_6\text{O}_{13}$ and Ti_2O_3 with calcined MTNTs is able to photocatalyze trichloroethylene. MTNTs calcined with the presence of H_2 also exhibit a superior photocatalytic performance to P25 TiO_2 .

1. Introduction

Titanate nanotubes (TNTs) have received engrossing interests owing to the vast applications including solar cells, photocatalysis, and electroluminescent hybrid device [1–5]. An overview regarding the fabrication, characterization, and application of TNTs was also demonstrated in [6]. In spite of the debate on the formation mechanism and chemical structure of TNTs, the application of TNT or even its derivatives (nanoparticles and nanorods) on the photocatalytic field has been emerging [3–5]. Several studies have reported that TNTs without further treatment have no powerful photocatalytic ability [3, 4, 7]. Tsai and Teng [3] indicated that the thermal-treated TNTs versus P25 TiO_2 exhibited a better performance on NO conversion. Similar result was indicated by Yu et al. [4] in terms of the microstructure of calcined TNTs. Furthermore, Štengl et al. [7] investigated the preparation, microstructure characterization, and photocatalytic activity of sodium titanate nanorods which were fabricated by using TNTs as materials. The single-crystalline TiO_2 nanorods with highly activity and long-term stability have also been demonstrated in [8].

Our previous reports have characterized microwave-assisted TNTs (MTNTs) whose chemical structure was preferentially assigned for $\text{Na}_x\text{H}_{2-x}\text{Ti}_3\text{O}_7$ [5, 9]. The intercalation amount of Na(I) within MTNTs increases with enhancing applied level of irradiation powers during fabrication process [9]. The photocatalytic oxidation of aqueous ammonia over microwave-induced MTNTs was also examined recently in [5]. A specific degradation mechanism of photocatalytic ammonia over MTNTs was also proposed that the reaction of photocatalytic ammonia was not suffered from shielding effect. In the present study, the thermal effects including calcination temperature and atmosphere on the phase transformation of MTNTs were examined. The photocatalytic ability of calcined MTNTs towards gaseous trichloroethylene (TCE) degradation was also investigated.

2. Experimental Section

2.1. Preparation and Thermal Treatment of MTNTs. The fabrication of MTNTs is described in detail elsewhere in our previous studies in [5, 9]. In a typical process, the microwave digestion system (Ethos Touch Control,

MILESTONE Corporation) with a double-walled consists of an inner Teflon liner and outer shell of high strength Ultem polyetherimide, was used. The applied temperature, power level, as well as treatment time, are programmable with an integrated computer. The slurry containing 0.6 g P25 TiO₂ and 70 mL 10 N NaOH was treated at 130°C for 3 hours under different microwave irradiation powers of 70, 400, and 700 W which are abbreviated as MTNTs-70 W, MTNTs-400 W, and MTNTs-700 W, respectively. After microwave thermal treatment, the resulting powders were washed by 0.5 N HCl until the pH of slurry achieved 7. The resulting powders were subsequently washed by deionized water repeatedly to remove the excess of HCl adhered on the surface of MTNTs. MTNTs were subsequently obtained after the filtration and dried under the vacuum freeze dried for 20 hours (-56°C; 100~200 Mtorr). Regarding the thermal treatment of TNTs, the experiments were conducted in the tubular oven under the atmospheres of 20% O₂/80% N₂ and 20% H₂/80% N₂ at the progressively elevated temperatures for 3 hours (100, 300, 500, and 700°C). The ramping rate was controlled at 2°C/min. The following powders subsequently cooled down to room temperature and were characterized by phase determinations.

2.2. XRPD Determinations of MTNTs. The X-ray powder diffractometer (XRPD) was employed to determine the crystalline phases of MTNTs after thermal treatment. The patterns were recorded from 5 to 70° with a scan rate of 2°/min by Philips X' Pert Pro MPD which was equipped with a CuK α X-ray source ($\lambda = 1.5405 \text{ \AA}$) operating under a voltage of 40 kV and a current of 30 mA, respectively.

2.3. Photocatalytic Oxidation of TCE over MTNTs. Batch experiments of photocatalytic TCE over MTNTs were conducted in a flat-plate photoreactor, which has been described in detail in our previous publication [10]. MTNTs sample was coated on a silica board with the normalized concentration of 0.83 mg/cm². The as-prepared photocatalyst was deposited on the bottom of the reactor without further treatment. The initial concentration of TCE was prepared at $70 \pm 2.5 \mu\text{M}$, and the initial relative humidity and oxygen concentration were controlled at $25 \pm 2.5\%$ and 3.53 mM, respectively. Illumination provided by three 8W black-light fluorescent lamps principally emits at 365 nm with the light intensity of $2.34 \pm 0.23 \text{ mW/cm}^2$. The concentration of TCE, under a series of time sequence during photocatalytic experiments, was quantified via the manual injection into the gas chromatograph (5890II) equipped with the flame ionization detector. The photocatalytic ability of TNTs was quantitatively evaluated by the corresponding observed rate constants (k_{obs}) of TCE degradation.

3. Results and Discussion

3.1. XRD Determinations on the MTNTs after Thermal Treatment. XRPD determination was used to investigate the phase of MTNTs after calcination at increasing temperatures (100~700°C) under the atmosphere of either O₂ or H₂. In

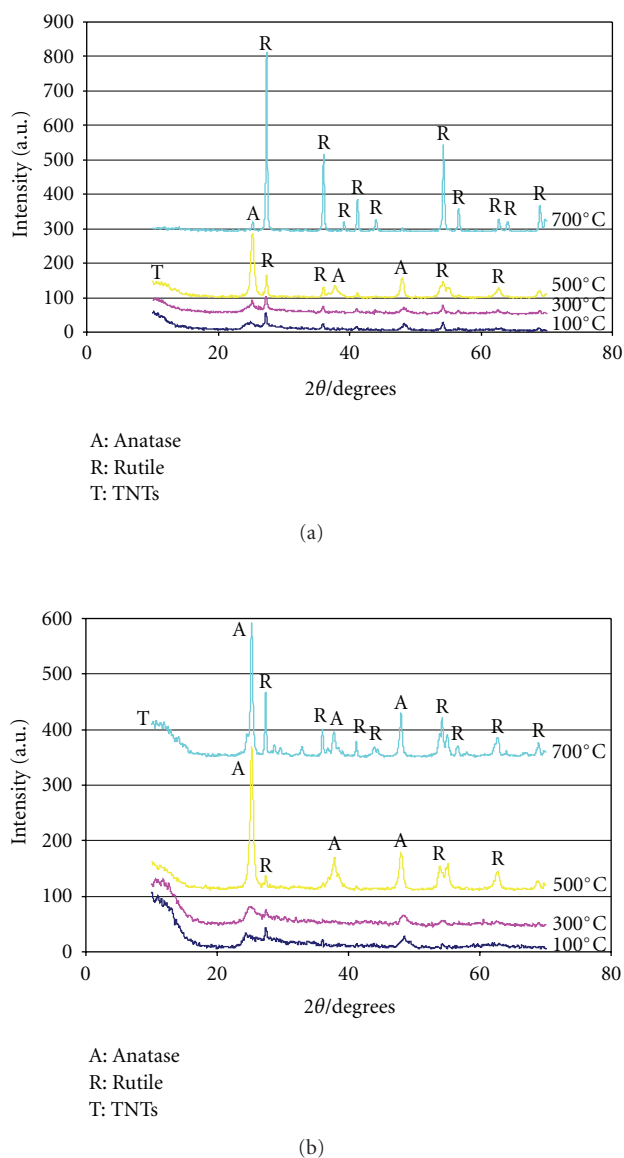


FIGURE 1: XRPD patterns of MTNTs-70W calcined at elevated temperatures under the atmosphere of (a) 20% O₂/80% N₂ and (b) 20% H₂/80% N₂.

the following materials, samples indexed as MTNTs_{X-Y}°C represent MTNTs calcined at Y°C under X atmosphere. Figures 1–3 show the dependence of phase change of MTNTs on the heating temperature and atmosphere. Either in the presence of O₂ and H₂, no appreciable change of MTNTs phase was observed as the heating temperature was lower than 300°C. In addition, an interesting phenomenon was observed that the phase transformation of MTNTs-70W begins at 500°C whereas no phase change was observed for MTNTs-700W calcined at the same temperature. According to our previous report [5, 9], a high level of microwave irradiation during fabrication process favors the intercalation of Na(I) into MTNTs. In other words, the intercalated Na(I) is advantageous to the stability of MTNTs during thermal treatment.

As for MTNTs-70W, anatase phase dominates for either MTNTs-70W_{O₂-500°C} (Figure 1(a)) or MTNTs-70W_{H₂-500°C} (Figure 1(b)), and an increasing temperature results in the transformation of anatase phase into rutile phase (TNTs-70W_{H₂-700°C} and MTNTs-70W_{O₂-700°C}). TNTs-70W_{H₂-700°C} versus MTNTs-70W_{O₂-700°C} exhibits a stronger intensity of the anatase phase, suggesting that H₂ is beneficial to maintain anatase phase. In the case of MTNTs-400W (Figure 2), anatase phase along with a trace amount of rutile phase exists in MTNTs-400W_{O₂-500°C} and an increase in temperature to 700°C results in the formation of Na₂Ti₆O₁₃ at the expense of anatase phase (Figure 2(a)). Comparatively, TNTs phase still dominates at MTNTs-400W_{H₂-500°C} whereas TNTs-400W_{H₂-700°C} presents the relatively significant anatase, rutile, and Na₂Ti₆O₁₃ phase (Figure 2(b)). This result not only corresponds to the aforementioned conclusion in that H₂ helps to establish anatase phase within MTNTs but also indicates that O₂ provides the prevailing ability to transform TNTs phase. Regarding the phase transformation of TNTs-700W, Na₂Ti₆O₁₃ is the predominant phase in MTNTs-700W_{O₂-700°C} (Figure 3(a)) whereas Ti₂O₃ and Na₂Ti₆O₁₃ with trace anatase phase appear in the TNTs-700W_{H₂-700°C} (Figure 3(b)). These results reveal that the presence of H₂ leads to a selective transformation pathway as MTNTs was intercalated with abounding amount of Na(I).

Usually, for pure anatase TiO₂ samples, the rutile phase starts to appear at ca. 700°C [11]. Tsai and Teng [3] have also indicated that the rutile phase arose at 900°C as far as the traditional TNTs are concerned. In our study, rutile phase can be observed as MTNTs were treated at 500°C under O₂ atmosphere (Figure 1(a)), which suggests that [TiO₆] octahedra are easy to be transformed. This result can be ascribed to the application of microwave irradiation during fabrication process of MTNTs. Furthermore, the appearance of Na₂Ti₆O₁₃ can be derived from the dehydration of Na_xTi_{2-x}Ti₂O₅ (H₂O) and is found to be more abundant for TNTs washed and suspended under more basic conditions, that is, more Na(I) was intercalated into TNTs [12, 13]. The demonstration in our result is consistent to the results of above researches and again confirms that the applied microwave irradiation favors the intercalation of Na(I) into MTNTs structure.

3.2. Photocatalytic Oxidation of Gaseous TCE over MTNTs.

Figure 4 demonstrates the dependence of k_{obs} on the heating temperature and atmosphere. No TCE degraded over MTNTs without thermal treatment, suggesting that MTNTs have no powerful ability to TCE degradation. This result corresponds to the XRPD determination that anatase phase, a major crystalline phase responsible for organic degradation, arose at the heating temperature higher than 300°C. As for MTNTs-70W_{O₂} and MTNTs-400W_{O₂} (Figure 4(a)), k_{obs} increase with increasing calcination temperature until 500°C. A further increase in heating temperature to 700°C results in a decrease in k_{obs} . The phenomenon can be ascribed to the absence or low crystallization of anatase phase as MTNTs calcined at 700°C. Na₂Ti₆O₁₃ phase appearing in MTNTs-700W_{O₂-700°C} is also effective to the degradation

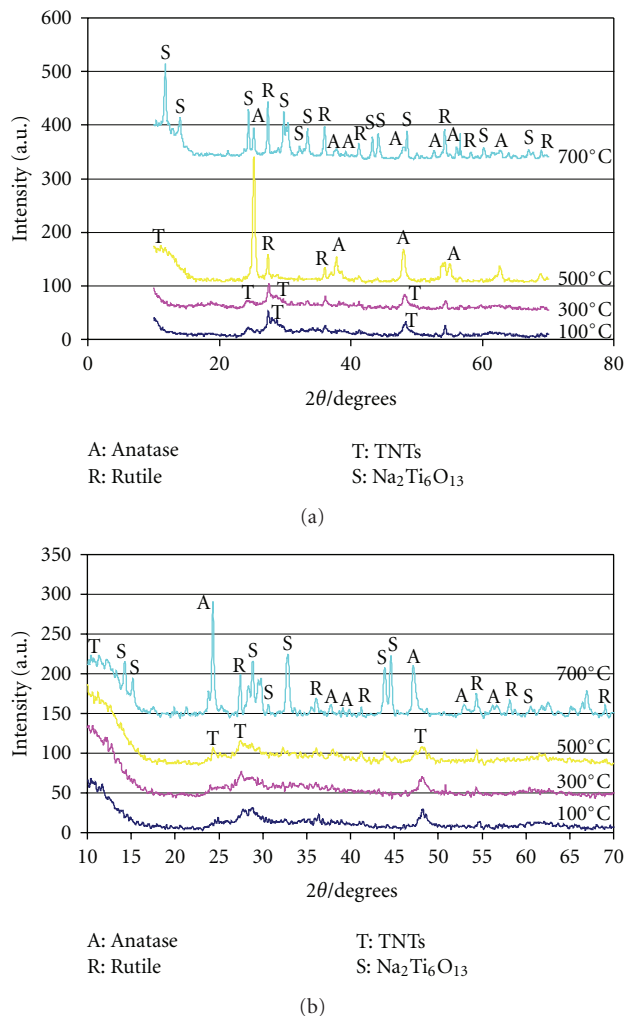
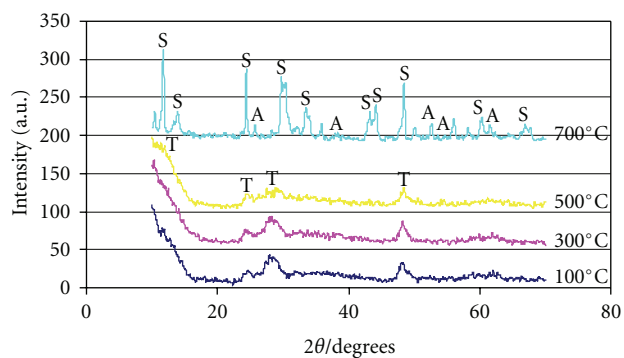


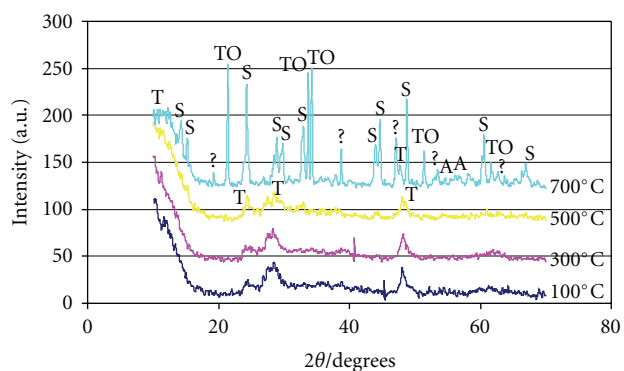
FIGURE 2: XRPD patterns of MTNTs-400W calcined at elevated temperatures under the atmosphere of (a) 20% O₂/80% N₂ and (b) 20% H₂/80% N₂.

of TCE despite the k_{obs} value ($0.74 \pm 0.15 \text{ min}^{-1}$) is not excellent. The photocatalytic ability of Na₂Ti₆O₁₃ can be attributed to the corresponding tunnel structure, which provides a number of active sites and has a significant effect on the efficiency of separation of the irradiated generated photos [14, 15]. Regarding the MTNTs calcined under H₂ atmosphere (Figure 4(b)), k_{obs} increase with an increase in calcination temperature no matter which type of MTNTs was investigated. An interesting result was also noticed that TNTs-700W_{H₂-700°C} without the presence of anatase phase has k_{obs} of $3.29 \pm 0.27 \text{ min}^{-1}$ (Figure 4(b)). In other words, Ti₂O₃ and Na₂Ti₆O₁₃ are able to photocatalyze TCE. Most significantly, MTNTs-70W_{H₂-700°C} and MTNTs-400W_{H₂-700°C} present superior performances to that P25 catalysts ($6.63 \pm 0.18 \text{ min}^{-1}$) do. This result may attribute to the different pore structure, exhibited crystal phase of TNTs samples. Further experiments on the pore size distribution of MTNTs after thermal treatment are under investigation.



A: Anatase
T: TNTs
S: $\text{Na}_2\text{Ti}_6\text{O}_{13}$

(a)

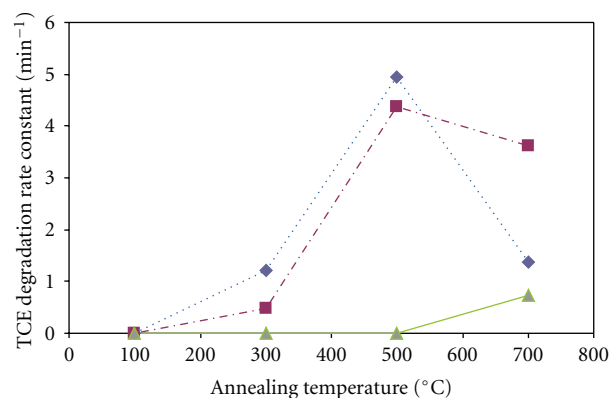


A: Anatase
T: TNTs
S: $\text{Na}_2\text{Ti}_6\text{O}_{13}$
TO: Ti_2O_3

(b)

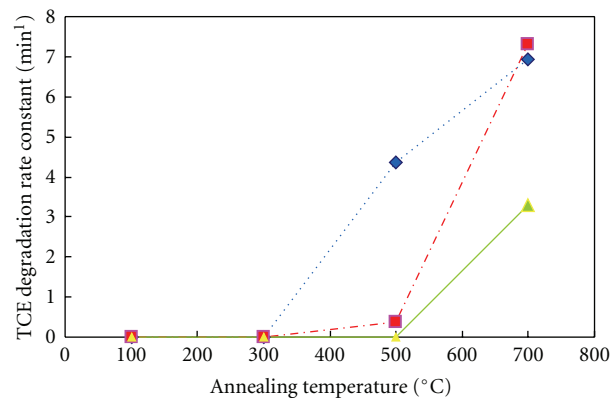
FIGURE 3: XRPD patterns of MTNTs-700W calcined at elevated temperatures under the atmosphere of (a) 20% $\text{O}_2/80\%$ N_2 and (b) 20% $\text{H}_2/80\%$ N_2 .

In addition to the contribution of anatase phase in the photocatalytic reaction, the photocatalytic ability can be attributed to the well-known interparticle electron process (IPET process) [16, 17]. The band gaps between two coupled semiconductors/crystal phases establish a selective pathway for irradiated electrons to migrate. This candidate pathway is able to result in an efficient separation between irradiated photoholes and photoelectrons. Therefore, more hydroxyl radicals ($\text{OH}\cdot$) are expected to produce with IPET process. This effect can be evidenced in terms of the comparison of k_{obs} between $\text{MTNTs-70W}_{\text{H}_2-500^\circ\text{C}}$ and $\text{MTNTs-70W}_{\text{H}_2-700^\circ\text{C}}$. $\text{MTNTs-70W}_{\text{H}_2-500^\circ\text{C}}$ and $\text{MTNTs-70W}_{\text{H}_2-700^\circ\text{C}}$ exhibit a comparative intensity of anatase phase (Figure 1(b)) but the degradation of TCE is better for $\text{TNTs-70W}_{\text{H}_2-700^\circ\text{C}}$ versus $\text{TNTs-70W}_{\text{H}_2-500^\circ\text{C}}$. This is owing to the coexistence of anatase and rutile phases in $\text{TNTs-70W}_{\text{H}_2-700^\circ\text{C}}$ whereas only anatase phase was observed in $\text{TNTs-70W}_{\text{H}_2-500^\circ\text{C}}$. The same result was found between the cases of $\text{TNTs-70W}_{\text{H}_2-700^\circ\text{C}}$ and $\text{TNTs-400W}_{\text{H}_2-700^\circ\text{C}}$ that $\text{TNTs-400W}_{\text{H}_2-700^\circ\text{C}}$ exhibits diversified phases including



◆ 70 W
■ 400 W
▲ 700 W

(a)



◆ 70 W
■ 400 W
▲ 700 W

(b)

FIGURE 4: The dependence of k_{obs} on the MTNTs calcined at the progressively temperatures (25~700°C) under the atmospheres of 20% $\text{O}_2/80\%$ N_2 and (b) 20% $\text{H}_2/80\%$ N_2 .

anatase, rutile, and $\text{Na}_2\text{Ti}_6\text{O}_{13}$ (Figure 2(b)). However, despite $\text{TNTs-700W}_{\text{H}_2-700^\circ\text{C}}$ includes four crystal types, the contribution of IPET process is not manifested since the prevailing oxidant phase (anatase phase) is weak (Figure 3(b)).

4. Conclusions

MTNTs with less amount of Na(I) prefer to form anatase phase after thermal treatment. In contrast, $\text{Na}_2\text{Ti}_6\text{O}_{13}$ is a predominant phase as MTNTs with abounding amount of Na(I) was thermally treated. The presence of H_2 during thermal treatment establishes a selective crystalline pathway in which Ti_2O_3 phase forms for MTNTs with abounding amount of Na(I). Regarding the TCE degradation over MTNTs, both the presence of anatase phase and IPET process contribute to the TCE degradation. Despite not all calcined

MTNTs are superior to commercial P25 TiO₂ in TCE degradation, MTNTs fabricated via microwave hydrothermal process exhibit a well-defined behavior during thermal treatment. We are confident that some insight into the nature and behavior of MTNTs during thermal treatment can be useful for designing some novel catalysts.

Acknowledgment

The authors would like to thank the National Science Council of the Republic of China for financially supporting this research under Contract no. NSC 95-2221-E-002-143-MY3.

References

- [1] L. Yu and X. Zhang, "Hydrothermal synthesis and characterization of vanadium oxide/titanate composite nanorods," *Materials Chemistry and Physics*, vol. 87, no. 1, pp. 168–172, 2004.
- [2] R. Dominko, E. Baudrin, P. Umek, D. Arçon, M. Gaberšček, and J. Jamnik, "Reversible lithium insertion into Na₂Ti₆O₁₃ structure," *Electrochemistry Communications*, vol. 8, no. 4, pp. 673–677, 2006.
- [3] C.-C. Tsai and H. Teng, "Regulation of the physical characteristics of titania nanotube aggregates synthesized from hydrothermal treatment," *Chemistry of Materials*, vol. 16, no. 22, pp. 4352–4358, 2004.
- [4] J. Yu, H. Yu, B. Cheng, and C. Trapalis, "Effects of calcination temperature on the microstructures and photocatalytic activity of titanate nanotubes," *Journal of Molecular Catalysis A*, vol. 249, no. 1-2, pp. 135–142, 2006.
- [5] H.-H. Ou, C.-H. Liao, Y.-H. Liou, J.-H. Hong, and S.-L. Lo, "Photocatalytic oxidation of aqueous ammonia over microwave-induced titanate nanotubes," *Environmental Science and Technology*, vol. 42, no. 12, pp. 4507–4512, 2008.
- [6] H.-H. Ou and S.-L. Lo, "Review of titania nanotubes synthesized via the hydrothermal treatment: fabrication, modification, and application," *Separation and Purification Technology*, vol. 58, no. 1, pp. 179–191, 2007.
- [7] V. Štengl, S. Bakardjieva, J. Šubrt, et al., "Sodium titanate nanorods: preparation, microstructure characterization and photocatalytic activity," *Applied Catalysis B*, vol. 63, no. 1-2, pp. 20–30, 2006.
- [8] Y. Yu and D. Xu, "Single-crystalline TiO₂ nanorods: highly active and easily recycled photocatalysts," *Applied Catalysis B*, vol. 73, no. 1-2, pp. 166–171, 2007.
- [9] H. H. Ou, S. L. Lo, and Y. H. Liou, "Microwave-induced titanate nanotubes and the corresponding behaviour after thermal treatment," *Nanotechnology*, vol. 18, no. 17, Article ID 175702, 2007.
- [10] H.-H. Ou and S.-L. Lo, "Photocatalysis of gaseous trichloroethylene (TCE) over TiO₂: the effect of oxygen and relative humidity on the generation of dichloroacetyl chloride (DCAC) and phosgene," *Journal of Hazardous Materials*, vol. 146, no. 1-2, pp. 302–308, 2007.
- [11] J.-G. Yu, H.-G. Yu, B. Cheng, X.-J. Zhao, J. C. Yu, and W.-K. Ho, "The effect of calcination temperature on the surface microstructure and photocatalytic activity of TiO₂ thin films prepared by liquid phase deposition," *Journal of Physical Chemistry B*, vol. 107, no. 50, pp. 13871–13879, 2003.
- [12] J.-N. Nian and H. Teng, "Hydrothermal synthesis of single-crystalline anatase TiO₂ nanorods with nanotubes as the precursor," *Journal of Physical Chemistry B*, vol. 110, no. 9, pp. 4193–4198, 2006.
- [13] C.-C. Tsai and H. Teng, "Structural features of nanotubes synthesized from NaOH treatment on TiO₂ with different post-treatments," *Chemistry of Materials*, vol. 18, no. 2, pp. 367–373, 2006.
- [14] Y. Inoue, T. Niiyama, and K. Sato, "Photocatalysts using hexa- and octa-titanates with different tunnel space for water decomposition," *Topics in Catalysis*, vol. 1, no. 1-2, pp. 137–144, 1994.
- [15] Y. Inoue, T. Kubokawa, and K. Sato, "Photocatalytic activity of alkali-metal titanates combined with Ru in the decomposition of water," *Journal of Physical Chemistry*, vol. 95, no. 10, pp. 4059–4063, 1991.
- [16] N. Serpone, P. Maruthamuthu, P. Pichat, E. Pelizzetti, and H. Hidaka, "Exploiting the interparticle electron transfer process in the photocatalysed oxidation of phenol, 2-chlorophenol and pentachlorophenol: chemical evidence for electron and hole transfer between coupled semiconductors," *Journal of Photochemistry and Photobiology A*, vol. 85, no. 3, pp. 247–255, 1995.
- [17] H.-H. Ou, S.-L. Lo, and C.-H. Wu, "Exploring the interparticle electron transfer process in the photocatalytic oxidation of 4-chlorophenol," *Journal of Hazardous Materials*, vol. 137, no. 3, pp. 1362–1370, 2006.

Research Article

First-Principles Studies on the Structural Transition of ZnO Nanowires at High Pressure

Zhanjun Gao, Yousong Gu, and Yue Zhang

Department of Material Physics and Chemistry, University of Science and Technology Beijing, Beijing 100083, China

Correspondence should be addressed to Yue Zhang, yuezhang@ustb.edu.cn

Received 30 October 2009; Revised 4 February 2010; Accepted 8 March 2010

Academic Editor: Yanqiu Zhu

Copyright © 2010 Zhanjun Gao et al. This is an open access article distributed under the Creative Commons Attribution License, which permits unrestricted use, distribution, and reproduction in any medium, provided the original work is properly cited.

The structural transition of ZnO nanowires at high pressures from wurtzite to rocksalt structure has been studied by first-principles density functional calculations using the SIESTA code. The size effect was studied by calculating a series of nanowires with different diameters, and the doping effect was studied by ion substitution. It is found that the critical pressure of structural transition for nanowires is lower than that of the bulk, and it decreases as the diameter of the nanowire decreases. It is also found that Mn doping can reduce the transition pressure. The size effect and doping effect are discussed in terms of the chemical bonding and energies of the nanowires.

1. Introduction

It is well known that zinc oxide is a wide band gap ($E_g = 3.37$ eV) semiconductor with interesting electronic, piezoelectric, and photoconducting properties. It has a wide range of applications in electronics, optoelectronics, photovoltaic, and sensors [1, 2]. One of the research highlights is the structural transition from the wurtzite (B4) structure (space group P63mc) to the rocksalt (B1) structure (space group FM $\bar{3}$ M) at high pressure. Experimentally, in situ observations were performed, such as energy dispersive X-ray diffraction [3–5], Raman scattering [6], and X-ray-absorption near-edge structure (EXAFS) [7]. At the same time, theoretical efforts were also made by first-principle calculation using various methods, such as the early Hartree-Fock method [8], LDA and GGA [9], and SIC [10]. Recently, the transition path has also been studied [11–13]. Experimental investigations on the phase transformation of ZnO nano-materials have appeared recently, such as ZnO nano-particles [14, 15], nanorods [16], nanotubes [17], and nanocrystalline [18]. Theoretical works on the structural transition have appeared recently, such as the phase transformation in ZnO nanowires under tensile load [19, 20] and the critical dimension for phase transition of nanowires [21]. However, experimental results about the structure transition are scattered in a wide range, and far

from conclusive. Theoretical studies on the pressure-induced phase transitions in ZnO nanomaterials are in the early stage and further studies are needed.

In this work, the pressure-induced-phase transitions in ZnO nanowires were investigated by first-principles calculations, and the size effect and doping effect were investigated.

2. Theoretical Details

First-principles calculations were performed using the SIESTA package [22, 23] employing pseudopotential and numeric atomic orbits basis. In the calculation, GGA-PBE type of exchange correlation functionals and DZP basis set were used. The mesh cutoff was 400 Ry and Kgrid_cutoff 25 Å. The transition pressure is evaluated by calculating the ground state energy versus cell volume ($E\sim V$) curves. First, the ground state energy of the fully relaxed unit cell is calculated. Then, a series of ground state energies are calculated for unit cells scaled by a set of scale factors. The parameters regarding the structural transition were obtained from the common tangent of the $E\sim V$ curves of the two phases, since the enthalpy $H = U + PV$ is minimum for stable phases in constant pressure systems. The structural transitions of the bulks are calculated first to serve as a basis for further comparison. In order to calculate nanowires, the supercell used in the calculation is a rectangle box

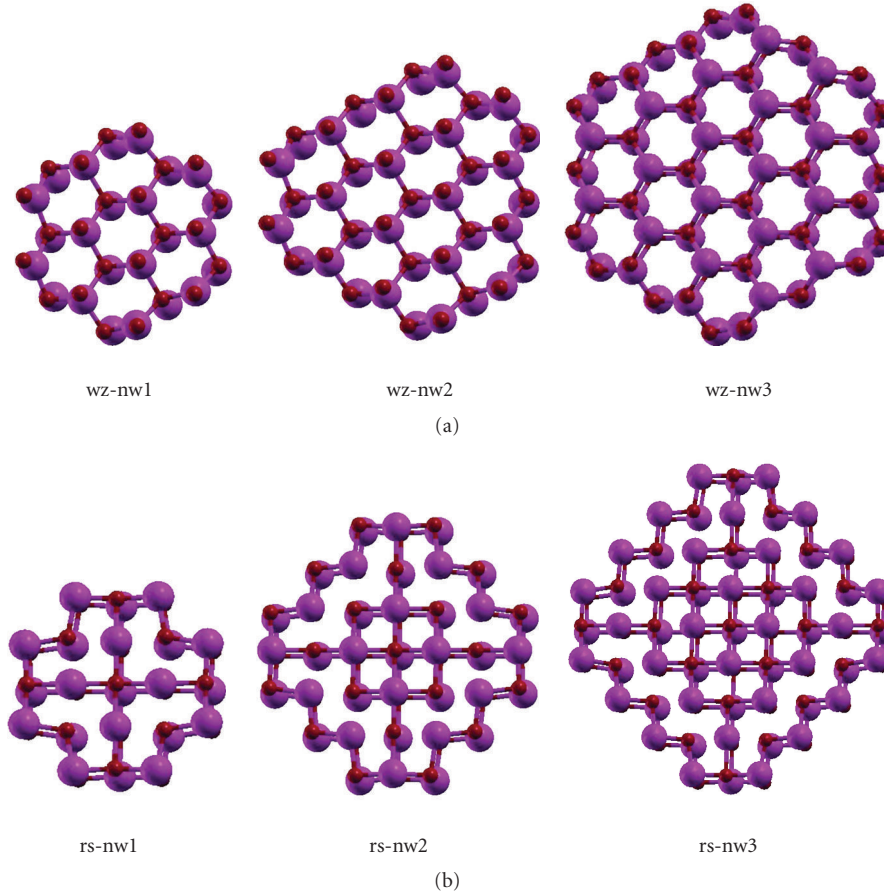


FIGURE 1: The cross-section views of the ZnO nanowires, (a) wurtzite, (b) rocksalt structures. The diameter increases from left to right and the names of the nanowires are shown.

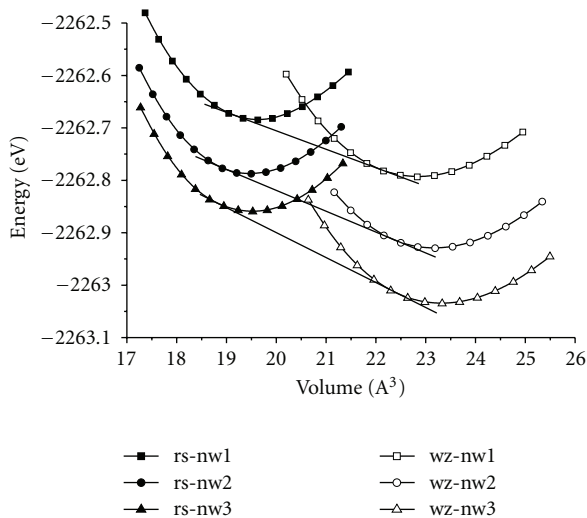


FIGURE 2: The calculated $E\sim V$ curves of three pairs of ZnO nanowires.

with a nanowire in the center. The separations between the nanowires are larger than 10 \AA to eliminate the interactions between the adjacent nanowires. The cross-sections of the nanowires are shown in Figure 1.

3. Results and Discussion

3.1. Pure ZnO Nanowires with Different Diameters. The calculated $E\sim V$ curves of the three pairs of nanowires are plotted in Figure 2. To facilitate comparison, the energy and volume are for each ZnO formula unit. We can see that as the diameter of the nanowires decreases, the ground state energy per ZnO unit increases. This is understandable because the amount of surface atoms and broken bonds increases as the diameter decreases. The equilibrium volume of rs-ZnO nanowires is lower than that of wz-ZnO nanowires, as in the case of bulks. Common tangents are drawn for all the three pairs of $E\sim V$ curves, and the E and V values at each tangent points, where structural transition occurs, were obtained and listed in Table 1.

From the obtained energy and volume data at the points of structural transition, the volume change ($\Delta V/V_0$) and transition pressure (P_{tr}) can be calculated. For comparison, the structure transition of bulk ZnO was calculated using exactly the same calculation parameters, and all the results are listed in Table 1. It can be seen clearly that both the volume change and the transition pressure of ZnO nanowires are lower than that of the bulk and decrease as the diameter of the nanowires decreases. Comparing the experimental transition pressure of $13\sim 14$ and 10.5 GPa for

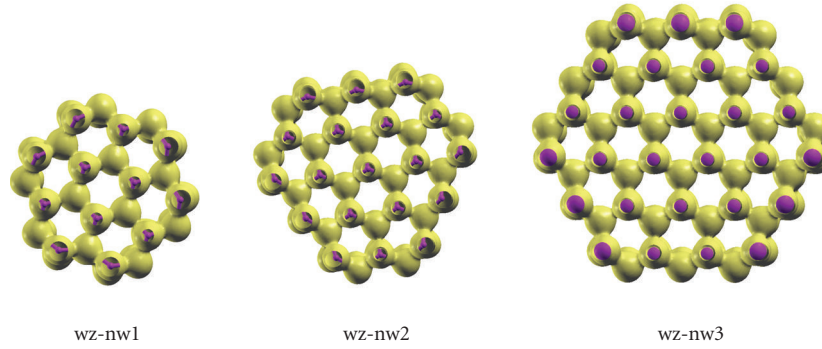


FIGURE 3: The isosurface at $0.06/\text{\AA}^2$ of wz-ZnO nanowires with different diameters.

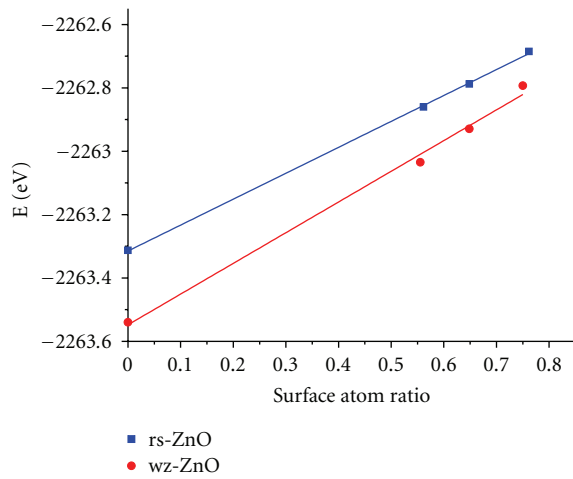


FIGURE 4: The ground state energy per ZnO formula unit as functions of surface atom ratio for wurtzite and rocksalt ZnO nanowires.

nanocrystalline [14, 18], 8.0 GPa for nanorods [16], 11.0 GPa for nanotube [17], and the theoretical results of 8.2 GPa for nanowires by molecular dynamics [20], our results are reasonable.

In order to understand the physical origin of the change in transition pressures, the structure of the nanowires and its change with diameter were investigated. From Figure 1, it can be seen that after geometry relaxation, the positions of the atoms are moved to form compact surface layers. To get a more clear view of the picture, the electron density isosurfaces for the three wz-ZnO nanowires at $0.06/\text{\AA}^3$ are shown in Figure 3. It can be seen that connections between the surface atoms are stronger than those of the inner atoms, as indicated by the larger open connection circles and thicker necks between the atoms. Strong surface bonds and weak core bonds are presented in the ZnO nanowires.

Recently, Ding and Wang observed reconstructed ZnO surfaces [24], and Zhang and Huang claimed that surface reconstruction can affect structural transition [21]. In order to get a clear picture on how the surface layers contribute to the change of transition pressure, the crystal structure and bonding in the nanowires were investigated. The lattice

constants along the c axis are 5.350, 5.331, 5.320 and 5.234 \AA for the three nanowires and the bulk, respectively. It is quite clear that the lattice constant c is larger than that of the bulk and increases as the diameter decreases. Measurement of the lattice constants in the cross-section found that the distances between the core atoms are almost unchanged and those between the surface atoms are shortened. Thus, the chemical bonds between the core atoms are weakened and the extent of the weakness increases as the diameter of the nanowires decreases, which may lead to the observed results.

There is another factor that is directly related to the observed phenomena: the dangling bonds of the surface atoms. The smaller the diameter of the nanowires, the larger the surface to bulk atom ratio, and resulting in more dangling bonds. Figure 4 shows the ground state energies of the ZnO nanowires as functions of surface atomic ratio. It is quite clear that the ground state energy increases almost linearly as the surface atomic ratio increases. Dangling bonds dominate over the close packed reconstructed surfaces in the structure transformation of ZnO nanowires. From the slopes of the two curves, it can be seen clearly that the ground state energy of the wurtzite structure increases much faster than that of the rocksalt structure, and the energy difference decreases which directly leads to the decrease of transition pressure. This can be explained in terms of the bonding characteristics. The coordinate numbers of ZnO in wurtzite and rocksalt structures are 4 and 6, and the surface atoms have 1/4 and 1/6 dangling bonds, respectively. Thus the increase in energy is high for wurtzite structure.

3.2. Mn-Doped ZnO Nanowires. In order to investigate the effect of doping on the structural transformation of ZnO nanowires, first-principles calculations were performed on Mn-doped ZnO nanowires. Doping was realized by substituting a Zn ion with a Mn ion in the supercell. Favorable doping sites were selected by calculating the ground state energies of all the distinct doping sites and searching for the most stable site. Figure 5 shows the relaxed ball-and-stick models of the favorable doping site after geometry relaxation. It can be seen that the favorable dopant sites are near the surface of the nanowires and distortion induced by doping can be seen clearly. In the case of rocksalt ZnO nanowires, distortion due to doping extend to a large area and changes

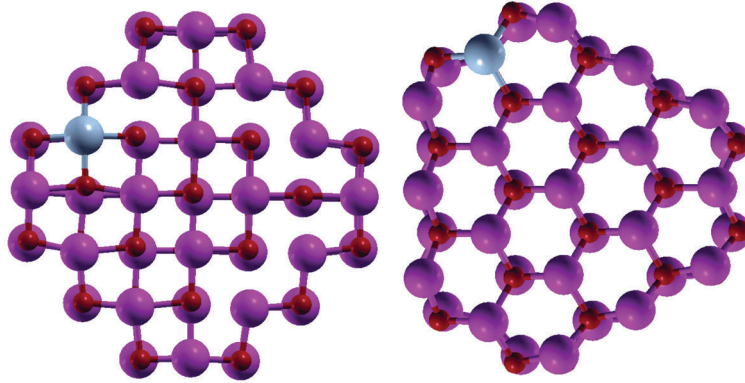


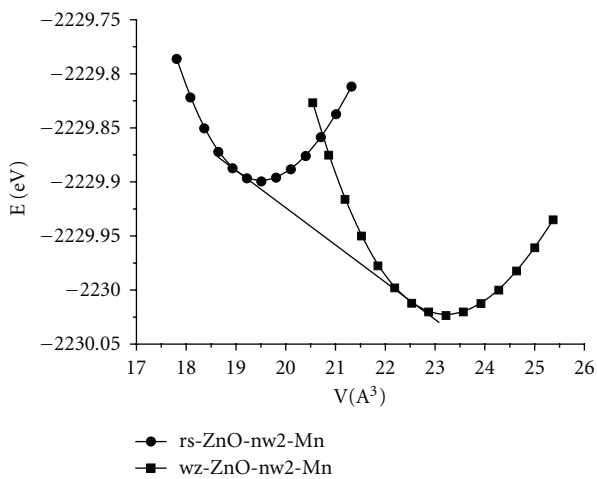
FIGURE 5: The ball-and-stick models of Mn-doped ZnO nanowires after geometrical relaxation.

TABLE 1: The calculated results of structural transition of ZnO nanowires.

Subject	Volume (\AA^3)		$\Delta V/V_0(\%)$	Energy (eV)		P_{tr} (GPa)
	rs-ZnO	wz-ZnO		rs-ZnO	wz-ZnO	
nw1	19.132	22.097	13.4	-2262.675	-2262.779	5.64
nw2	18.933	22.330	15.2	-2262.777	-2262.912	6.35
nw3	18.785	22.369	16.0	-2262.842	-2263.013	7.63
Bulk	18.804	22.736	17.3	-2263.291	-2262.779	8.92

TABLE 2: The calculated results of structural transition for Mn-doped ZnO nanowires.

Sample	Volume (\AA^3)		$\Delta V/V_0$	Energy (eV)		P_{tr} (GPa)
	rs-ZnO	wz-ZnO		rs-ZnO	wz-ZnO	
Bulk	18.804	22.736	0.173	-2263.291	-2263.510	8.92
nw2	18.933	22.330	0.152	-2262.777	-2262.912	6.35
Mn-nw2	19.045	22.480	0.153	-2229.891	-2230.009	5.51

FIGURE 6: The calculated $E \sim V$ curves of the pure and Mn-doped ZnO nanowires.

in bonding can be seen clearly beyond two bonds, while distortion due to doping is restricted in local area for wurtzite ZnO due to their bonding characteristics.

A pair of $E \sim V$ curves were calculated in the same way as in the pure ZnO nanowires and were shown in Figure 6. The results about structural transition are obtained for Mn-doped ZnO nanowires and listed in Table 2, together with the results of the pure nanowires and the bulk for comparison. It can be seen that the critical pressure for structural transition (P_{tr}) of Mn doped ZnO nanowires is lower than that of the pure ones. This is in agreement with experimental results [25].

The decrease of transition pressure in Mn doped ZnO nanowires can be explained in terms of the doping energy affected by bonding characteristics. The elastic energies induced by doping are different for the two structures. Due to the ionic bonds and high coordinate number, strain is extended to a large region in the rocksalt phase, resulting in a moderate strain energy; meanwhile, due to the covalent bonds and low coordinate number, strain is concentrated in a small region for the wurtzite phase, resulting in a high strain energy. Therefore, relative energy of the two phases was reduced and the slope of the common tangent of the two $E \sim V$ curves decreased, which leads to the decrease in transition pressure.

4. Conclusions

Study on the transitions of ZnO nanowires from wurtzite to rocksalt structure at high pressures by first-principles calculations found that the transition pressure of ZnO nanowires is lower than that of the bulk, and it decreases as the diameter of the nanowire decreases. After investigating the structure and chemical bonds of the nanowires, it is found that surface reconstruction leads to close-packed surface layers and sparse core regions. Dangling bonds of the surface atoms lead to the increase of the ground state energy and the large increasing rate of the wurtzite structure caused the decrease of the transition pressure. Mn doping can reduce the critical pressure of structural transition, which is due to the different elastic energies of Mn doping in the two structures.

Acknowledgments

This work has been supported by the Basic Research Project from Ministry of Science and Technology of China under Grant no. 2007CB936202 and the Program from the National Natural Science Foundation of China under Grant no. 50972009.

References

- [1] S. C. Minne, S. R. Manalis, and C. F. Quate, "Parallel atomic force microscopy using cantilevers with integrated piezoresistive sensors and integrated piezoelectric actuators," *Applied Physics Letters*, vol. 67, no. 26, pp. 3918–3920, 1995.
- [2] C. R. Gorla, N. W. Emanetoglu, S. Liang, et al., "Structural, optical, and surface acoustic wave properties of epitaxial ZnO films grown on (0112) sapphire by metalorganic chemical vapor deposition," *Journal of Applied Physics*, vol. 85, no. 5, pp. 2595–2602, 1999.
- [3] S. Desgreniers, "High-density phases of ZnO: structural and compressive parameters," *Physical Review B*, vol. 58, no. 21, pp. 14102–14105, 1998.
- [4] H. Liu, Y. Ding, M. Somayazulu, et al., "Rietveld refinement study of the pressure dependence of the internal structural parameter u in the wurtzite phase of ZnO," *Physical Review B*, vol. 71, no. 21, Article ID 212103, 4 pages, 2005.
- [5] H. Liu, J. S. Tse, and H.-K. Mao, "Stability of rocksalt phase of zinc oxide under strong compression: synchrotron X-ray diffraction experiments and first-principles calculation studies," *Journal of Applied Physics*, vol. 100, no. 9, Article ID 093509, 2006.
- [6] F. Decremps, J. Pellicer-Porres, A. M. Saitta, J.-C. Chervin, and A. Polian, "High-pressure Raman spectroscopy study of wurtzite ZnO," *Physical Review B*, vol. 65, no. 9, Article ID 092101, 4 pages, 2002.
- [7] F. Decremps, F. Datchi, A. M. Saitta, et al., "Local structure of condensed zinc oxide," *Physical Review B*, vol. 68, no. 10, Article ID 104101, 10 pages, 2003.
- [8] J. E. Jaffe and A. C. Hess, "Hartree-Fock study of phase changes in ZnO at high pressure," *Physical Review B*, vol. 48, no. 11, pp. 7903–7909, 1993.
- [9] J. E. Jaffe, J. A. Snyder, Z. Lin, and A. C. Hess, "LDA and GGA calculations for high-pressure phase transitions in ZnO and MgO," *Physical Review B*, vol. 62, no. 3, pp. 1660–1665, 2000.
- [10] A. Qteish, "Self-interaction-corrected local density approximation pseudopotential calculations of the structural phase transformations of ZnO and ZnS under high pressure," *Journal of Physics Condensed Matter*, vol. 12, no. 26, pp. 5639–5653, 2000.
- [11] S. Limpijumng and S. Jungthawan, "First-principles study of the wurtzite-to-rocksalt homogeneous transformation in ZnO: a case of a low-transformation barrier," *Physical Review B*, vol. 70, no. 5, Article ID 054104, 2004.
- [12] J. Cai and N. Chen, "First-principles study of the wurtzite-to-rocksalt phase transition in zinc oxide," *Journal of Physics Condensed Matter*, vol. 19, no. 26, Article ID 266207, 2007.
- [13] M. A. Blanco, J. M. Recio, A. Costales, and R. Pandey, "Transition path for the B3 \leftrightarrow B1 phase transformation in semiconductors," *Physical Review B*, vol. 62, no. 16, pp. R10599–R10602, 2000.
- [14] J. Y. Liang, G. Lin, X. H. Bin, et al., "A novel synthesis route and phase transformation of ZnO nanoparticles modified by DDAB," *Journal of Crystal Growth*, vol. 252, no. 1–3, pp. 226–229, 2003.
- [15] S.-Y. Chen, P. Shen, and J. Jiang, "Polymorphic transformation of dense ZnO nanoparticles: implications for chair/boat-type Peierls distortions of AB semiconductor," *Journal of Chemical Physics*, vol. 121, no. 22, pp. 11309–11313, 2004.
- [16] X. Wu, Z. Wu, L. Guo, et al., "Pressure-induced phase transformation in controlled shape ZnO nanorods," *Solid State Communications*, vol. 135, no. 11–12, pp. 780–784, 2005.
- [17] S. J. Chen, Y. C. Liu, C. L. Shao, et al., "Photoluminescence study of ZnO nanotubes under hydrostatic pressure," *Applied Physics Letters*, vol. 88, no. 13, Article ID 133127, 2006.
- [18] R. S. Kumar, A. L. Cornelius, and M. F. Nicol, "Structure of nanocrystalline ZnO up to 85 GPa," *Current Applied Physics*, vol. 7, no. 2, pp. 135–138, 2007.
- [19] A. J. Kulkarni, M. Zhou, K. Sarasamak, and S. Limpijumng, "Novel phase transformation in ZnO nanowires under tensile loading," *Physical Review Letters*, vol. 97, no. 10, Article ID 105502, 2006.
- [20] A. J. Kulkarni, K. Sarasamak, J. Wang, F. J. Ke, S. Limpijumng, and M. Zhou, "Effect of load triaxiality on polymorphic transitions in zinc oxide," *Mechanics Research Communications*, vol. 35, no. 1–2, pp. 73–80, 2008.
- [21] L. Zhang and H. Huang, "Structural transformation of ZnO nanostructures," *Applied Physics Letters*, vol. 90, no. 2, Article ID 023115, 2007.
- [22] Information on <http://www.icmab.es/siesta/>.
- [23] J. M. Soler, E. Artacho, J. D. Gale, et al., "The SIESTA method for ab initio order-N materials simulation," *Journal of Physics Condensed Matter*, vol. 14, no. 11, pp. 2745–2779, 2002.
- [24] Y. Ding and Z. L. Wang, "Profile imaging of reconstructed polar and non-polar surfaces of ZnO," *Surface Science*, vol. 601, no. 2, pp. 425–433, 2007.
- [25] X. Q. Yan, Y.S. Gu, X. M. Zhang, et al., "Doping effect on high-pressure structural stability of ZnO nanowires," *Journal of Physical Chemistry C*, vol. 113, no. 4, pp. 1164–1167, 2009.

Research Article

Synthesis of GaN Nanorods by a Solid-State Reaction

Keyan Bao,¹ Liang Shi,² Xiaodi Liu,¹ Changzhong Chen,¹ Wutao Mao,¹
Lingling Zhu,² and Jie Cao²

¹ College of Chemistry and Pharmacy Engineering, Nanyang Normal University, Henan 473061, China

² Hefei National Laboratory for Physical Science at Microscale and Department of Chemistry,
University of Science and Technology of China, Hefei, Anhui 230026, China

Correspondence should be addressed to Keyan Bao, bkeyan@mail.ustc.edu.cn

Received 28 November 2009; Accepted 17 March 2010

Academic Editor: Renzhi Ma

Copyright © 2010 Keyan Bao et al. This is an open access article distributed under the Creative Commons Attribution License, which permits unrestricted use, distribution, and reproduction in any medium, provided the original work is properly cited.

An atom-economical and eco-friendly chemical synthetic route was developed to synthesize wurtzite GaN nanorods by the reaction of NaNH_2 and the as-synthesized orthorhombic GaOOH nanorods in a stainless steel autoclave at 600°C . The lengths of the GaN nanorods are in the range of 400–600 nm and the diameters are about 80–150 nm. The process of orthorhombic GaOOH nanorods transformation into wurtzite GaN nanorods was investigated by powder X-ray diffraction (XRD) and field emission scanning electron microscope (FESEM), indicating that the GaN product retained essentially the same basic topological morphology in contrast to that of the GaOOH precursor. It was found that rhombohedral Ga_2O_3 was the intermediate between the starting orthorhombic GaOOH precursor and the final wurtzite GaN product. The photoluminescence measurements reveal that the as-prepared wurtzite GaN nanorods showed strong blue emission.

1. Introduction

GaN, an important III–V semiconductor with a direct band gap of 3.39 eV at room temperature, has a wide use in optical devices operating at blue and ultraviolet wavelengths and in high-temperature electronic devices [1]. The recent development of commercial blue-light emitters based on GaN has propelled these materials into the mainstream of interest. Up to now, many structures of GaN such as nanowires [2–6], nanorods [7–11], nanobelts [12], and tubes [13–17] have been successfully synthesized. Many reports showed that these one-dimensional (1D) structures of GaN have been grown by many methods, such as chemical vapor deposition [18], metal-organic chemical vapor deposition [19], molecular beam epitaxy [20], halide vapor-phase epitaxy [21], arc discharge [22], magnetron sputtering [23], chemical thermal-evaporation process [24], etching [25], and ammonolysis [26–29]. For example, GaN nanowires were fabricated on Si substrates coated with NiCl_2 thin films using chemical vapor deposition method by evaporating Ga_2O_3 powder at 1100°C in ammonia gas flow [30]. Wurtzite GaN nanowires were synthesized via sublimation sandwich method using Ga and NH_3 as starting reagents [31].

However, among most of these methods, an atmosphere of superfluous NH_3 is obligatory, which caused air pollution and waste.

In this paper, we reported an economical and eco-friendly chemical synthetic method for synthesis wurtzite GaN nanorods. In detail, the preparation of wurtzite GaN nanorods involved two steps: first, hydrothermal synthesis of orthorhombic GaOOH nanorods at 180°C for 12 hours, and second, preparation of GaN nanorods using NaNH_2 and the as-prepared orthorhombic GaOOH nanorods as reactants in a stainless steel autoclave at 600°C for 5 hours.

2. Experimental Section

2.1. Synthesis of GaOOH Nanorods. In a typical synthesis, under continually stirring, 0.88 g of GaCl_3 (5 mmol) was dissolved into a mixture of 40 mL of deionized water. After 5 minutes, 5 mL of sodium hypochlorite solution was introduced to the above solution. Then the solution was transferred to a 50 mL Teflon-lined autoclave. The autoclave was sealed, maintained at 180°C for 12 hours, and then allowed to cool to room temperature naturally. The product

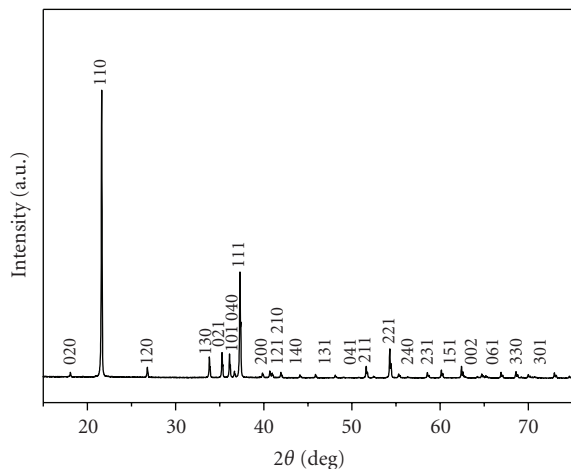


FIGURE 1: XRD pattern of the as-prepared GaOOH product.

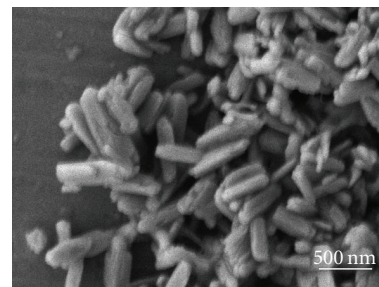
was retrieved by filtration, washed several times with distilled water, and absolute ethanol, and dried under vacuum at 60°C for 6 hours.

2.2. Preparation of GaN Nanorods. 1.03 g (10 mmol) of the as-prepared GaOOH nanorods and 0.63 g (16 mmol) of NaNH_2 were mixed and then put into a stainless steel autoclave. The autoclave was maintained at 600°C for 5 hours and then cooled to room temperature naturally. A yellow powder was retrieved by centrifugation, washed several times with dilute hydrochloric acid, distilled water and absolute alcohol, and finally dried in a vacuum oven at 60°C for 6 hours.

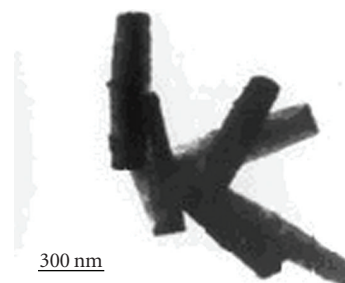
2.3. Characterization. Powder X-ray diffraction (XRD) measurements were carried out with a Philips X'Pert diffractometer ($\text{Cu K}\alpha$ $\lambda = 1.541874 \text{ \AA}$; Nickel filter; 40 kV, 40 mA). Field emission scanning electron microscope (FESEM) images were taken on a JEOL JSM-6300F SEM. Transmission electron microscopy (TEM) images, high-resolution transmission electron microscopy (HRTEM) images, and selected area electron diffraction (SAED) patterns were performed on JEOL JEM-2010 microscope operating at 200 kV. The Raman spectrum was obtained on the JY LABRAM-HR laser micro-Raman spectrometer with 514.5 nm emission lines. Photoluminescence (PL) measurements were carried out on a Perkin-Elmer LS-55 luminescence spectrometer using a pulsed Xe lamp.

3. Results and Discussion

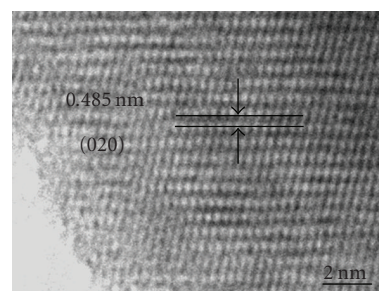
3.1. Characterization of GaOOH Nanorods. Figure 1 shows the X-ray diffraction (XRD) pattern of the GaOOH nanorods. It can be observed that orthorhombic phase of GaOOH formed in our synthesis. All the reflection peaks can be indexed as orthorhombic phase of GaOOH (JCPDS PDF No. 26-0674, $a = 4.5 \text{ \AA}$, $b = 9.75 \text{ \AA}$, $c = 2.97 \text{ \AA}$). No peaks of impurities were detected.



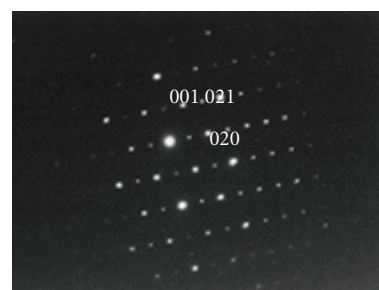
(a)



(b)



(c)



(d)

FIGURE 2: (a) FESEM image, (b) TEM image, (c) HRTEM image, and (d) corresponding SAED pattern of the as-synthesized orthorhombic GaOOH nanorods.

Figure 2(a) shows a typical the field-emission scanning electron microscopy (FESEM) image of the as-prepared orthorhombic GaOOH, which clearly exhibits that the product consists of uniform nanorods with lengths in the range of 400–600 nm and diameters of about 80–120 nm. Figure 2(b) is a representative transmission electron microscopy (TEM) image of the GaOOH product, indicating that the nanorods are solid structure, about 500 nm in length. A high-resolution transmission electron microscopy

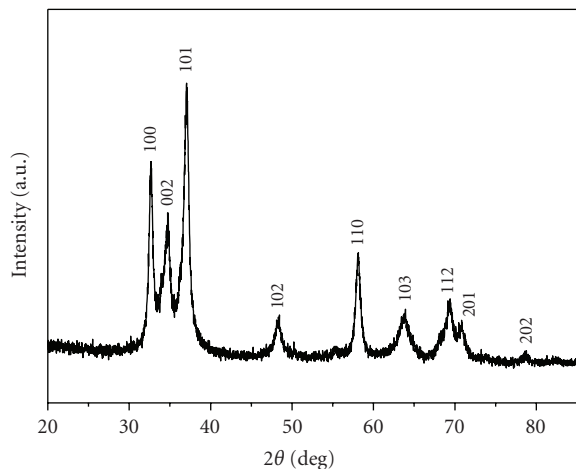


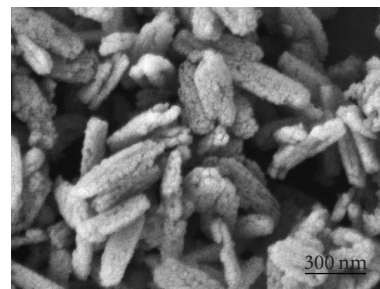
FIGURE 3: XRD pattern of the as-prepared GaN nanorods.

(HRTEM) image of a single GaOOH nanorod is shown in Figure 2(c). As can be seen from the image, this nanorod is structurally uniform single crystal. The observed interplanar spacing is about 0.485 nm, which corresponds to the separation between (020) lattice planes of orthorhombic GaOOH. The corresponding SAED pattern (Figure 2(d)) also indicates that the as-prepared GaOOH is single crystal and the SAED spots can be indexed as orthorhombic GaOOH (001), (021) and (020) planes.

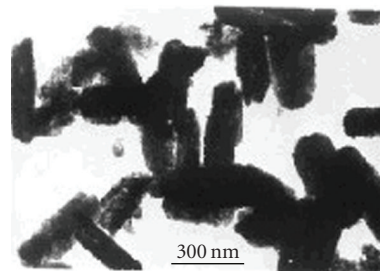
3.2. Characterization of GaN Nanorods. The GaN nanorods were prepared via a solid-state reaction using NaNH_2 and the as-prepared orthorhombic GaOOH nanorods as reactants in a stainless steel autoclave. Figure 3 indicates the XRD pattern of the as-prepared product. All the reflection peaks can be indexed as wurtzite GaN, which is in good agreement with the standard data (JCPDS PDF No. 74-0243, $a = 3.195 \text{ \AA}$, $c = 5.182 \text{ \AA}$). No peaks of impurities such as Ga_2O_3 and Ga were detected, revealing that the orthorhombic GaOOH precursor was completely converted into wurtzite GaN under the experimental conditions.

FESEM, TEM, and HRTEM analyses were used to explore the morphologies and crystal structures of the as-synthesized wurtzite GaN nanorods. Figure 4(a) presents a panoramic FESEM image of the GaN product, indicating that the nanorods have rough surfaces which consist of densely packed GaN nanoparticles about 100–200 nm. Figure 4(b) is a representative TEM image of the GaN nanorods, displaying that the product is solid structure, about 500 nm in length and 100 nm in diameter. Figure 4(c) is the HRTEM image, showing that the crystal planes have lattice spacing of about 0.275 nm corresponding to (100) plane of wurtzite GaN. The corresponding SAED pattern (Figure 4(d)) also confirmed its wurtzite structure.

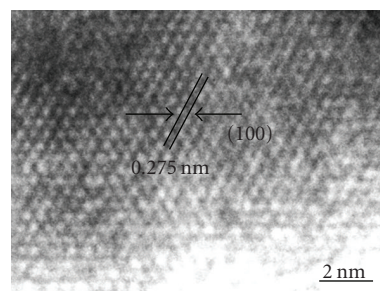
Further study shows that reaction temperature has a dramatic effect on the formation of GaN nanorods. When the reaction temperature was lower than 300°C , the obtained sample was still orthorhombic phase of GaOOH. If increases the reaction temperature to 500°C , the product



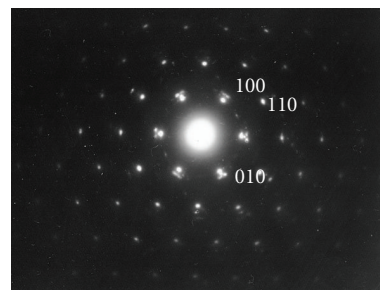
(a)



(b)



(c)



(d)

FIGURE 4: (a) FESEM image, (b) TEM image, (c) HRTEM image, and (d) corresponding SAED pattern of the as-synthesized wurtzite GaN nanorods.

was rhombohedral Ga_2O_3 instead of orthorhombic GaOOH. This is to say at 500°C rhombohedral Ga_2O_3 could not react with NaNH_2 and no wurtzite GaN was obtained. Pure wurtzite GaN could be obtained when the reaction temperature was higher than 600°C . Further study suggests that varying reaction temperature in the range of $600\text{--}700^\circ\text{C}$ led to obvious change in the morphologies of wurtzite GaN products. When the temperature was moderated at 600°C , the product was GaN nanorods, while at 700°C the product

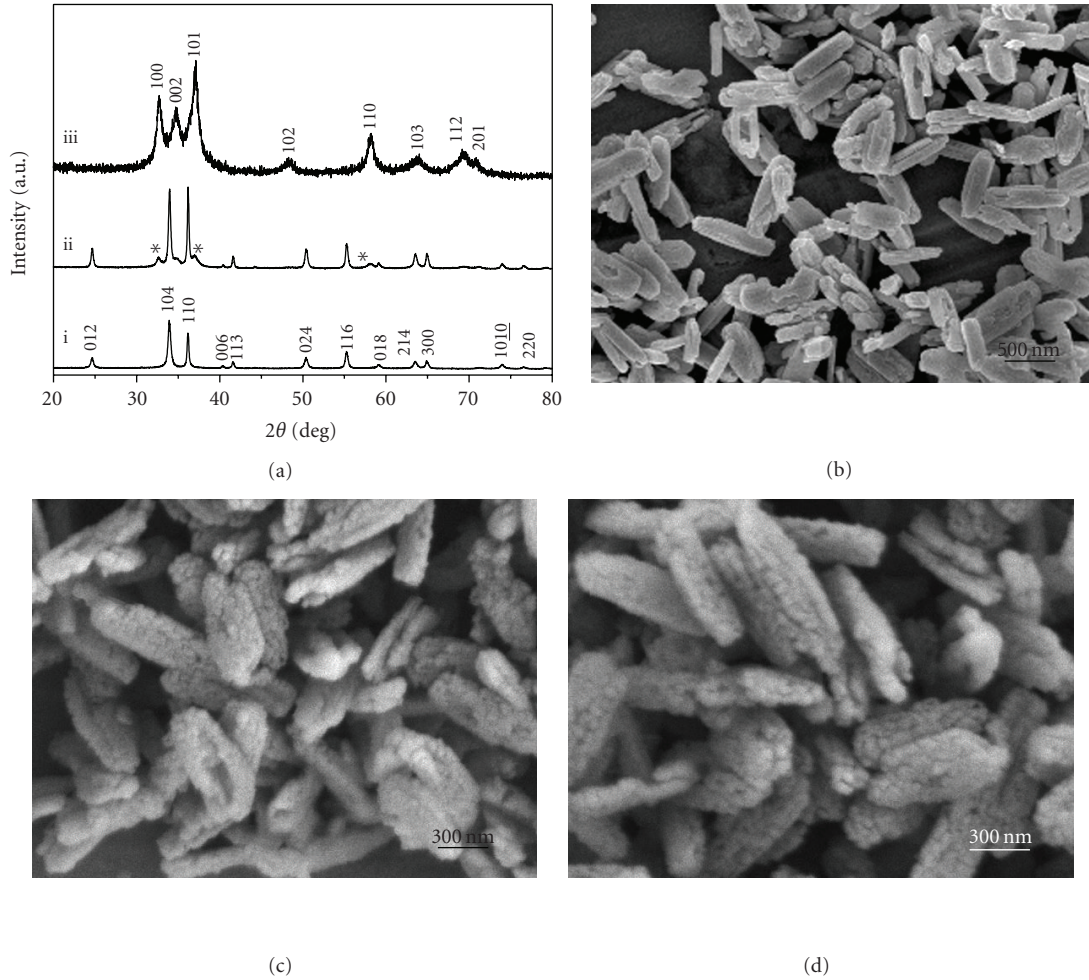


FIGURE 5: (a) i, ii, and iii are the XRD patterns of the products shown in (b), (c), and (d), respectively. ((b)–(d)) FESEM images of the products obtained at 600°C for 15 minutes, 1 hour, and 5 hours, respectively.

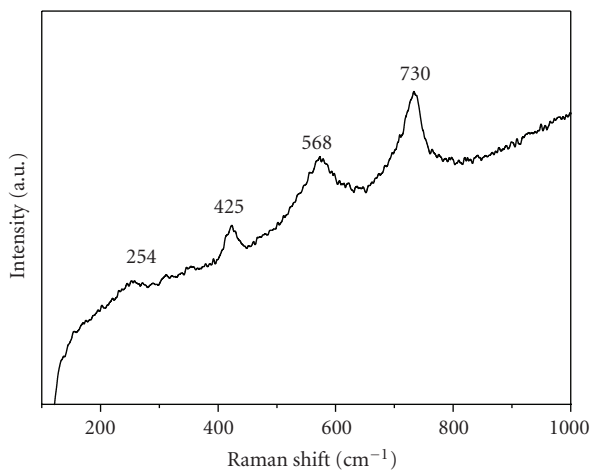


FIGURE 6: Raman spectrum of the as-prepared GaN nanorods.

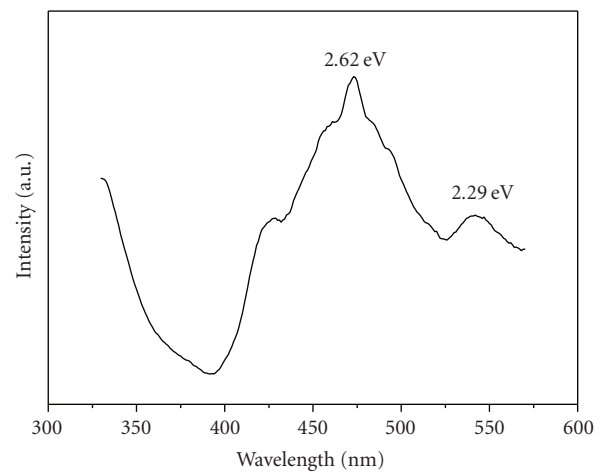


FIGURE 7: Room-temperature photoluminescence (PL) spectrum of the as-prepared GaN nanorods.

was composed of nanoparticles. All the data show that 600°C is the optimal reaction temperature for preparing wurtzite GaN nanorods.

To substantially understand the process of orthorhombic GaOOH nanorods transformation into wurtzite GaN nanorods, we systematically surveyed the growth process by

analyzing the samples at different growth stages. Figure 5(a) exhibits the XRD patterns of the three products obtained at 600°C for 15 minutes, 1 hour, and 5 hours, indicating that the three products were rhombohedral structure of Ga₂O₃ (JCPDS PDF No. 74-1610, $a = 4.98 \text{ \AA}$, $c = 13.43 \text{ \AA}$), rhombohedral Ga₂O₃ with minor amount of wurtzite GaN, and wurtzite GaN, respectively.

Figures 5(b)–5(d) show the FESEM images of the products obtained at 600°C for 15 minutes, 1 hour, and 5 hours, respectively. As shown in Figure 5(b), when the reaction was processed at 600°C for 15 minutes, 1D skeleton of Ga₂O₃ with relatively smooth surfaces was obtained. When the reaction time was increased to 1 hour, the sample was a mixture of Ga₂O₃ and GaN. The FESEM image (Figure 5(c)) indicates that product consists of nanorods with rough surfaces. Pure GaN could be obtained at 600°C for 5 hours. Figure 5(d) displays the FESEM image of the sample reacting for 5 hours, revealing that GaN nanorods assembled from small nanoparticles were formed. Based on the above investigations, the mechanism includes two steps.

- (1) *In the initial step:* the orthorhombic GaOOH nanorods decomposed into rhombohedral Ga₂O₃ nanorods without destroying the 1D framework. As shown in Figure 5(b), the rhombohedral Ga₂O₃ product is composed of nanorods with lengths in the range 400–600 nm.
- (2) *Second step:* with reaction time increasing, rhombohedral Ga₂O₃ nanorods transformed into wurtzite GaN nanorods via a high-temperature reaction. When the reaction time was increased to 1 hour, rhombohedral Ga₂O₃ with minor amount of wurtzite of GaN coexisted in the product, and pure wurtzite GaN could be obtained at 600°C for 5 hours. Figures 5(c)–5(d) display the FESEM images of the products obtained at 600°C for 1 hour and 5 hours, respectively, revealing that the initial 1D structural motifs were unaffected.

4. Optical Properties Measurement

Figure 6 is the Raman spectrum of the as-prepared GaN nanorods. The spectrum clearly indicates that Raman peaks appear at about 254, 425, 568, and 730 cm⁻¹. The first-order modes at 568 and 730 cm⁻¹ exhibit the feature of red-shifts compared to values of 570 and 735 cm⁻¹ for bulk GaN, which is attributed to the nanometer size effect [2]. The second-order Raman modes at 254 and 425 cm⁻¹ are assigned to the zone-boundary phonon, activated by crystal imperfections and finite size effects, and the acoustic overtone of wurtzite GaN [6, 7].

GaN is one of the most promising optoelectronic semiconductors in solid-state devices and its optical properties are directly related to its potential applications. The room temperature photoluminescence (PL) spectrum of the GaN nanorods recorded with excitation wavelength of 300 nm is shown in Figure 7. The PL spectrum exhibits a broad emission band in the range of 2.3–2.9 eV. The blue-emission band with peak at 2.62 eV is attributed to a variety of

defects [7]. The green-emission bands with peak at 2.29 eV comes from intrinsic point defects [2, 6]. In a word, the PL emission displays the presence of a high quantity of defects in the as-prepared GaN nanorods. The defects, which can directly serve as radiative centers, may be helpful for electro-optical properties and extend the potential optical and optoelectronic application to the field of high-temperature electron devices.

5. Conclusions

We have demonstrated a convenient chemical route to synthesize wurtzite GaN nanorods via a solid-state reaction. The formation of GaN nanorods involves two steps: first, the orthorhombic GaOOH nanorods decomposed into rhombohedral Ga₂O₃ nanorods; then the rhombohedral Ga₂O₃ nanorods transformed into wurtzite GaN nanorods without destroying the 1D framework. The lengths of the as-obtained wurtzite GaN are in the range of 400–600 nm and the diameters are about 100 nm. The photoluminescence (PL) of GaN nanorods exhibits emission peak in the blue region, which is possibly attributable to the existence of defect.

Acknowledgment

The authors are grateful to Professor Yitai Qian (University of Science and Technology of China) for his support and enormous help for this research work.

References

- [1] B. Ha, S. H. Seo, J. H. Cho, et al., “Optical and field emission properties of thin single-crystalline GaN nanowires,” *Journal of Physical Chemistry B*, vol. 109, no. 22, pp. 11095–11099, 2005.
- [2] T. Kuykendall, P. J. Pauzauskie, Y. Zhang, et al., “Crystallographic alignment of high-density gallium nitride nanowire arrays,” *Nature Materials*, vol. 3, no. 7, pp. 524–528, 2004.
- [3] R. Calarco, R. J. Meijers, R. K. Debnath, T. Stoical, E. Sutter, and H. Luth, “Nucleation and growth of GaN nanowires on Si(111) performed by molecular beam epitaxy,” *Nano Letters*, vol. 7, no. 8, pp. 2248–2251, 2007.
- [4] B. D. Liu, Y. Bando, C. C. Tang, F. F. Xu, and D. Golberg, “Excellent field-emission properties of P-doped GaN nanowires,” *Journal of Physical Chemistry B*, vol. 109, no. 46, pp. 21521–21524, 2005.
- [5] S. D. Hersee, X. Sun, and X. Wang, “The controlled growth of GaN nanowires,” *Nano Letters*, vol. 6, no. 8, pp. 1808–1811, 2006.
- [6] C.-C. Chen, C.-C. Yeh, C.-H. Chen, et al., “Catalytic growth and characterization of gallium nitride nanowires,” *Journal of the American Chemical Society*, vol. 123, no. 12, pp. 2791–2798, 2001.
- [7] J. K. Jian, X. L. Chen, Q. Y. Tu, Y. P. Xu, L. Dai, and M. J. Zhao, “Preparation and optical properties of prism-shaped GaN nanorods,” *Journal of Physical Chemistry B*, vol. 108, no. 32, pp. 12024–12026, 2004.
- [8] S. Y. Bae, H. W. Seo, J. Park, H. Yang, H. Kim, and S. Kim, “Triangular gallium nitride nanorods,” *Applied Physics Letters*, vol. 82, no. 7, pp. 4564–4566, 2003.

- [9] X. Xiang and H. Zhu, "One-dimensional gallium nitride micro/nanostructures synthesized by a space-confined growth technique," *Applied Physics A*, vol. 87, no. 4, pp. 651–659, 2007.
- [10] J. Chen, C. Xue, H. Zhuang, et al., "Catalytic synthesis and optical properties of large-scale GaN nanorods," *Journal of Alloys and Compounds*, vol. 468, no. 1–2, pp. L1–L4, 2009.
- [11] L. Qin, C. Xue, Y. Duan, and L. Shi, "Fabrication and photoluminescence of GaN nanorods by ammoniating Ga₂O₃ films deposited on Co-coated Si(111) substrates," *Physica B: Condensed Matter*, vol. 404, no. 2, pp. 190–193, 2009.
- [12] X. Xiang, C. Cao, and H. Zhu, "Catalytic synthesis of single-crystalline gallium nitride nanobelts," *Solid State Communications*, vol. 126, no. 6, pp. 315–318, 2003.
- [13] J. Goldberger, R. He, Y. Zhang, et al., "Single-crystal gallium nitride nanotubes," *Nature*, vol. 422, no. 4, pp. 599–602, 2003.
- [14] J. Q. Hu, Y. Bando, D. Golberg, and Q. L. Liu, "Gallium nitride nanotubes by the conversion of gallium oxide nanotubes," *Angewandte Chemie—International Edition*, vol. 42, no. 30, pp. 3493–3497, 2003.
- [15] S. Gao, L. Zhu, Y. Xie, and X. Qian, "Formation of cubic GaN nanocrystals: a study of the thermal stability of GaP nanocrystals under nitrogen," *European Journal of Inorganic Chemistry*, no. 3, pp. 557–561, 2004.
- [16] S. Ding, P. Lu, J.-G. Zheng, et al., "Textured tubular nanoparticle structures: precursor-templated synthesis of GaN submicrometer sized tubes," *Advanced Functional Materials*, vol. 17, no. 12, pp. 1879–1886, 2007.
- [17] J. Dinesh, M. Eswaramoorthy, and C. N. R. Rao, "Use of amorphous carbon nanotube brushes as templates to fabricate GaN nanotube brushes and related materials," *Journal of Physical Chemistry C*, vol. 111, no. 2, pp. 510–513, 2007.
- [18] J. J. Carvajal, M. Aguilo, F. Diaz, and J. C. Rojo, "Green and red emissions at room temperature on Er-doped GaN submicrometer rods synthesized by a simple chemical vapor deposition technique," *Chemistry of Materials*, vol. 19, no. 26, pp. 6543–6547, 2007.
- [19] Z. Yu, Z. Yang, S. Wang, et al., "Growth of GaN nanorods via Au catalyst-assisted CVD," *Chemical Vapor Deposition*, vol. 11, no. 10, pp. 433–436, 2005.
- [20] K. A. Bertness, A. Roshko, L. M. Mansfield, T. E. Harvey, and N. A. Sanford, "Nucleation conditions for catalyst-free GaN nanowires," *Journal of Crystal Growth*, vol. 300, no. 1, pp. 94–99, 2007.
- [21] T. B. Wei, Q. Hu, R. F. Duan, et al., "Growth of (10 $\bar{1}$)over-bar(3)over-bar semipolar GaN on m-plane sapphire by hydride vapor phase epitaxy," *Journal of Crystal Growth*, vol. 311, no. 17, pp. 4153–4157, 2009.
- [22] W. Q. Han, P. Redlich, F. Ernst, and M. Ruhle, "Synthesis of GaN—carbon composite nanotubes and GaN nanorods by arc discharge in nitrogen atmosphere," *Applied Physics Letters*, vol. 76, no. 1, pp. 652–654, 2000.
- [23] L. Yang, C. Xue, C. Wang, and H. Li, "Growth of GaN nanowires by ammoniating Ga₂O₃ thin films deposited on quartz with radio frequency magnetron sputtering," *Nanotechnology*, vol. 14, no. 1, pp. 50–52, 2003.
- [24] B. D. Liu, Y. Bando, C. C. Tang, G. Z. Shen, D. Golberg, and F. F. Xu, "Size-dependent crystallization of Si nanoparticles," *Applied Physics Letters*, vol. 88, no. 9, pp. 88–91, 2006.
- [25] S. C. Hung, Y. K. Su, S. J. Chang, S. C. Chen, T. H. Fang, and L. W. Ji, "GaN nanocolumns formed by inductively coupled plasmas etching," *Physica E: Low-Dimensional Systems and Nanostructures*, vol. 28, no. 2, pp. 115–120, 2005.
- [26] A. P. Purdy, S. Case, and N. Muratore, "Synthesis of GaN by high-pressure ammonolysis of gallium triiodide," *Journal of Crystal Growth*, vol. 252, no. 1–3, pp. 136–143, 2003.
- [27] S. Y. Bae, H. W. Seo, J. Park, H. Yang, J. C. Park, and S. Y. Lee, "Metal-dependent conductance quantization of nanocontacts in solution," *Applied Physics Letters*, vol. 81, no. 1, pp. 126–128, 2002.
- [28] S. Kikkawa, K. Nagasaka, T. Takeda, M. Bailey, T. Sakurai, and Y. Miyamoto, "Preparation and lithium doping of gallium oxynitride by ammonia nitridation via a citrate precursor route," *Journal of Solid State Chemistry*, vol. 180, no. 7, pp. 1984–1989, 2007.
- [29] S. Cho, J. Lee, I. Y. Park, and S. Kim, "Structural and optical properties of GaN fine particles prepared from GaOOH," *Japanese Journal of Applied Physics Part 1*, vol. 41, no. 9, pp. 5533–5537, 2002.
- [30] Y. Wang, C. Xue, H. Zhuang, et al., "Synthesis and characterization of GaN nanowires," *Applied Surface Science*, vol. 255, no. 17, pp. 7719–7722, 2009.
- [31] P. G. Li, X. Guo, X. Wang, and W. H. Tang, "Single-crystalline wurtzite GaN nanowires and zigzagged nanostructures fabricated by sublimation sandwich method," *Journal of Alloys and Compounds*, vol. 475, no. 1–2, pp. 463–468, 2009.

Research Article

Solvothermal Synthesis of $\text{Gd}_2\text{O}_3 : \text{Eu}^{3+}$ Luminescent Nanowires

Guixia Liu, Song Zhang, Xiangting Dong, and Jinxian Wang

School of Chemistry and Environmental Engineering, Changchun University of Science and Technology, Changchun 130022, China

Correspondence should be addressed to Guixia Liu, liuguixia22@yahoo.com.cn

Received 23 November 2009; Revised 20 February 2010; Accepted 19 April 2010

Academic Editor: Raymond Whitby

Copyright © 2010 Guixia Liu et al. This is an open access article distributed under the Creative Commons Attribution License, which permits unrestricted use, distribution, and reproduction in any medium, provided the original work is properly cited.

Uniform $\text{Gd}_2\text{O}_3 : \text{Eu}^{3+}$ luminescent nanowires were prepared on a large scale by a facile solvothermal method using polyethylene glycol (PEG-2000) as template and ethanol as solvent; the properties and the structure were characterized. X-ray diffraction (XRD) patterns and Fourier transform infrared spectrometry (FTIR) showed that the precursors are hexagonal phase $\text{Gd}(\text{OH})_3$ crystals, and the samples calcined at 800°C are cubic phase Gd_2O_3 . Transmission Electron Microscopy (TEM) images indicated that the samples are nanowires with a diameter of 30 nm and a length of a few microns. Photoluminescence (PL) spectra showed that the ratio of ${}^5D_0 \rightarrow {}^7F_2$ to ${}^5D_0 \rightarrow {}^7F_1$ transition peak of the calcined samples is stronger than that of the precursors, which confirmed that the color purity of the $\text{Gd}_2\text{O}_3 : \text{Eu}^{3+}$ is better than that of the precursors. The as-obtained $\text{Gd}_2\text{O}_3 : \text{Eu}^{3+}$ luminescent nanowires show a strong red emission corresponding to ${}^5D_0 \rightarrow {}^7F_2$ transition (610 nm) of Eu^{3+} under ultraviolet excitation (250 nm), which has potential application in red-emitting phosphors and field emission display devices.

1. Introduction

Recently, 1D nanomaterials have been attracted much attention for their unique properties owing to their low dimension and high surface/volume ratio; therefore, they have potential applications in fabricating nanoscale electronic, optoelectronic, and magnetic devices and also provide an ideal model system to quantized conductance and size effects [1]. 1D rare earth oxide nanomaterials are a kind of advanced materials and have extensive applications on the fields of high-performance luminescent devices, catalysts, and other functional materials for their special electronic, optical, and chemical characteristics arising from their 4f electron. Several strategies have been developed for preparing 1D rare earth oxide nanomaterials, including template method [2–7], hydrothermal or solvothermal method [8–18], and chemical reaction [19–22]. Among these methods, the hydrothermal or solvothermal techniques are powerful and important means to synthesize 1D rare earth oxide nanomaterials due to their great chemical flexibility and synthetic tenability.

As well known, in rare earth oxide luminescence materials, Europium-doped Gd_2O_3 phosphor is one of the most important red-emitting phosphors and has been widely used in X-ray scintillator materials, high definition projection

televisions, flat panel displays, and photoelectronic apparatus [23]. Over the past decade, $\text{Gd}_2\text{O}_3 : \text{Eu}^{3+}$ nanoparticles had been investigated extensively [24–27]. When $\text{Gd}_2\text{O}_3 : \text{Eu}^{3+}$ is prepared in the form of one-dimensional nanomaterials such as nanowires, nanorods or, nanotubes, its application would be widely extended due to the shape-specific and quantum confinement effects. However, compared with the study of $\text{Gd}_2\text{O}_3 : \text{Eu}^{3+}$ nanoparticles, there have been few reports on the synthesis of 1D $\text{Gd}_2\text{O}_3 : \text{Eu}^{3+}$ nanomaterials; for example, Jia et al. [19] had prepared $\text{Gd}_2\text{O}_3 : \text{Eu}^{3+}$ nanotubes via a wet-chemical route and a subsequent heat-treatment. Li et al. [28] had prepared $\text{Gd}_2\text{O}_3 : \text{Eu}^{3+}$ nanowires via AAO templated method, the method is complex, and the size of the obtained samples is limited by the template. Zhang et al. [29] had prepared $\text{Gd}_2\text{O}_3 : \text{Eu}^{3+}$ nanorods by surfactant-assisted hydrothermal method. Liu et al. [30] used MWCNTs as a template, coating gadolinium compounds on the carbon nanotube surface, followed by firing the carbon nanotube to obtain the $\text{Gd}_2\text{O}_3 : \text{Eu}^{3+}$ nanotubes, but the MWCNT template was difficult to remove afterwards. Herein, a large-scale uniform $\text{Gd}_2\text{O}_3 : \text{Eu}^{3+}$ nanowires were successfully prepared by a simple solvothermal method at the presence of polyethylene glycol followed by a subsequent calcination process, and the structure and properties were characterized.

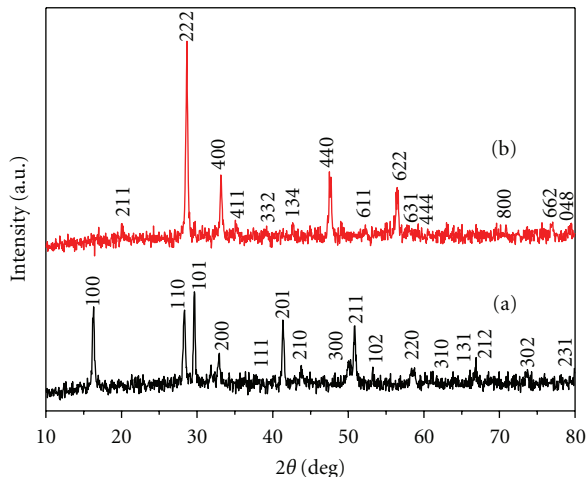


FIGURE 1: XRD patterns of the precursors (a) and the samples annealing at 800°C (b).

2. Experimental Section

2.1. Preparation. In a typical synthesis, first, 4.5349 g Gd_2O_3 and 1.7608 g Eu_2O_3 (purity: 99.99%, Shanghai Yuelong Non-Ferrous Metals Limited, China) were dissolved in a minimum amount of diluted nitric acid ($V_{HNO_3} : V_{H_2O} = 1 : 1$) and evaporated to dryness then dissolved in distilled water to form $0.1 \text{ mol} \cdot \text{L}^{-1}$ gadolinium nitrate and $0.05 \text{ mol} \cdot \text{L}^{-1}$ europium nitrate solutions.

Secondly, 30 mL absolute ethanol and 12.8 g polyethylene glycol (PEG, A.R., molecular weight is 2000, Shanghai Linger Chemical Company, China) were added into the mixture of a certain amount of $Gd(NO_3)_3$ and $Eu(NO_3)_3$ solutions according to the molar ratio of $Gd/Eu = 95 : 5$, in which the molar ratio of rare earth ion and the surfactant PEG is $1 : 2$. And then $4 \text{ mol} \cdot \text{L}^{-1}$ NaOH was added to adjust pH of 13; after being stirred for 30 minutes, the mixture was transferred into a 50 mL autoclave, sealed and heated at 180°C for 48 hours. After the autoclave was cooled to room temperature naturally, the precursors were filtered and washed with distilled water and absolute ethanol for three times, respectively. The final white products were obtained through a heat-treatment at 800°C in air for 2 hours after being dried at 80°C for 2 hours.

2.2. Characterization. The sample crystal structure was characterized by an Aolong Y-2000 X-ray Diffractometer (XRD) equipped with a $Cu K_{\alpha 1}$ radiation source ($\lambda = 0.154056 \text{ nm}$) and Ni filter at a scanning rate of $4^\circ \cdot \text{min}^{-1}$ (2θ from 10 to 80°), X-ray tube voltage and current were 40 kV and 20 mA, respectively, and the step was 0.02° . FTIR spectra were measured with Perkin-Elmer 580B Infrared Spectrophotometer with the KBr pellet technique. The morphologies of the samples and the selected area electron diffraction (SAED) pattern were observed using a JEOL JEM-2010 Transmission Electron Microscopy (TEM), and the voltage was 160 kV. Photoluminescence (PL) excitation and emission spectra of the samples were recorded with a

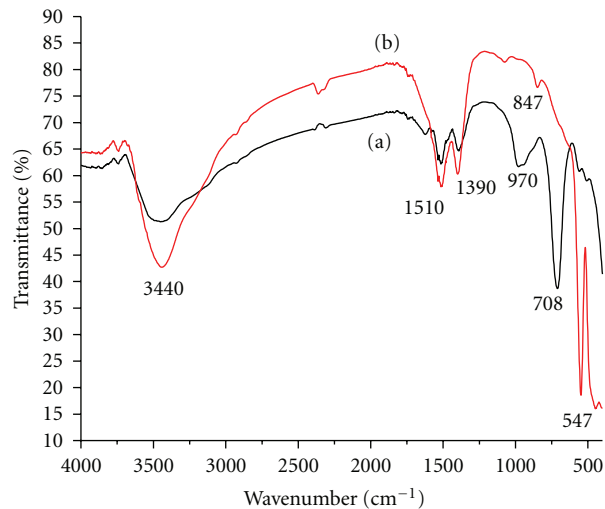


FIGURE 2: FTIR spectra of the precursors (a) and the samples annealing at 800°C (b).

HITACHI F-4500 Fluorescence Spectrophotometer using a Xe lamp as the excitation source, the measurement range is 200–800 nm, scanning rate is 1200 nm/min, and step length is 0.2 nm. All the measurements were performed at room temperature.

3. Results and Discussion

3.1. XRD Patterns. XRD patterns of the precursors and the calcined samples are shown in Figure 1, it is noted that the precursors are well indexed to be a pure hexagonal phase $Gd(OH)_3$, identical to the reported data in JCPDS card (83-2037), because the Eu content is low, there are no peaks of $Eu(OH)_3$, and the cell constants of $Gd(OH)_3$ are almost not changed. After annealing at the temperature of 800°C, the intensities and the positions of the peaks are all changed, and the diffraction peaks are coincided with the data of JCPDS card of (12-0797), which indicated that the calcined samples are pure cubic phase Gd_2O_3 . Moreover, it can be observed that the diffraction peaks of the calcined samples are very sharp and strong, indicating that the Gd_2O_3 samples with high crystallinity are synthesized by this method.

3.2. FTIR Spectra. Figure 2 shows the FTIR spectra of the precursors and the calcined samples; from Figure 2(a), the absorption peak at 3440 cm^{-1} is due to vibration of $-OH$ in H_2O , and the peaks at 1510 cm^{-1} and 1390 cm^{-1} are ascribed to the vibration of NO_3^- [31], which originated from the residue NO_3^- in the sample. The peak near 703 cm^{-1} is designed to vibration of $Gd-OH$, which indicated that the precursors are $Gd(OH)_3$. From Figure 2(b), it can be seen that the absorption peaks at 3440 cm^{-1} , 1510 cm^{-1} and 1390 cm^{-1} are stronger than those of the precursors; it is reported that the peaks in the wavelength range of 1400–1600 come from the carbonate groups and a weak peak at 847 cm^{-1} is due to the absorption of CO_3^{2-} [32]. Perhaps



FIGURE 3: TEM images of the calcined samples ((a), low magnification (b), high magnification) with its SAED pattern (c).

the samples absorbed the CO_2 and H_2O from the atmosphere during the measurement process and the storage course, and which led to the overlap of CO_3^{2-} and the residue NO_3^- . The important absorption peak at 547 cm^{-1} is ascribed to vibration of Gd-O , suggesting that the Gd(OH)_3 had

converted to Gd_2O_3 after calcinating; this result confirms the analysis from XRD patterns.

3.3. TEM Images. In order to study the morphology and the size of the as-prepared $\text{Gd}_2\text{O}_3:\text{Eu}^{3+}$ nanomaterials, the samples were investigated by TEM, which are shown in Figures 3(a) and 3(b). It is seen clearly that the samples comprise wire shapes and are generally well dispersed. The diameter of the wires is about 30 nm and the length reaches to micrometer scale. It is also observed that the samples are smooth and uniform. Figure 3(c) is the corresponding SAED pattern; one can see the (211), (222), (400), and (440) planes of the cubic phase Gd_2O_3 , which is in agreement with the XRD results.

3.4. Photoluminescence Spectra. The uniform $\text{Gd}_2\text{O}_3:\text{Eu}$ nanowires obtained by the solvothermal method exhibit a strong red emission under short UV irradiation, and the spectral properties are typical of the well-known $\text{Gd}_2\text{O}_3:\text{Eu}$ [24, 25, 27].

The excitation spectra of the precursors and the samples calcined at 800°C are drawn in Figure 4; the monitoring wavelength is $^5D_0 \rightarrow ^7F_2$ transition at 610 nm of the Eu^{3+} . It is noted that the excitation peaks of the precursors are weaker than those of the calcined samples. From the magnified spectrum of the inset, it is obvious that the strong excitation peak is near 250 nm, which originated from the charge transfer band of $\text{O}^{2-}-\text{Eu}^{3+}$, and the weak peak near 394 nm is due to the $^7F_0 \rightarrow ^5L_6$ transition of Eu^{3+} . After being calcined at 800°C , the excitation spectrum becomes stronger and it consists of an intense broad band near 232 and 247 nm, the former is due to the host absorption of Gd_2O_3 , and the latter is attributed to the charge transfer band (CTB) of $\text{O}^{2-}-\text{Eu}^{3+}$ [33]. The weak shoulder at 276 nm superimposed on the CTB of Eu^{3+} can be assigned to the 8S_6 transition line of Gd^{3+} [34]. The presence of the Gd_2O_3 host band and Gd^{3+} excitation line in the excitation spectrum of Eu^{3+} indicates that there exists an energy transfer from the Gd_2O_3 host band and Gd^{3+} to the doped Eu^{3+} [34]. At the same time, a series of weak intensity peaks near 314 nm, 394 nm, and 465 nm can be seen, which is supported to the $^7F_0 \rightarrow ^5H_6$, $^7F_0 \rightarrow ^5L_6$, $^7F_0 \rightarrow ^5D_2$ energy level transition of Eu^{3+} [34, 35].

Figure 5 shows the emission spectra of the precursors and the calcined samples, the excitation wavelength is the CTB of Eu^{3+} at 250 nm. From the magnified spectrum of the precursors, it can be seen that the emission spectrum consists of $^5D_0 \rightarrow ^7F_j$ ($j = 0, 1, 2$) line emissions of Eu^{3+} , the strongest emission peak is near 610 nm, which corresponds to the hypersensitive $^5D_0 \rightarrow ^7F_2$ transition of Eu^{3+} , and the line peak at 590 nm is due to $^5D_0 \rightarrow ^7F_1$ magnetic dipole transition, which emits orange red light. After being calcined at 800°C , the emission spectrum consists of $^5D_{0,1} \rightarrow ^7F_j$ ($J = 0, 1, 2, 3, 4$) line peaks of Eu^{3+} , that is 532 nm ($^5D_1 \rightarrow ^7F_1$), 578 nm ($^5D_0 \rightarrow ^7F_0$), 586, 590, 596 nm ($^5D_0 \rightarrow ^7F_1$), 610, 626 nm ($^5D_0 \rightarrow ^7F_2$), 647 nm ($^5D_0 \rightarrow ^7F_3$) and 704 nm ($^5D_0 \rightarrow ^7F_4$) [33–35]. The strongest emission peak is also at 610 nm ($^5D_0 \rightarrow ^7F_2$), which is the characteristic red emission of Eu^{3+} . In contrast to the peak

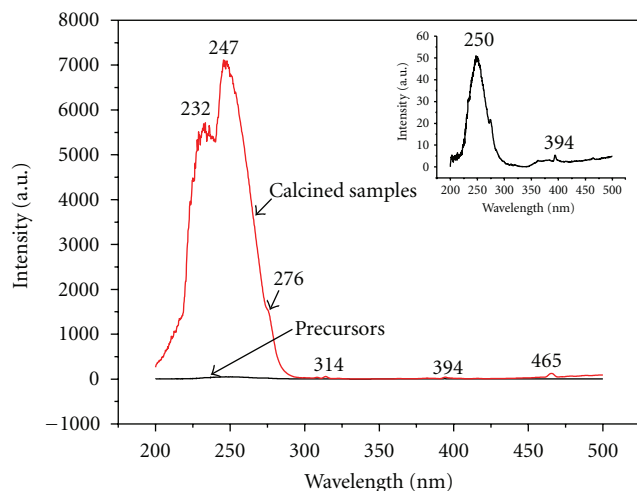


FIGURE 4: Excitation spectra of the precursors and the samples annealing at 800°C (the inset is the magnified spectrum of the precursors).

of 610 nm (${}^5D_0 \rightarrow {}^7F_2$), the peak at 590 nm (${}^5D_0 \rightarrow {}^7F_1$) is very weak. According to the selection rules and transition probabilities, ${}^5D_0 \rightarrow {}^7F_2$ electron dipole transition is the strongest emission when Eu^{3+} is located at a noninversion symmetry site. In a site with inversion symmetry the ${}^5D_0 \rightarrow {}^7F_1$ magnetic dipole transition is dominant. It is known that the ratio of ${}^5D_0 \rightarrow {}^7F_2$ (red light) to ${}^5D_0 \rightarrow {}^7F_1$ (orange red light) can be used to confirm the red color purity of the phosphors. Comparing the emission spectra of the precursors with the calcined samples, it is found that the ratio of ${}^5D_0 \rightarrow {}^7F_2$ to ${}^5D_0 \rightarrow {}^7F_1$ of the calcined samples is larger than that of the precursors, which confirmed that as red luminescence materials, the color purity of $\text{Gd}_2\text{O}_3:\text{Eu}^{3+}$ is superior to that of $\text{Gd}(\text{OH})_3:\text{Eu}^{3+}$, and also suggesting that as luminescence host, Gd_2O_3 is better than $\text{Gd}(\text{OH})_3$.

From the luminescence spectra, one can see that the intensity of the calcined samples ($\text{Gd}_2\text{O}_3:\text{Eu}^{3+}$) is much stronger than that of the precursors ($\text{Gd}(\text{OH})_3:\text{Eu}^{3+}$); it is supported that, in the precursors, the $-\text{OH}$ group originated from $\text{Gd}(\text{OH})_3:\text{Eu}^{3+}$, absorption surface H_2O and the impurities on the samples' surface are served as the quenching center for the luminescent materials, which decrease the intensity of the precursors. After the annealing process, the $\text{Gd}(\text{OH})_3$ converted to $\text{Gd}_2\text{O}_3:\text{Eu}^{3+}$, and the impurities dramatically decreased, which resulted in the increase of the intensity of the calcined samples.

4. Conclusion

In summary, large-scale $\text{Gd}_2\text{O}_3:\text{Eu}^{3+}$ luminescent nanowires have been successfully synthesized by a facile solvothermal method and followed by a subsequent heat-treatment. The morphology, crystal structure, and luminescence properties were characterized by TEM, XRD, FTIR, and PL. The results showed that the precursors are hexagonal phase $\text{Gd}(\text{OH})_3$ and the calcined samples are pure cubic phase Gd_2O_3 . The

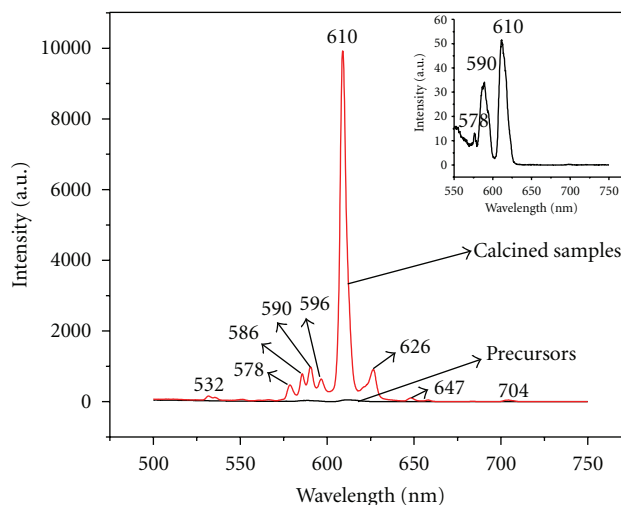


FIGURE 5: Emission spectra of the precursors and the samples annealing at 800°C (the inset is the magnified spectrum of the precursors).

as-obtained $\text{Gd}_2\text{O}_3:\text{Eu}^{3+}$ luminescent nanowires have the diameter of 30 nm and can stretch to micrometer lengths. The ratio of ${}^5D_0 \rightarrow {}^7F_2$ to ${}^5D_0 \rightarrow {}^7F_1$ for the intensity of the calcined sample is stronger than that of the precursors, confirming that the color purity of $\text{Gd}_2\text{O}_3:\text{Eu}^{3+}$ is better than that of $\text{Gd}(\text{OH})_3:\text{Eu}^{3+}$ for red phosphors. The as-prepared $\text{Gd}_2\text{O}_3:\text{Eu}^{3+}$ luminescent nanowires are potentially applied in red-emitting phosphors and field emission display devices. This facile method can be used to synthesize other rare earth oxide luminescence materials.

Acknowledgments

This work was financially supported by the National Nature Science Foundation of China (NSFC 50972020) and the Science and Technology Development Planning Project of Jinlin Province (Grant no. 20090528).

References

- [1] Y. Tian, Y. He, and Y. Zhu, "Low temperature synthesis and characterization of molybdenum disulfide nanotubes and nanorods," *Materials Chemistry and Physics*, vol. 87, no. 1, pp. 87–90, 2004.
- [2] G. Wu, L. Zhang, B. Cheng, T. Xie, and X. Yuan, "Synthesis of Eu_2O_3 nanotube arrays through a facile sol-gel template approach," *Journal of the American Chemical Society*, vol. 126, no. 19, pp. 5976–5977, 2004.
- [3] M. Yada, M. Mihara, S. Mouri, M. Kuroki, and T. Kijima, "Rare earth (Er, Tm, Yb, Lu) oxide nanotubes templated by dodecylsulfate assemblies," *Advanced Materials*, vol. 14, no. 4, pp. 309–313, 2002.
- [4] A. Vantomme, Z.-Y. Yuan, G. Du, and B.-L. Su, "Surfactant-assisted large-scale preparation of crystalline CeO_2 nanorods," *Langmuir*, vol. 21, no. 3, pp. 1132–1135, 2005.
- [5] J. Zhang and G. Hong, "Synthesis and photoluminescence of the $\text{Y}_2\text{O}_3:\text{Eu}^{3+}$ phosphor nanowires in AAO template," *Journal of Solid State Chemistry*, vol. 177, no. 4–5, pp. 1292–1296, 2004.

- [6] C. Wu, W. Qin, G. Qin, D. Zhao, J. Zhang, S. Huang, S. Lü, H. Liu, and H. Lin, "Photoluminescence from surfactant-assembled $Y_2O_3:Eu$ nanotubes," *Applied Physics Letters*, vol. 82, no. 4, pp. 520–523, 2003.
- [7] G. Liu and G. Hong, "Synthesis and photoluminescence of $Y_2O_3:RE^{3+}$ (RE = Eu, Tb, Dy) porous nanotubes templated by carbon nanotubes," *Journal of Nanoscience and Nanotechnology*, vol. 6, no. 1, pp. 120–124, 2006.
- [8] X. Bai, H. Song, L. Yu, L. Yang, Z. Liu, G. Pan, S. Lu, X. Ren, Y. Lei, and L. Fan, "Luminescent properties of pure cubic phase Y_2O_3/Eu^{3+} nanotubes/nanowires prepared by a hydrothermal method," *Journal of Physical Chemistry B*, vol. 109, no. 32, pp. 15236–15242, 2005.
- [9] Y. Mao, J. Y. Huang, R. Ostroumov, K. L. Wang, and J. P. Chang, "Synthesis and luminescence properties of erbium-doped Y_2O_3 nanotubes," *Journal of Physical Chemistry C*, vol. 112, no. 7, pp. 2278–2285, 2008.
- [10] X. Wang and Y. Li, "Synthesis and characterization of lanthanide hydroxide single-crystal nanowires," *Angewandte Chemie - International Edition*, vol. 41, no. 24, pp. 4790–4793, 2002.
- [11] Q. Tang, J. Shen, W. Zhou, W. Zhang, W. Yu, and Y. Qian, "Preparation, characterization and optical properties of terbium oxide nanotubes," *Journal of Materials Chemistry*, vol. 13, no. 12, pp. 3103–3106, 2003.
- [12] X. Wu, Y. Tao, F. Gao, L. Dong, and Z. Hu, "Preparation and photoluminescence of yttrium hydroxide and yttrium oxide doped with europium nanowires," *Journal of Crystal Growth*, vol. 277, no. 1–4, pp. 643–649, 2005.
- [13] B. Tang, J. Ge, and L. Zhuo, "The fabrication of $La(OH)_3$ nanospheres by a controllable-hydrothermal method with citric acid as a protective agent," *Nanotechnology*, vol. 15, no. 12, pp. 1749–1753, 2004.
- [14] X. Wang and Y. Li, "Rare-earth-compound nanowires, nanotubes, and fullerene-like nanoparticles: synthesis, characterization, and properties," *Chemistry*, vol. 9, no. 22, pp. 5627–5635, 2003.
- [15] X. Wang, X. Sun, D. Yu, B. Zou, and Y. Li, "Rare earth compound nanotubes," *Advanced Materials*, vol. 15, no. 17, pp. 1442–1445, 2003.
- [16] M. H. Zahir, T. Suzuki, Y. Fujishiro, and M. Awano, "Synthesis and characterization of Sm^{3+} -doped $Y(OH)_3$ and Y_2O_3 nanowires and their NO reduction activity," *Journal of Alloys and Compounds*, vol. 476, no. 1–2, pp. 335–340, 2009.
- [17] Z. Xu, Z. Hong, Q. Zhao, L. Peng, and P. Zhang, "Preparation and luminescence properties of $Y_2O_3:Eu^{3+}$ nanorods via post annealing process," *Journal of Rare Earths*, vol. 24, no. 2, pp. 111–114, 2006.
- [18] G. Jia, Y. H. Zheng, K. Liu, Y. H. Song, H. P. You, and H. J. Zhang, "Facile surfactant- and template-free synthesis and luminescent properties of one-dimensional $Lu_2O_3:Eu^{3+}$ phosphors," *Journal of Physical Chemistry C*, vol. 113, no. 1, pp. 153–158, 2009.
- [19] G. Jia, K. Liu, Y. Zheng, Y. Song, M. Yang, and H. You, "Highly uniform $Gd(OH)_3$ and $Gd_2O_3:Eu^{3+}$ nanotubes: facile synthesis and luminescence properties," *Journal of Physical Chemistry C*, vol. 113, no. 15, pp. 6050–6055, 2009.
- [20] N. Du, H. Zhang, X. Ma, D. Li, and D. Yang, "Controllable chemical reaction synthesis of $Tb(OH)_3$ nanorods and their photoluminescence property," *Materials Letters*, vol. 63, no. 13–14, pp. 1180–1182, 2009.
- [21] N. Du, H. Zhang, B. Chen, J. Wu, D. Li, and D. Yang, "Low temperature chemical reaction synthesis of single-crystalline $Eu(OH)_3$ nanorods and their thermal conversion to Eu_2O_3 nanorods," *Nanotechnology*, vol. 18, no. 6, Article ID 065605, 2007.
- [22] N. Du, H. Zhang, B. Chen, X. Ma, and D. Yang, "Ligand-free self-assembly of ceria nanocrystals into nanorods by oriented attachment at low temperature," *Journal of Physical Chemistry C*, vol. 111, no. 34, pp. 12677–12680, 2007.
- [23] A. Bril and W. L. Wanmaker, "Fluorescent properties of some europium-activated phosphors," *Journal of Electrochemistry Society*, vol. 111, pp. 1363–1368, 1964.
- [24] Y. Li, G. Liu, and G. Hong, "Synthesis and luminescence properties of $Gd_2O_3:Eu^{3+}$ phosphors," *Journal of Rare Earths*, vol. 22, no. 1, pp. 70–74, 2004.
- [25] B. Mercier, C. Dujardin, G. Ledoux, C. Louis, O. Tillement, and P. Perriat, "Observation of the gap blueshift on $Gd_2O_3:Eu^{3+}$ nanoparticles," *Journal of Applied Physics*, vol. 96, no. 1, pp. 650–653, 2004.
- [26] G.-X. Liu, G.-Y. Hong, and D.-X. Sun, "Preparation of spherical nanometer $Gd_2O_3:Eu$ luminescent materials," *Chinese Journal of Inorganic Chemistry*, vol. 20, no. 11, pp. 1367–1370, 2004 (Chinese).
- [27] G.-X. Liu, J.-X. Wang, X.-T. Dong, and G.-Y. Hong, " $Gd_2O_3:Eu^{3+}$ luminescent nano-materials prepared by sol-lyophilization method," *Journal of Inorganic Materials*, vol. 22, no. 5, pp. 803–806, 2007 (Chinese).
- [28] S. Li, H. Song, H. Yu, S. Lu, X. Bai, G. Pan, Y. Lei, L. Fan, and T. Wang, "Influence of annealing temperature on photoluminescence characteristics of $Gd_2O_3:Eu/AAO$ nanowires," *Journal of Luminescence*, vol. 122–123, no. 1–2, pp. 876–878, 2007.
- [29] S. Zhang, G.-X. Liu, X.-T. Dong, J.-X. Wang, and H. Y. Bao, "Preparation and photoluminescence properties of $Gd_2O_3:Eu^{3+}$ nanorods," *Chemical Journal of Chinese Universities*, vol. 30, no. 1, pp. 7–10, 2009 (Chinese).
- [30] G. Liu, G. Hong, X. Dong, and J. Wang, "Preparation and characterization of $Gd_2O_3:Eu^{3+}$ luminescence nanotubes," *Journal of Alloys and Compounds*, vol. 466, no. 1–2, pp. 512–516, 2008.
- [31] Z. Xu, J. Yang, Z. Hou, C. Li, C. Zhang, S. Huang, and J. Lin, "Hydrothermal synthesis and luminescent properties of $Y_2O_3:Tb^{3+}$ and $Gd_2O_3:Tb^{3+}$ microrods," *Materials Research Bulletin*, vol. 44, no. 9, pp. 1850–1857, 2009.
- [32] C. Louis, R. Bazzi, M. A. Flores, W. Zheng, K. Lebbou, O. Tillement, B. Mercier, C. Dujardin, and P. Perriat, "Synthesis and characterization of $Gd_2O_3:Eu^{3+}$ phosphor nanoparticles by a sol-lyophilization technique," *Journal of Solid State Chemistry*, vol. 173, no. 2, pp. 335–341, 2003.
- [33] M. L. Pang, J. Lin, J. Fu, R. B. Xing, C. X. Luo, and Y. C. Han, "Preparation, patterning and luminescent properties of nanocrystalline $Gd_2O_3:A(A = Eu^{3+}, Dy^{3+}, Sm^{3+}, Er^{3+})$ phosphor films via Pechini sol-gel soft lithography," *Optical Materials*, vol. 23, no. 3–4, pp. 547–558, 2003.
- [34] J. Yang, C. Li, Z. Cheng, X. Zhang, Z. Quan, C. Zhang, and J. Lin, "Size-tailored synthesis and luminescent properties of one-dimensional $Gd_2O_3:Eu^{3+}$ nanorods and microrods," *Journal of Physical Chemistry C*, vol. 111, no. 49, pp. 18148–18154, 2007.
- [35] J. Yang, Z. Quan, D. Kong, X. Liu, and J. Lin, " $Y_2O_3:Eu^{3+}$ microspheres: solvothermal synthesis and luminescence properties," *Crystal Growth and Design*, vol. 7, no. 4, pp. 730–735, 2007.

Research Article

Synthesis and Fluorescence Property of Mn-Doped ZnSe Nanowires

Dongmei Han,^{1,2} Chunfeng Song,^{1,3} and Xiaoyu Li^{1,3}

¹ School of Materials Science and Engineering, Beijing University of Chemical Technology, Beijing 100029, China

² State Key Laboratory of Chemical Resource Engineering, Beijing University of Chemical Technology, Beijing 100029, China

³ Key Laboratory for Nanomaterials, Beijing University of Chemical Technology, Ministry of Education, Beijing 100029, China

Correspondence should be addressed to Xiaoyu Li, lixy@mail.buct.edu.cn

Received 1 November 2009; Revised 27 April 2010; Accepted 27 May 2010

Academic Editor: Raymond Whitby

Copyright © 2010 Dongmei Han et al. This is an open access article distributed under the Creative Commons Attribution License, which permits unrestricted use, distribution, and reproduction in any medium, provided the original work is properly cited.

Water-soluble Mn-doped ZnSe luminescent nanowires were successfully prepared by hydrothermal method without any heavy metal ions and toxic reagents. The morphology, composition, and property of the products were investigated. The experimental results showed that the Mn-doped ZnSe nanowires were single well crystallized and had a zinc blende structure. The average length of the nanowires was about 2–3 μm , and the diameter was 80 nm. With the increase of Mn^{2+} -doped concentration, the absorbance peak showed large difference. The UV-vis absorbance spectrum showed that the Mn-doped ZnSe nanowires had a sharp absorption band appearing at 360 nm. The PL spectrum revealed that the nanowires had two distinct emission bands centered at 432 and 580 nm.

1. Introduction

As biomedical labeling reagents, high-quality colloidal luminescent semiconductor nanocrystals, such as CdSe, have attracted much attention because of their apparent, narrow, and symmetric photoluminescence, broad and intense absorption band, and tunable emission peak positions [1, 2]. However, many results indicate that any leakage of cadmium from the nanocrystals would be toxic and fatal to biological systems. Some attempts have been made to develop non-cadmium materials. Transition metal ion-doped quantum dots (d-dots) can meet this requirement. The sp-d exchange interaction between the semiconductor and the transition metal ions induces unique optoelectronic properties [3]; Mn-doped II-VI semiconductors arouse general interest in particular, [4–6]. As a wide-band-gap material, ZnSe is suitable for the fabrication of various optoelectronic devices, biolabeling, and hosts for the formation of doped nanocrystal [7–9]. Recent researches have been carried out to explore for the synthesis of transition metal ion-doped ZnSe nanocrystals such as Cu⁺, Mn²⁺, and Co-doped ZnSe nanomaterials. [10–12]

At present, the main method of preparing transition metal ion-doped ZnSe nanomaterials is colloid chemistry

route. The experiments are typically carried out with high temperature, toxic, and explosive chemical reagents. In particular, as-prepared products cannot be directly dispersed in the water phase due to their hydrophobic surfaces. A further reaction is needed to achieve the phase transfer for the aqueous environment. More recently, Nie and his co-workers [13] developed an alternative method to synthesize nanocrystals in aqueous solution. On the basis of those and other encouraging results [14, 15], we recently focused on the possibilities to synthesize metal ion-doped ZnSe directly in aqueous solution and explored the impact of system on morphology and performance of the nanomaterials.

In this paper, we report on the preparation of high-crystalline Mn-doped ZnSe nanowires (NWs) by a simple method, solution synthetic methodology using α -cyclodextrins as stabilizer, and investigated the relationship between the structures and the properties.

2. Experimental

All chemicals and solvents in our work were commercial products used as received without further purification. α -cyclodextrin (α -CD) was a product of Alfa Company, selenium powder (99.95%) was obtained from Beijing Reagent

Company. Zinc acetate ($\text{Zn}(\text{OAc})_2 \cdot 2\text{H}_2\text{O}$), manganese acetate ($\text{Mn}(\text{OAc})_2 \cdot 4\text{H}_2\text{O}$), sodium sulfite, sodium hydroxide (NaOH), sodium citrate, and anhydrous ethanol were analytical grade and purchased from Beijing Reagent Company. Deionized water was used throughout all experiments.

The synthesis of ZnSe and Mn-doped ZnSe nanowires was adapted from a procedure developed for CdSe nanoparticles [16]. A brief description is provided as follows. A total of 0.2588 g of sodium citrate, 10 mL of 0.04 M $\text{Zn}(\text{OAc})_2$ solution and 0.08 mmol $\text{Mn}(\text{OAc})_2$ were added to 225 mL of deionized water. Under the magnetic agitation, 2 g of α -CD was introduced to the flask. After the pH value was adjusted to 10 with 1 M NaOH solution, the mixture was purged with N_2 for 30 min. Then 6 mL of 0.05 M Na_2SeSO_3 solution was added. When mixed uniformly, the solution was transferred to the vessel. It was laid to the oven with temperature 180°C for 4 days. After being naturally cooled to the room temperature, the mixture was centrifuged at 5000 rpm/min for 10 minutes and washed several times by deionized water and absolute ethanol. Having dried in vacuum at 80°C for 3 hours, the yellow products were obtained.

The transmission electron microscope (TEM) images were taken by H-800 microscope with an acceleration voltage of 80 kV. The high-resolution TEM images were obtained by employing a JEOL 3010 microscopy with a 300 kV accelerating voltage. Samples for TEM were prepared by placing a drop of the sample suspension on a copper grid coated with carbon and were allowed to dry in air. The samples were characterized by X-ray diffraction (XRD), with scanning rate $10^\circ/\text{min}$, on D/max 2500 VB2+/PC X-ray diffractometer using graphite monochromatized $\text{Cu K}\alpha$ radiation ($\lambda = 1.5406 \text{ \AA}$). The UV-vis absorbance spectra were obtained on a Shimadzu UV-3150 spectrophotometer in the range of 200~800 nm at room temperature. Optical densities were kept within 0.2 at the excitation wavelength. The photoluminescence (PL) spectra of the as-prepared Mn-doped ZnSe nanomaterials were measured using a Varian Cary-Eclipse fluorophotometer.

3. Results and Discussion

The XRD patterns of the ZnSe and Mn-doped ZnSe NWs are displayed in Figure 1. The XRD peaks of the undoped ZnSe NWs can be well indexed to zinc blende ZnSe crystals (JCPDS Card No. 37-1463). In the case of Mn-doped ZnSe NWs synthesized under the same conditions, the peaks are also indexed to zinc blende ZnSe. However, the main peaks of (111), (220), and (311) planes move 0.19° to the left because Mn was implanted to ZnSe internal lattice. The peak intensities at 2θ of $\sim 31.0^\circ$ [(200) plane] and $\sim 57.0^\circ$ [(222) plane] are markedly increased, which indicates that these Mn-doped nanowires have more advantages on growth along the two directions. The peaks which are observed at $\sim 38.0^\circ$ and 49.5° match those of wurtzite phase [(102) plane] and [(103) plane] because the synthesis process is affected by the introduction of impurity ions Mn^{2+} into the host lattice which can significantly affect the reaction rate, which is reflected by a reduction in the crystal phase [17].

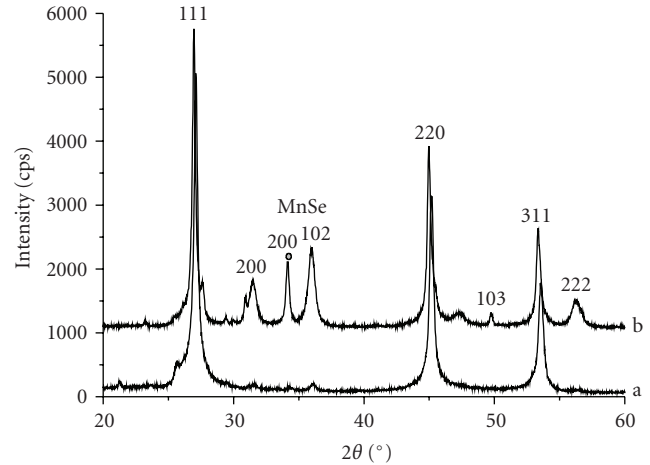


FIGURE 1: XRD patterns of the ZnSe (a) and Mn-doped ZnSe (b) nanowires.

It is similar to the characters of the Mn-ZnSe nanoparticles reported by Mahamuni and coworkers [18]. A similar effect has also been reported for Mn^{2+} -doped ZnSe nanowires prepared using the high-temperature organometallic synthesis route [19]. The peak at $\sim 34.0^\circ$ is observed that matches those of MnSe [(200) plane] which indicates that there may be a small amount of MnSe produced.

Figure 2 shows the TEM images for Mn-doped ZnSe nanowires. The average length is about 2-3 μm . It reveals that they are all straight and have a smooth surface without any nanoparticle impurities. Their average diameter is 80 nm. This result is different from other cases. Colloidal Mn-doped ZnSe nanomaterials prepared in the solvent of the typical TOP/HDA/TOPO system are generally particles with the size of several nanometers. In an improved method, nanowires are obtained mostly with the diameter of several nanometers and length up to 200 nm [17].

The high-resolution TEM image of the nanowires and corresponding fast Fourier transformed electron diffraction (FFT ED) pattern are displayed, respectively. From the further analysis, it was found that the growths of crystal lattice are clear, even though the nanowires are very thick. The selected area ED pattern, consisted of discrete and bright spots, indicating that the nanowires are all typically single well-crystallized diffraction pattern of ZnSe. The ED pattern confirms that the zinc blende-structured ZnSe nanowires grow along the (200) direction. The image shows that the highly crystalline (200) planes, separated by 2.819 \AA , are close to that of cubic structured ZnSe crystal 2.834 \AA .

UV-vis absorption spectra of Mn-doped ZnSe NWs with different Mn^{2+} -doped concentrations are presented in Figure 3. An interesting pattern was revealed by this set of experiments. The absorption peaks of all samples are very strong. With the increase of Mn^{2+} -doped concentration, the absorbance shows large difference. The two weak absorption peaks of 5% Mn-doped ZnSe NWs emerge at 250 nm and 370 nm. While Mn^{2+} -doped concentration is increased to 10%, the location of absorption peak is at 360 nm with stronger absorption intensity, but the absorption peaks are

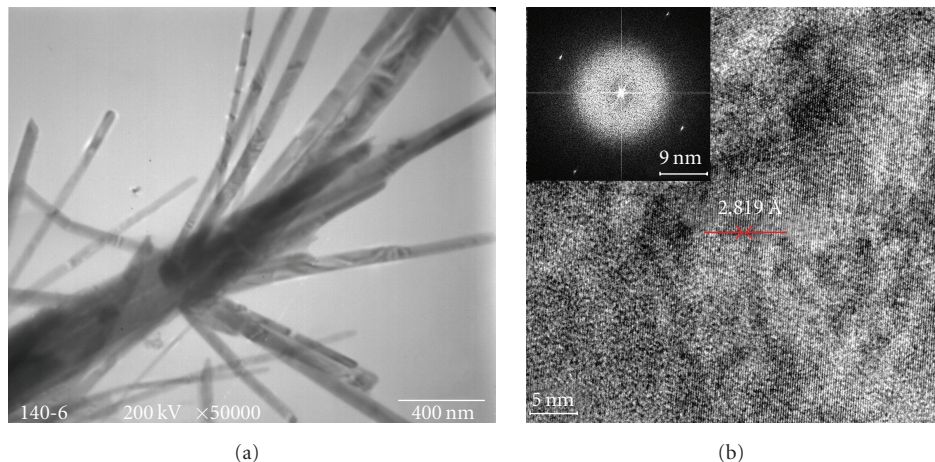


FIGURE 2: TEM images of the Mn-doped ZnSe nanowires, HRTEM, and its SAED pattern images (inset).

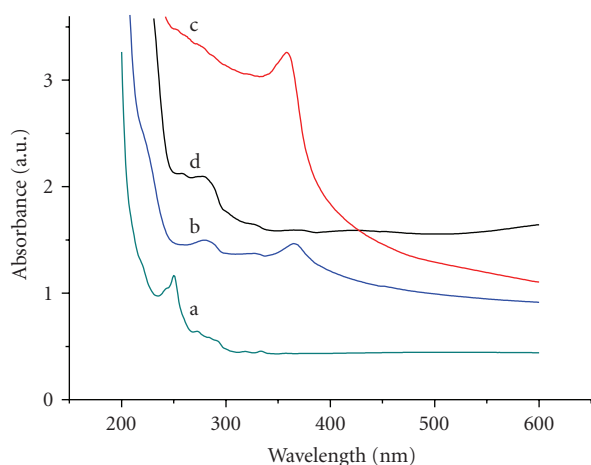


FIGURE 3: Absorption spectra of Mn-doped ZnSe with different Mn^{2+} -doped concentrations (a: 0; b: 5%; c: 10%; d: 20%).

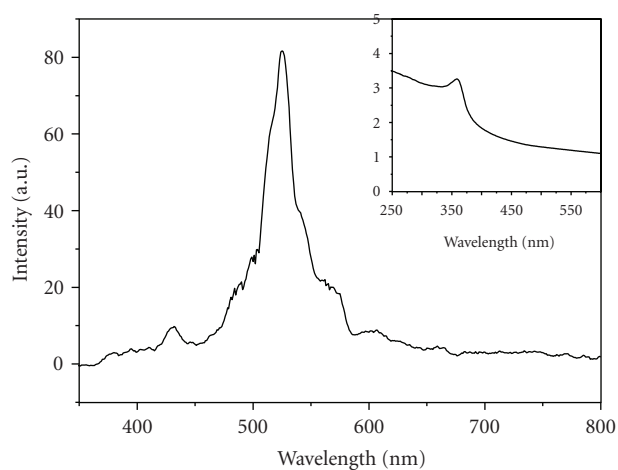


FIGURE 4: Photoluminescence spectrum and the absorption spectrum (inset) of Mn-doped ZnSe.

similar with the pure ZnSe except of small red shift when the doped concentration is 20%. It has been reported that the transition metal ion-doped semiconductor could form a doping energy level with the band gap of ZnSe [20]. The doping concentration could have an influence on optical properties to a large extent.

In our case, when doping concentration is low (5%), the content of Mn is inadequate to reduce the band gap of ZnSe which results in ZnSe characteristic absorption and doped absorption emerging at the same time. The optimal doping concentration is 10%. The dopant can serve to retard charge traps and effectively reduce the band gap within the suitable concentration. When the doping concentration is too high (20%), the inconsistency of precipitation reaction may lead to precipitation separation and dopants failure to enter the internal lattice [20].

Figure 4 shows the optical absorption feature of Mn-doped ZnSe NWs (10% Mn^{2+} -doped concentration). A

sharp absorption band appears at 360 nm. A red shift in the absorption band compared with pure ZnSe nanoparticles [14] suggests that the injected metal ions are isomorphic to Zn^{2+} ions and decrease the band gap. The corresponding luminescence spectrum with 350 nm excitation wavelength shows signs of two distinct emission bands centered at 432 and 540 nm, respectively. These bands can be assigned to ZnSe trap state and $\text{Mn}^{2+} {}^4T_1 \rightarrow {}^6A_1$ emission. The half-peak-wide of the highest emission peak is 29 nm, which is very narrow and almost symmetrical.

Band-edge luminescence and Mn^{2+} -related luminescence are competing processes. The absorption of a photon leads to the formation of an exciton. Luminescence results from recombination of the exciton as well as from the energy transfer to Mn^{2+} d-d levels. Mn^{2+} doping clearly leads the near-band-edge luminescence at 412 nm to the disappearance of, and the manganese orange emission band emerges at about 580 nm in Mn-doped ZnSe nanowires [18].

4. Conclusion

In summary, Mn-doped ZnSe nanowires were synthesized by hydrothermal method using α -cyclodextrins as stabilizer. It was a convenient, efficient method to obtain the transition metal ion-doped one-dimensional ZnSe nanomaterial which can be directly dispersed in the water phase. The average length of nanowires was about 2–3 μm , and the diameter was 80 nm. Mn-doped ZnSe NWs were indexed to zinc blende ZnSe crystals. After being doped, the peak of the absorption spectra of the nanowires appeared at 360 nm, and their emission band lied at about 580 nm. This method is simple for synthesizing Mn-doped ZnSe nanowires and provides a flexible approach for applications of biomedical labeling reagents.

Acknowledgment

This paper was financially supported by the National Natural Science Foundation of China (no. 50673008).

References

- [1] X. Peng, M. C. Schlamp, A. V. Kadavanich, and A. P. Alivisatos, "Epitaxial growth of highly luminescent CdSe/CdS core/shell nanocrystals with photostability and electronic accessibility," *Journal of the American Chemical Society*, vol. 119, no. 30, pp. 7019–7029, 1997.
- [2] B. O. Dabbousi, J. Rodriguez-Viejo, F. V. Mikulec et al., "(CdSe)ZnS core-shell quantum dots: synthesis and characterization of a size series of highly luminescent nanocrystallites," *Journal of Physical Chemistry B*, vol. 101, no. 46, pp. 9463–9475, 1997.
- [3] B. Steitz, Y. Axmann, H. Hofmann, and A. Petri-Fink, "Optical properties of annealed Mn^{2+} -doped ZnS nanoparticles," *Journal of Luminescence*, vol. 128, no. 1, pp. 92–98, 2008.
- [4] P. V. Radovanovic, C. J. Barrelet, S. Gradecak, F. Qian, and C. M. Lieber, "General synthesis of manganese-doped II-VI and III-V semiconductor nanowires," *Nano Letters*, vol. 5, no. 7, pp. 1407–1411, 2005.
- [5] P. Lommens, F. Loncke, P. F. Smet et al., "Dopant incorporation in colloidal quantum dots: a case study on Co^{2+} doped ZnO," *Chemistry of Materials*, vol. 19, no. 23, pp. 5576–5583, 2007.
- [6] D. -L. Hou, X. -J. Ye, H. -J. Meng et al., "Magnetic properties of Mn-doped ZnO powder and thin films," *Materials Science and Engineering B*, vol. 138, no. 2, pp. 184–188, 2007.
- [7] R. Tu, B. Liu, Z. Wang et al., "Amine-capped ZnS- Mn^{2+} nanocrystals for fluorescence detection of trace TNT explosive," *Analytical Chemistry*, vol. 80, no. 9, pp. 3458–3465, 2008.
- [8] N. Pradhan, D. Goorskey, J. Thessing, and X. Peng, "An alternative of CdSe nanocrystal emitters: pure and tunable impurity emissions in ZnSe nanocrystals," *Journal of the American Chemical Society*, vol. 127, no. 50, pp. 17586–17587, 2005.
- [9] L. Zu, D. J. Norris, T. A. Kennedy, S. C. Erwin, and A. L. Efros, "Impact of ripening on manganese-doped ZnSe nanocrystals," *Nano Letters*, vol. 6, no. 2, pp. 334–340, 2006.
- [10] B. Xi, D. Xu, S. Xiong et al., "Preparation and characterization of cubic and hexagonal polytypes of ZnSe: Cu^{2+} one-dimensional nanostructures," *Journal of Physical Chemistry C*, vol. 112, no. 14, pp. 5333–5338, 2008.
- [11] N. Pradhan and X. Peng, "Efficient and color-tunable Mn-doped ZnSe nanocrystal emitters: control of optical performance via greener synthetic chemistry," *Journal of the American Chemical Society*, vol. 129, no. 11, pp. 3339–3347, 2007.
- [12] N. S. Norberg, G. L. Parks, G. M. Salley, and D. R. Gamelin, "Giant excitonic zeeman splittings in colloidal Co^{2+} -doped ZnSe quantum dots," *Journal of the American Chemical Society*, vol. 128, no. 40, pp. 13195–13203, 2006.
- [13] W. C. W. Chan and S. Nie, "Quantum dot bioconjugates for ultrasensitive nonisotopic detection," *Science*, vol. 281, no. 5385, pp. 2016–2018, 1998.
- [14] N. Murase and M. Gao, "Preparation and photoluminescence of water-dispersible ZnSe nanocrystals," *Materials Letters*, vol. 58, no. 30, pp. 3898–3902, 2004.
- [15] N. O. Dantas, L. Damigo, F. Qu et al., "Raman investigation of ZnO and $\text{Zn}_{1-x}\text{Mn}_x\text{O}$ nanocrystals synthesized by precipitation method," *Journal of Non-Crystalline Solids*, vol. 354, no. 42–44, pp. 4827–4829, 2008.
- [16] K. Palaniappan, C. Xue, G. Arumugam, S. A. Hackney, and J. Liu, "Water-soluble, cyclodextrin-modified CdSe-CdS core-shell structured quantum dots," *Chemistry of Materials*, vol. 18, no. 5, pp. 1275–1280, 2006.
- [17] P. T. K. Chin, J. W. Stouwdam, and R. A. J. Janssen, "Highly luminescent ultranarrow Mn doped ZnSe nanowires," *Nano Letters*, vol. 9, no. 2, pp. 745–750, 2009.
- [18] S. Mahamuni, A. D. Lad, and S. Patole, "Photoluminescence properties of manganese-doped zinc selenide quantum dots," *Journal of Physical Chemistry C*, vol. 112, no. 7, pp. 2271–2277, 2008.
- [19] T. J. Norman Jr., D. Magana, T. Wilson et al., "Optical and surface structural properties of Mn^{2+} -doped ZnSe nanoparticles," *Journal of Physical Chemistry B*, vol. 107, no. 26, pp. 6309–6317, 2003.
- [20] Y. Zhang, C. Gan, J. Muhammad, D. Battaglia, X. Peng, and M. Xiao, "Enhanced fluorescence intermittency in Mn-doped single ZnSe quantum dots," *Journal of Physical Chemistry C*, vol. 112, no. 51, pp. 20200–20205, 2008.

Review Article

The Progress of Photoluminescent Properties of Rare-Earth-Ions-Doped Phosphate One-Dimensional Nanocrystals

Lixin Yu and Hai Liu

Department of Materials Science and Engineering, Nanchang University, Nanchang 330031, China

Correspondence should be addressed to Lixin Yu, yulixin72@yahoo.com.cn

Received 5 November 2009; Accepted 3 March 2010

Academic Editor: Renzhi Ma

Copyright © 2010 L. Yu and H. Liu. This is an open access article distributed under the Creative Commons Attribution License, which permits unrestricted use, distribution, and reproduction in any medium, provided the original work is properly cited.

One-dimensional (1D) nanostructures, such as tubes, wires, rods, and belts, have aroused remarkable attentions over the past decade due to a great deal of potential applications, such as data storage, advanced catalyst, and photoelectronic devices. On the other hand, in comparison with zero-dimensional (0D) nanostructures, the space anisotropy of 1D structures provided a better model system to study the dependence of electronic transport, optical and mechanical properties on size confinement and dimensionality. Rare earth (RE) compounds, were intensively applied in luminescent and display devices. It is expected that in nanosized RE compounds the luminescent quantum efficiency (QE) and display resolution could be improved. In this paper, we systematically reported the research progress of luminescent properties of RE-doped 1D orthophosphate nanocrystal, including the synthesis of 1D nanostructures doped with RE ions, local symmetry of host, electronic transition processes, energy transfer (ET), and so forth.

1. Introduction

It is well known that the reduction of particle size of crystalline system can result in remarkable modification of their properties which are different from those of microsized hosts because of surface effect and quantum confinement effect of nanometer materials. In 1994, Bhargava et al. reported that radiative transition rate of ZnS:Mn nanocrystals increased five orders in comparison with bulk one [1]. Although this result was strongly criticized later, the studies on nanosized luminescent semiconductor attracted great interests [2–6]. RE compounds were extensively applied in luminescence and display, such as lighting, field emission display (FED), cathode ray tubes (CRT), and plasma display panel (PDP) [7–11]. Lanthanide orthophosphate (LnPO_4) belongs to two polymorphic types, the monoclinic monazite type (for La to Gd) and quadratic xenotime type (for Tb to Lu). Due to its high QE, bulk lanthanide phosphate as an ideal host in fluorescent lamps, CRT and PDP, has been extensively investigated [12–14]. It is expected that nanosized RE compounds can increase luminescent QE and display resolution. To improve

luminescent properties of nanocrystalline phosphors, many preparation methods have been used, such as solid state reactions, sol-gel techniques, hydroxide precipitation, hydrothermal synthesis, spray pyrolysis, laser-heated evaporation, and combustion synthesis. Currently, the luminescent RE-doped 1D nanocrystals such as LaPO_4 :RE nanowires [15–19], Y_2O_3 :RE and La_2O_3 :Eu nanotubes/nanowires [20–25], and YVO_4 :Eu nanowires/nanorods [26–28]. have also attracted considerable interests. 1D structures, such as tubes, wires, rods, and belts, have aroused remarkable attentions over past decade due to a great deal of potential applications, such as data storage [29], advanced catalyst [30], and photoelectronic devices [31]. On the other hand, in comparison with 0D structures, the space anisotropy of 1D structures provided a better model system to study the dependence of electronic transport and optical and mechanical properties on size confinement and dimensionality [32]. To develop 1D phosphors, a basic question should be answered: could the photoluminescent properties for 1D nanocrystals be improved than 0D ones as well as the micrometer materials, the so-called bulk materials? In this review, we concentrated

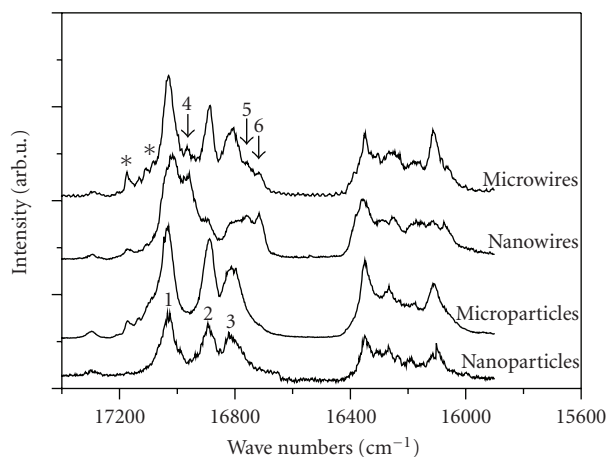


FIGURE 1: High-resolution spectra of $\text{LaPO}_4:\text{Eu}^{3+}$ bulk, nanoparticles, and nanowires at 10 K under 266 nm light excitation (delay time is 50 μs). (J. Phys. Chem. B 2004, 108, 16697; Appl. Phys. Lett. 2004, 85, 470).

on the study progress of photoluminescent properties of RE ions in phosphate 1D nanocrystals.

2. The Synthesis of Phosphate 1D Nanocrystals Doped with RE

In 1999, Meyssamy et al. reported the preparation of $\text{LaPO}_4:\text{Eu}^{3+}/\text{Tb}^{3+}$ nanowires by a hydrothermal method and studied their luminescent properties for the first time [15]. After then, researchers prepared phosphate 1D nanocrystals doped with RE ions by different synthesis techniques, such as hydrothermal method to prepare $\text{LaPO}_4:\text{Ce}^{3+}/\text{Eu}^{3+}$ nanofibers [33], $\text{CePO}_4:\text{Tb}^{3+}$ colloidal nanocrystals [34], $\text{CePO}_4:\text{Tb}^{3+}/\text{LaPO}_4$ nanowires core-shell structures [35, 36], and LnPO_4 ($\text{Ln} = \text{RE}$) nanowires and nanosheets [19]. It should be noted that these reports mainly emphasize the morphology control through changing synthesis conditions. To our knowledge, although LnPO_4 1D nanocrystals doped with RE ions with different shapes were prepared by the wet chemistry method by many groups, the luminescent properties, especially electronic transition processes and ET processes, were not further studied. Our group systemically reported luminescent characteristics of $\text{LnPO}_4:\text{RE}$ ($\text{Ln} = \text{La}, \text{Gd}$) nanowires and nanorods. Song and Yu et al. systemically and further investigated the $\text{LaPO}_4:\text{Eu}^{3+}/\text{Tb}^{3+}$ nanowires photoluminescent properties in comparison with 0D nanoparticles and bulk materials, especial electronic transition process and ET.

3. Local Symmetry of Eu^{3+} in 1D Nanocrystals

Because Eu^{3+} ions were hypersensitive to local structures, they can be used as a fluorescent probe to detect the microstructures surrounding Eu^{3+} ions. In previous research, the local environmental around Eu^{3+} ions in 0D nanoparticles was systematically studied. Many groups reported the appearance of additional sites of Eu^{3+} ions in Y_2O_3 and

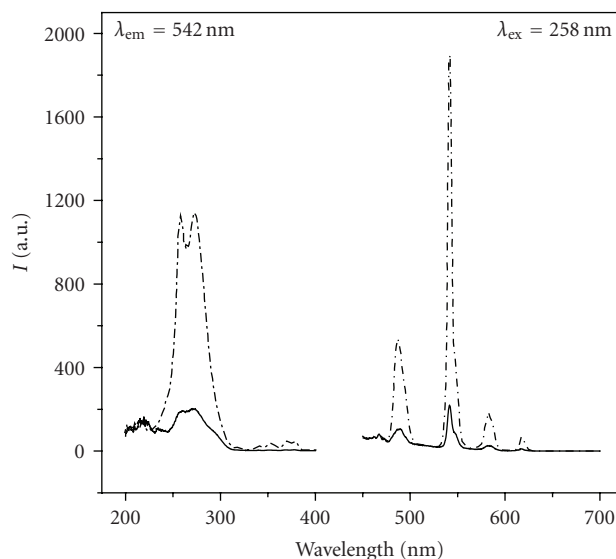


FIGURE 2: The excitation spectra (left) and emission (right) for $\text{LaPO}_4:1\%\text{Ce}, 2.5\%\text{Tb}$ samples. Solid lines and dash dots represented the microrods and nanowires, respectively. (J. Phys. Chem. B 2005, 109, 11450).

YBO_3 nanoparticles through high-resolution spectra at low temperature [37–40]. They contributed the origin of additional sites of Eu^{3+} doped nanoparticles to the surface effect because the disorder of atoms at the surface of nanoparticles increased on comparison with the inside atoms. Although $\text{LnPO}_4:\text{Eu}^{3+}$ 1D nanowires/nanorods were prepared and their basic spectra were researched, the dependence of local symmetry on shape was not studied. Song and Yu et al. investigated the microstructures of Eu^{3+} doped 1D LaPO_4 nanowires in contrast with 0D nanoparticles and corresponding micrometer hosts (micrometer particles and rods) [16, 18, 41]. The LaPO_4 nanoparticles, nanowires, and bulk materials were synthesized by the same synthesis technique, a hydrothermal method. All samples were at monazite phase and no additional phases were observed. The size of $\text{LaPO}_4:\text{Eu}^{3+}$ nanoparticles is ranging from 10 to 20 nm. The diameter of $\text{LaPO}_4:\text{Eu}^{3+}$ nanowires ranges from 10 to 20 nm, and the length is about several hundreds nanometer. They observed that the Eu^{3+} ions locate new site in nanowires due to shape effect. Figure 1 shows the high-resolution spectra of $\text{LaPO}_4:\text{Eu}^{3+}$ nanomaterials and bulk materials at 266 nm pulsed laser excitation at 10 K. The emission associated with ${}^5\text{D}_0\text{-}{}^7\text{F}_1$ transitions is quite different between nanoparticles and nanowires at 10 K. In the nanoparticles, three ${}^5\text{D}_0\text{-}{}^7\text{F}_1$ emission lines were observed, locating at $17025 \pm 2 \text{ cm}^{-1}$ (L1), $16898 \pm 2 \text{ cm}^{-1}$ (L2), and $16815 \pm 2 \text{ cm}^{-1}$ (L3), respectively. In the nanowires, besides the same lines 1–3, three additional lines 4–6 were observed, locating at $16963 \pm 2 \text{ cm}^{-1}$ (L4), $16758 \pm 2 \text{ cm}^{-1}$ (L5), and $16718 \pm 2 \text{ cm}^{-1}$ (L6), respectively. The ${}^5\text{D}_0\text{-}{}^7\text{F}_1$ lines in the microparticles are identical with the nanoparticles. For the microrods, lines 1–6 were also observed. However, the relative intensity of lines 4–6 becomes weaker in comparison with that in nanowires. ${}^7\text{F}_1$ associated with one site symmetry can split into three

TABLE 1: A list of parameters W_1 , $W_{10}(0)$ and the internal luminescent QE at 0 K in different powders.

Parameters	nanoparticles	nanowires	microparticles	microrods
W_1 (ms ⁻¹)	14.9	28.9	17.6	16.5
W_{10} (ms ⁻¹)	24.1	19.7	17.8	18.5
QE	38%	59%	49%	47%

Stark lines in the crystal field. The results in Figure 1 indicate that in nanoparticles and microrods, the 5D_0 - 7F_1 transitions are from one crystalline site, A, while in nanowires and microrods, the 5D_0 - 7F_1 transitions come from the same site (L1-L3), A, and an additional site (L4-L6), B. The relative number of Eu^{3+} at site B decreases as the powders vary from the nanowires to the microrods. In the present case, from the microparticles to the nanoparticles, the ratio of surface to volume increases greatly, but no additional site is observed. From the microrods to the nanowires, the ratio of surface to volume do not increase so much; however, the additional site B appears and the relative number of Eu^{3+} at site B changes greatly. We thus believe that the appearance of the additional site B is not caused by the surface effect, but by the shape anisotropy. This is the first time to report that the shape effect affects the local structures of Eu^{3+} doped 1D nanocrystals.

4. Electronic Transition Processes and QE of Eu^{3+} in LaPO_4 1D Nanocrystals

In 0D nanoparticles, many groups reported that the QE and luminescent intensity of Eu^{3+} ions decreased in comparison with the bulk materials due to higher nonradiative transition rate in nanoparticles [42, 43]. An important problem should be answered: does the QE of Eu^{3+} in 1D nanocrystals increase in contrast with nanoparticles and bulk materials? Song and Yu et al. systematically studied the electronic transition processes of Eu^{3+} in LaPO_4 nanowires [16, 18, 41]. The luminescence QE of 5D_1 level of Eu^{3+} was determined by the following equation:

$$\tau(T) = \frac{1}{W_1 + W_{10}(T)}, \quad (1)$$

where W_1 is the radiative transition rate of ${}^5D_1 - \sum_j {}^7F_j$, $W_{10}(T)$ is nonradiative transition rate at a certain temperature, T . According to the theory of multiphonon relaxation, W_{10} can be written as

$$W_{10}(T) = W_{10}(0)(1 + \langle n \rangle)^{\Delta E_{10}/\hbar\omega}, \quad (2)$$

where $W_{10}(0)$ is nonradiative transition rate at 0 K, ΔE_{10} is the energy separation between 5D_1 and 5D_0 , $\hbar\omega$ is the phonon energy, k is Boltzmann' constant, and $\langle n \rangle = 1/(e^{\hbar\omega/kT} - 1)$ is the phonon occupation number. According to (1) and (2), the lifetime of 5D_1 can be expressed as

$$\tau = \frac{1}{W_1 + W_{10}(0)[1 - \exp(-\hbar\omega/kT)]^{-\Delta E_{10}/\hbar\omega}}. \quad (3)$$

They measured the lifetime of 5D_1 level of Eu^{3+} ions at different temperatures and obtained the radiative and

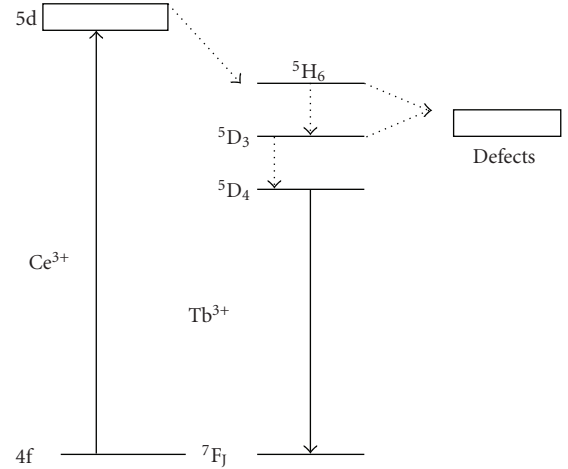


FIGURE 3: Schematic for the ET and luminescence processes in $\text{Ce}^{3+}/\text{Tb}^{3+}$ codoped LaPO_4 nanowires and microrods. (J. Phys. Chem. B 2005, 109, 11450).

nonradiative transition rate by fitting according to (3). The results were listed in Table 1. It is obvious that the radiative transition rate and QE of 5D_1 level in nanowires were higher than that in nanoparticles and bulk crystals. This result indicates that the 1D nanocrystal-doped RE ions is ideal phosphors. After then, they also studied the electronic transition processes of Eu^{3+} ions in Y_2O_3 and La_2O_3 nanowires [24, 25]. The results indicate that the radiative transition rate of Eu^{3+} in oxide nanowires hardly changes in comparison with the bulk hosts.

5. ET between RE Ions in LaPO_4 1D Nanowires

Ce^{3+} and Tb^{3+} ions are important RE ions, which have been applied in blue and green phosphors. The ET processes between Ce^{3+} and Tb^{3+} in some micrometer-sized materials, such as lanthanum oxybromide [44], aluminate [45], alkaline earth sulphate [46], and so on, were intensively investigated. As efficient green phosphors, Ce^{3+} and Tb^{3+} coactivated LaPO_4 bulk powders were extensively applied to fluorescent lamps, cathode ray tube (CRT), and plasma display panel (PDP) due to the high ET efficiency between Ce^{3+} and Tb^{3+} ions [13]. To obtain the efficient green phosphors of 1D $\text{LaPO}_4:\text{Ce}^{3+}/\text{Tb}^{3+}$ nanowires, the electronic transition and ET processes in 1D nanowires should be studied, and compared with the corresponding bulk powders. However, the studies on ET processes between Ce^{3+} and Tb^{3+} , even between different RE impurity centers, are rather rare. Song and Yu et al. fabricated Ce^{3+} and Tb^{3+} coactivated LaPO_4 nanowires as well as the micrometer-sized rods by the same hydrothermal method [17, 47]. They systematically studied and compared their electronic transition and ET processes by the luminescent spectra and dynamics analysis. Figure 2 shows the excitation and emission spectra of $\text{LaPO}_4:\text{Ce}^{3+},\text{Tb}^{3+}$ nanowires and microrods. It is obvious and important that the luminescent intensity of Tb^{3+} in $\text{LaPO}_4:\text{Ce}^{3+},\text{Tb}^{3+}$ nanowires is much stronger than that in

TABLE 2: List of dynamic results of $\text{LaPO}_4:0.01\text{Ce}^{3+}, 0.025\text{Tb}^{3+}$ nanowires and microrods.

Samples	Electronic transition rate of Ce^{3+} (ns^{-1})	Lifetime of Tb^{3+} (ms)	ET ($\text{ns}^{-1}\text{mol}^{-1}$)
nanowires	6.3×10^{-2}	2.72	0.44
microrods	5.2×10^{-2}	2.58	1.30

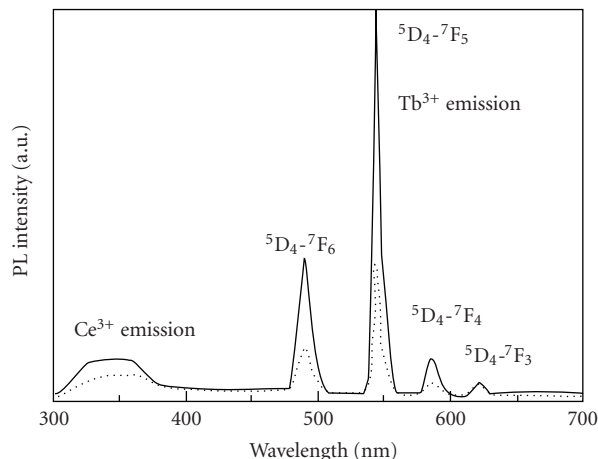


FIGURE 4: Fig. 4 Luminescence emission ($\lambda_{\text{ex}} = 278 \text{ nm}$) spectra of the dilute colloidal solutions of the $\text{Ce}_{0.9}\text{Tb}_{0.1}\text{PO}_4$ 1D nanostructures (dashed line) and the $\text{Ce}_{0.9}\text{Tb}_{0.1}\text{PO}_4@ \text{LaPO}_4$ 1D nanocable heterostructures (solid). (J. Phys. Chem. B 2008, 109, 14461).

microrods corresponding to the excitation of Ce^{3+} ions. It should be noted that the emission of Ce^{3+} or Tb^{3+} in single-doped nanowires is lower than that in microrods. The dynamic results were listed in Table 2. The dynamic measurements and analysis indicate that the electronic transition rate of Ce^{3+} and Tb^{3+} , the ET rate from Ce^{3+} to Tb^{3+} in Ce^{3+} - Tb^{3+} codoped LaPO_4 nanowires, is lower than that in microrods. They attributed the increased intensity of Tb^{3+} in nanowires to the lower ET efficiency from Tb^{3+} to other quench centers, shown in Figure 3. According to the Eu^{3+} and Tb^{3+} doped LaPO_4 nanowires, we suggested that the RE-doped 1D nanowires were ideal nanophosphors. In addition, we also observed the ET from Gd^{3+} to Tb^{3+} in $\text{GdPO}_4:\text{Tb}^{3+}$ nanorods [48].

6. The Core Shell Nanostructures of LaPO_4 Nanowires Doped with RE

Due to the increased disorder of surface atoms for nanomaterials, the nonradiative transition rate of RE-doped nanocrystals will increase. The surface modification can effectively eliminate the quenching centers at surface of nanocrystal. In 1999, Li et al prepared $\text{Y}_2\text{O}_3:\text{Eu}^{3+}@ \text{SiO}_2/\text{Al}_2\text{O}_3$ nanoparticles heterostructures and observed the increase of Eu^{3+} luminescence [49]. In 2003, Haase prepared the $\text{CePO}_4:\text{Tb}^{3+}/\text{Eu}^{3+}@ \text{LaPO}_4$ nanoparticles core-shell structures and observed that the quantum yield of Tb^{3+} was increased from 43% to 70% [50, 51]. Lin group systematically studied 0D nanoparticles doping with RE coated with SiO_2 [52–67]. Recently, 1D nanosized core-shell structures

doped with RE have been reported. Bu et al. reported uniform $\text{CePO}_4@ \text{LaPO}_4$ and $\text{CePO}_4:\text{Tb}^{3+}@ \text{LaPO}_4$ 1D single-crystalline nanocable heterostructures with highly enhanced photoluminescent emission [36]. The resulting 1D single-crystalline nanocable heterostructures have smooth and uniform LaPO_4 sheaths, which is of great significance in effectively eliminating surface trap-states and suppressing the energy quenching in ET processes. The photoluminescence results for these 1D nanocable heterostructures illustrate that the uniform LaPO_4 sheaths remarkably increase the luminescent efficiency. Figure 4 shows the emission spectra of ($\lambda_{\text{ex}} = 278 \text{ nm}$) the dilute colloidal solutions of the $\text{Ce}_{0.9}\text{Tb}_{0.1}\text{PO}_4$ 1D nanostructures (dashed line) and the $\text{Ce}_{0.9}\text{Tb}_{0.1}\text{PO}_4@ \text{LaPO}_4$ 1D nanocable heterostructures (solid lines). It is obvious that the emission intensity of Tb^{3+} and Ce^{3+} in $\text{LaPO}_4:\text{Ce}^{3+}, \text{Tb}^{3+}$ nanowires coated with LaPO_4 is much high than that in noncoated samples.

Fang et al. also reported that $\text{CePO}_4:\text{Tb}^{3+}/\text{LaPO}_4$ core/shell nanowires synthesized by a simple hydrothermal method, and the resulting 1D core/shell nanostructures have high photoluminescence efficiency [35]. Until recently, it has been considered difficult to obtain a nanocrystal phosphor material with the quantum yield being close to that of the corresponding bulk material. The novel core/shell nanostructures, which are more robust than organically passivated nanowires, may be used as building blocks for optoelectronic nanodevice applications. $\text{CePO}_4:\text{Tb}/\text{LaPO}_4$ core/shell nanowires with high quantum yield would also be a new class of biomedical labels for ultrasensitive, multicolor, and multiplexing applications owing to their nontoxicity and biocompatibility.

In summary, we introduced the recent progresses of phosphate 1D nanowires doped with RE. We suggest that the research focus should be the application of 1D nanowires in biological probe, photonic crystals, optical communication, etc in future.

References

- [1] R. N. Bhargava, D. Gallagher, X. Hong, and A. Nurmikko, "Optical properties of manganese-doped nanocrystals of ZnS ," *Physical Review Letters*, vol. 72, no. 3, pp. 416–419, 1994.
- [2] S. B. Qadra, E. F. Skelton, D. Hsu, et al., "Elastic constants and charge ordering in α' - NaV_2O_5 ," *Physical Review B*, vol. 60, no. 13, pp. 9194–9197, 1999.
- [3] M. Ihara, T. Igarashi, T. Kusunoki, and K. Ohno, "Cathodoluminescence and photoluminescence of nanocrystal phosphors," *Journal of the Electrochemical Society*, vol. 149, no. 3, pp. H72–H75, 2002.
- [4] C. Donega, A. Bol, and A. Meijerink, "Time-resolved luminescence of $\text{ZnS}:\text{Mn}^{2+}$ nanocrystals," *Journal of Luminescence*, vol. 96, no. 2–4, pp. 87–93, 2002.

- [5] L. Li, C. Tsung, Z. Yang, et al., "Rare-earth-doped nanocrystalline titania microspheres emitting luminescence via energy transfer," *Advanced Materials*, vol. 20, no. 5, pp. 903–908, 2008.
- [6] J. Del-Castillo, V. Rodriguez, A. Yanes, and J. Méndez-Ramos, "Energy transfer from the host to Er^{3+} dopants in semiconductor SnO_2 nanocrystals segregated in sol-gel silica glasses," *Journal of Nanoparticle Research*, vol. 10, no. 3, pp. 499–506, 2008.
- [7] J. Dhanaraj, R. Jagannathan, T. Kutty, and C. Lu, "Photoluminescence characteristics of $\text{Y}_2\text{O}_3:\text{Eu}^{3+}$ nanophosphors prepared using sol-gel thermolysis," *Journal of Physical Chemistry B*, vol. 105, no. 45, pp. 11098–11105, 2001.
- [8] Z. Wei, L. Sun, C. Liao, C. Yan, and S. Huang, "Fluorescence intensity and color purity improvement in nanosized $\text{YBO}_3:\text{Eu}$," *Applied Physics Letters*, vol. 80, no. 8, pp. 1447–1449, 2002.
- [9] R. S. Meltzer, S. Feofilov, and B. Tissue, "Dependence of fluorescence lifetimes of $\text{Y}_2\text{O}_3:\text{Eu}^{3+}$ nanoparticles on the surrounding medium," *Physical Review B*, vol. 60, no. 20, pp. R14012–R14015, 1999.
- [10] D. Williams, B. Bihari, B. M. Tissue, and J. McHale, "Preparation and fluorescence spectroscopy of bulk monoclinic $\text{Eu}^{3+}:\text{Y}_2\text{O}_3$ and comparison to $\text{Eu}^{3+}:\text{Y}_2\text{O}_3$ nanocrystals," *Journal of Physical Chemistry B*, vol. 102, no. 6, pp. 916–920, 1998.
- [11] K. Hong, R. Meltzer, B. Bihari, D. Williams, and B. Tissue, "Spectral hole burning in crystalline Eu_2O_3 and $\text{Y}_2\text{O}_3:\text{Eu}^{3+}$ nanoparticles," *Journal of Luminescence*, vol. 76-77, pp. 234–237, 1998.
- [12] U. Rambabu, D. Amalnerkar, B. Kale, and S. Buddhudu, "Optical properties of $\text{LnPO}_4:\text{Tb}^{3+}$ ($\text{Ln} = \text{Y}, \text{La}$ and Gd) powder phosphors," *Materials Chemistry and Physics*, vol. 70, no. 1, pp. 1–6, 2001.
- [13] J. Dexpert-Ghys, R. Mauricot, and M. Faucher, "Spectroscopy of Eu^{3+} ions in monazite type lanthanide orthophosphates LnPO_4 , $\text{Ln} = \text{La}$ or Eu ," *Journal of Luminescence*, vol. 69, no. 4, pp. 203–215, 1996.
- [14] X. Wu, H. You, H. Gui, et al., "Fabrication and characterization of heteroepitaxial bilayers of $\text{La-Ca-Mn-O/Y-Ba-Cu-O}$," *Materials Research Bulletin*, vol. 37, no. 15, pp. 2531–2538, 2002.
- [15] H. Meyssamy, K. Riwotzki, A. Kornowski, S. Nased, and M. Haase, "Wet-chemical synthesis of doped colloidal nanomaterials: particles and fibers of $\text{LaPO}_4:\text{Eu}$, $\text{LaPO}_4:\text{Ce}$, and $\text{LaPO}_4:\text{Ce,Tb}$," *Advanced Materials*, vol. 11, no. 10, pp. 840–844, 1999.
- [16] L. Yu, H. Song, S. Lu, Z. Liu, L. Yang, and X. Kong, "Luminescent properties of $\text{LaPO}_4:\text{Eu}$ nanoparticles and nanowires," *Journal of Physical Chemistry B*, vol. 108, no. 43, pp. 16697–16702, 2004.
- [17] L. Yu, H. Song, Z. Liu, L. Yang, S. Lu, and Z. Zheng, "Electronic transition and energy transfer processes in $\text{LaPO}_4-\text{Ce}^{3+}/\text{Tb}^{3+}$ nanowires," *The Journal of Physical Chemistry B*, vol. 109, no. 23, pp. 11450–11455, 2005.
- [18] H. Song, L. Yu, S. E. Lu, T. Wang, Z. Liu, and L. Yang, "Remarkable differences in photoluminescent properties between $\text{LaPO}_4:\text{Eu}$ one-dimensional nanowires and zero-dimensional nanoparticles," *Applied Physics Letters*, vol. 85, no. 3, pp. 470–472, 2004.
- [19] Y. Fang, A. Xu, R. Song, et al., "Systematic synthesis and characterization of single-crystal lanthanide orthophosphate nanowires," *Journal of the American Chemical Society*, vol. 125, no. 51, pp. 16025–16034, 2003.
- [20] C. Wu, W. Qin, G. Qin, et al., "Photoluminescence from surfactant-assembled $\text{Y}_2\text{O}_3:\text{Eu}$ nanotubes," *Applied Physics Letters*, vol. 82, no. 4, pp. 520–522, 2003.
- [21] M. Yada, M. Mihara, S. Mouri, M. Kuroki, and T. Kijima, "Rare earth (Er, Tm, Yb, Lu) oxide nanotubes templated by dodecylsulfate assemblies," *Advanced Materials*, vol. 14, no. 4, pp. 309–313, 2002.
- [22] X. Wang and Y. Li, "Rare-earth-compound nanowires, nanotubes, and fullerene-like nanoparticles: synthesis, characterization, and properties," *Chemistry—A European Journal*, vol. 9, no. 22, pp. 5627–5635, 2003.
- [23] M. Yada, C. Taniguchi, T. Torikai, T. Watri, S. Furuta, and H. Katsuki, "Versatile helical polymer films: chiroptical inversion switching and memory with re-writable (RW) and write-once read-many (WORM) modes," *Advanced Materials*, vol. 16, no. 18, pp. 1448–1450, 2004.
- [24] L. Yu, H. Song, Z. Liu, L. Yang, and S. Lu, "Fabrication and photoluminescent characteristics of $\text{La}_2\text{O}_3:\text{Eu}^{3+}$ nanowires," *Physical Chemistry Chemical Physics*, vol. 8, no. 2, pp. 303–308, 2006.
- [25] X. Bai, H. Song, L. Yu, et al., "Luminescent properties of pure cubic phase $\text{Y}_2\text{O}_3/\text{Eu}^{3+}$ nanotubes/nanowires prepared by a hydrothermal method," *Journal of Physical Chemistry B*, vol. 109, no. 32, pp. 15236–15242, 2005.
- [26] H. Song, G. Pan, X. Bai, S. Li, H. Yu, and H. Zhang, "One-dimensional rare earth compounds and complexes: preparation and improved photoluminescence properties," *Journal of Nanoscience and Nanotechnology*, vol. 8, no. 3, pp. 1316–1325, 2008.
- [27] H. Yu, H. Song, G. Pan, et al., "Preparation and luminescent properties of $\text{YVO}_4:\text{Eu}^{3+}$ nanofibers by electrospinning," *Journal of Nanoscience and Nanotechnology*, vol. 8, no. 3, pp. 1432–1436, 2008.
- [28] X. Wu, Y. Tao, C. Song, C. Mao, L. Dong, and J. Zhu, "Morphological control and luminescent properties of $\text{YVO}_4:\text{Eu}$ nanocrystals," *Journal of Physical Chemistry B*, vol. 110, no. 32, pp. 15791–15796, 2006.
- [29] L. H. Peng, Y. C. Zhang, and Y. C. Lin, "Zinc oxide doping effects in polarization switching of lithium niobate," *Applied Physics Letters*, vol. 78, no. 1, pp. 4–6, 2001.
- [30] X. Duan, Y. Yang, Y. Cui, J. Wang, and C. Lieber, "Indium phosphide nanowires as building blocks for nanoscale electronic and optoelectronic devices," *Nature*, vol. 409, no. 6816, pp. 66–69, 2001.
- [31] Z. Pan, Z. Dai, and Z. Wang, "Nanobelts of semiconducting oxides," *Science*, vol. 291, no. 5510, pp. 1947–1949, 2001.
- [32] Y. Xia and P. Yang, "Chemistry and physics of nanowires," *Advanced Materials*, vol. 15, no. 5, pp. 351–352, 2003.
- [33] M. Haase, K. Riwotzki, H. Meyssamy, and A. Kornowski, "Synthesis and properties of colloidal lanthanide-doped nanocrystals," *Journal of Alloys and Compounds*, vol. 303-304, pp. 191–197, 2000.
- [34] K. Riwotzki, H. Meyssamy, A. Kornowski, and M. Haase, "Liquid-phase synthesis of doped nanoparticles: colloids of luminescing $\text{LaPO}_4:\text{Eu}$ and $\text{CePO}_4:\text{Tb}$ particles with a narrow particle size distribution," *Journal of Physical Chemistry B*, vol. 104, no. 13, pp. 2824–2828, 2000.
- [35] Y. Fang, A. Xu, and W. Dong, "Highly improved green photoluminescence from $\text{CePO}_4:\text{Tb}/\text{LaPO}_4$ core/shell nanowires," *Small*, vol. 1, no. 10, pp. 967–971, 2005.
- [36] W. Bu, Z. Hua, H. Chen, and J. Shi, "Epitaxial synthesis of uniform cerium phosphate one-dimensional nanocable heterostructures with improved luminescence," *Journal of Physical Chemistry B*, vol. 109, no. 30, pp. 14461–14464, 2005.

- [37] Z. Wei, L. Sun, C. Liao, J. Yin, X. Jiang, and C. Yan, "Size-dependent chromaticity in $\text{YBO}_3:\text{Eu}$ nanocrystals: correlation with microstructure and site symmetry," *Journal of Physical Chemistry B*, vol. 106, no. 41, pp. 10610–10617, 2002.
- [38] Z. Wei, L. Sun, C. Liao, et al., "Size dependence of luminescent properties for hexagonal $\text{YBO}_3:\text{Eu}$ nanocrystals in the vacuum ultraviolet region," *Journal of Applied Physics*, vol. 93, no. 12, pp. 9783–9788, 2003.
- [39] Z. Wei, L. Sun, C. Liao, J. Yin, X. Jiang, and C. Yan, "Fluorescence intensity and color purity improvement in nanosized $\text{YBO}_3:\text{Eu}$," *Applied Physics Letters*, vol. 80, no. 8, p. 1447, 2002.
- [40] H. Peng, H. Song, B. Chen, S. Lu, and S. Huang, "Spectral difference between nanocrystalline and bulk $\text{Y}_2\text{O}_3:\text{Eu}^{3+}$," *Chemical Physics Letters*, vol. 370, no. 3–4, pp. 485–489, 2003.
- [41] H. Song, S. Lu, Z. Liu, and L. Yang, "Influence of shape anisotropy on photoluminescence characteristics in $\text{LaPO}_4:\text{Eu}$ nanowires," *Chemical Physics Letters*, vol. 399, no. 4–6, pp. 384–388, 2004.
- [42] H. Peng, H. Song, B. Chen, et al., "Temperature dependence of luminescent spectra and dynamics in nanocrystalline $\text{Y}_2\text{O}_3:\text{Eu}^{3+}$," *Journal of Chemical Physics*, vol. 118, no. 7, pp. 3277–3282, 2003.
- [43] H. Song, J. Wang, B. Chen, H. Peng, and S. Lu, "Size-dependent electronic transition rates in cubic nanocrystalline europium doped yttria," *Chemical Physics Letters*, vol. 376, no. 1–2, pp. 1–5, 2003.
- [44] J. Hölsä, M. Leskelä, and L. Niinistö, "Sensitization of Tb^{3+} luminescence with Ce^{3+} in $\text{LaOBr}:\text{Tb}^{3+}, \text{Ce}^{3+}$," *Journal of Solid State Chemistry*, vol. 37, no. 3, pp. 267–270, 1981.
- [45] D. Jia, W. Jia, X. Wang, and W. Yen, "Quenching of thermo-stimulated photo-ionization by energy transfer in $\text{CaAl}_2\text{O}_7:\text{Tb}^{3+}, \text{Ce}^{3+}$," *Solid State Communications*, vol. 129, no. 1, pp. 1–4, 2004.
- [46] M. Jose and A. Lakshmanan, " Ce^{3+} to Tb^{3+} energy transfer in alkaline earth (Ba, Sr or Ca) sulphate phosphors," *Optical Materials*, vol. 24, no. 4, pp. 651–659, 2004.
- [47] L. Yu, H. Song, Z. Liu, L. Yang, S. Lu, and Z. Zheng, "Remarkable improvement of brightness for the green emissions in Ce^{3+} and Tb^{3+} co-activated LaPO_4 nanowires," *Solid State Communications*, vol. 134, no. 11, pp. 753–757, 2005.
- [48] L. Yu, D. Li, and M. Yue, "Fabrication and characterization of the photoluminescent properties of Tb^{3+} doped one-dimensional GdPO_4 nanorods," *Materials Letters*, vol. 61, no. 22, pp. 4374–4376, 2007.
- [49] Q. Li, L. Gao, and D. Yan, "Effects of the coating process on nanoscale $\text{Y}_2\text{O}_3:\text{Eu}^{3+}$ powders," *Chemistry of Materials*, vol. 11, no. 3, pp. 533–535, 1999.
- [50] K. Kömpe, H. Borchert, J. Storz, et al., "Green-emitting $\text{CePO}_4:\text{Tb}/\text{LaPO}_4$ core-shell nanoparticles with 70 % photoluminescence quantum yield," *Angewandte Chemie International Edition*, vol. 42, no. 44, pp. 5513–5516, 2003.
- [51] O. Lehmann, K. Kömpe, and M. Haase, "Synthesis of Eu^{3+} -doped core and core/shell nanoparticles and direct spectroscopic identification of dopant sites at the surface and in the interior of the particles," *Journal of the American Chemical Society*, vol. 126, no. 45, pp. 14935–14942, 2004.
- [52] M. Yu, J. Lin, and J. Fang, "Silica spheres coated with $\text{YVO}_4:\text{Eu}^{3+}$ layers via sol-gel process: a simple method to obtain spherical core-shell phosphors," *Chemistry of Materials*, vol. 17, no. 7, pp. 1783–1791, 2005.
- [53] C. Lin, H. Wang, D. Kong, et al., "Silica supported submicron $\text{SiO}_2@\text{Y}_2\text{SiO}_5:\text{Eu}^{3+}$ and $\text{SiO}_2@\text{Y}_2\text{SiO}_5:\text{Ce}^{3+}/\text{Tb}^{3+}$ spherical particles with a core-shell structure: sol-gel synthesis and characterization," *European Journal of Inorganic Chemistry*, vol. 2006, no. 18, pp. 3667–3675, 2006.
- [54] C. Lin, D. Kong, X. Liu, H. Wang, M. Yu, and J. Lin, "Monodisperse and core-shell-structured $\text{SiO}_2@\text{YBO}_3:\text{Eu}^{3+}$ spherical particles: synthesis and characterization," *Inorganic Chemistry*, vol. 46, no. 7, pp. 2674–2681, 2007.
- [55] H. Wang, C. Lin, X. Liu, J. Lin, and M. Yu, "Fluorescence intensity and color purity improvement in nanosized $\text{YBO}_3:\text{Eu}$," *Applied Physics Letters*, vol. 87, Article ID 181907, 2005.
- [56] H. Wang, M. Yu, C. Lin, X. Liu, and J. Lin, "Synthesis and luminescence properties of monodisperse spherical $\text{Y}_2\text{O}_3:\text{Eu}^{3+}/\text{SiO}_2$ particles with core-shell structure," *Journal of Physical Chemistry C*, vol. 111, no. 30, pp. 11223–11230, 2007.
- [57] D. Kong, M. Yu, C. Lin, X. Liu, J. Lin, and J. Fang, "Sol-gel synthesis and characterization of $\text{Zn}_2\text{SiO}_4:\text{Mn}/\text{SiO}_2$ spherical core-shell particles," *Journal of the Electrochemical Society*, vol. 152, no. 9, pp. H146–H151, 2005.
- [58] P. Jia, X. Liu, G. Li, M. Yu, J. Fang, and J. Lin, "Sol-gel synthesis and characterization of $\text{SiO}_2@\text{CaWO}_4$, $\text{SiO}_2@\text{CaWO}_4:\text{Eu}^{3+}/\text{Tb}^{3+}$ core-shell structured spherical particles," *Nanotechnology*, vol. 17, no. 3, pp. 734–742, 2006.
- [59] G. Li, M. Yu, Z. Wang, J. Lin, R. Wang, and J. Fang, "Sol-gel fabrication and photoluminescence properties of $\text{SiO}_2@\text{Gd}_2\text{O}_3:\text{Eu}^{3+}$ core-shell particles," *Journal of Nanoscience and Nanotechnology*, vol. 6, no. 5, pp. 1416–1422, 2006.
- [60] X. Liu, P. Jia, J. Lin, and G. Li, "Monodisperse spherical core-shell structured $\text{SiO}_2-\text{CaTiO}_3:\text{Pr}^{3+}$ phosphors for field emission displays," *Journal of Applied Physics*, vol. 99, no. 12, Article ID 124902, 2006.
- [61] P. Jia, X. Liu, M. Yu, Y. Luo, J. Fang, and J. Lin, "Luminescence properties of sol-gel derived spherical $\text{SiO}_2@\text{Gd}_2(\text{WO}_4)_3:\text{Eu}^{3+}$ particles with core-shell structure," *Chemical Physics Letters*, vol. 424, no. 4–6, pp. 358–363, 2006.
- [62] M. Yu, H. Wang, C. Lin, G. Li, and J. Lin, "Sol-gel synthesis and photoluminescence properties of spherical $\text{SiO}_2@\text{LaPO}_4:\text{Ce}^{3+}/\text{Tb}^{3+}$ particles with a core-shell structure," *Nanotechnology*, vol. 17, no. 13, pp. 3245–3252, 2006.
- [63] H. Wang, M. Yu, C. Lin, and J. Lin, "Core-shell structured $\text{SiO}_2@\text{YVO}_4:\text{Dy}^{3+}/\text{Sm}^{3+}$ phosphor particles: sol-gel preparation and characterization," *Journal of Colloid and Interface Science*, vol. 300, no. 1, pp. 176–182, 2006.
- [64] G. Li, Z. Wang, M. Yu, Z. Quan, and J. Lin, "Fabrication and optical properties of core-shell structured spherical $\text{SiO}_2@\text{GdVO}_4:\text{Eu}^{3+}$ phosphors via sol-gel process," *Journal of Solid State Chemistry*, vol. 179, no. 8, pp. 2698–2706, 2006.
- [65] G. Li, M. Yu, R. Wang, Z. Wang, Z. Quan, and J. Lin, "Fabrication and photoluminescence properties of core-shell structured spherical $\text{SiO}_2@\text{Gd}_2\text{Ti}_2\text{O}_7:\text{Eu}^{3+}$ phosphors," *Journal of Materials Research*, vol. 21, no. 9, pp. 2232–2240, 2006.
- [66] C. Lin, B. Zhao, Z. Wang, et al., "Spherical $\text{SiO}_2@\text{GdPO}_4:\text{Eu}^{3+}$ core-shell phosphors: sol-gel synthesis and characterization," *Journal of Nanoscience and Nanotechnology*, vol. 7, no. 2, pp. 542–548, 2007.
- [67] P. Jia, X. Liu, Y. Luo, M. Yu, and J. Lin, "Sol-gel synthesis and characterization of $\text{SiO}_2@\text{NaGd}(\text{WO}_4)_2:\text{Eu}^{3+}$ core-shell structured spherical phosphor particles," *Journal of the Electrochemical Society*, vol. 154, no. 1, pp. J39–J43, 2007.

Research Article

Diameter-Controllable Magnetic Properties of Co Nanowire Arrays by Pulsed Electrodeposition

Youwen Yang,¹ Yanbiao Chen,¹ Yucheng Wu,² Xiangying Chen,¹ and Mingguang Kong³

¹ School of Chemical Engineering, Hefei University of Technology, Hefei 230009, China

² School of Material Science and Engineering, Hefei University of Technology, Hefei 230009, China

³ Key Laboratory of Material Physics, Institute of Solid State Physics, Chinese Academy of Science, Hefei 230031, China

Correspondence should be addressed to Youwen Yang, hfutyw@163.com

Received 24 November 2009; Revised 16 January 2010; Accepted 20 January 2010

Academic Editor: Yanqiu Zhu

Copyright © 2010 Youwen Yang et al. This is an open access article distributed under the Creative Commons Attribution License, which permits unrestricted use, distribution, and reproduction in any medium, provided the original work is properly cited.

The Co nanowires with different diameters were prepared by pulsed electrodeposition into anodic alumina membranes oxide templates. The micrographs and crystal structures of nanowires were studied by FE-SEM, TEM, and XRD. Due to their cylindrical shape, the nanowires exhibit perpendicular anisotropy. The coercivity and loop squareness (M_r/M_s) of Co nanowires depend strongly on the diameter. Both coercivity and M_r/M_s decrease with increasing wire diameter. The behavior of the nanowires is explained briefly in terms of localized magnetization reversal.

1. Introduction

Magnetic nanowires have attracted much interest in the recent years for their potential applications in high-density magnetic recording devices. To realize these applications, the structure and the growth direction of nanowires need to be controlled precisely because the magnetic properties are related to these [1–3]. The synthesis and control of the magnetic nanostructure on a large scale is a challenging issue in the field of material science. One of the solutions is the method to combine electrodeposition with template [4]. Template-assisted electrodeposition is usually advantageous over other “dry” coating technologies due to its low cost, simple equipment, and large-scale processing [5]. Magnetic studies involving template synthesized ferromagnetic nanowire arrays are mainly focused on low-density arrays, even single ferromagnetic nanowire arrays of transition metals [6]. As for high density arrays, usually the magnetic behavior of very large aspect ratio wires is comparatively investigated between different metals [7, 8] and crystal structures [9, 10]. Therefore, more studies involving densely packed arrays are needed to understand the effect of aspect ratio, packing density on array magnetic properties, and to improve their potential in data storage applications.

As we know, cobalt is a hard magnetic material with tailorable magnetic properties through variation of the structural parameters. It was demonstrated in hcp Co nanowires that depending on texture, the shape and magnetocrystal anisotropies can either compete or add up to yield a partially controllable effective anisotropy [11, 12]. Highly ordered Co nanowire arrays with uniform diameter are essential for studying their properties and application in the high-density magnetic recording devices in future. Consequently, it has recently become a popular trend to try to control the crystal structure and magnetic properties of Co nanowire arrays by modifying the deposition parameters [13, 14]. In this study, the different diameters hcp Co nanowire arrays were fabricated by pulsed electrodeposition into anodic alumina membranes (AAMs). The magnetic properties of Co nanowires have also been investigated.

2. Experimental

The AAMs were prepared by a two-step anodization process [15, 16]. The barrier layer was dissolved in H_3PO_4 solution at 30°C for 30 minutes and the pore diameter of the as-prepared AAM is about 50 nm. While the AAM with pore size of 65 nm, 90 nm is obtained by etching in H_3PO_4 solution at 30°C for 40 minutes and 60 minutes, respectively.

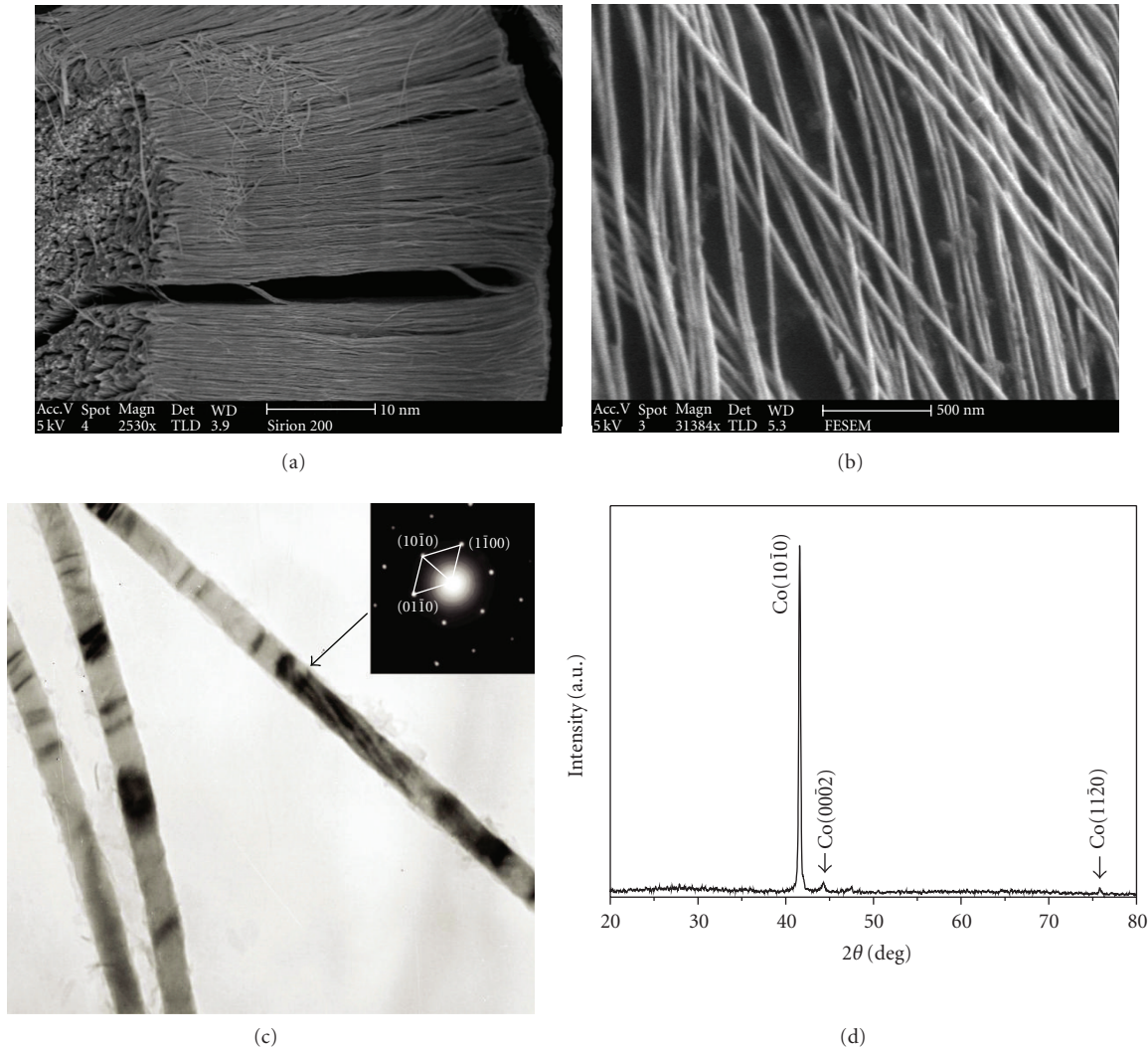


FIGURE 1: FE-SEM images, TEM images, and XRD pattern of Co nanowires.

Finally a layer of Au film (about 200 nm) was sputtered onto one side of AAM to serve as the working electrode. The pulsed electrodeposition of the Co nanowire arrays was performed in a two-electrode electrochemical cell controlled by computer, and a graphite plate was used as the counter electrode. The typical electrolyte solution contains 0.2 M $\text{CoSO}_4 \cdot 7\text{H}_2\text{O}$, 40 g/L H_3BO_3 solution. The pH value of the electrolyte was adjusted to 5.0 by 1 M NaOH and the fabrication was performed at 27°C at the voltage of -3.0 V. The pulse frequency was 200 Hz ($T_{\text{on}} = 3.75$ ms, $T_{\text{off}} = 1.25$ ms).

The X-ray powder diffraction (XRD) pattern of the nanowire arrays was obtained by an X-ray diffractometer (D/MAX-rA) with Cu K α radiation ($\lambda = 1.54178$ Å). The morphologies were observed with field emission scanning electron microscope (FE-SEM) performed on JEOL JSM-6700F and a transmission electron microscope (TEM) on H-800. For the FE-SEM investigation, the sample was immersed in 3 wt% NaOH solution to partially remove the alumina template and then washed several times with deionized water.

The TEM specimen was obtained by completely dissolving the AAM in 5 wt% NaOH solution and then rinsed with absolute ethanol and immersed in an ultrasonic bath for 8 minutes. A Physical Property Measurement System (PPMS) was used to measure the hysteresis loops of the samples at room temperature.

3. Results and Discussion

The Microscopic morphology and XRD pattern of the Co nanowire arrays are shown in Figure 1. A large-area, high density, and high-order Co nanowires were liberated from the AAM and bundled together after partly dissolving the AAM can be seen. The nanowires are long and continuous, the surface is smooth, and diameter is uniform. The length of the nanowires is about 30 μm (Figure 1(a)), and the diameter is about 65 nm (Figures 1(b) and 1(c)). The aspect ratio (length/diameter) of the nanowires is about 460. The XRD pattern of as-prepared Co nanowire arrays is shown in Figure 1(d). All peaks can be indexed to the hcp phase, and

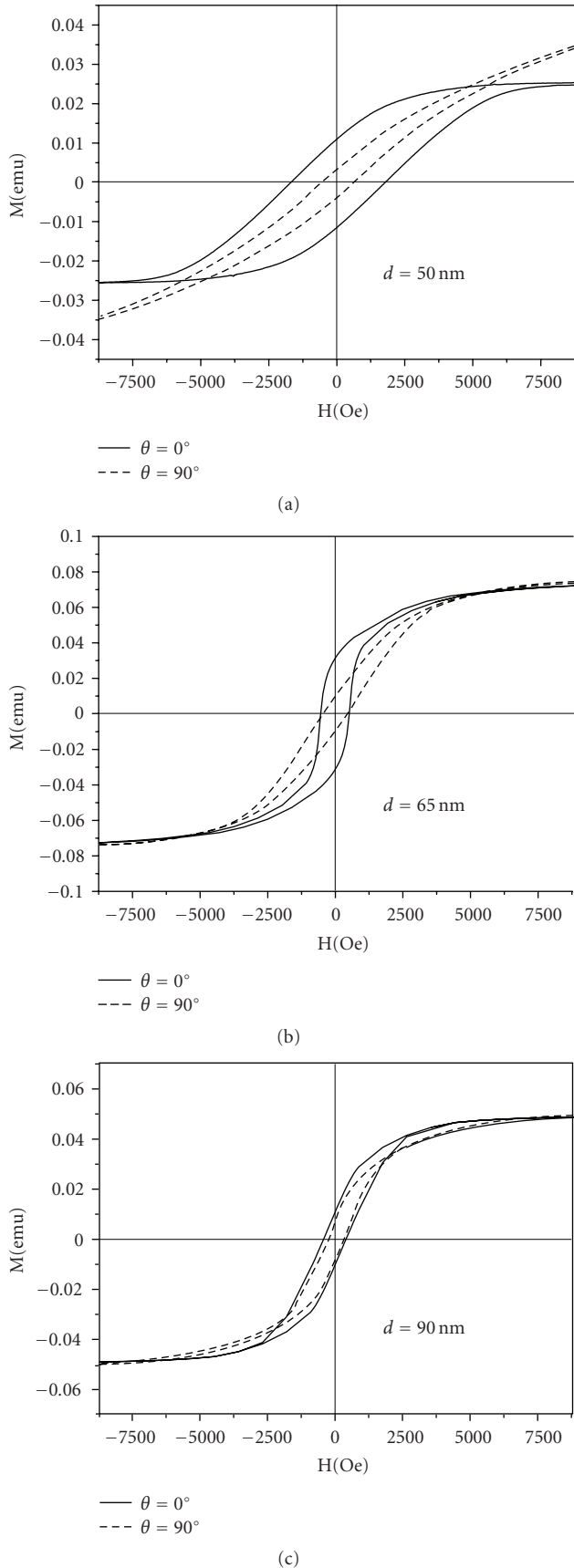


FIGURE 2: The magnetic hysteresis loops for different diameters Co nanowire arrays of 50 nm (a), 65 nm (b), and 90 nm (c).

match well with the standard diffraction peaks of Co (JCPDF 89-4308). The intensity for $(10\bar{1}0)$ planes is very strong and higher than others, which indicates that the nanowires have highly preferential orientation. The diffraction pattern which is corresponding to the area signed by the arrow can be indexed to hcp structure, and Co nanowires has a preferred orientation along the $[10\bar{1}0]$ direction (Figure 1(c)), which is in consistent with the result of the XRD.

Figure 2 shows the magnetic hysteresis loops for the Co nanowire arrays with different diameter, and the direction of the applied magnetic field is either parallel ($\theta = 0^\circ$, solid lines) or perpendicular ($\theta = 90^\circ$, dashed lines) to the axis of the nanowires. It is worth mentioning that bigger coercivity and loop squareness (M_r/M_s) (M_r is the remanent magnetization) indicate a strong magnetic anisotropy. It can be seen that, as the diameter increases, the H_c ($\theta = 0^\circ$)/ H_c ($\theta = 90^\circ$) values are 1424/584, 502/396, and 402/349 Oe; the M_r/M_s ($\theta = 0^\circ$) are 50%, 36.4%, 21.5%, while M_r/M_s ($\theta = 90^\circ$) are 20.3%, 15.7%, 9.8%. The results of the values of coercivity with the diameter of the nanowires illustrate that the shape anisotropy in the magnetization process plays an important role, and the easy axis along the wire (perpendicular to the film plane).

Nanowire magnetization process is generally in three areas by the following factors [17, 18]: magnetocrystalline anisotropy, shape anisotropy, and the interaction between the nanowires. Some works [19, 20] have reported that the effective anisotropy of the magnetic nanowire arrays comes from the competition between the magnetocrystalline anisotropy and the shape anisotropy. For hcp-phase Co, magnetocrystalline anisotropy energy density $K_1 = 5 \times 10^6$ erg/cm³ is comparable to the shape anisotropy energy density $\pi M_s^2 = 6.0 \times 10^6$ erg/cm³ [10], where M_s is the saturation magnetization of Co. Magnetocrystalline anisotropy of the hcp Co nanowires will make the magnetic moment arrange along the c -axis which perpendicular to the nanowire's axis in our experiments, but the shape anisotropy tends to arrange the magnetic moment along the axis of the nanowires [20]. So the competition between magnetocrystalline anisotropy and shape anisotropy results in a relatively weak effective anisotropy along the nanowire's axis, which leads to the low coactivity. When the diameter of the nanowires is small, each magnetic nanowire can be seen as a single domain magnetic structure. As the diameter increases, the single domain structure becomes multidomain. In the magnetization process, single domain structure of nanowires is through the atomic magnetic moment rotation to complete. The energy required to achieve this process than the energy of magnetic domain movement required is much greater. It makes small diameter nanowires with large coercivity. In contrast, the multidomain structure of nanowires is simply by moving magnetic domain to achieve in the magnetization process. This movement of energy consumed is small [21], so large diameter nanowire coercivity is smaller. The M_r/M_s changed by varying diameter is also this reason, when the external magnetic field becomes zero, the M_r/M_s decreases fast by the interaction of magnetic domains in the multidomain structure nanowires. That is the main reason that coercivity and M_r/M_s decrease

rapidly with increasing wire diameter from 50 nm to 65 nm.

Moreover, with increasing d , in-plane saturation field decreases (with perpendicular loop becoming more square) and out-of-plane saturation field dramatically rises (with parallel loop becoming more sheared). Contrary to square-like hysteresis loops of isolated (i.e., noninteracting) Co NWs [22] the parallel hysteresis loops are significantly sheared, hinting further on the presence of strong magnetostatic interactions between NWs. Even though the sample with the thickest wires ($d = 90$ nm) behaves similar to bulk-like ferromagnetic thin films, the out-of-plane (in-plane) coercivity still remains large (small). This can be attributed to the wire-like nature of the studied films. As the diameter increases from 65 nm to 90 nm, the coercivity and M_r/M_s decrease slowly. It should primarily be attributed to the evolution of magnetic interactions.

4. Conclusions

In summary, densely packed hcp Co nanowire arrays of varying diameter were obtained via pulsed electrodeposition into the pores of AAM. Dependence of magnetic properties on diameter, that is, aspect ratio, was investigated using PPMS at room temperature. It was observed that the magnetization easy axis lies parallel to Co nanowire axis. At the same time, the magnetic parameters, including coercivity, squareness, are highly correlated with diameter. So we can manipulate the magnetic property of Co nanowire arrays by changing the diameter of the nanowires.

Acknowledgment

The project was supported by the National Natural Science Foundation of China (10847115).

References

- [1] K. Nielsch, R. B. Wehrspohn, J. Barthel, et al., "Electrochemical control and selection of the structural and magnetic properties of cobalt nanowires," *Applied Physics Letter*, vol. 79, p. 1360, 2001.
- [2] F. Tian, J. Zhu, and D. Wei, "Fabrication and magnetism of radial-easy-magnetized Ni nanowire arrays," *Journal of Physical Chemistry C*, vol. 111, no. 34, pp. 12669–12672, 2007.
- [3] H. P. Liang, Y. G. Guo, J. S. Hu, et al., "Ni-Pt multilayered nanowire arrays with enhanced coercivity and high remanence ratio," *Inorganic Chemistry*, vol. 44, no. 9, pp. 3013–3015, 2005.
- [4] G. W. She, L. X. Mu, and W. S. Shi, "Electrodeposition of one-dimensional nanostructures," *Recent Patents on Nanotechnology*, vol. 3, no. 3, pp. 182–191, 2009.
- [5] X. W. Wang, G. T. Fei, P. Tong, X. J. Xu, and L. D. Zhang, "Structural control and magnetic properties of electrodeposited Co nanowires," *Journal of Crystal Growth*, vol. 300, no. 2, pp. 421–425, 2007.
- [6] R. Ferre, K. Ounadjela, J. M. George, L. Piroux, and S. Dubois, "Magnetization processes in nickel and cobalt electrodeposited nanowires," *Physical Review B*, vol. 56, no. 21, pp. 14066–14075, 1997.
- [7] Q. Liu, J. Wang, Z. Yan, and D. Xue, "Characterization and magnetic properties of $\text{Fe}_{1-x}\text{Ni}_x$ nanowire arrays," *Physical Review B*, vol. 72, no. 14, pp. 1–6, 2005.
- [8] W. Chen, S. L. Tang, M. Lu, and Y. W. Du, "The magnetic properties and reversal of Fe-Co nanowire arrays," *Journal of Physics Condensed Matter*, vol. 15, no. 26, pp. 4623–4630, 2003.
- [9] J. U. Cho, J. H. Wu, J. H. Min, et al., "Control of magnetic anisotropy of Co nanowires," *Journal of Magnetism and Magnetic Materials*, vol. 303, no. 2, pp. e281–e285, 2006.
- [10] J. Silverberg, A. Friedman, and L. Menon, "Growth and magnetic properties of polycrystalline self-assembled bifurcated Co nanowires," *Journal of Nanomaterials*, vol. 2008, Article ID 782930, 7 pages, 2008.
- [11] O. Yaçın, F. Yildiz, M. Özdemir, et al., "Ferromagnetic resonance studies of Co nanowire arrays," *Journal of Magnetism and Magnetic Materials*, vol. 272–276, no. 3, pp. 1684–1685, 2004.
- [12] X. W. Wang, Z. H. Yuan, S. Q. Sun, et al., "Thermal expansion behaviors of hcp and fcc Co nanowire arrays," *Physics Letters A*, vol. 373, no. 32, pp. 2887–2889, 2009.
- [13] J. U. Cho, J. H. Min, S. P. Ko, et al., "Effect of external magnetic field on anisotropy of Co/Cu multilayer nanowires," *Journal of Applied Physics*, vol. 99, no. 8, p. 08C909, 2006.
- [14] J. H. Min, J. U. Cho, Y. K. Kim, et al., "Substrate effects on microstructure and magnetic properties of electrodeposited Co nanowire arrays," *Journal of Applied Physics*, vol. 99, no. 8, Article ID 08Q510, 2006.
- [15] Y. W. Yang, L. Li, X. H. Huang, G. H. Li, and L. D. Zhang, "Fabrication and optical property of single-crystalline InSb nanowire arrays," *Journal of Materials Science*, vol. 42, no. 8, pp. 2753–2757, 2007.
- [16] L. Li, Y. W. Yang, X. H. Huang, G. H. Li, and L. D. Zhang, "Pulsed electrodeposition of single-crystalline Bi_2Te_3 nanowire arrays," *Nanotechnology*, vol. 17, no. 6, pp. 1706–1712, 2006.
- [17] H. N. Hu, H. Y. Chen, S. Y. Yu, et al., "Textured Co nanowire arrays with controlled magnetization direction," *Journal of Magnetism and Magnetic Materials*, vol. 295, no. 3, pp. 257–262, 2005.
- [18] M. Vazquez, K. Pirota, J. Torrejon, D. Navas, and M. Hernandez-Velez, "Magnetic behaviour of densely packed hexagonal arrays of Ni nanowires: influence of geometric characteristics," *Journal of Magnetism and Magnetic Materials*, vol. 294, no. 2, pp. 174–181, 2005.
- [19] K. Ounadjela, R. Ferré, L. Louail, et al., "Magnetization reversal in cobalt and nickel electrodeposited nanowires," *Journal of Applied Physics*, vol. 81, p. 5455, 1997.
- [20] F. Li, T. Wang, L. Ren, and J. Sun, "Structure and magnetic properties of Co nanowires in self-assembled arrays," *Journal of Physics Condensed Matter*, vol. 16, no. 45, pp. 8053–8060, 2004.
- [21] A. H. Morrish, *The Principles of Magnetism*, Wiley, New York, NY, USA, 1965.
- [22] M. Darques, A. Encinas, L. Vila, and L. Piroux, "Controlled changes in the microstructure and magnetic anisotropy in arrays of electrodeposited Co nanowires induced by the solution pH," *Journal of Physics D*, vol. 37, no. 10, pp. 1411–1416, 2004.